DISSERTATION

submitted to the
Combined Faculties for the Natural Sciences and for Mathematics
of the Ruperto-Carola University of Heidelberg, Germany
for the degree of
Doctor of Natural Sciences

presented by
Dipl.-Biol. **Michaela Schäfer**
born in Mönchengladbach, Germany

Oral examination:

_____

Tumor-borne mediators trigger heart atrophy and alter cardiac metabolism in cancer cachexia

Referees:

PD Dr. Karin Müller-Decker

Prof. Dr. Stephan Herzig

Statement of authorship (Selbstständigkeitserklärung)

I hereby declare that this thesis has been written only by the undersigned, without any unauthorized use of services of a third party. No sources or aids have been used in the preparation of this thesis other than those indicated in the thesis itself. Where the work of others has been quoted or reproduced, the source is always given. This thesis, in same or similar form, has not been available to any audit authority yet.

Ich erkläre hiermit, dass Ich die vorliegende Arbeit selbstständig und ohne unzulässige Hilfe Dritter verfasst habe. Ich habe keine anderen als die angegebenen Hilfsmittel und Quellen verwendet. Insbesondere habe ich wörtlich oder sinngemäß aus anderen Werken übernommene Inhalte als solche kenntlich gemacht. Die Arbeit ist in dieser oder ähnlicher Form noch nicht als Prüfungsarbeit eingereicht worden.

Michaela Schäfer
Heidelberg, October 2014

Summary

Cancer cachexia affects the majority of patients suffering from advanced cancers, thereby reducing response to cancer treatment, quality of life and survival. Despite the tremendous research in the cancer cachexia field, the etiology remains elusive and cachexia still represents an unmet medical need as preventive or therapeutic approaches are lacking. While skeletal muscle and adipose tissue have been studied extensively in this context, the impact of cancer cachexia on other peripheral organs remains mostly unknown.

Therefore, the present study investigated the impact of cancer-related cachexia on the cardiac muscle and the role of tumor-secreted factors in this context.

By using the cachectic Colon-26 (C26) allograft and the adenomatous polyposis coli (APC) mouse model for colorectal cancer it was shown that cardiac performance was impaired in the course of cachexia. This was associated with reduced expression of genes encoding for contractile proteins, but not an increase in fibrosis. In addition, cachectic mice developed atrophy resulting from a reduction in cardiomyocyte size which was primarily mediated through autophagy. In contrast to previous studies in skeletal muscle, activation of the ubiquitin-proteasome system was not detected. Additionally, the non-cachectic mouse colon 38 (MC38) allograft model did not show any alterations in heart function, size or gene expression.

To identify cell-specific molecular changes in cardiomyocytes, an *in vitro* model was established where primary cardiomyocytes were exposed to conditioned medium from cachexia- or non-cachexia-inducing cells. Similar to the observations in cachectic animals, primary cardiomyocytes treated with conditioned medium from C26 cells developed atrophy.

Gene expression analysis of hearts from the C26-bearing mice and of primary mouse cardiomyocytes treated with C26-conditioned medium revealed that cardiac fatty acid (FA) metabolism was altered under cachectic conditions. Transcription levels of genes encoding for proteins involved in FA transport and mitochondrial β-oxidation were elevated, whereas expression of genes encoding for glucose transporters were reduced. Further analysis showed that triglyceride storage in both hearts and primary cardiomyocytes was diminished, and functional analysis by metabolic flux analysis revealed that palmitate-driven β-oxidation and uncoupling capacity were increased under cachectic conditions.

The results obtained from the established *in vitro* model suggested that the cachexia-induced effects on the heart were mediated by tumor-secreted factors in a cell autonomous manner. Therefore, an unbiased differential secretome analysis of C26 cells combined with high-throughput cardiomyocyte phenotyping was performed to define a set of tumor-secreted mediators with cachexia-inducing capacities. A signature of seven “cachexokines” was sufficient to mediate atrophy and aberrant FA metabolism in primary cardiomyocytes. The most promising candidate amongst these seven was Ataxin10 which showed elevated serum levels in cachectic mice.

Taken together, this study demonstrates that cardiac dysfunction is an understudied clinical feature of cancer cachexia and that alterations in FA metabolism represent a distinct feature of the cachectic heart. In addition, this study provides an unbiased and functional screening setup for the investigation of tumor-secreted factors with cachexia-inducing capacity and delivers a new therapeutic starting point.

Zusammenfassung

Patienten mit Krebs im fortgeschrittenen Stadium entwickeln sehr häufig Kachexie, wodurch Therapieerfolg, Lebensqualität und Überlebensrate herabgesetzt werden. Trotz intensiver Forschung im Bereich der Krebskachexie bleiben die Ursachen weitgehend unbekannt, wodurch es bisher keine effektiven Behandlungsmethoden gibt. Während der Einfluss von Krebskachexie auf den Skelettmuskel und das Fettgewebe umfangreich untersucht wurde, ist sehr wenig über die Auswirkungen auf andere Organe bekannt.

In diesem Projekt wurde untersucht, wie sich Krebskachexie auf das Herz auswirkt und welche Tumor-sezernierten Faktoren das Herz beeinflussen.
Durch Untersuchungen an zwei Mausmodellen für kolorektalen Krebs (Colon-26 (C26) Allotransplantatmodell und adenomatöses Polyposis Coli (APC) Modell), die Kachexie entwickeln, wurde gezeigt, dass sich die Herzfunktion im Krankheitsverlauf schrittweise verschlechtert. Dies war mit einer verminderten Genexpression kontraktiler Proteine verbunden, während eine Herzfibrose nicht nachgewiesen werden konnte. Die kachektischen Mäuse entwickelten Herzatrophie, die aus einer Autophagie-induzierten Verkleinerung der Herzmuskelzellen resultierte. Eine Aktivierung des Ubiquitin-Proteasom-Systems, wie sie für die Kachexie-induzierte Skelettmuskelatrophie beschrieben wurde, konnte für das Herz nicht gezeigt werden. Im Gegensatz zu den kachektischen C26- und APC-Modellen wies ein Mausmodell für kolorektalen Krebs (Mouse Colon 38 (MC38) Allotransplantatmodell), das keine Kachexie entwickelt, keine Veränderungen in Herzfunktion, -größe und -Genexpression auf.
Um Herzmuskelzell-spezifische molekulare Veränderungen zu identifizieren, wurden primäre Kardiomyozyten mit konditioniertem Medium von Kachexie- und Nicht-Kachexie-auslösenden Zellen behandelt. In Übereinstimmung mit dem C26-Mausmodell entwickelten auch primäre Kardiomyozyten, die in C26-konditioniertem Medium gehalten wurden, Atrophie.
Genexpressionsanalysen von C26-Mausherzen und mit C26-Medium behandelten Kardiomyozyten zeigten, dass der Fettsäurestoffwechsel verändert war. Die Transkriptionslevel von Genen, die für Proteine codieren, die am Fettsäuretransport und mitochondrialer β-Oxidation beteiligt sind, waren erhöht, während die Expression von Genen, die für Glukosetransporter codieren, herunterreguliert waren. Zusätzlich waren die Triglyzeridspiegel sowohl in Herzen als auch in primären Kardiomyozyten reduziert. Funktionelle Untersuchungen zeigten weiterhin, dass die Palmitinsäure-getriebene β-Oxidation und die Entkopplungskapazität unter kachektischen Bedingungen erhöht waren.
Die *in-vitro*-Daten wiesen darauf hin, dass die Kachexie-induzierten Veränderungen des Herzens durch von den Tumorzellen sezernierte Faktoren vermittelt wurden. Deshalb wurde eine Sekretomanalyse der C26-Zellen, der eine Hochdurchsatz-Phänotypisierung folgte, durchgeführt. Sieben Faktoren waren in der Lage, sowohl Atrophie als auch Fettsäurestoffwechsel-Störungen in primären Kardiomyozyten zu induzieren. Der vielversprechendste Kandidat war Ataxin10, welcher in erhöhter Konzentration im Serum der Kachexie-Mäuse nachgewiesen wurde.

Es konnte gezeigt werden, dass die kardiale Dysfunktion ein bisher medizinisch unterschätztes Merkmal der Krebskachexie darstellt und dass Störungen im Fettsäurestoffwechsel ein Hauptcharakteristikum des kachektischen Herzens ist. Zusätzlich liefert dieses Projekt einen funktionellen Untersuchungsaufbau, der es ermöglicht, die Kachexie-induzierende Fähigkeit von Tumor-sezernierten Faktoren zu analysieren und damit einen neuen Ansatzpunkt für Therapien liefert.

Acknowledgements

First of all, I would like to thank Prof. Dr. Stephan Herzig for giving me the opportunity to perform this study in his lab, for constant advice, for very valuable discussions and for his boundless optimism. My appreciation also goes to Prof. Dr. Johannes Backs for also providing me the opportunity to work on this project, for helpful advice and for extensive collaboration.
My gratitude also goes to Karin Müller-Decker for valuable discussions and suggestions during my TAC meetings. Many thanks go to my examiner committee for reading and evaluating my thesis.

Also, I wish to thank all former and current A170 lab members for helpful discussions and input during lab meetings, for friendly support and for creating a nice working atmosphere. I am incredibly grateful to Daniela Strzoda and Yvonne Feuchter for their tremendous help and effort. With this I also would like to thank all the other technicians and our HIWIs for occasional help throughout my time in the lab. I further want to thank Christian Stoy for helpful assistance at the microscope, sharing protocols, endless conversations about "Horst" which helped to survive him without getting crazy and for amusing discussions. My gratitude also goes to Mauricio Berriel Diaz and Tobias Schafmeier for writing animal licenses for me.
Special thanks go to the "Bitchy Box" (Maria, Julia, Dany, Anja, Anke, Yvonne) for helpful scientific and non-scientific discussions, extreme carbo-loading ("Frustlade", cakes, cookies …), making lab life much more enjoyable and much else. I furthermore want to thank my "Cachexia sisters" Maria Rohm and Carolyn Algire for sharing samples and opinions with me.
Many thanks go to Julia Jäger, Ashley Eheim, Christian Stoy and Maria Rohm for proofreading the manuscript of my thesis.

I also take the opportunity to thank Ezgi Baysal, Lorenz Lehmann and Christian Oeing of the Backs Lab, who had a valuable impact on this project. With this I also would like to thank the technicians and Jessica Dietrich from the Backs Lab for isolating primary cardiomyocytes.

I am very grateful to all collaborators in Mannheim and Heidelberg, Maria Muciek and Carsten Sticht (Affymetix Chips), Katrin Eichelbaum and Jeroen Krijgsveld (secretome analysis), Hans Christian Volz and Michael Boutros (high-throughput analysis of cardiomyocyte size), Lab of Prof. Hermann-Josef Gröne (paraffin-embedding and staining), Ralf Bauer (PV-loop measurement) and Oliver Strobel (sera from pancreatitis patients), whose work directly contributed to this study.

Finally, I would like to thank my family for helping and supporting me in so many ways. I am truly thankful to Christoph who always believed in me, for cheering me up and pushing me when I needed to be pushed, and for helpful scientific discussions.

Index

1 Introduction

1.1 Cancer cachexia

1.1.1 Epidemiology

Cancer-related cachexia affects up to 80% of patients suffering from advanced cancers (Tan B.H., 2008). It is estimated that cachexia is responsible for approximately 30% of all cancer-related deaths (van Haehling S., 2010). The incidence rate for gastric/pancreatic cancer patients to develop cachexia is ~85%, patients diagnosed with colon, prostate or lung cancer ~50% and for patients with acute leukemia or breast cancer ~30% (Dewys W.D., 1980).

1.1.2 Definition

The earliest report describing cachexia was already written by Hippocrates who observed the following: "the flesh is consumed and becomes water, … the abdomen fills with water, the feet and legs swell, the shoulders, clavicles, chest and thighs melt away … This illness is fatal" (Katz A.M., Katz P.B., 1962). The term cachexia is composed of the two Greek words kakós (bad) and hexis (condition) which appropriately describes the patients' over-all constitution. The latest definition of cachexia according to the International Consensus Statement which was approved by the experts working on sarcopenia, cachexia and wasting disorders (SCWD) in 2011 is: "cachexia, is a multifactorial syndrome characterized by an ongoing loss of skeletal muscle mass (with or without loss of fat mass) that cannot be fully reversed by conventional nutritional support and leads to progressive functional impairment" (Fearon K., 2011). Cachexia is not only associated with cancer but also with acute and chronic inflammatory diseases (e.g. chronic heart failure (Katz A.M., Katz P.B., 1962; Friedberg C.K., 1966), autoimmune deficiency syndrome (AIDS) (Gottlieb M.S., 1983) and chronic obstructive pulmonary disease (COPD) (Fowler J.K., Godlee R.J., 1898).

1.1.3 Pathophysiology

Cachexia emerges by creating an environment which is characterized depending on the type of cancer by increased systemic inflammation, insulin resistance, catabolic processes, anorexia, anemia (Evans W.J., 2008) and resting energy expenditure (REE) (Tisdale M.J., 2009). The developing metabolic abnormalities generally result in a loss of whole body mass due to increased muscle protein breakdown and lipolysis in adipose tissue. All aforementioned clinical features contribute to the poor response to several cancer therapies and the decreased quality of life. Affected patients develop severe weakness and fatigue which are accompanied by reduced physical performance and survival (Dodson S., 2011). Cachexia in cancer patients is diagnosed by the following criteria which were also defined in

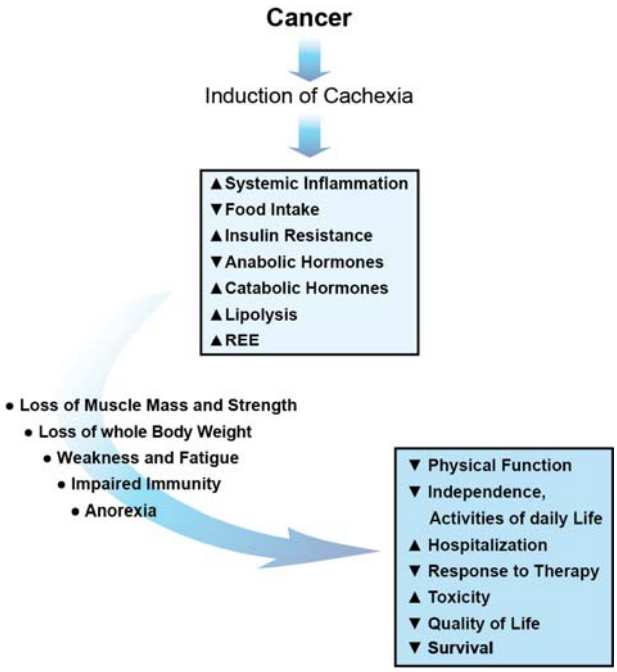

Fig. 1: Pathophysiology of cancer cachexia.
Scheme was adapted from Dodson S., 2011.

the International Consensus Statement: 1) >5% weight loss over the past 6 months, 2) Body mass index (BMI) <20 and proceeding weight loss >2% or 3) sarcopenia and proceeding weight loss >2%. Patients with early clinical and metabolic changes are staged as pre-cachectic, whereas patients with advanced cachectic symptoms and a life expectancy <3 months are classified as patients with refractory cachexia (Fearon K., 2011) (Fig. 1).

1.1.4 Mediators, signaling and target tissues

The severe metabolic changes that occur during cachexia cannot be explained by lack of nutrients alone (Tisdale M.J., 1997). Metabolic demand of the tumor also cannot account for the energy wasting because the tumor mass only equals <1% of body mass although the patients already entered the refractory cachexia stage (Fearon K., 2012). Norton and his colleagues demonstrated by performing a parabiotic transfer of cachexia in rats that circulating factors are the cause for the energy wasting (Norton J.A., 1985). Nevertheless, the etiology of cancer cachexia whether it is driven by the tumor or a result of the host response to the tumor is still unknown. However, a variety of factors have been described to contribute to the cachectic syndrome. So far, it is believed that inflammatory cytokines are the predominant driving force behind the cachectic process. Several experiments with animals showed a correlation between increased cytokine level and the degree of weight loss and/or reduced survival. Prominent pro-inflammatory cytokines that were detected under cachectic conditions include the host response-derived factors tumor necrosis factor-alpha (TNF-α) (Oliff A., 1987; Tracey K.J., 1988), also known as “cachectin” (Beutler B., Cerami A., 1986), interleukin-1 (IL-1) (Fong Y., 1989) and interferon-gamma (IFN-γ) (Mathys P., 1991) and the tumor-derived protein interleukin-6 (IL-6) (Strassmann G., 1992). Single or combined chronic treatment with the aforementioned cytokines was sufficient to reduce food intake and to increase other distinct features of the cachexia syndrome (Suzuki H., 2013).
Nuclear factor-κB (NF-κB) plays a major role in the activation of the inflammatory response which includes: 1) upregulation of the gene expression of cytokines and acute phase response (APR) proteins and 2) transduction of TNF-α signals. Tumor growth is also positively affected by NF-κB activation (Suzuki H., 2013).

1.1.4.1 Skeletal muscle

The cachexia-associated skeletal muscle atrophy is mediated by a depression in protein synthesis as well as concurrent activation of protein breakdown. The mechanisms behind this wasting process are complex with multiple factors involved. However, it is believed that the proteolysis in skeletal muscle is mainly resulting from induction of the adenosine triphosphate-dependent (ATP) ubiquitin-proteasome system (UPS). It is estimated that this pathway accounts for up to 20% of body weight loss (Khal J., 2005). Proteolytic pathways such as the autophagic/lysosomal, the Ca^{2+}-dependent and the caspase-dependent pathway do not play a major role in cancer cachexia. The key players of the cachexia induced UPS pathway are the two muscle-specific E3 ubiquitin ligases muscle atrophy F box (MAFbx/Atrogin-1) and muscle RING finger 1 (MuRF1). These proteins trigger the polyubiquitination of myofibrillar proteins targeted for degradation. The expression of the two E3 ubiquitin ligases is regulated by forkhead-box O (FoxO) transcription factors, which are normally phosphorylated and inactivated by the phosphatidylinositol 3 kinase (PI3K) - AKT pathway. The tumor-derived proteolysis-inducing factor (PIF) detected in urine of patients with various types of cancers (Todorov P., 1996) and TNF-α activate this cascade. Both factors and IFN-γ also promote muscle atrophy by decreasing protein synthesis via inhibition of the eukaryotic initiation factor 2 alpha (eIF2α). A further player in

this context is the anabolic factor insulin-like growth factor-1 (IGF-1). It inhibits the UPS and activates protein synthesis via the mammalian target of rapamycin (mTOR) - p70 S6 kinase (p70 S6K) signaling pathway. Consequently, low levels of IGF-1 were detected in the cachectic state (Donohoe C.L., 2011; Suzuki H., 2013).

A further mechanism that promotes muscle wasting is the inhibition of muscle differentiation resulting from decreased myogenic differentiation (MyoD) expression. This effect is mediated by TNF-α and also IFN-γ via the transcription factor NF-κB (Gordon J.N., 2005; Fearon K., 2012).

Another cytokine that was investigated in more detail quite recently is the transforming growth factor beta (TGF-β) family member myostatin. So far, it was believed that this protein is only synthesized and secreted from skeletal muscle cells, but recently it was shown that also cachexia-inducing tumor cells secrete myostatin (Lokireddy S., 2012). It signals via the activin type II receptor (ActRIIB) leading to an activation of the mothers against decapentaplegic homolog 2/3 (SMAD2/3) transcription factor complex which then finally results in reduced AKT-mediated protein synthesis. Elevated concentrations of myostatin as seen in cachexia trigger profound muscle atrophy via this mechanism. Normally, myostatin is blocked by IGF-1-mediated inhibition of appropriate transcription factors (Suzuki H., 2013) (Fig. 2).

Aside from direct effects of cytokines on protein synthesis and breakdown, it has been suggested that the activation of the APR contributes to muscle wasting as increased amounts of amino acids which are lacking due to reduced food intake are needed for the synthesis of APR reactants (Fearon K., 2012).

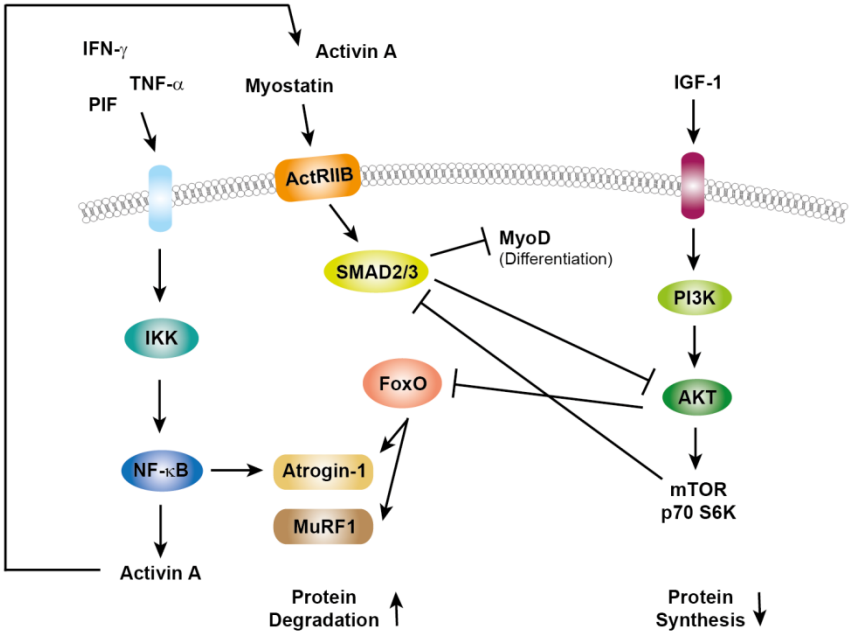

Fig. 2: Muscle protein degradation and synthesis pathways affected by cancer cachexia. *Cancer cachexia enhances the protein degradation pathways while inhibiting protein synthesis in the skeletal muscle. The main synthesis pathway signals via insulin-like growth factor 1 (IGF-1) receptor by activating the phosphatidylinositol 3 kinase (PI3K) - AKT - mammalian target of rapamycin (mTOR) cascade. Myostatin and activin A induce atrophy via the (activin type II receptor) ActRIIB receptor, which acts via mothers against decapentaplegic homolog 2/3 (SMAD2/3) resulting in an activation of forkhead-box O (FoxO) and blockage of AKT and muscle differentiation (MyoD). Cytokines such as tumor necrosis factor-alpha (TNF-α) and interferon-gamma (IFN-γ) and the tumor- secreted factor proteolysis-inducing factor (PIF) induce nuclear factor-kappa B (NF-κB) signaling. Both FoxO and NF-κB signaling induce the synthesis the two muscle-specific E3 ubiquitin ligases muscle atrophy F box (MAFbx/Atrogin-1) and muscle RING finger 1 (MuRF1) which are part of the ubiquitin-proteasome system (UPS) and trigger the polyubiquitination of myofibrillar proteins targeted for degradation. Adapted from Fearon K., 2012.*

1.1.4.2 Adipose tissue

Cancer cachexia-induced adipose tissue loss is primarily driven by increased lipolysis and by inhibition of lipogenesis. Lipolysis is catalyzed by the rate-limiting enzymes hormone sensitive lipase (HSL) and adipose triglyceride lipase (ATGL). During this process triglycerides are hydrolyzed to free fatty acids (FFAs) and glycerol, which are subsequently released into the blood stream. Increased activation of HSL as well as elevated levels of FFAs and glycerol have been determined in cancer cachexia patients. Elevated levels of the lipid-mobilizing factor (LMF), also known as zinc-alpha-2 glycoprotein (ZAG) were detected in urine of cancer cachexia patients (Hirai K., 1998). It has been shown that this protein is secreted by adenocarcinomas and acts directly on adipose tissue through a cyclic adenosine monophosphate (cAMP)-dependent pathway that activates lipolysis. Also TNF-α and IL-1 are able to induce lipolysis in adipose tissue. These two cytokines and additionally IFN-γ were shown to mediate inhibition of lipoprotein lipase (LPL) resulting in reduced lipid storage (Inui A., 2002; Gordon J.N., 2005; Fearon K., 2012).

In addition, it is reported that elevated levels of LMF (Bing C., 2002), tumor-derived parathyroid hormone-related protein (PTHrP) (Kir S., 2014), IL-6 and TNF-α (Tsoli M., Robertson G., 2012) can increase levels of uncoupling proteins (UCPs) in brown adipose tissue as well as skeletal muscle. These effects can be direct or indirect via the hypothalamic axis. The activated uncoupling process leads to increased thermogenesis which results in enhanced REE and tissue catabolism.

1.1.4.3 Liver

It has been shown that the release of pro-inflammatory cytokines, e.g. IL-6 (Castell J.V., 1989) triggers the APR in the liver. The activation and degree of the APR is mostly assessed by increased C-reactive protein (CRP) concentrations which are associated with a reduction in albumin production. The modified Glasgow Prognostic Score (mGPS) combines CRP and albumin concentrations to create a scoring system that provides a prognostic marker for survival (Suzuki H., 2013). An increase of ARP is one cause of enhanced REE.

The activation of NF-κB and signal transducer and activator of transcription 3 (STAT3) in hepatocytes via PIF mediates the production of IL-6, Interleukin-8 (IL-8) and CRP (Donohoe C.L., 2011).

1.1.4.4 Brain

Pro-cachectic factors such as cytokines (e.g. IL-1) that are secreted during a tumor burden can mimic the effects of leptin, thereby suppressing orexigenic ghrelin, neuropeptide Y (NPY) and other appetite-stimulating neuropeptides and increasing the activity of anorexigenic neuropeptides such as melanocortin and corticotropin-releasing factor (CRF) in the hypothalamus. Consequently, persistent anorexia is induced and energy expenditure is enhanced by activating thermogenesis. (Inui A., 2002; Suzuki H., 2013).

1.1.4.5 Heart

The first detailed report on how cancer cachexia affects the cardiac muscle was written in 1968 by Burch and his colleagues (Burch G.E., 1968). They documented that patients with different types of cancer developed cardiac atrophy accompanied by a decrease in the amplitude and duration of the QRS complex, indicating that the performance is impaired. They summed up their observations under the title “syndrome of the cachectic heart” (SOCH). An observational study from 1975 reported that cardiovascular insufficiency was the cause of death in 7% and a contributory factor in 3% of cancer

patients (Ambrus J.L., 1975). Lundholm and his colleagues described later that lysosomal enzyme activity was increased, protein content was reduced and that the cross-sectional area of cardiomyocytes, mitochondria content, myofibrils, and myosin filaments per myofibrils were decreased in tumor-influenced hearts (Lundholm K., 1978; Sjöström M., 1987). Despite these alterations they showed in their *ex vivo* studies that cardiac function was preserved (Sjöström M., 1987; Drott C., 1989). Subsequently, they also reported that cancer cachexia-induced heart atrophy is associated with reduced glucose uptake (Drott C. and Lundholm K., 1990).
More recent studies confirmed the old studies. They reported that the heart weight is reduced in cancer cachectic mice (Strassmann G., 1992) and that this is associated with an activation of Ca^{2+}-dependent proteolysis (Costelli P., 1993; Costelli P., 2001).

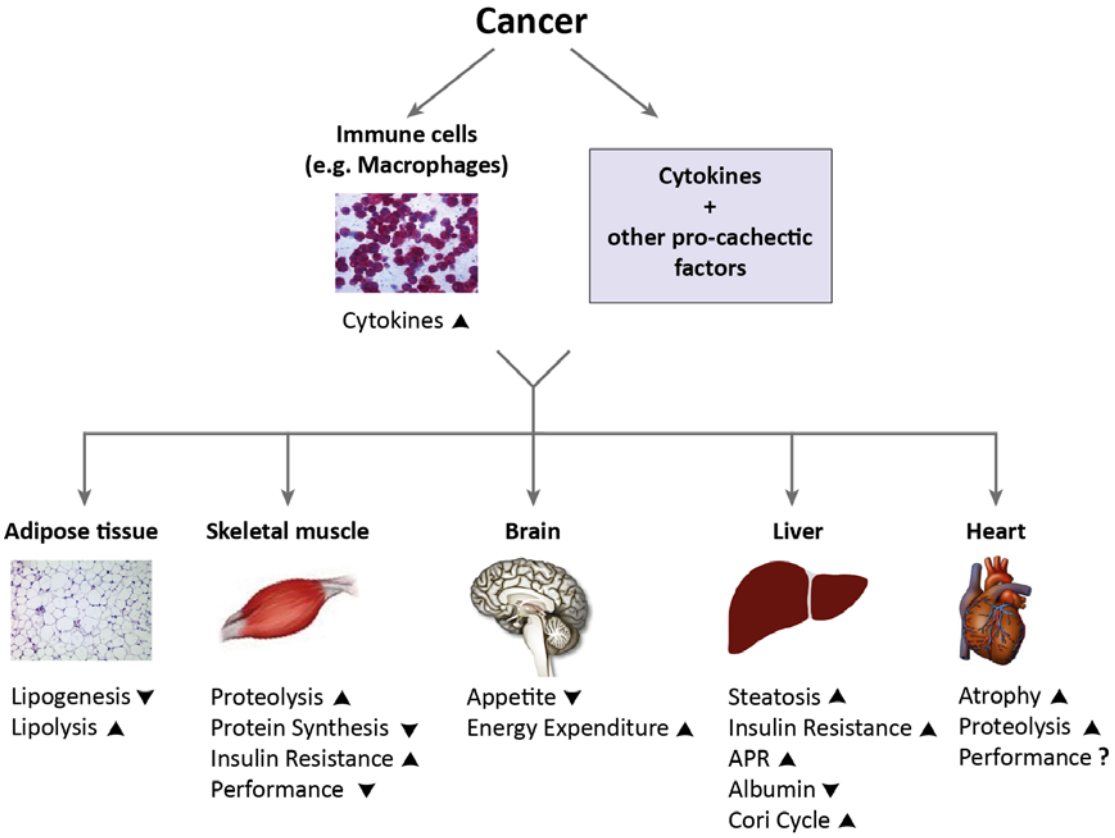

Fig. 3: Overview of the main effects of cancer cachexia on different target tissues. *Upward arrows indicate that these pathways are enhanced and downward arrows that they are blocked. Effects that are not completely clear are denoted by a question mark.*

1.1.5 Therapeutic targeting of mediators and their signaling pathways

To date, therapeutic studies have focused on the inhibition of the immune response, especially TNF-α and IL-6, and the increase of caloric intake in cancer cachexia. This chapter will focus on the manipulation of pro-cachectic factors. Several studies attempted to block pro-cachectic mediator signaling by using neutralizing antibodies, peptides or agents that directly interfere with parts of the activated pathway.

1.1.5.1 TNF-α

Animal studies that were performed shortly after the discovery of TNF-α and its role during cancer cachexia already demonstrated that blockage of TNF-α is a potential approach. Treatment with repetitive low-dose recombinant TNF-α prolonged survival by postponing body weight loss and anorexia (Sheppard B.C., 1990). Two studies using antibodies to TNF-α showed that protein degradation and lipolysis were diminished and hypertriglyceridemia could be prevented (Sherry B.A., 1989; Costelli P., 1993). The translation of the findings obtained from animal models into the human system was difficult and not entirely promising. Medical trial studies of infliximab, a monoclonal TNF-α antibody, in pancreatic cancer cachexia as well as in patients with non-small cell lung cancer did not show any beneficial effects (Wiedenmann B., 2008; Jatoi A., 2010). However, patient studies using thalidomide in the treatment of pancreatic and metastatic terminal cancer cachexia showed that inhibition of TNF-α signaling was effective in attenuating loss of body weight and lean mass and in improving the medical condition (Bruera E., 1999; Gordon J.N., 2005). Khan and his colleagues even demonstrated in a randomized controlled trial with thalidomide in esophageal cancer cachexia, that patients displayed an increase in lean body mass (Khan Z.H., 2003). Thalidomide, also known as contergan, inhibits NF-κB activation mediated by TNF-α and PIF.

1.1.5.2 PIF and LMF

Cancer cachexia animal experiments with the polyunsaturated fatty acid eicosapentanoic acid (EPA), which is contained in fish oil, showed a blockage of lipolysis and muscle protein breakdown. This FA interrupts the signaling of the two tumor derived factors, PIF and LMF, by interfering with their second-messenger production. The same results were obtained in patient studies through the administration of fish oil. Additionally, EPA is able to reduce the APR in cancer cachexia patients by the suppression of IL-6 action (Wigmore S.J., 1997). A benefit of the inhibition of PIF signaling was also shown in an animal study where antisera were used that were raised against the N-terminal region of the PIF receptor. Body and muscle weight were attenuated in these mice due to an increase in protein synthesis and a reduction in protein degradation (Todorov P., 2007). The same group tried to inhibit this axis by using an N-terminal peptide of the PIF receptor to neutralize PIF action, but this approach was not successful (Mirza K.A., 2011).

1.1.5.3 IL-6

The investigators who first described the involvement of IL-6 in experimental cancer cachexia already demonstrated that inhibition of IL-6 signaling through monoclonal antibody treatment was sufficient to suppress the development of cachectic key features (Strassmann G., 1992). Several studies followed that partially confirmed these observations. Treatment with a monoclonal antibody to IL-6 (CNTO 328) in human tumor-induced cachexia mouse models resulted in gain of body weight (Zaki M.H., 2004). A more recent study also showed that there is a benefit by blocking the IL-6 axis, but therapy with an IL-6 receptor antibody was only sufficient to suppress protein degradation and body weight loss, however it could not reverse effects as for example the inhibition of protein synthesis which would result in weight gain (White J.P., 2011).
A recent study proposes tocilizumab, an IL-6 receptor antibody, as a potential cancer cachexia therapy, because this treatment was sufficient to increase survival rate and quality of life, to attenuate body weight loss and food intake, and to minimize cachectic features in the blood (Ando K., 2014), which overlaps with the results from the original reports.

1.1.5.4 Myostatin

A promising therapeutic option is the treatment with an ActRIIB decoy receptor (sActRIIB). The blockage of the ActRIIB signaling which is activated by myostatin or activin A in different cachexia mouse models did not only prevent muscle wasting but even restored muscle mass. Additionally, cardiac atrophy was reversed and survival was significantly prolonged. However, tumor growth and adipose tissue loss were not inhibited (Zhou X., 2010). Similar results were reported for the usage of a neutralizing antibody to myostatin (Lokireddy S., 2012).

1.1.5.5 PTHrP

A recent study demonstrated that the blockage of Lewis Lung Cancer (LLC)-derived PTHrP inhibited both adipose tissue wasting and thermogenesis using a neutralizing antibody. Surprisingly, muscle wasting and function were also improved after antibody treatment (Kir S., 2014).

1.1.6 Rodent model for cancer cachexia

To investigate the complexity of the cancer cachexia syndrome, rodent models were developed. The predominantly used model is the syngeneic allograft model. Therefore, cancer cells are implanted subcutaneously or orthotopically in the same animal species. Key differences to human neoplasms are: the rapid growth of the tumors, the fast development of the cachectic syndrome and most of the tumors do not metastasize. Upon review of the literature, the most widely utilized models are: 1) mouse model: Lewis lung cancer (LLC) (Bertram J.S., Janik P., 1980), Colon-26 (C26) (Tanaka Y., 1990) and Murine adenocarcinoma 16 (MAC16) (Bibby M.C., 1987); 2) rat model: Yoshida AH-130 hepatoma (Tessitore L., 1987) and Walker 256 carcinosarcoma (Guaitani A., 1982).
Furthermore, xenograft models are used. They resemble the syngeneic model except that human cancer cells are implanted in immunosuppressed animals. The main disadvantage of these models is the missing tumor-host immune cell response which is important for cancer cachexia progression.
Human cancer cachexia is best moldeled by using genetically modified animals that spontaneously develop a tumor burden (e.g. $APC^{min/+}$ mice). However, they are not used that often due to the following reasons: assessment of tumor growth is difficult; tumor burden and cachectic syndrome develop slowly and with a higher variability.
No single animal model reproduces the full spectrum of the cachectic disease. For that reason, the choice of the correct model depends on the investigators' question. For example, the usage of a xenograft model can be useful to investigate the influence of a tumor on different tissues independent of cytokine signaling. Additionally, a combination of different models can also be used to produce several aspects of the syndrome (DeBoer M.D., 2009; Bennani-Baiti N., Walsh D., 2011).

1.2 Colorectal cancer

1.2.1 The gastrointestinal tract and the formation of colorectal cancer

1.2.1.1 The digestive system

The largest structure of the digestive system is the gastrointestinal (GI) tract, which includes the colon and the rectum. The digestive system starts with the stomach and the small intestine where food is broken down and nutrients are absorbed. In the right lower abdomen the small intestine joins the large intestine which is mostly made up by the colon. In this sectionof the bowel water and salts are absorbed from the food. The colon is segmented into the following four parts in order from proximal to distal: ascending colon, transverse colon, descending colon and sigmoid colon. The sigmoid colon joins the rectum, the final segment of the GI tract (Fig. 4).

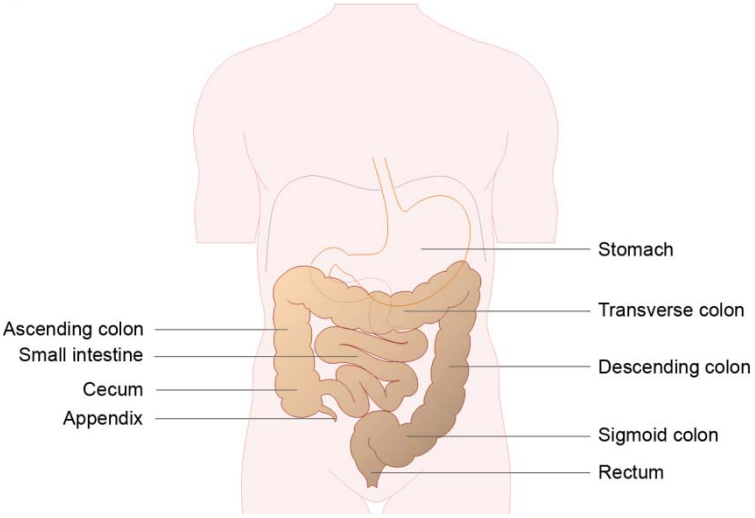

Fig. 4: Overview of the human gastrointestinal tract.

1.2.1.2 Structure of the colorectal wall

The wall of the colon and rectum is built up by several layers. The innermost layer is the bowel mucosa which forms the intestinal villa. It is made up of three different layers: the innermost layer is the epithelium followed by the lamina propria (connective tissue) and the muscularis mucosae. The mucosa joins the submucosa, a connective tissue that includes small blood vessels, lymph vessels and nerves. This layer is followed by a circular and a longitudinal muscle layer which are summarized under muscularis externa. The outermost layer is the serosa, a thin connective tissue (Fig. 5).

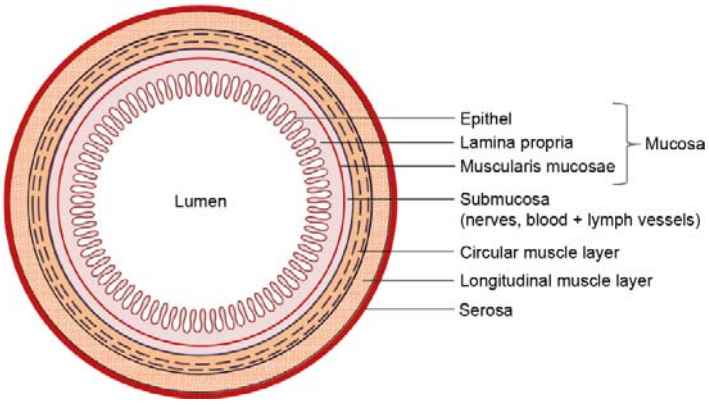

Fig. 5: Overview of the several layers of the colorectal wall.

1.2.1.3 Development of colorectal cancer

Colorectal cancer lesions start growing in the grandular epithelium which usually begins with the formation of benign polyp. Cancer that originates from these polyps is called adenocarcinoma and is the most common type of colorectal cancer. Whether a polyp becomes cancerous depends on the type of polyp. There are two types: adenomatous polyps (adenomas), and hyperplastic and inflammatory polyps. Mainly adenomas change into cancer (carcinomas) which can take up to 10 years. Polyps undergo malignant transformation when they start growing into the wall and connect to blood and lymph vessels.

Less common types of colorectal cancer are sarcomas, carcinoid tumors and GI stromal tumors (GISTs). Sarcomas start in blood vessels, in muscle and/or connective tissue in the colon or rectal wall. Lymphomas originate from lymph nodes. GISTs start growing from the intestinal cells of Cajal which are located in the muscularis externa and regulate the muscle contraction. Carcinoid tumors originate from hormone-producing cells.

1.2.1.4 Staging of colorectal cancer

The staging of colorectal cancers is based on the degree of invasion into the colon or rectal wall as well as into neighboring structures. The most commonly used staging system is the tumor-node-metastases (TNM)-system of the World Health Organization (WHO), the Union of International Cancer Control (UICC) and the American Joint Committee on Cancer (AJCC). The TNM-system describes the following three key criteria: **T** indicates how far the primary tumor has invaded into the wall of the colon or rectum and whether it has spread into nearby structures; **N** describes the extent of spread to regional lymph nodes; **M** indicates whether the cancer has metastasized. The three scorings are subcategorized by numbers which follow the characters. The greater the number the more the tumor has invaded into the wall (T1 - T4) and the more lymph nodes are affected (N0 - N2). The absence or presence of metastases is stated by M0 or M1, respectively.

1.2.1.5 Pathogenesis

Colorectal cancer is initiated by a cascade of genetic and epigenetic alterations. The most commonly mutated gene is the adenomatous polyposis coli (*APC*) gene as seen for familiar adenomatous polyposis (FAP) but also for sporadic cancers. In contrast to FAP, the ablation of the *APC* gene is not the initiator of adenoma formation in sporadic tumors. A lack of the APC protein results in the accumulation of the transcription factor β-catenin. It activates the transcription of genes such as v-myc avian myelocytomatosis viral oncogene homolog (*MYC*) and cyclin D1 (*CCND1*) which are normally involved in stem cell renewal and cell differentiation (Wnt-signaling). However, mutations in mismatch-repair (MMR) genes (e.g. MutL homolog 1 (*MLH1*) or MutS homolog 2 (*MSH2*)) as shown for hereditary non-polyposis colorectal cancer (HNPCC) can also initiate colorectal cancer by accumulating mutations in oncogenes and tumor suppressor genes. Mutations in MMR genes are believed to be induced by aberrant CpG island methylation or point mutations. The increase in CpG island methylation is associated with the mutation of the oncogene v-raf murine sarcoma viral oncogene homolog B (*BRAF*). BRAF is a protein kinase downstream of the rat sarcoma (RAS) G-protein in the RAS/RAF/MEK/ERK pathway, which affects cell division and differentiation. The loss in DNA repair leads to microsatellite instability which results in frameshifts.
It is reported that the mutation of the deleted in colon cancer (*DCC*) gene promotes the transition of an intermediate adenoma to a late adenoma. This neural cell adhesion molecule normally promotes apoptosis thereby suppressing tumor growth. Mutations in the tumor protein 53 (*TP53*) gene, which normally regulates cell division and apoptosis, or in the Kirsten rat sarcoma viral oncogene homolog (*KRAS*), which promotes cell division, are described to promote the transition to carcinoma. Further examples for gene mutations that facilitate the progression from late adenoma to carcinoma are mutations in the TGF-β receptor type 2 (*TGFBR2*), B cell lymphoma 2 (*BCL2*) associated X protein (*BAX*) and activin receptor type 2 (*ACVR2*) genes. TGF-β (NF-κB signaling) as well as activin normally control cell growth, cell proliferation, cell differentiation and apoptosis. The BAX protein is also a regulator of apoptosis (Cappell M.S., 2005; Grady W.M., Carethers J.M., 2008).

1.2.1.6 Epidemiology

In 2010, 13.4% of all newly diagnosed cancer cases in men and 12.7% in women were colorectal in Germany, placing intestinal cancer as the third and second most common tumor entity in men and women, respectively. In other words, in Germany every 7th tumor burden was related to the intestine. Colorectal cancer was with 11.4% the second most frequent and with 12.5% the third most frequent of all cancer deaths in men and women, respectively. The five-years survival rate was ~65% in both sexes. The survival correlates with the stage of diagnosis. The incidence for developing colorectal cancer is increasing with age. The mean age of a person diagnosed with colorectal cancer was between 71 and 75 years (Robert-Koch-Institut, 2013). For other industrialized countries the picture is similar. The American Cancer Society estimated for the year 2013 that colorectal cancer was the third most common cancer diagnosed in men and women and it was the third leading cause of cancer-related deaths in the U.S.

Roughly two-thirds of all intestinal cancers develop in the colon and ~30% affect the rectum. That is why intestinal cancer is commonly referred to as colorectal cancer. About 85% of these tumors were characterized as adenocarcinoma (Robert-Koch-Institut, 2013).

1.2.1.7 Risk factors for the development of colorectal cancer

The most prominent risk factors for colorectal cancer are cigarette smoking, obesity and type-2 diabetes. Physical inactivity, low fiber diet, frequent consumption of alcohol as well as red meat also increase incidence of colorectal cancer. Chronic inflammatory bowel diseases such as Chrohn's disease and ulcerative colitis can contribute to the development of cancer, but to a lesser degree. Besides that, the hereditary colorectal cancer diseases FAP and HNPCC only account for a small percentage of colorectal cancers. However, patients with first degree relatives diagnosed with colorectal cancer with hereditary factors in the absence of FAP and HNPCC have a 2 - 3 fold increased risk (St John D.J., 1993).

1.2.2 Mouse models for colorectal cancer

1.2.2.1 Mouse models with mutations in colorectal cancer-associated genes

The first mouse model for human FAP was the multiple intestinal neoplasia (Min) model (Moser A.R., 1990). These APC$^{min/+}$ mice are heterozygous for a germline mutation of codon 850 in the *Apc* gene (Su L.K., 1992). This results in the production of a truncated Apc protein that lacks the β-catenin degradation domain. APC$^{min/+}$ mice develop multiple adenomatous polyps but mainly in the small intestine and not in the colon as observed for human FAP. Also other Apc mouse models carrying a germline mutation at a different codon are developing adenomatous polyps preferentially in the small intestine. Depending on the location of the mutation, Apc mice can develop 3 - 300 polyps in their intestine. The APC$^{min/+}$ mice are commonly used to study cancer cachexia in a genetically modified mouse model.

More recently generated Apc mouse models develop adenomatous polyps in the distal colon. One example is the Apc mouse model that carries a germline mutation in exon 14. The induced frameshift results in a truncated polypeptide with a length of 605 amino acids, of which the first 580 amino acids correspond to the normal Apc protein (Colnot S., 2004; Kuraguchi M., 2006). These mice are named APC$^{\Delta 14/+}$ or APC$^{\Delta 580/+}$.

However, the transformation of adenomas to carcinomas is rare in all Apc mouse models (Taketo M.M., Edelmann W., 2009).

Most mouse models for HNPCC carry ablations either in the *Msh2* gene or in the *Mlh1* gene. These mice develop adenomas and also adenocarcinomas in the small and large intestine. More sufficient for HNPCC studies are mice with intestine-specific ablations of these genes because whole body knockout mice such as the $Msh^{2-/-}$ and the $Mlh^{1-/-}$ mice predominantly develop lymphomas and only with advanced age adenomas and adenocarcinomas in the intestine (Reitmair A.H., 1996; Edelmann W., 1999) but also cancers in other tissues. A recent example is the conditional knockout mouse in which *Msh2* is only knocked-down in villin-expressing tissues which are mainly the small and large intestine (Kucherlapati M.H., 2010). The combination of *Mlh1*-deficient mice with Apc1638N mutant mice (Edelmann W., 1999) as well as the combination of *Msh2*-deficient mice with $APC^{min/+}$ mice (Reitmair A.H., 1996) enhances the rate of tumorigenesis. This demonstrated that accelerated intestinal tumorigenesis is caused by cascades of genetic alterations.

In addition to the aforementioned colorectal cancer mouse models, there are numerous mouse strains available with knockouts or knockdowns of further MMR genes as well as other genes that encode for signaling molecules such as TGF-β_1 (Engle S.J., 1999) and Kras (Janssen K.P., 2002). There are also more examples for the combination of mutations in the *Apc* gene and genes of the so called modifiers of Apc such as mothers against decapentaplegic homolog 4 (*Smad4*) (Takaku K., 1998). These modifiers enable the transition of the Apc-induced adenomas to carcinomas.

1.2.2.2 Colorectal cancer mouse models beside the genetically modified models

Aside from directed mutagenesis, chemicals are also used to induce colorectal tumors. One prominent example is azoxymethane (AOM). This carcinogen induces mainly tumor formation in the distal colon (Papanikolaou A., 1997). AOM-induced tumors display aberrant protein expression for Apc (Maltzman T., 1997) and several more molecular signatures that are described in human colorectal cancer.

The disadvantage of all the aforementioned mouse models is the lack of metastasis. To investigate the process of metastasis researches often employ xenograft models. In these models human colon cancer cells are injected subcutaneously in the hind limbregion or directly onto the serosa of the intestine or into the colonic submucosa via colonoscopy (orthotopic implantation). Additionally, human colon specimens can be implanted (Fu X., 1991).
Syngeneic mouse models that are extensively investigated in the context of metastasis formation are the CT26, CT38 and CMT93 mice. The implanted cells were derived from chemically-induced mouse colon or rectal carcinoma cells.

1.3 The heart

1.3.1 Heart structure

The heart is located within the rib cage between the lungs. It is surrounded by a protective thin membrane, the pericardium. The heart looks like a triangle, with a broad base at the top where the great veins (superior and inferior venae cavae) and arteries (aorta and pulmonary trunk) are attached and a rounded tip at the bottom, the apex. The heart is separated into the left and right heart. The left heart has a greater muscle mass because it has to exert a higher pressure. Both sides of the heart are divided into two chambers: the atrium and the ventricle. The wall that separates the left and the right heart is called septum. The atria and the ventricles are horizontally divided by the atrioventricular valves (right: tricuspid valve; left: mitral valve) (Fig. 6).
The heart wall consists of three layers: the endocardium (innermost), myocardium (middle) and the epicardium (outermost). The epicardium is a thin layer of connective tissue. The myocardium makes up the majority of the wall and is mainly composed of cardiac muscle cells. The endocardium is a thin layer of endothelium that is joined to the myocardium with a thick layer of connective tissue that includes smooth muscles (Fig. 6).

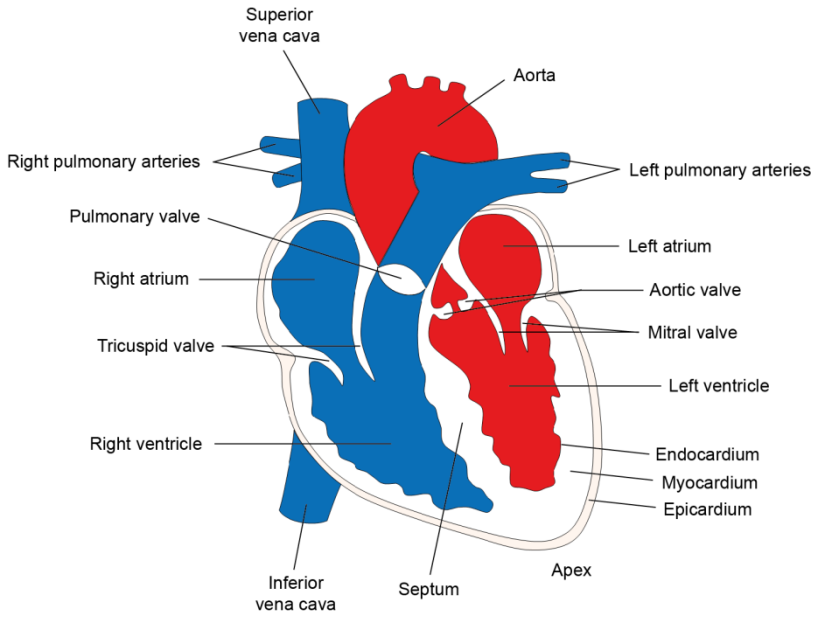

Fig. 6: Schematic illustration of the human heart. *The deoxygenated blood flow is highlighted in blue and the oxygenated blood flow in red.*

The postnatal heart mainly consists of the following four cell types: cardiomyocytes, cardiac fibroblasts, endothelial cells and vascular smooth muscle cells. Roughly 70% of an adult rat or human heart is composed of non-myocytes whereas the fibroblasts built up the majority. Only ~30% of the heart is made up by cardiac myocytes, although they occupy most of the heart volume (Zak R., 1974; Nag A., 1980). But there are differences between species: postnatal mouse hearts consist to ~60% of cardiomyocytes and only to ~40% of non-myocytes (Banerjee I., 2007). These results are explained by the difference in the heart rate which is for example approximately two times greater in mice compared to rats.

1.3.2 Cardiomyocyte structure

Cardiomyocytes have the striated structure of skeletal muscle cells, but that is only one of few similar characteristics. Cardiac muscle cells have only one centered nucleus, whereas the skeletal muscle cells are syncytial and the nuclei are located at the border. Cardiomyocytes possess much more mitochondria compared to skeletal muscle cells. Additionally, they are often branched and their actin filaments are thinner and their microtubuli thicker.
The myofilaments which are in the cytoplasm are not arranged in uniform cylindrical myofibrils but in joined strip-type structures. Large mitochondria, glycogen granules and lipid droplets are enclosed between the myofibrillar structures. Lipid droplets and glycogen granules can also be found in the myofilament-free areas at the top and the bottom of the nuclei.

1.3.3 Cardiac cycle

The pumping cycle consists mainly of two phases: diastole and systole. During the diastole the ventricles are relaxed. In this time period deoxygenated blood enters the right atrium via the venae cavae and concurrently oxygenated blood fills the left atrium via the pulmonary veins. Subsequently, the blood is passively flowing into the corresponding ventricles through the atrioventricular valves. At the end of the diastole, both atria contract, to fill the ventricles completely. After that, the atrioventricular valves close and the ventricles start contracting. This sets the beginning of the systole. During this time phase blood is ejected from the right ventricle into the pulmonary arteries and from the left ventricle into the aorta.

1.3.4 Assessment of cardiac performance

1.3.4.1 Echocardiography

An echocardiogram uses sound waves to display a moving picture of the heart, which allows the analysis of the pumping capacity. Additionally, it gives information on the heart shape.
Echocardiographic one-dimensional M(otion)-Mode function allows the assessment of the size of the heart caves and nearby vessels, the thickness of the heart wall as well as the motion of the atrioventricular valves. A two-dimensional transthoracic echocardiogram (2D Echo), which is capable of imaging a cross-sectional slice of the beating heart can, in addition, measure the actual contractions. This measurement can be used for the determination of the stroke volume (SV), the ejection fraction (EF) and the fractional shortening (FS) of the heart. The stroke volume represents the volume of blood that is ejected by one ventricle during one cardiac cycle. To calculate the SV, the blood volume in the ventricle at the end of the systole (end-systolic volume (ESV)) is subtracted from the volume prior to the contraction (end-diastolic volume (EDV)). The EF reflects the volumetric fraction of the end-diastolic volume which is pumped out by one ventricle with each heartbeat. EF is given as: (SV/EDV)x100%. FS describes the degree of shortening of the left ventricular diameter between diastole and systole. To calculate this fraction, the left ventricular internal diameter as the largest anteroposterior diameter in either diastole (left ventricular end-diastolic diameter (LVEDD)) or systole (left ventricular end systolic-diameter (LVESD)) is determined. FS is expressed as ((LVEDD-LVESD)/LVEDD)x100%.

1.3.4.2 Pressure Volume (PV) loop measurement

The invasive PV loop measurement allows the real-time assessment of systolic and diastolic pump properties within the left ventricle. To perform a PV loop measurement a catheter is placed into the

left ventricle. Several clinically relevant hemodynamic events such as cardiac output, ejection fraction and myocardial contractility can be determined. To display a PV loop, the ventricular pressure is plotted against the ventricular volume at several time points throughout an entire cardiac cycle.
A cardiac cycle starts with increasing tension in the left ventricle (contraction phase). Once the pressure reached the diastolic aortic pressure, the aortic valve opens and the blood is ejected into the aorta whereby the pressure rises more (ejection phase). With that, the systole is finished and the diastole begins. The pressure in the left ventricle decreases, the aortic valve closes and the heart relaxes (relaxation phase). When the left ventricular tension comes below the pressure of the left atrium, the mitral valve opens and the atrium gets filled (filling phase). Under normal conditions the contraction and relaxation phase proceed with constant volume (isovolumic). A schematic scheme of a PV loop is depicted in Figure 11 J.

1.3.5 Markers of heart failure

Heart failure is associated with cardiac remodeling which includes alterations in the extracellular matrix, contractile proteins, metabolism and cardiac gene expression. A reliable marker for the assessment of alterations in cardiac gene expression is the re-activation of the fetal gene expression, such as atrial natriuretic peptide (ANP), brain natriuretic peptide (BNP) and beta-myosin heavy chain (β-MHC). These genes are normally highly expressed in the fetal heart, with significant reduced expression in the postnatal heart. ANP and BNP are hormones that are mainly secreted by atrial cardiomyocytes in response to hemodynamic or metabolic stress and maintain the cardiorenal homeostasis (Cameron V.A., Ellmers L.J., 2003). The contractile protein β-MHC is replaced by α-MHC, which has a higher ATPase activity, in the adult rodent heart (Lompre A.M., 1984). However, also in this case species differences exist. In humans β-MHC is predominantly expressed in both the fetal and the postnatal heart but during heart failure α-MHC expression increases (Lowes B.D., 1997).
In addition, the failing postnatal heart switches from fatty acids as carbon source to glucose, which corresponds to fetal metabolism. This switch is associated with a decreased expression of the glucose transporter 4 (GLUT4) and enhanced expression of glucose transporter 1 (GLUT1). The insulin-dependent GLUT4 is predominantly expressed in the adult heart and the insulin-independent GLUT1 is mainly expressed in the fetal heart (Postic C., 1994).

1.3.6 Cardiac fatty acid metabolism

The heart is the organ with the highest energy demand and for this reason it has to continuously generate adenosine triphosphate (ATP) at a high rate. Almost 95% of ATP is generated via mitochondrial oxidative phosphorylation. Thereby, roughly 70% of energy is obtained from FAs in a healthy adult heart, although more oxygen per molecule of ATP is consumed. While glucose and lactate are preferred, the heart can metabolize nearly all carbon substrates making it easily adaptive to changes in nutrient supply (Bing R.J., 1954). However, there are species differences with mice only generating ~40% of the cardiac energy from FAs.
The heart metabolizes especially long-chain FFAs ligated to albumin and esterified FAs bound to chylomicrons and very-low density lipoproteins (VLDL). FFAs are taken up into the cardiomyocytes via passive diffusion or directed via FA translocase (FAT/CD36) and the FA transporters 1 and 6 (FATP1/6). The majority (50-60%) of FAs are transferred into the cardiomyocytes through FAT/CD36-mediated transport. FAs from chylomicrons or VLDL are released by lipoprotein lipase (LPL) and subsequently taken up by the aforementioned transporters. LPL is synthesized in cardiac myocytes

and is transferred to the capillary endothelial cell surface. FAs are not only metabolized but also a proportion of ~20% are stored in lipid droplets as triglycerides (TGs). Perilipins 2 - 5 (PLIN2 - 5) are proteins associated with cardiac lipid droplets. FAs entering the cardiomyocytes are esterified to long-chain acyl-coenzyme A (CoA) by the enzyme acyl-CoA synthetase long-chain family member 1 (ACSL1). For storage, the enzyme diglyceride acyltransferase (DGAT1) catalyzes the formation of TGs from diacylglycerol and the generated acyl-CoA. For the transport into the mitochondria the acyl-CoA esters are bound to carnitine via the mitochondrial key enzyme carnitine palmitoyltransferase 1 (CPT1) to produce long-chain acylcarnitine. CPT1 activity is inhibited by malonyl-CoA, which is synthesized from acetyl-CoA via acetyl-CoA carboxylase (ACC). Once ACC gets phosphorylated by adenosine monophosphate-activated protein kinase (AMPK) it loses its activity. Thus, increased levels of AMPK and decreased activity of ACC correlate with increased FA β-oxidation. The acylcarnitine is transported into the mitochondrial matrix by a carnitine:acylcarnitine translocase (CT) that involves the exchange of carnitine and acylcarnitine. After entering the mitochondrial matrix, acylcarnitine is converted back to long-chain acyl-CoA by CPT2 so that it can finally enter the β-oxidation pathway. Here, they are metabolized by sequential breakdown into acyl-CoAs by acyl-CoA dehydrogenase (ACAD), enoyl-CoA hydratase (ECH), 3-hydroxyacyl-CoA dehydrogenase (HADH) and 3-ketoacyl-CoA thiolase (3-KAT) (Fig. 7).
Most of the enzymes that are involved in cardiac FA metabolism are under transcriptional control. A major transcriptional regulator of this process is the peroxisomal proliferator activated receptor alpha (PPARα) (Lopaschuk G.D., 2010).

An increase in fatty acid utilization as observed for obesity and diabetes, results in increased uncoupling and/or futile cycling. Uncoupling decreases the cardiac efficiency by lowering ATP synthesis rate and futile cycling by wasting ATP for non-contractile purposes. It has been shown that oxygen consumption is increased under these conditions, which was accompanied by a decrease in cardiac efficiency by 30% (Mjos O.D., 1971). Uncoupling is activated due to an increased delivery of acetyl-CoA which results in enhanced production of reducing equivalents ($FADH_2$ and NADH) and elevated levels of reactive oxygen species (ROS). Proteins that are mainly involved in cardiac uncoupling are the uncoupling proteins 2 and 3 (UCP2/3) and the adenine nucleotide translocases 1 and 2 (ANT1/2). The UCPs are inner mitochondrial membrane-bound proteins that uncouple ATP production from oxidative metabolism. Thereby, UCP2 reduces the generation of ROS in the mitochondria whereas UCP3 translocates FA anions out of the mitochondrial matrix. FA anions are generated by the cleavage of long-chain acyl-CoA esters by the mitochondrial thioesterase (MTE). These actions result in a proton leak. ANT1 and 2 are also inner mitochondrial membrane-bound proteins which are commonly known as ADP/ATP translocators. They are required for the export of ATP from the mitochondrial matrix and the import of ADP into the matrix. Additionally, it was reported that the ANTs possess uncoupling capacity which is equivalent to the function of UCP3 (Skulachev V.P., 1991) (Fig. 7).
One futile cycle is generated via UCP3 action. The translocated FA anions are converted to acyl-CoA esters and subsequently they are transported back into the mitochondrial matrix. There they are again metabolized via β-oxidation. For that process ACSL1 is required which wastes two molecules of ATP. Furthermore, the inhibition of ANT by long-chain acyl-CoAs is believed to generate a futile cycle as ATP cannot be exported to the cytosol for hydrolysis (Pande S.V. and Blanchaer M.C., 1971). A third futile cycle is present in the FFA-TG-storage cycle. The release of FFAs from the lipid droplets as well as their reincorporation into the pool requires the conversion to acyl-CoA esters which occurs in an ATP-dependent manner. ATP wasting is also promoted by increasing levels of sarcolemmal Ca^{2+} in

the cytosol which result from an enhanced activation of Ca^{2+}-channels by a surplus of long-chain FAs. The maintenance of cytosolic Ca^{2+}-homeostasis consumes ATP (Lopaschuk G.D., 2010).

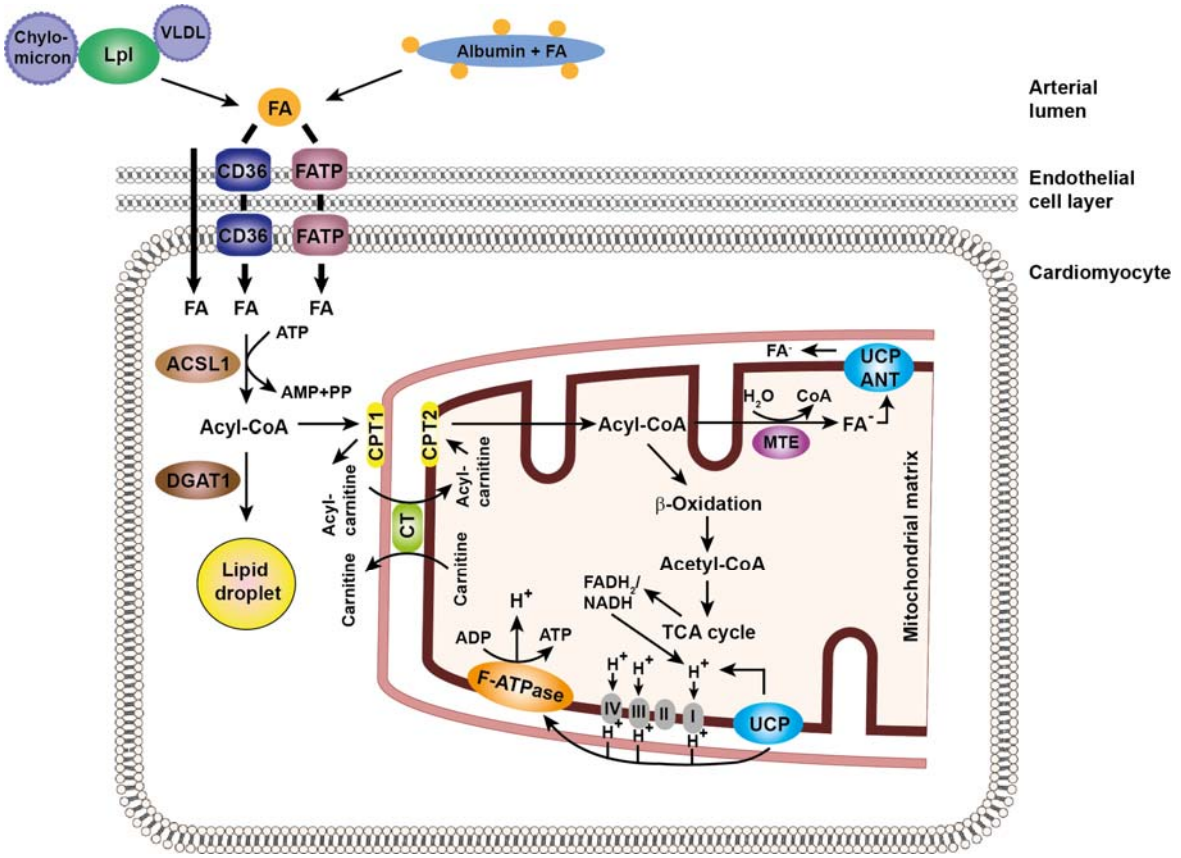

Fig. 7: Overview of cardiac fatty acid metabolism. *Fatty acids (FAs) metabolized by the heart are delivered bound to albumin or contained within very-low density lipoproteins (VLDL) or chylomicrons. FAs bound to lipoproteins are released by the lipoprotein lipase (LPL). Free FAs enter the cardiomyocytes via passive diffusion or active transport through fatty acid translocase (FAT/CD36) or the fatty acid transporters 1 and 6 (FATP1/6). Once in the cell FAs are esterified by acyl-coenzyme A (CoA) synthetase long-chain family member 1 (ACSL1) to long-chain acyl-CoA which can be either used for lipid storage or β-oxidation. For storage, the enzyme diglyceride acyltransferase (DGAT1) catalyzes the formation of TGs from diacylglycerol and the generated acyl-CoA. For the transport into the mitochondrium acyl-CoA is bound to carnitine by the carnitine palmitoyltransferase 1 (CPT1). Subsequently, acylcarnitine is transported into the mitochondrial matrix by carnitine:acylcarnitine translocase (CT) where CPT2 converts it back to acyl-CoA. Then, it enters the β-oxidation cycle for the generation of acetyl-CoA. Under certain conditions energy wasting occurs via uncoupling and/or futile cycling. Proteins that are involved in this processes are the uncoupling proteins 2 and 3 (UCP2/3) and the adenine nucleotide translocases 1 and 2 (ANT1/2). Adapted from Lopaschuk G.D., 2010 and Goldberg I.J., 2012.*

1.4 Aim of the study

The vast majority of previous research in the cancer cachexia field addressed the mechanisms of skeletal muscle atrophy although several studies suggest that the cardiac muscle represents an understudied component of cancer cachexia. Additionally, the question of the etiology of cancer-related cachexia remains elusive, and preventive and therapeutic approaches are still missing. Nevertheless, most studies are still focusing on the mediators that have been known for decades although these factors display weak prognostic and therapeutic potential.

Thus, the aim of this project was to investigate whether cancer cachexia induces functional, morphological, molecular and metabolic changes in the heart, and whether these alterations are mediated by tumor-secreted factors in a cell-autonomous manner.

2 Results

2.1 Phenotypic analysis of C26 cancer cachexia mouse model

2.1.1 Transplantation of C26 colon adenocarcinoma cells induces cachexia

To investigate the influence of cancer cachexia on morphological, physiological, molecular and metabolic properties of the heart, the well-established C26 cancer cachexia mouse model was used (Corbett T.H., 1975; Tanaka Y., 1990). 9 - 10 week old Balb/c male were subcutaneously injected with 1.5 x 10^6 C26 cells. Body weight, body composition, heart function and tumor growth were monitored for 21 days after tumor cell inoculation. Tumors were palpable 5 days after C26 cell injection. Inoculation of the established C26 cell line clone resulted in a significant reduction of total body weight (~10%) (Fig. 8 A). This was associated with a significant loss of skeletal muscle mass (Fig. 8 B), represented by gastrocnemius muscle weight, and total body fat mass (Fig. 8 C). The wasting processes began between day 7 and 14 after tumor implantation (Fig. 8 A - C). Total body lean mass was not affected (Fig. 8 D).

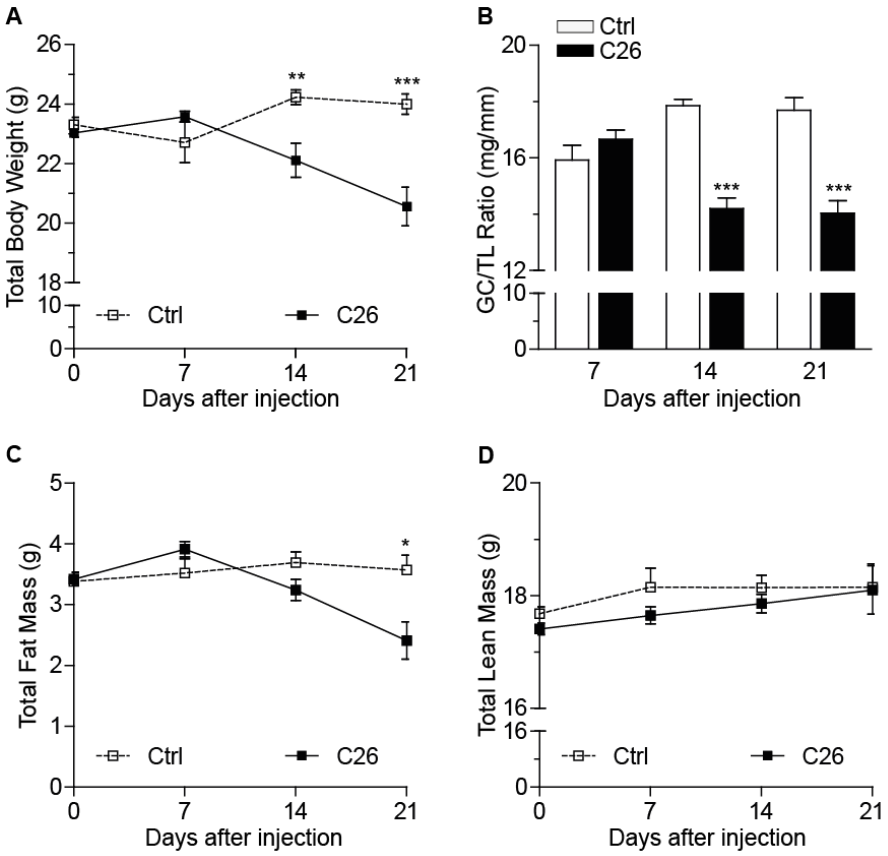

***Fig. 8**: **Mice inoculated with C26 colon carcinoma cells developed a cachectic phenotype.** 9 - 10 week old Balb/c male mice were subcutaneously injected with 1.5 x 10^6 C26 cells or DPBS (Control (Ctrl)). Cohorts of mice were sacrificed 7, 14 and 21 days post injection. **A)** Total body weight change. **B)** Gastrocnemius (GC) muscle weight to tibia length (TL) ratio development over time. **C)** Total body fat mass and **D)** lean mass development, determined using EchoMRI™ technology. **A) - D)** n ≥ 6, mean ± SEM. *indicates significance using 2-way ANOVA, Bonferroni post-test, *p < 0.05, **p < 0.01, ***p < 0.001.*

2.1.2 Development of C26 tumors affects the heart

2.1.2.1 C26-induced cachexia causes morphological changes of the heart

C26-induced cachexia triggered a significant loss of heart weight (Fig. 9 A) as well as reduction of the heart size (Fig. 9 B). The atrophic phenotype of the hearts could be attributed to a decrease in cardiac myocyte size (Fig. 9 C). As already observed for muscle and adipose tissues (Fig. 8 B + C), the first phenotypic changes in the heart occurred between day 7 and 14 after tumor cell injection (Fig. 9 A).

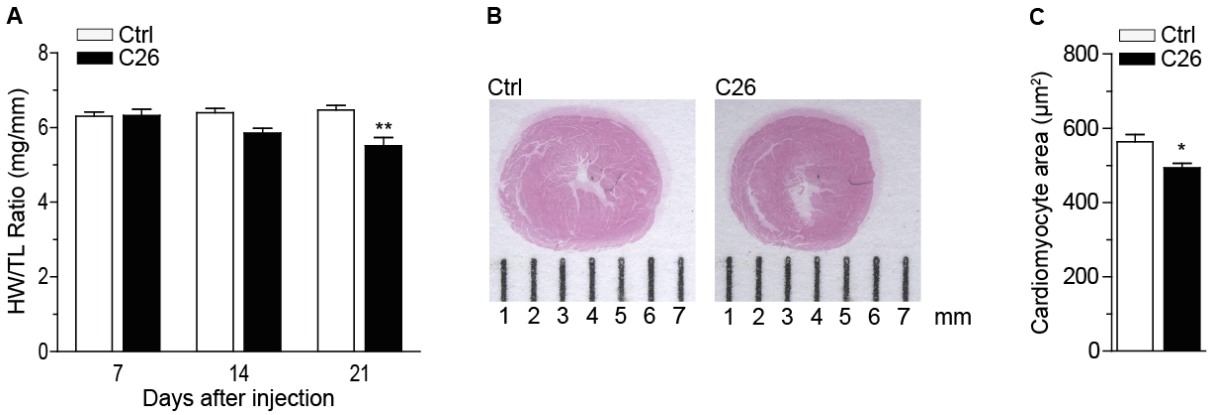

Fig. 9: Induction of cancer cachexia by transplantation of C26 cells causes cardiac atrophy. *Results are shown for the same cohort of mice as in Fig. 8.* ***A)*** *Heart weight (HW) to tibia length (TL) ratio development over time.* ***B)*** *Representative overview pictures of H&E stained heart cross-sections of a Ctrl and a tumor-bearing mouse on day 21 after C26 cell injection.* ***C)*** *Quantification of cardiomyocyte cross-sectional areas at day 21.* ***A)*** *n ≥ 6, mean ± SEM. *indicates significance using 2-way ANOVA, Bonferroni post-test, **p < 0.01.* ***C)*** *n = 5, mean ± SEM. *indicates significance using Student's t-test with Welch correction, *p < 0.05.*

2.1.2.2 Cardiac function is impaired by C26-induced cachexia

Morphological changes of the heart are often accompanied by alterations in heart function. According to the "Law of LaPlace", the load of the heart can be given as follows: (pressure × radius)/2 × wall thickness. Thus, a reduction in wall thickness as observed in the C26 model (Fig. 9 B) should be accompanied by a decrease in pressure.

The assessment of cardiac function by echocardiography indeed revealed an impairment of cardiac function. As shown in Figure 10 A, the fractional shortening of the left ventricle which reflects the shortening of the heart during one heart beat decreased significantly (~6%) over time in tumor-bearing mice compared to control littermates. The impairment of cardiac function in C26-bearing mice was caused by a significant increase of the left ventricular end-systolic diameter (LVESD) (Fig. 10 B). The left ventricular end-diastolic diameter was not affected (Fig. 10 C).

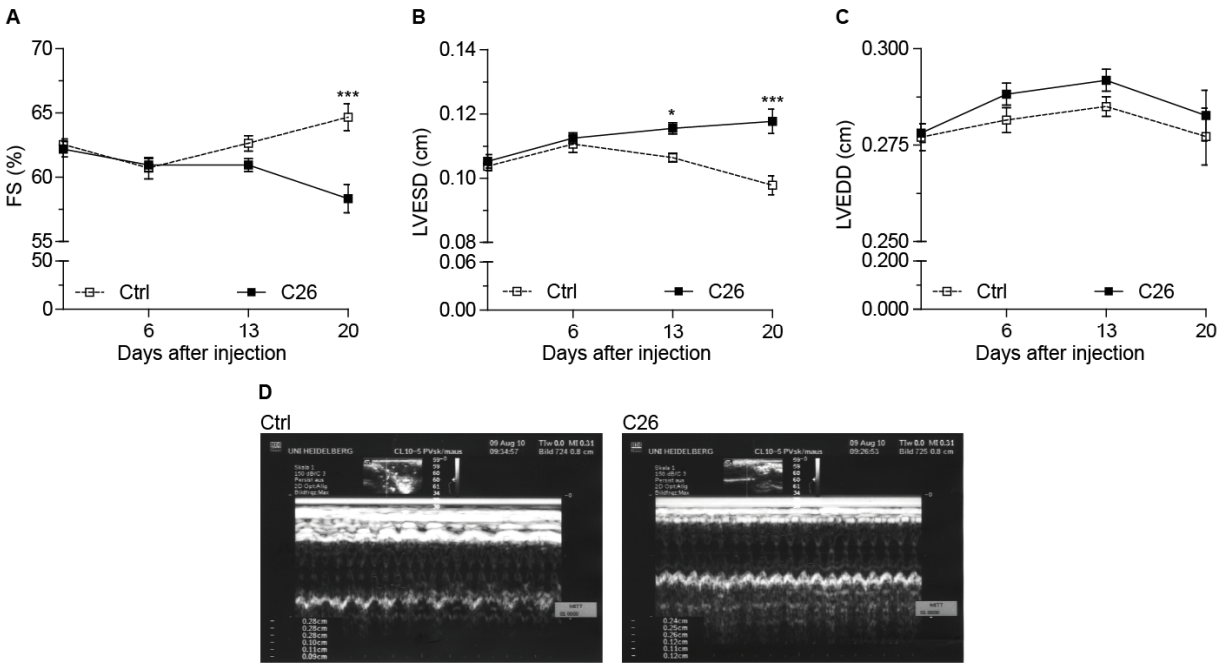

Fig. 10: Fractional shortening of the heart is significantly deteriorated in C26-bearing mice. *Results are shown for the same cohort of mice as in Fig. 8.* ***A)*** *Fractional shortening (FS),* ***B)*** *Left ventricular end-systolic diameter (LVESD) and* ***C)*** *Left ventricular end-diastolic diameter (LVEDD) progression determined by echocardiography.* ***D)*** *Representative echocardiography M-Mode records for a Ctrl and a C26-bearing mouse at day 20. These images were used for the quantitative analysis shown in A) - C).* ***A) - C)*** *n ≥ 6, mean ± SEM. *indicates significance using 2-way ANOVA, Bonferroni post-test, *p < 0.05, ***p < 0.001.*

In addition to the echocardiography, pressure-volume loops (PV loops) were performed to assess cardiac performance. The PV loop measurement is the more reliable method for evaluation of left ventricular (LV) contractility, and allows the simultaneous assessment of not only LV volume but also pressure. This technique allows for determination of more hemodynamic parameters.

The PV loop analysis could only deliver data for day 7 and 14. A viable measurement at day 21 was nearly impossible as most of the C26-bearing mice were already in a poor health state. The PV loop analysis revealed that the systolic function with reduced myocardial contractility assessed by measurement of end-systolic pressure (ESP), dP/dt_{max} (maximal rate of pressure change in the left ventricle), ejection fraction (EF) and stroke volume (SV) was significantly impaired in tumor-bearing mice compared to control littermates (Fig. 11 A - D). As shown in Figure 11 E - G, diastolic dysfunction with impaired active and passive relaxation evolved in C26 mice which was demonstrated by reduced tau_{weiss} (rate of pressure decay during relaxation) and dP/dt_{min} (minimal rate of pressure change in the left ventricle) and increased end-diastolic pressure (EDP). Heart rate was also affected in C26-injected mice (Fig. 11 H). The PV loop diagram, on which all analysis was based, showed a shift towards higher volumes, lower end-systolic pressures and higher end-diastolic pressures in C26 mice compared to control littermates (Fig. 11 I).

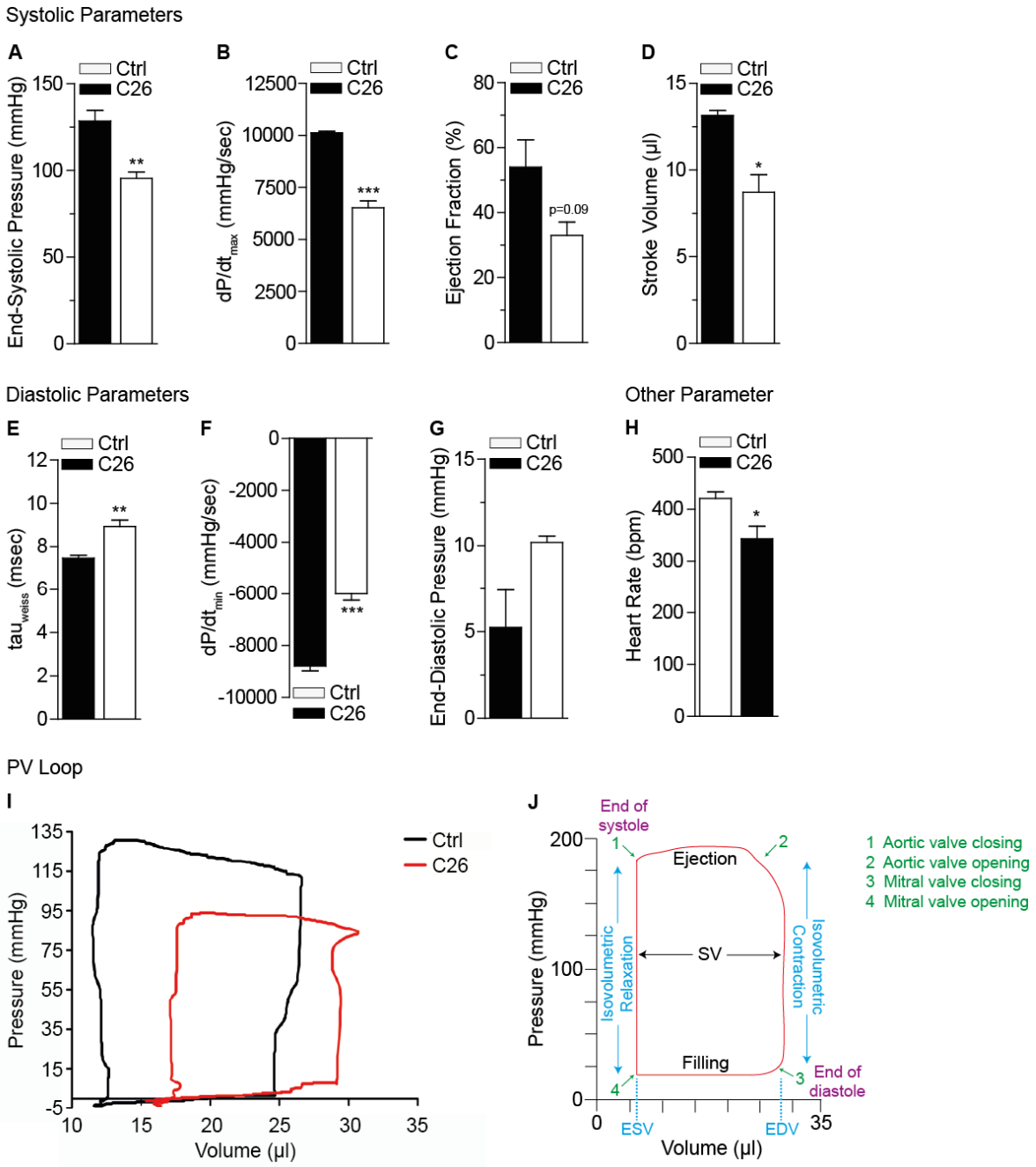

Fig. 11: C26-induced cardiac atrophy is associated with impaired cardiac hemodynamics. *Results are shown for the cohort of C26 mice that was sacrificed at day 14.* ***A) - D)*** *Systolic parameters assessed by PV loop analysis:* ***A)*** *End-systolic pressure (ESP),* ***B)*** *dP/dt_{max},* ***C)*** *Ejection fraction (EF) and* ***D)*** *Stroke volume (SV).* ***E) - G)*** *Diastolic parameters determined by PV loop measurement:* ***E)*** *Tau_{weiss},* ***F)*** *dP/dt_{min} and* ***G)*** *End-diastolic pressure (EDP).* ***H)*** *Heart rate (HR).* ***I)*** *Representative PV loops for a Ctrl and a C26-bearing mouse which were used for the quantifications shown in* ***A) - H).*** ***J)*** *Schematic diagram of a PV loop.* ***A) - H)*** *n = 4 - 5, mean ± SEM. *indicates significance using Student's t-test with Welch correction, *p < 0.05, **p < 0.01, ***p < 0.001.*

2.1.2.3 Classical molecular markers for heart performance are altered in the hearts of C26 mice

Genes of the so called fetal gene program were analyzed in the hearts of C26 mice as reactivation of these genes in postnatal hearts is described as a reliable marker for the assessment of heart failure. Atrophic hearts of C26 mice showed decreased expression levels of atrial natriuretic peptide (*Anp*) and brain natriuretic peptide (*Bnp*) as well as of α-myosin heavy chain (α-*Mhc*) and β-myosin heavy

chain (*β-Mhc)* (Fig. 12 A - D), whereas only the transcription levels of *Bnp* were significantly downregulated at any time point (Fig. 12 B). Changes on molecular level occured already around day 7 after tumor cell injection.

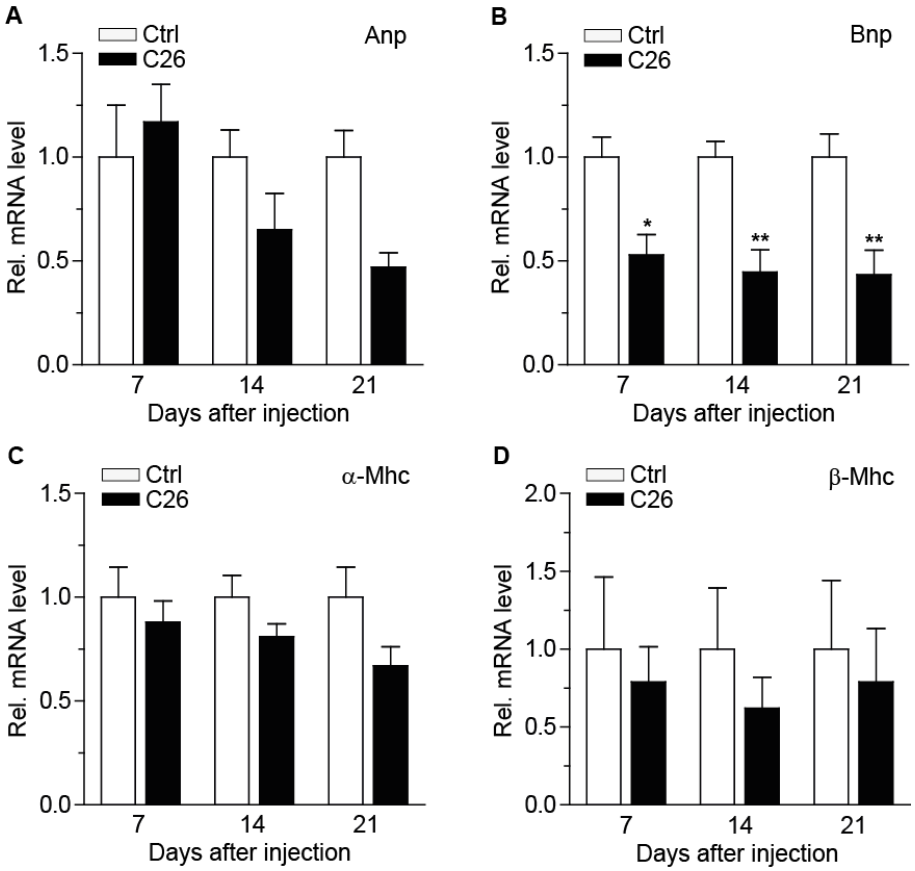

Fig. 12: Gene expression levels of prominent markers for heart performance are decreased in C26-induced atrophic hearts. *Results are shown for the same cohort of mice as in Fig. 8. RNA was isolated from the apex of the heart using the RNeasy® Mini Kit. Transcription levels of indicated genes were assessed by using the TaqMan system. Relative expression levels of the natriuretic peptides* ***A)*** *Anp and* ***B)*** *Bnp and the contractile proteins* ***C)*** *α-Mhc and* ***D)*** *β-Mhc. n ≥ 6, mean ± SEM. *indicates significance using 2-way ANOVA, Bonferroni post-test, *p < 0.05, **p < 0.01.*

2.1.2.4 C26-induced impairment of heart function is not associated with fibrosis

Reduced heart function is often associated with cardiac fibrosis which results in matrix stiffness (Conrad C.H., 1995). To determine an induction of fibrosis in the C26 mice the transcription levels of periostin (*Postn*) and the procollagens collagen type I alpha 2 (*Col1a2*) and collagen type III alpha 1 (*Col3a1*) were analyzed. Periostin is a matricellular protein which is described as critical regulator of fibrosis by modulating the attachment and deposition of collagen (Zhao S., 2014). Additionally, trichrome staining of cardiac cross-sections was performed to determine collagen deposition.

The expression levels of periostin decreased significantly over time in atrophic hearts of C26 mice (Fig. 13 A). Trichrome stainings analyzed by eye revealed that even less collagen was present in hearts of tumor-bearing mice at the end of the experiment (Fig. 13 B). As shown in Figure 13 C + D, the expression levels of *Col1a2* increased significantly over time but the expression levels of *Col3a1* decreased.

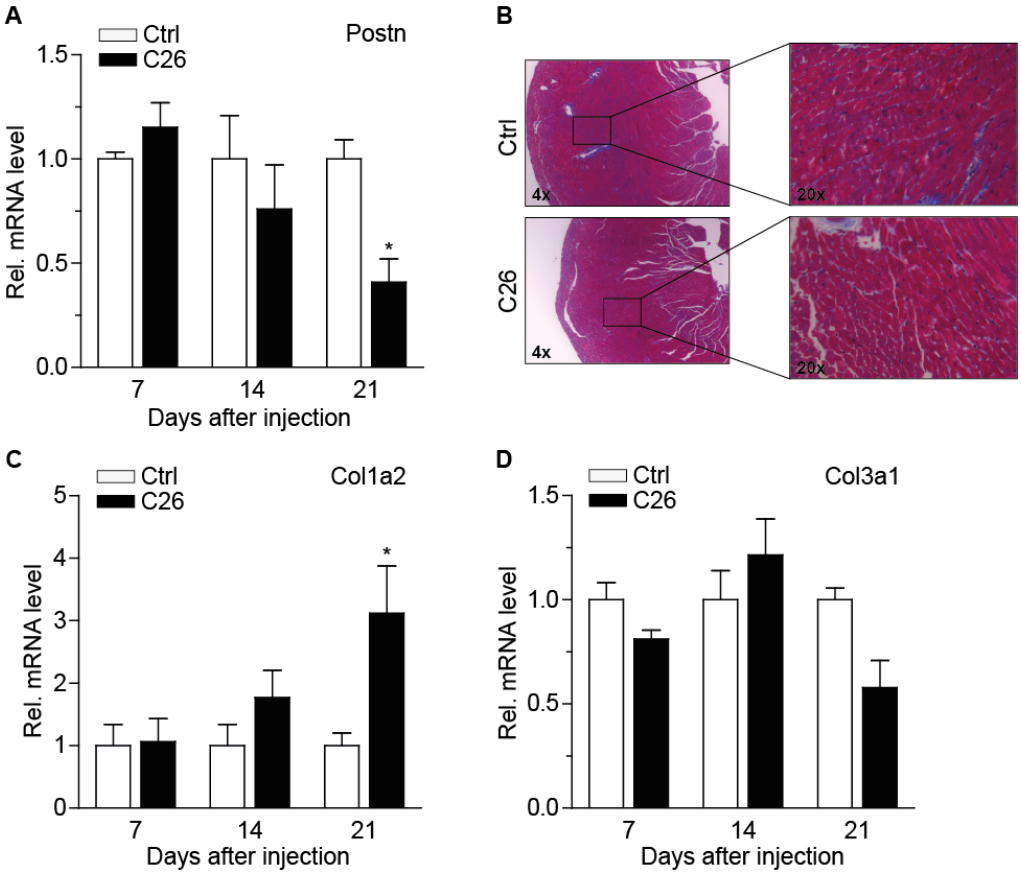

Fig. 13: Cardiac fibrosis is not detectable in C26 hearts. *Results are shown for the same cohort of mice as in Fig. 8. RNA was isolated from the apex of the heart using the RNeasy® Mini Kit. Transcription levels of indicated genes were assessed by using the TaqMan system.* ***A)*** *Relative expression levels of the fibrosis marker periostin (Postn).* ***B)*** *Representative pictures of trichrome stained heart cross-sections of a Ctrl and a C26-bearing mouse of day 21. Magnification: 4x and 20x. Relative transcription levels of the procollagens* ***C)*** *Col1a2 and* ***D)*** *Col3a1.* ***A), C) + D)*** *n ≥ 6, mean ± SEM. *indicates significance using 2-way ANOVA, Bonferroni post-test, *p < 0.05.*

2.1.2.5 Cardiac atrophy of C26 mice is induced by the activation of a protein degradation pathway

It is described that the skeletal muscle atrophy is accompanied by the activation of the E3 ubiquitin ligases MuRF1 and Atrogin-1. An increased transcription of these two ligases was also detected in the skeletal muscle (GC muscle) of the C26 mice (Fig. 14 E). Due to the structural similarity between skeletal muscle and heart the question arose if the cardiac atrophy was also induced by an increased expression of the two mentioned E3 ubiquitin ligases. As shown in Figure 14 A, the expression levels of *MuRF1* were not changed. The transcription level of *Atrogin-1* was slightly reduced at day 7 and 21 and was even significantly decreased at day 14 in tumor-bearing mice (Fig. 14 B). Additionally, the levels of poly-ubiquitinated proteins were assessed which did not show differences between control littermates and C26 mice at any time point (Fig. 14 C + D; representative immunoblot is shown from day 21).

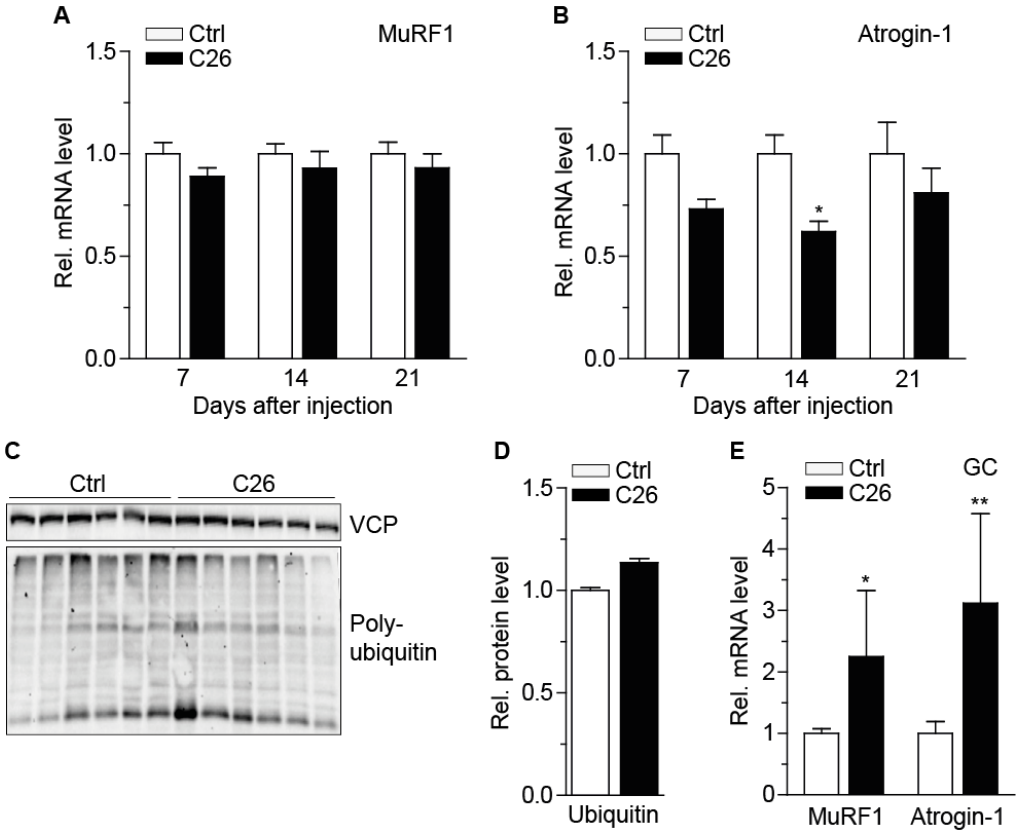

Fig. 14: Ubiquitin-proteasome system is not activated in atrophic hearts of C26-bearing mice. *Results are shown for the same cohort of mice as in Fig. 8. RNA was isolated from the apex of the heart using the RNeasy® Mini Kit. Transcription levels of indicated genes were assessed by using the TaqMan system. Transcription levels of the E3 ubiquitin ligases* ***A)*** *MuRF1 and* ***B)*** *Atrogin-1 in the hearts of Ctrl and C26 mice.* ***C)*** *Protein levels were detected from protein lysates which were isolated from the upper part (without atria) of the hearts from day 21 by immunoblotting using ubiquitin and valosin containing protein (VCP) antibodies.* ***D)*** *Relative ubiquitin levels determined by densitometric analysis of the displayed immunoblot.* ***E)*** *Transcription levels of the E3 ubiquitin ligases MuRF1 and Atrogin-1 in the GC muscle of Ctrl and C26 mice at day 21.* ***A) + B)*** *n ≥ 6, mean ± SEM. *indicates significance using 2-way ANOVA, Bonferroni post-test, *p < 0.05.* ***D) + E)*** *n ≥ 6, mean ± SEM. *indicates significance using Student´s t-test with Welch correction, *p < 0.05, **p < 0.01.*

A second proteolytic mechanism by which large quantities of intracellular components are degraded is autophagy. It is described that under nutrient deprivation most of the proteins in the heart are degraded by this mechanism (Gustafsson A.B., Gottlieb R.A., 2009). The microtubule-associated protein light chain 3 (LC3; mammalian homolog to yeast *Atg8*) is a well-characterized marker for autophagy activation because it is a key regulator of autophagosome formation. During the process of autophagy activation cytosolic LC3-I is processed and lipidated to membrane-bound LC3-II which specifically localizes to membranes of autophagosomes. The conversion of LC3-I to LC3-II can be used for the determination of autophagy induction. The densitometric analysis of LC3B-II protein levels showed a significant increase of LC3B-II in atrophic hearts of C26 mice compared to hearts of control littermates at day 21 (Fig. 15 A - B).

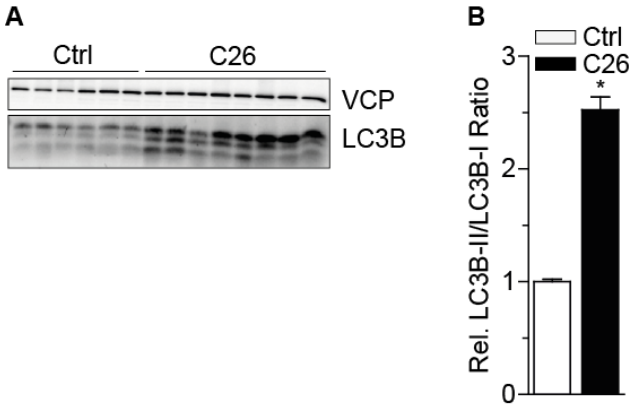

Fig. 15: Autophagy is activated in atrophic hearts of C26 mice. *Results are shown for the same cohort of mice as in Fig. 8.* ***A)*** *Protein levels were detected from protein lysates which were isolated from the upper part (without atria) of the hearts from day 21 by immunoblotting using light chain 3 B (LC3B) and valosin containing protein (VCP) antibodies. The upper lanes of the LC3B blot represent the LC3B-I proteins, the lanes in the middle the LC3B-II proteins and the lower lanes are unspecific signals.* ***B)*** *Relative ratio of LC3B-II to LC3B-I determined by densitometric analysis of the displayed immunoblot. n ≥ 6, mean ± SEM. *indicates significance using Student's t-test with Welch correction, *p < 0.05.*

2.2 Phenotypic analysis of MC38 cancer mouse model

2.2.1 Implantation of MC38 colorectal carcinoma cells did not cause cachexia

The MC38 cancer mouse model was used to answer the question whether all types of colon cancer cells are capable to induce the heart phenotype seen in the C26 mouse model or whether this is a specific feature of cachexia inducing cells. 9 - 10 week old C57BL/6 male mice subcutaneously injected with MC38 cells did not develop a cachectic phenotype as proven by unchanged body weight (Fig. 16 A), skeletal muscle (Fig. 16 C) and adipose tissue mass (Fig. 16 B). Additionally, an activation of the E3 ubiquitin ligases *MuRF1* and *Atrogin-1* which is associated with skeletal muscle atrophy under cachectic conditions was not detected in skeletal muscles of mice injected with MC38 cells (Fig. 16 D).

2.2.2 Development of MC38 tumors has no influence on the heart

The MC38 tumors did not induce morphological changes in the skeletal muscles. This was also observed for the hearts of tumor-bearing mice. As shown in Figure 17 A, the heart weight to tibia length ratio of MC38 mice was not reduced. Additionally, hearts and cardiomyocytes of tumor-bearing mice did not shrink in size (Fig. 17 B + C).

Furthermore, the heart function of the MC38 mice was not impaired (Fig. 18 A). These results were supported by the fact that the expression of the fetal gene program was not altered (Fig. 18 B + C). Also the expression levels of the fibrosis marker *Postn* were not changed in MC38 mice (Fig. 18 D). The trichrome stainings of heart cross-sections from control littermates and tumor-bearing mice showed no difference between the two groups (Fig. 18 E).

In line with the absence of any effects on cardiac morphology and function, protein degradation pathways (ubiquitin-proteasome system and autophagy (Fig. 19 A - C) were also not affected.

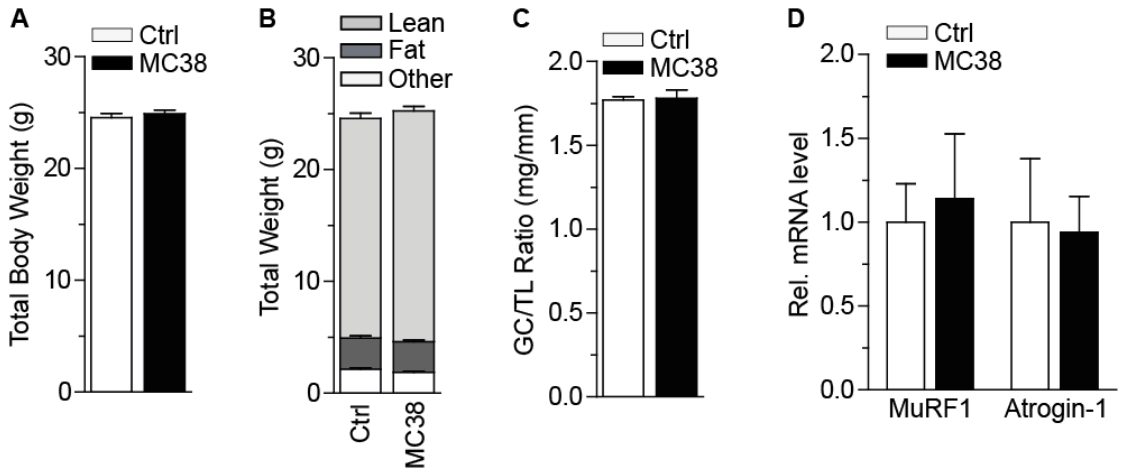

***Fig. 16**: **Mice injected with MC38 cells do not develop a cachectic phenotype.** 9 - 10 week old male C57BL/6 mice were subcutaneously injected with 5 x 10^5 MC38 cells or DPBS (Control (Ctrl)). Mice were sacrificed 30 days post injection. **A)** Total body weight. Tumor weight was excluded. **B)** Total lean and fat mass which were determined by using EchoMRI™ technology. **C)** Gastrocnemius (GC) muscle weight to tibia length ratio. RNA was isolated from the apex of the heart using the RNeasy® Mini Kit. Transcription levels of indicated genes were assessed by using the TaqMan system. **D)** Transcription levels of the E3 ubiquitin ligases MuRF1 and Atrogin-1 in the GC muscle of Ctrl and MC38-bearing mice. **A) - D)** n ≥ 6, mean ± SEM. No significance using Student's t-test with Welch correction.*

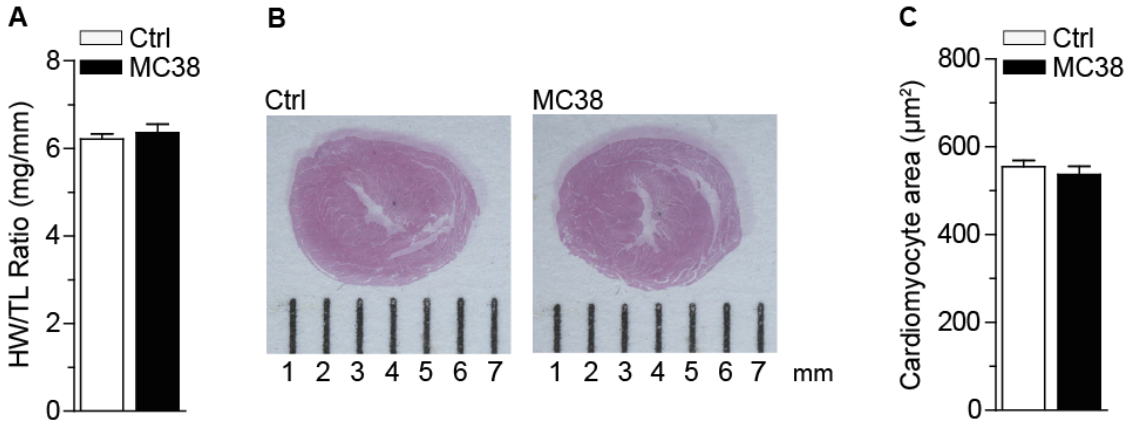

***Fig. 17: Implantation of MC38 cells does not affect the cardiac morphology.** Results are shown for the same cohort of mice as in Fig. 16. **A)** Heart weight (HW) to tibia length (TL) ratio. **B)** Representative overview pictures of H&E stained heart cross-sections of a Ctrl and a tumor-bearing mouse. **C)** Quantification of cardiomyocyte cross-sectional areas. **A) + C)** n ≥ 4, mean ± SEM. No significance using Student's t-test with Welch correction.*

Gene expression profiling was performed from RNA lysates of hearts from MC38-bearing mice and control littermates. These results were to be compared with the gene expression profiling of the C26 mouse experiment to identify genes that are commonly differentially expressed in both tumor groups. However as shown in Figure 20, all samples clustered together which means that the gene expression profiles from MC38 and control mice were the same, which in turn made a comparison between MC38 and C26 gene expression data unnecessary, as it confirmed the absence of any phenotype in the MC38 mice.

Overall these data indicate that the tumors formed by MC38 cells lack pro-cachectic properties when compared to the C26 mouse model.

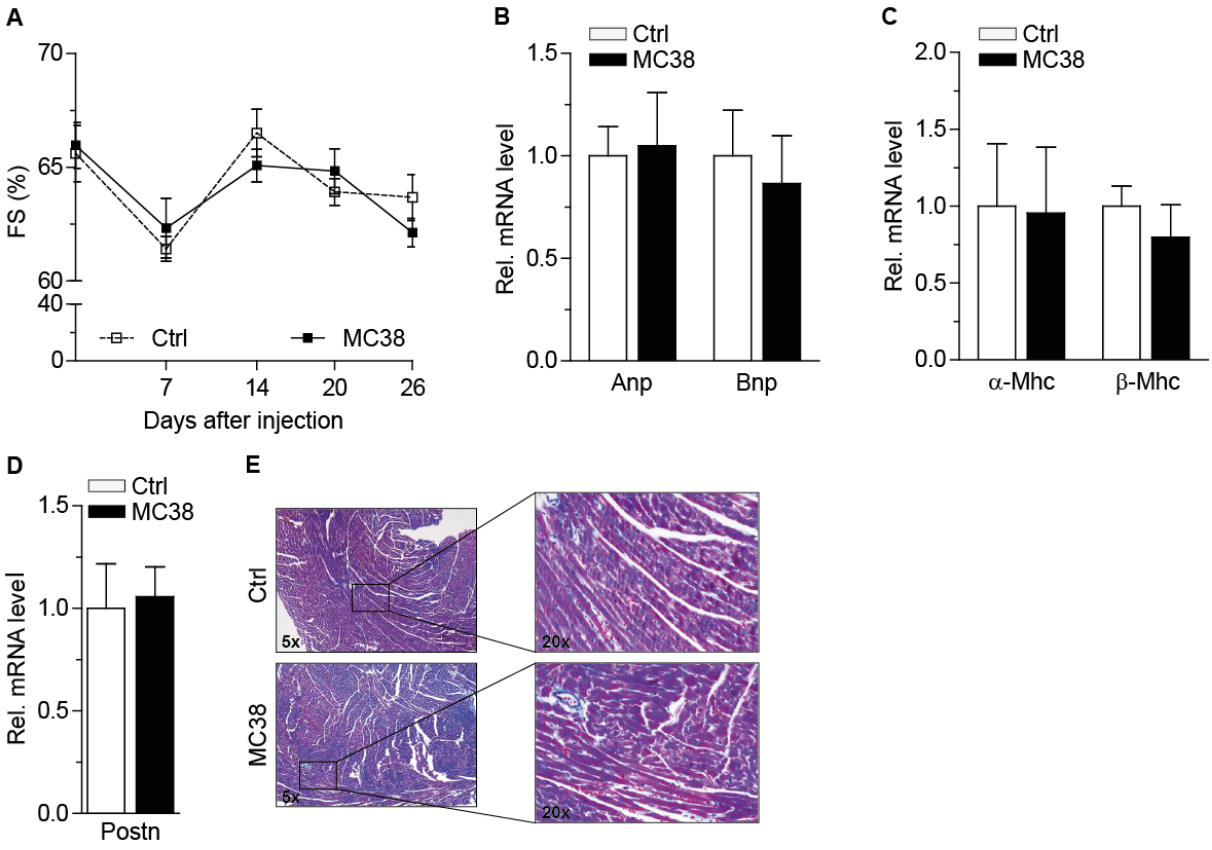

Fig. 18: Cardiac function is not impaired in mice bearing MC38 tumors. *Results are shown for the same cohort of mice as in Fig. 16.* ***A)*** *Progression of fractional shortening (FS) assessed by echocardiography. RNA was isolated from the apex of the heart using the RNeasy® Mini Kit. Transcription levels of indicated genes were assessed by using the TaqMan system. Relative transcription levels of* ***B)*** *the natriuretic peptides Anp and Bnp and* ***C)*** *the contractile proteins α-Mhc and β-Mhc at day 30.* ***D)*** *Relative expression levels of the fibrosis marker periostin (Postn) at day 30.* ***E)*** *Representative pictures of trichrome stained heart cross-sections of a Ctrl and a tumor-bearing mouse of day 30. Magnification: 5x and 20x.* ***A) - D)*** *n ≥ 6, mean ± SEM. No significance using Student's t-test with Welch correction.*

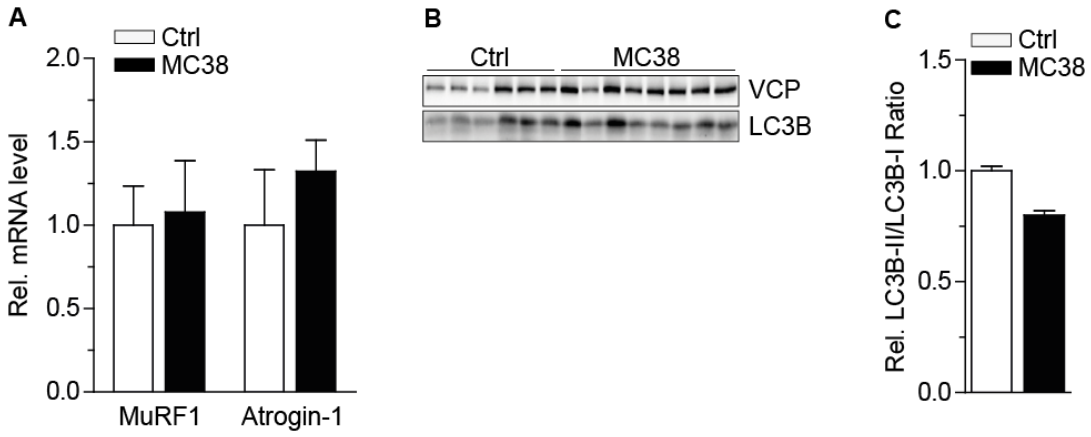

Fig. 19: Proteolytic pathways are not activated in hearts of mice injected with MC38 cells. *Results are shown for the same cohort of mice as in Fig. 16. RNA was isolated from the apex of the heart using the RNeasy® Mini Kit. Transcription levels of indicated genes were assessed by using the TaqMan system.* ***A)*** *Relative transcription levels of the E3 ubiquitin ligases MuRF1 and Atrogin-1 in hearts of Ctrl and tumor-bearing mice.* ***B)*** *Protein levels were detected from protein lysates which were isolated from the upper part (without atria) of the hearts by immunoblotting using light chain 3 B (LC3B) and valosin containing protein (VCP) antibodies. The upper lanes of the LC3B blot represent the LC3B-I proteins and the lower lanes the LC3B-II proteins.* ***C)*** *Relative ratio of LC3B-II to LC3B-I determined by densitometric analysis of the displayed immunoblot.* ***A) + C)*** *n ≥ 6, mean ± SEM. No significance using Student's t-test with Welch correction.*

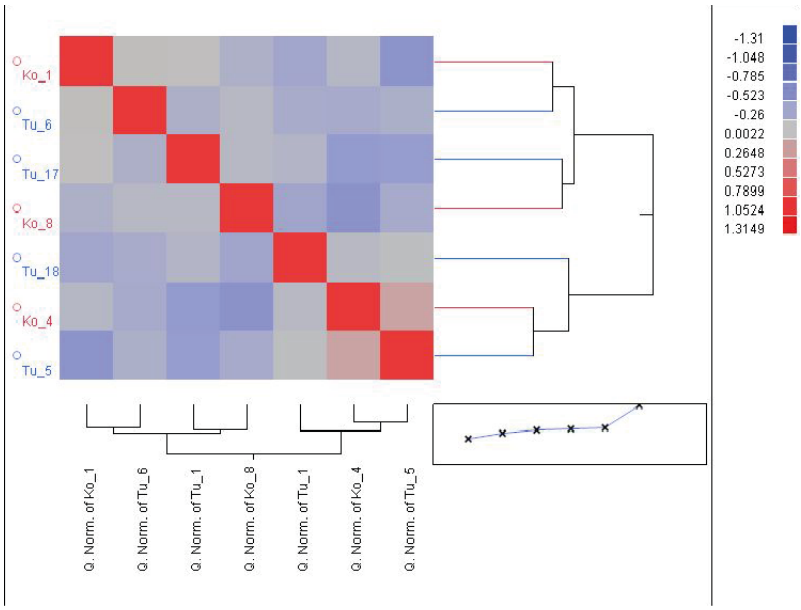

Fig. 20: Gene expression profiling of hearts from MC38-bearing mice and control littermates. *Results are shown for the same cohort of mice as in Fig. 16. RNA was isolated from the apex of the heart using the RNeasy® Mini Kit.* **A)** *Hierarchical heat map cluster of the samples which were labeled as follows: Ko: Kontrolle (control littermates) and Tu: Tumor (MC38-bearing mice). n = 3 - 4.*

2.3 Phenotypic analysis of adenomatous polyposis coli (APC) delta 580 mice

2.3.1 APC delta 580 mice develop cachexia

Due to the fact that allograft models do not always represent the full activity of solid tumors and particularly are not predictive for the full complexity of human tumors, a genetic mouse model for familial colon cancer was examined. Mutations in the *APC* gene are frequently detected in human colorectal cancer. Therefore, the so called APC delta 580 mouse model which carries a germ-line mutation in exon 14 of the *Apc* gene was used (Kuraguchi M., 2006). The development of a cachectic phenotype was not examined thus far in this particular mouse line which is also found as $APC^{\Delta 14/+}$ mice in the literature (Colnot S., 2004).
The heterozygous APC delta 580 mice (APC 580/+) developed a strong cachectic phenotype which was shown by a substantial loss in body, adipose tissue and skeletal muscle weight (Fig. 21 A - C). The activation of the ubiquitin-proteasome system which is typical for cachexia-induced skeletal muscle atrophy did not occur in APC 580/+ mice. *MuRF1* and *Atrogin-1* expression levels were only slightly, but not significantly increased in the atrophic GC muscles of APC 580/+ mice (Fig. 21 D).

A further clinic feature that is sometimes associated with cachexia is anemia. This was not observed in the C26 model. However, the APC 580/+ mice showed signs of anemia at the late disease stage. The skin of these mice was white and they had cold feet. A blood count revealed that the hemoglobin (Hb) levels were reduced in APC 580/+ compared to wild-type littermates (APC +/+) (Tab. 1). Further anemic markers such as the red cell distribution width (RDW), the mean corpuscular/cell volume (MCV) and the mean corpuscular/cell hemoglobin (MCH) were increased in APC 580/+ mice (Tab. 1). RDW describes the variation in red blood cell distribution. MCH represents the average mass of hemoglobin in red blood cells and MCV the average volume of red blood cells in a blood sample.

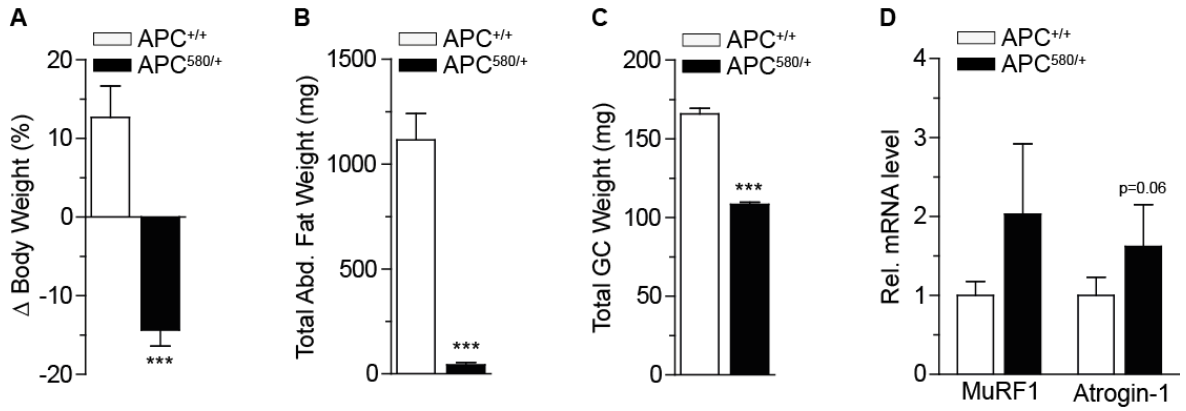

Fig. 21: Cachexia is induced in APC delta 580 mice. *Heterozygous APC delta 580 mice (APC 580/+) were sacrificed after onset of cachexia.* ***A)*** *Delta body weight change: Start body weight compared to body weight at sacrifice.* ***B)*** *Total abdominal (abd). adipose tissue weight which is shown representative for all fat pads.* ***C)*** *Total gastrocnemius (GC) muscle weight. RNA was isolated from the apex of the heart using the RNeasy® Mini Kit. Transcription levels of indicated genes were assessed by using the TaqMan system.* ***D)*** *Transcription levels of the E3 ubiquitin ligases MuRF1 and Atrogin-1 in the GC muscle of wild-type (APC +/+) and heterozygous (APC 580/+) mice.* ***A) - D)*** *n ≥ 6, mean ± SEM. *indicates significance using Student's t-test with Welch correction, ***p < 0.001.*

Test	APC 580/+	APC +/+
Hb (g/dl)	0.85±0.05	12.4±1
RDW (%)	28.2±0.95	16.9±0.7
MCV (fl)	82±2	46.5±0.5
MCH (pg)	22.5±3.5	15.5±0.5

Tab. 1: Blood count of APC delta 580 mice. *All results are mean ± SEM; n = 2.*

2.3.2 APC delta 580 mice also develop alterations in the heart

Hearts of APC 580/+ mice were atrophic and they weighed significantly less compared to wild-type littermates (Fig. 22 A + B). The cardiac atrophy was due to a reduction in cardiomyocyte size (Fig. 22 C).

Heart function, which was assessed by echocardiography, was reduced in APC 580/+ mice compared to wild-type littermates, but this impairment did not reach significance (Fig. 23 A). The reduced heart function resulted from an increase in the LVESD and the LVEDD (Fig. 23 B + C).

Impaired heart function was accompanied by a change in expression levels of the fetal gene program. The transcription levels of *Anp* and α-*Mhc* were significantly increased whereas *Bnp* and β-*Mhc* were slightly upregulated (Fig. 24 A + B). The expression levels of the fibrosis marker *Postn* were unchanged (Fig. 24 C). This result was confirmed by the trichrome staining which did not show any difference in collagen content comparing wild-type and APC 580/+ mice (Fig. 24 D). Transcription levels of procollagen *Col1a2* were upregulated and levels of procollagen *Col3a1* were slightly decreased in APC 580/+ mice (Fig. 24 E).

The detected cardiac atrophy in APC 580/+ mice was not due to the activation of the ubiquitin-proteasome system as the expression levels of the E3 ubiquitin ligases *MuRF1* and *Atrogin-1* were

downregulated (Fig. 25 A). In addition, the levels of polyubiquitinated proteins were unchanged (Fig. 25 B + C). Autophagy was slightly induced in hearts of APC 580/+ mice (Fig. 25 D + E).

By using the APC delta 580 mice as an independent mouse model it was possible to validate cardiac atrophy and dysfunction as a relevant clinical feature which is associated with colon cancer-induced cachexia.

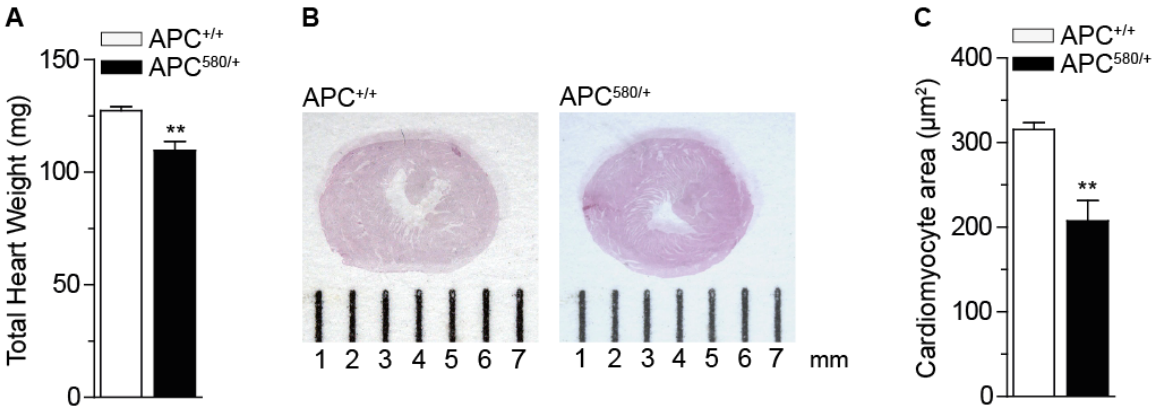

Fig. 22: APC 580/+ mice suffer from cardiac atrophy. *Results are shown for the same cohort of mice as in Fig. 21.* ***A)*** *Total heart weight.* ***B)*** *Representative overview pictures of H&E stained heart cross-sections of a wild-type (APC +/+) and a tumor-bearing mouse (APC 580/+).* ***C)*** *Quantification of cardiomyocyte cross-sectional areas.* ***A) + C)*** *n ≥ 6, mean ± SEM. *indicates significance using Student's t-test with Welch correction, **p < 0.01.*

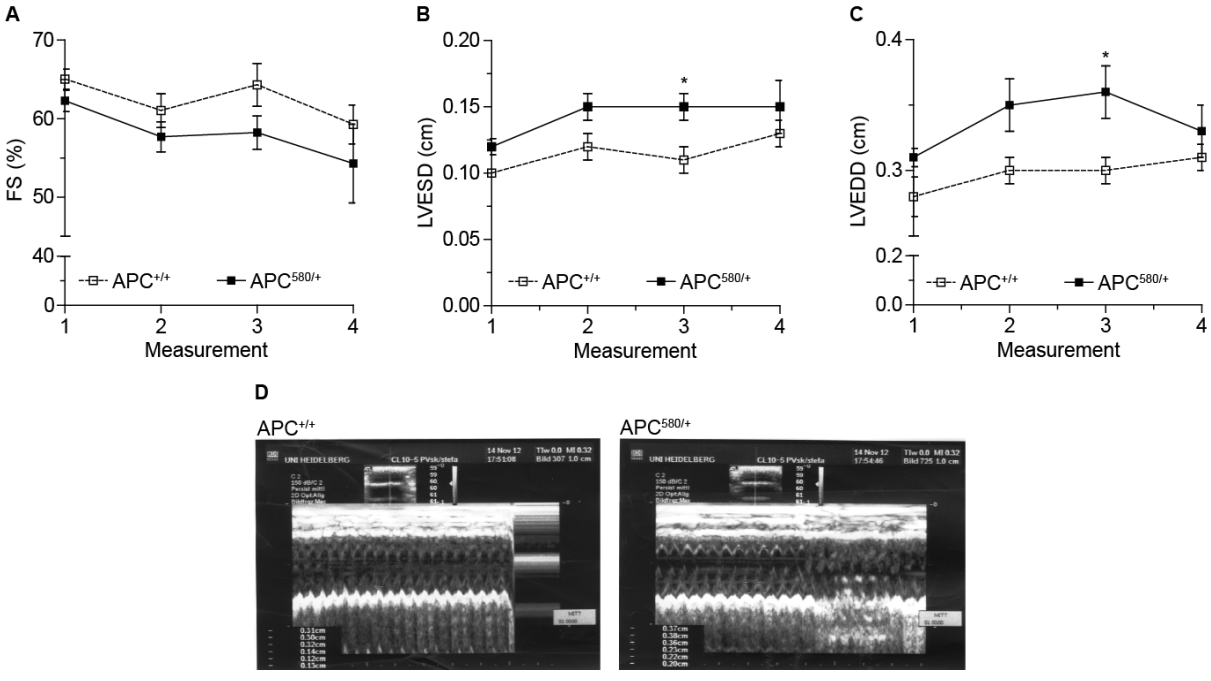

Fig. 23: Fractional shortening of the heart is reduced in APC 580/+ mice. *Results are shown for the same cohort of mice as in Fig. 21.* ***A)*** *Fractional shortening (FS),* ***B)*** *Left ventricular end-systolic diameter (LVESD) and* ***C)*** *Left ventricular end-diastolic diameter (LVEDD) progression determined by echocardiography.* ***D)*** *Representative echocardiography M-Mode records for a wild-type (APC +/+) and a tumor-bearing mouse (APC 580/+). These images were used for the quantitative analysis shown in A) - C).* ***A) - C)*** *n ≥ 6, mean ± SEM. *indicates significance using 2-way ANOVA, Bonferroni post-test, *p < 0.01.*

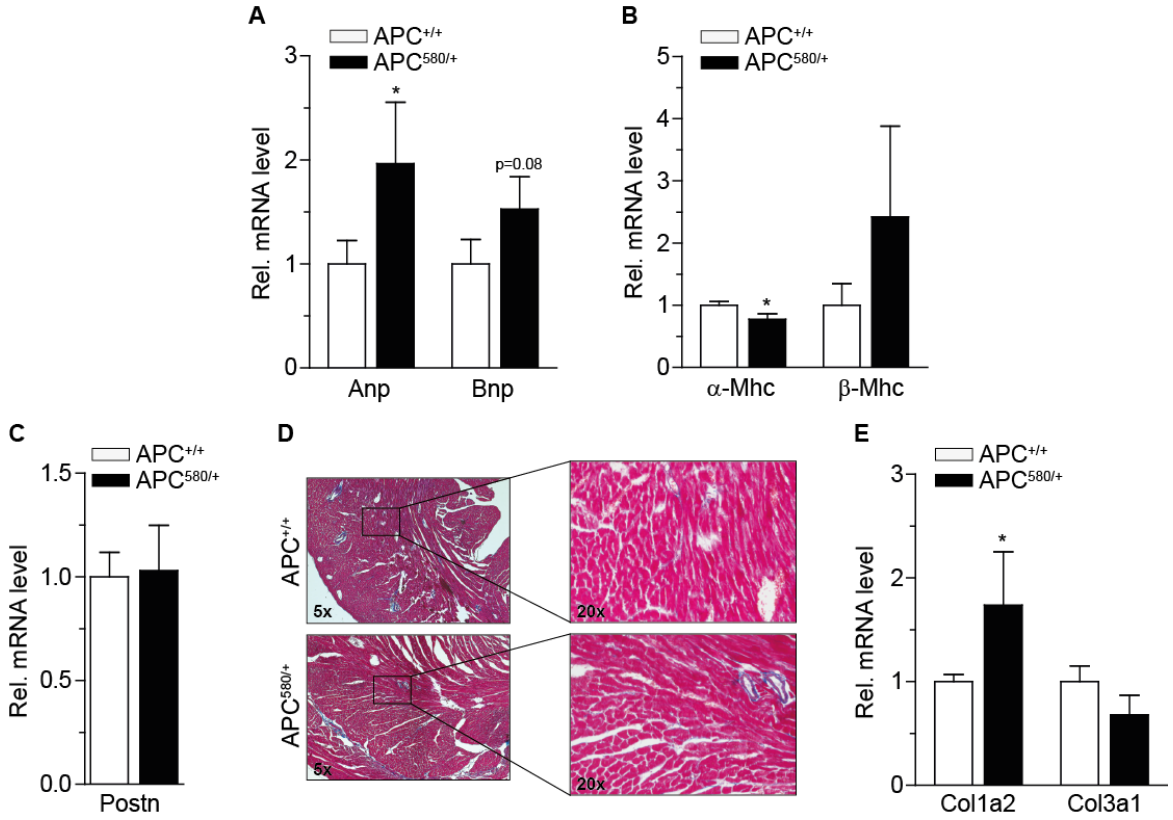

Fig. 24: Features that are accompanied with cardiac dysfunction are partially changed in hearts of APC 580/+ mice. *Results are shown for the same cohort of mice as in Fig. 21. RNA was isolated from the apex of the heart using the RNeasy® Mini Kit. Transcription levels of indicated genes were assessed by using the TaqMan system. Relative transcription levels of* ***A)*** *the natriuretic peptides Anp and Bnp and* ***B)*** *the contractile proteins α-Mhc and β-Mhc.* ***C)*** *Relative expression levels of the fibrosis marker periostin (Postn).* ***D)*** *Relative transcription levels of the procollagens Col1a2 and Col3a1.* ***E)*** *Representative pictures of trichrome stained heart cross-sections of a wild-type (APC +/+) and a tumor-bearing mouse (APC 580/+). Magnification: 5x and 20x.* ***A) - D)*** *n ≥ 6, mean ± SEM. *indicates significance using Student's t-test with Welch correction, *p < 0.01.*

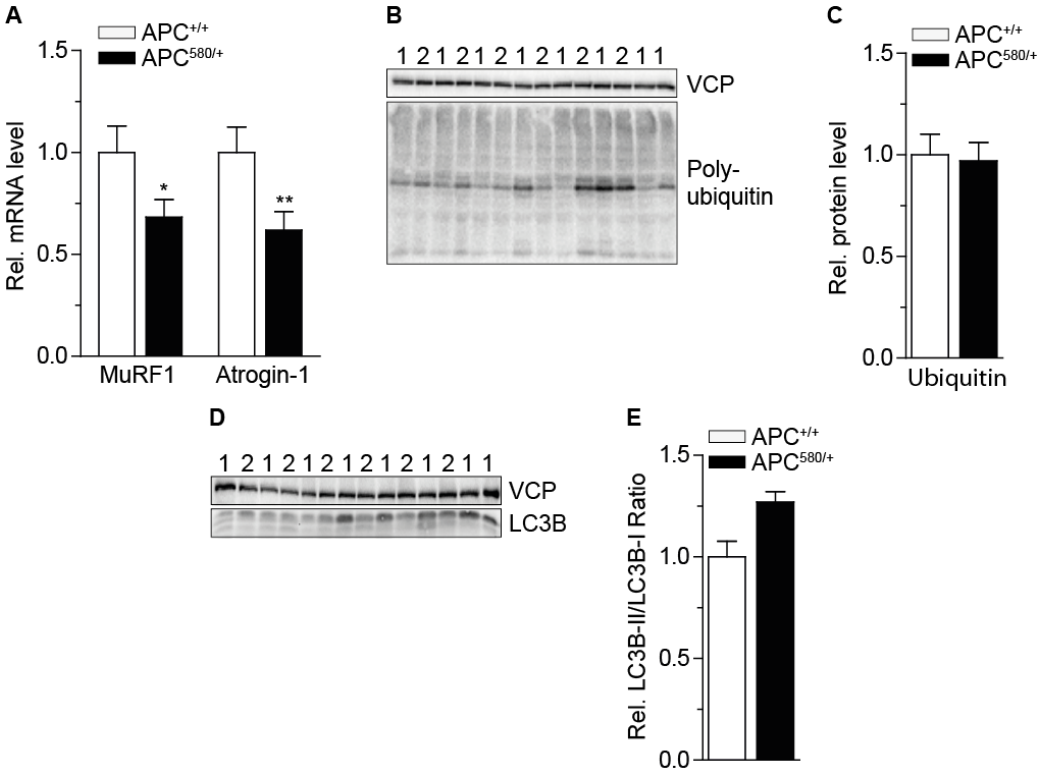

Fig. 25: The ubiquitin-proteasome system is not activated in hearts from APC 580/+ mice but autophagy is slightly induced. *Results are shown for the same cohort of mice as in Fig. 21. RNA was isolated from the apex of the heart using the RNeasy® Mini Kit. Transcription levels of indicated genes were assessed by using the TaqMan system. Protein levels were detected from protein lysates which were isolated from the upper part (without atria) of the hearts by immunoblotting. Protein samples from APC 580/+ mice are labeled with 1 and samples from APC +/+ with 2.* ***A)*** *Relative transcription levels of the E3 ubiquitin ligases MuRF1 and Atrogin-1.* ***B)*** *Immunoblot using ubiquitin and valosin containing protein (VCP) antibodies.* ***C)*** *Relative ubiquitin levels determined by densitometric analysis of the displayed immunoblot.* ***D)*** *Proteins were detected by immunoblotting using light chain 3 B (LC3B) and VCP antibodies. The upper lanes of the LC3B blot represent the LC3B-I proteins and the lower lanes the LC3B-II proteins.* ***E)*** *Relative ratio of LC3B-II to LC3B-I determined by densitometric analysis of the displayed immunoblot.* ***A), C) + E)*** *n ≥ 6, mean ± SEM. *indicates significance using Student's t-test with Welch correction, *p < 0.01.*

2.4 Cardiac fatty acid metabolism is altered under cachectic conditions

2.4.1 Gene expression profiling of hearts from C26 mice

To define molecular and metabolic properties that are affected in cachexia-induced atrophic hearts, gene expression profiling was performed using RNA extracts from hearts of C26 mice that were sacrificed two weeks after tumor cell implantation. The samples that were sent for analysis were categorized into the following three groups: control (DPBS-treated mice), tumor (mice with tumors but no cachexia) and tumor cachexia (tumor-bearing mice with cachexia). The hierarchical heat map showed that the three groups were very homogenous but distinct from each other (Fig. 26 A). Surprisingly, the gene expression pattern of tumor-bearing mice with and without cachexia did not cluster together. In total, 1800 genes were differentially regulated, of which only 189 genes were regulated both in hearts of C26-bearing mice with and without cachexia (Fig. 26 B). The volcano plots show all genes on the microarray (Fig. 26 C + D). All genes above the threshold are considered as significantly altered in expression ($p < 0.05$). Genes on the left are less expressed and genes on the right are more expressed compared to control mice. Increased expression of the fibrosis marker

periostin (*Postn*) that was determined by Taqman assay (Fig. 13 A) for hearts from C26 mice was also detected by the gene expression profiling (Fig. 26 D, green arrow). More interestingly, genes that encode for proteins which are involved in the regulation of circadian rhythms, such as aryl hydrocarbon receptor nuclear translocator-like (*Arntl*, also known as *Bmal1*) and period circadian protein homolog 1 (*Per1*) were differentially regulated in samples from both groups of C26 mice compared to control littermates. Furthermore, the gene expression of circadian clock targets such as D site of albumin promoter binding protein (*Dbp*) were changed in both C26 groups (Fig. 26 C + D, red arrows). To validate the involvement of the circadian clock in the cardiac phenotype several assays were performed but it was not possible to substantiate this finding. Unfortunately, a Kyoto Encyclopedia of Genes and Genomes (KEGG) pathway analysis of this dataset was not achievable because not enough genes were significantly regulated.

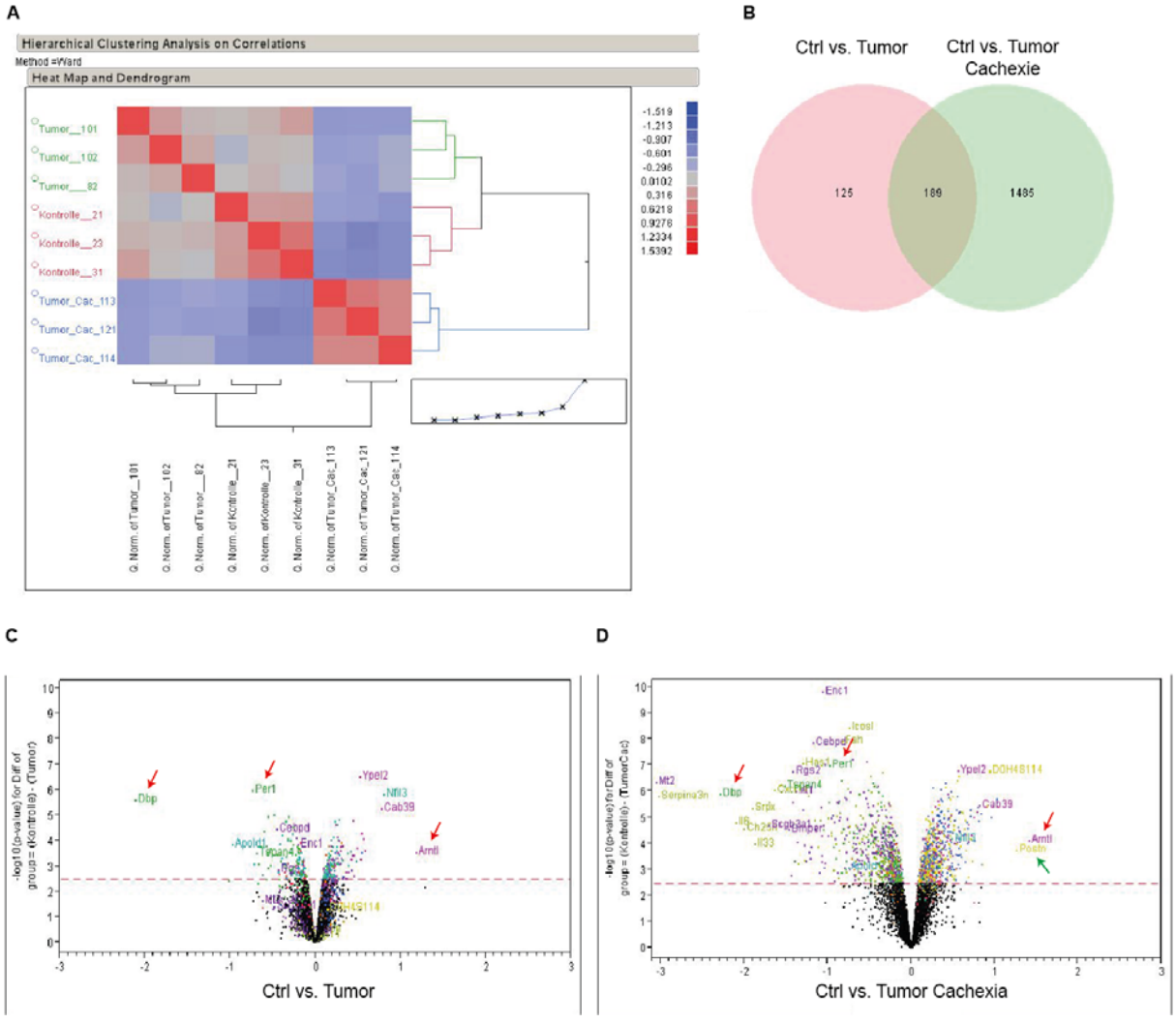

Fig. 26: Gene expression profiling of hearts from C26-bearing mice either with or without cachexia compared to control littermates. *Samples were analyzed from C26 mice which were sacrificed two weeks after tumor cell injection.* ***A)*** *Hierarchical heat map cluster of the samples which were labeled as follows: Kontrolle (DPBS-treated mice), Tumor (C26 mice without cachexia) and Tumor Cac (C26 mice with cachexia).* ***B)*** *Venn diagram of the distribution of differentially expressed genes. Volcano plots of* ***C)*** *control vs. C26 mice and* ***D)*** *control vs. C26 mice with cachexia. n = 3.*

2.4.2 Gene expression profiling of primary mouse cardiomyocytes cultured in C26 medium

The main focus of this project was to identify molecular changes that developed in the cardiomyocytes and to answer the question whether the cachexia-induced effects on the heart were mediated by tumor-borne factors in a cell-autonomous manner or whether they derived from secondary signals. Therefore, an *in vitro* model was established wherein primary cardiomyocytes, isolated from either neonatal rats or adult Balb/c mice, were plated onto multi-well cell culture plates and exposed to conditioned medium from cachexia or non-cachexia-inducing cell lines. Primary cardiomyocytes treated with conditioned medium from C26 cells also developed atrophy. These results will be discussed in more detail in chapter 2.5. This chapter will also focus on addressing the question whether a factor secreted by the tumor induced the observed cardiac phenotype.

To identify molecular mechanisms that were altered in cardiomyocytes under cachectic conditions, gene expression profiling was performed using RNA samples from primary adult mouse cardiomyocytes that were treated with conditioned medium from C26 cells for 48 h. For each condition three samples were prepared. As seen from the hierarchical heat map (Fig. 27 A), two samples of both groups were homogenous but still distinct from one another. Under these conditions more genes were significantly regulated (Fig. 27 B) which enabled a KEGG pathway analysis. This analysis revealed that the hypertrophic cardiomyopathy (HCM) and dilated cardiomyopathy pathway and the fatty acid (FA) metabolism pathway were highly significantly affected in primary mouse cardiomyocytes treated with C26-conditioned medium (Tab. 2). Most interesting was the dysregulation of the FA metabolism pathway. Therefore, the gene expression profiling data from the C26 mice were reanalyzed to perform a gene ontology enrichment analysis for biology processes (GO-BP) (Tab. 15). In this analysis processes that are involved in FA metabolism, transport and biosynthesis many times were noted as enriched. The aim of further experiments and analysis was to validate this finding.

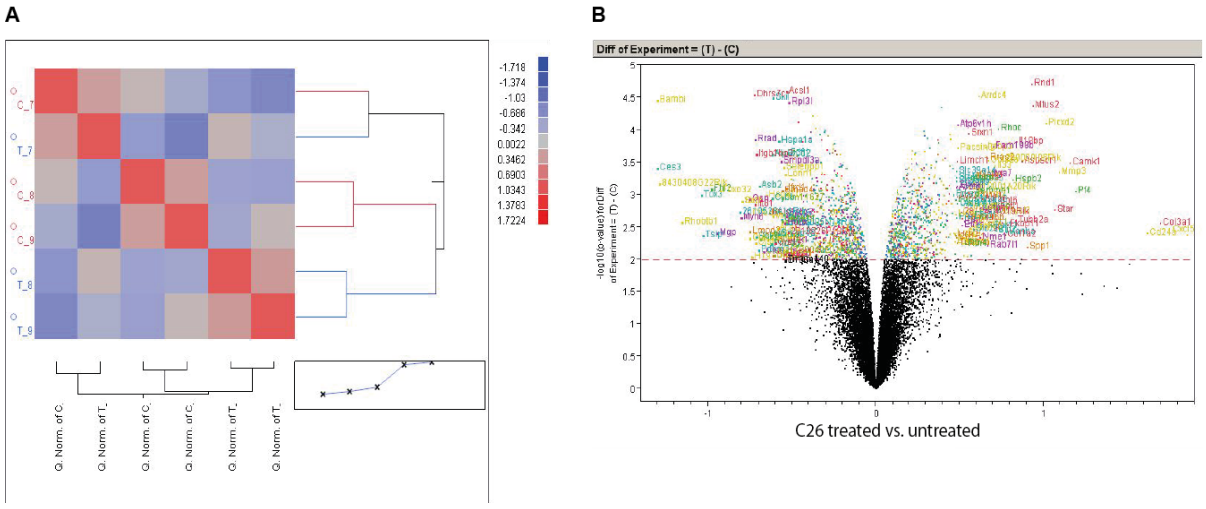

Fig. 27: Gene expression profiling of primary adult mouse cardiomyocytes cultured in C26-conditioned medium. *Primary mouse cardiomyocytes were plated at 50,000 rod-shaped myocytes/well on laminin-coated 6-well plates. After 1 h plating medium was removed and cardiomyocytes were treated with conditioned medium from C26 cells (T) or normal cardiomyocyte culture medium (C; untreated) for 48 h.* ***A)*** *Hierarchical heat map cluster. The numbers indicate the mouse where the heart was taken from. Numbers were randomly allocated. Same number means cells were isolated from the same heart.* ***B)*** *Volcano plot of treated vs. untreated cardiomyocytes. n = 3.*

Annotation Cluster 1	Enrichment Score: 2.67					
	Term	Count	PValue	List total	Pop Hits	Pop Total	FDR
mmu05410	Hypertrophic cardiomyopathy (HCM)	20	0.00006	488	84	5738	0.07
mmu05414	Dilated cardiomyopathy	19	0.0006	488	92	5738	0.73
mmu05412	Arrhythmogenic right ventricular cardiomyopathy (ARVC)	14	0.01	488	74	5738	11.26
mmu04260	Cardiac muscle contraction	12	0.06	488	78	5738	55.55

Annotation Cluster 2	Enrichment Score: 1.87					
	Term	Count	PValue	List Total	Pop Hits	Pop Total	FDR
mmu00071	Fatty acid metabolism	12	0.001	488	45	5738	1.28
mmu00380	Tryptophan metabolism	9	0.02	488	40	5738	19.34
mmu00650	Butanoate metabolism	8	0.03	488	37	5738	34.28
mmu00310	Lysine degradation	8	0.05	488	41	5738	50.00

Tab. 2: KEGG pathway analysis of genes regulated in primary adult mouse cardiomyocytes after treatment with conditioned medium from C26 cells*. Primary mouse cardiomyocytes were plated at 50,000 rod-shaped myocytes/well on laminin-coated 6-well plates. After 1 h plating medium was removed and cardiomyocytes were treated with conditioned medium from C26 cells or normal cardiomyocyte culture medium for 48 h. Enrichment score: measure of pathway cluster enrichment over the other clusters; count: number of regulated genes within the pathway; p-value: significance of pathway enrichment; list total: number of genes within the analyzed list of target genes having at least one KEGG annotation; pop hits: number of genes available on the entire microarray, annotated by the considered KEGG category or annotation cluster; pop total: number of genes available on the entire microarray and having at least one KEGG annotation; FDR: false discovery rate. Top hits are highlighted in black.*

2.4.3 Validation of changes in cardiac fatty acid metabolism under C26 conditions

For validation, gene expression levels of selected significantly regulated genes of the KEGG FA metabolism pathway (Tab. 16) and additional representative genes of this pathway were analyzed by quantitative PCR (qPCR) in hearts from the C26 mice.

The transcription levels of genes involved in fatty acid transport were affected (Fig. 28 A - C, FA transporter). The mRNA levels of the fatty acid transporter 4 (*Fatp4*) decreased significantly over time. Fatty acid transporter 6 (*Fatp6*) transcription levels were significantly elevated in heart samples taken one and two weeks after tumor cell injection and returned to basal levels at the end. Expression levels of *CD36* increased at the end of the experiment. Additionally, transcription levels of genes which encode for proteins that catalyze steps in mitochondrial beta-oxidation were altered (Fig. 28 A - C, beta-oxidation). Expression levels of the carnitine palmitoyltransferase 1 alpha (*Cpt1*α) were elevated at every time point. The Cpt1α protein is targeted to the outer mitochondrial membrane and catalyzes the mitochondrial uptake of long-chain fatty acids. The mRNA levels of the acyl-Coenzyme A dehydrogenase very long-chain (*Acadvl*) were slightly increased after one week of tumor cell injection and significantly elevated after three weeks. The protein that is encoded by this gene is located in the inner mitochondrial membrane where it catalyzes the first step of the fatty acid beta-oxidation pathway. Transcription levels of the hydroxyacyl-Coenzyme A (CoA) dehydrogenase/ 3-ketoacyl-CoA thiolase/enoyl-CoA hydratase (*Hadha*) were slightly increased after one and three weeks of tumor cell inoculation. The last three steps of the mitochondrial beta-oxidation are catalyzed by the trifunctional protein Hadha. The mRNA levels of the genes lipoprotein lipase (*Lpl*), diglyceride acyltransferase 1 (*Dgat1*), acetyl-Coenzyme A acetyltransferase 2 (*Acat2*) and Acyl-Coenzyme A synthase long-chain family member 1 (*Acsl1*) which were summarized under the superscription “lipid synthesis and breakdown” were not significantly affected (Fig. 28 A - C).

In C26 hearts transcription levels of *Acadvl*, *Hadha*, *Acat2* and *Acsl1* (Tab**.** 16) were different compared to the microarray data of the primary adult mouse cardiomyocytes. The mRNA levels of all these genes were decreased in the primary adult mouse cardiomyocytes (Tab**.** 16) and either unchanged (*Acat2, Acsl1*) or increased (*Hadha, Acadvl*) in the heart lysates (Fig. 28 A - C, beta-oxidation + lipid synthesis and breakdown).

As described in the introduction, the main energy source of a mammalian postnatal heart are fatty acids. It is described that heart failure is often accompanied by impaired cardiac energy metabolism. Under these conditions the heart switches from the utilization of lipids as substrate to glucose. This results in a changed expression of the glucose transporters 1 and 4.
In the hearts of the C26-bearing mice the transcription levels of *Glut4* decreased about 50% over time (Fig. 29 B + C). But also the expression levels of *Glut1* were significantly downregulated at the end of the experiment (Fig. 29 C).

The changes in transcription levels of genes involved in FA transport and beta-oxidation indicate that the hearts of C26 mice utilize more fatty acids to produce energy as under normal conditions. However, a fuel switch to glucose as substrate was not occurring. Increased utilization of fatty acids can result in alterations in the storage of fatty acids. To validate this, the triglyceride (TG) content in the hearts of C26 mice was determined by using an enzymatic assay. Additionally, the lipid droplet-associated protein adipophilin/perlipin-2 (Plin2) was detected on heart cross-sections of these mice performing immunohistochemistry (IHC). The TG levels were significantly reduced in hearts of C26 mice compared to the control mice (Fig. 30 A). The Plin2 staining showed that hearts from C26 mice with strong cachexia contained more but really little lipid droplets compared to control littermates (Fig. 30 B). Hearts from C26 mice with mild cachexia exhibited an intermediate phenotype. These hearts showed both large lipid droplets but less than the control littermates as well as an increased number of small lipid droplets but far less as compared to mice with end-stage cachexia (Fig. 30 B).

Overall these data indicate that the hearts of C26-bearing mice switch into a FA-dependent energy-wasting mode.

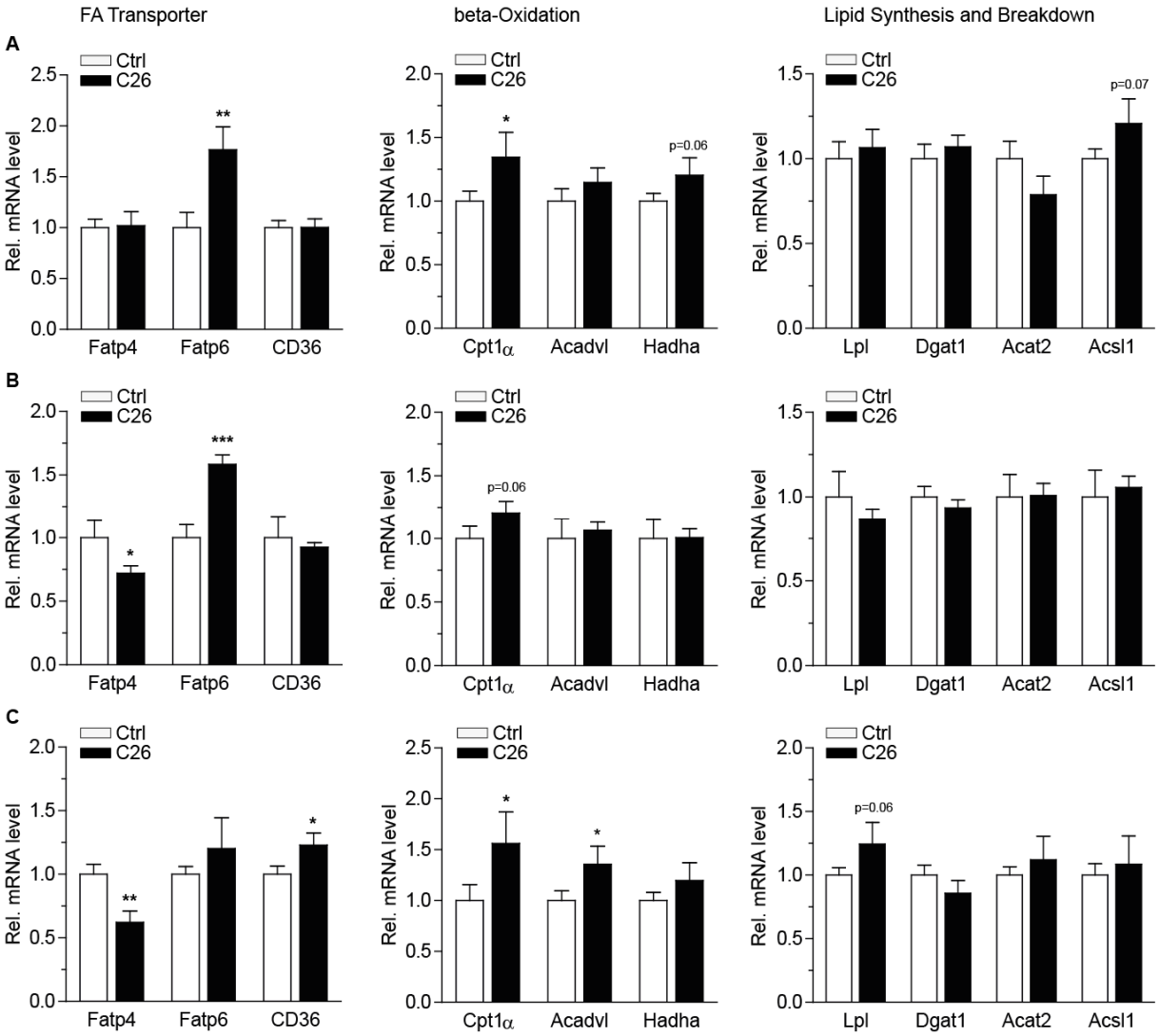

Fig. 28: Validation of the microarray data obtained from primary mouse cardiomyocytes in hearts from C26 mice revealed a dysregulation of genes involved in FA transport and beta-oxidation. *Results are shown for the same cohort of mice as in Fig. 8. RNA was isolated from the apex of the heart using the RNeasy® Mini Kit. Transcription levels of indicated genes were assessed for samples taken* ***A)*** *1 week,* ***B)*** *2 weeks and* ***C)*** *3 weeks after tumor implantation by using the TaqMan system. For each time point transcription levels of genes involved in FA transport (Fatty acid transporter 4 (Fatp4), Fatty acid transporter 6 (Fatp6) and Cluster of differentiation (CD36)), beta-oxidation (Carnitine palmitoyltransferase 1 alpha (Cpt1α), Acyl-Coenzyme A dehydrogenase very long-chain (Acadvl) and Hydroxyacyl-Coenzyme A dehydrogenase/3-Ketoacyl-Coenzyme A thiolase/Enoyl-Coenzyme A hydratase, alpha subunit (Hadha)) and lipid synthesis and breakdown (Lipoprotein lipase (Lpl), Diglyceride acyltransferase 1 (Dgat1), Acetyl-Coenzyme A acetyltransferase 2 (Acat2) and Acyl-Coenzyme A synthase long-chain family member 1 (Acsl1)) are shown. n ≥ 6, mean ± SEM. *indicates significance using Student's t-test with Welch correction, *p < 0.05, **p < 0.01, ***p < 0.001.*

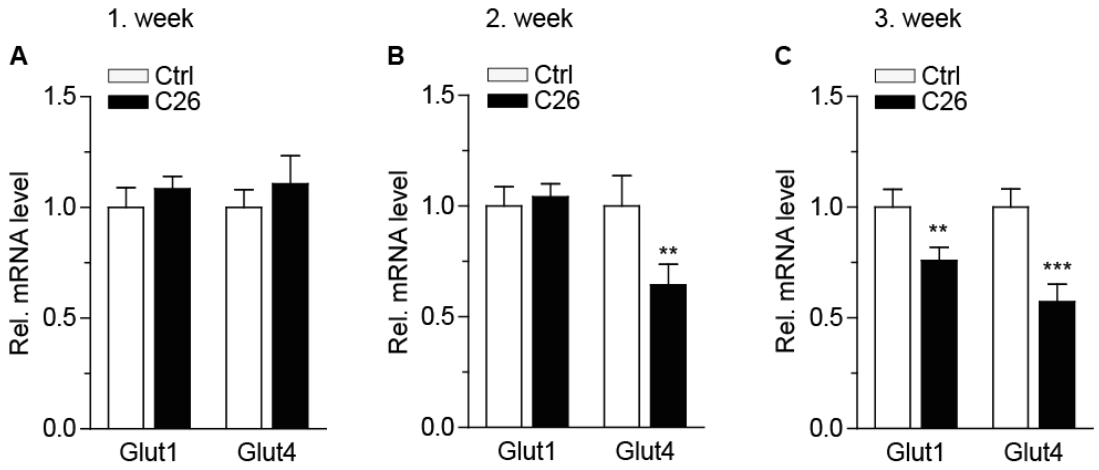

Fig. 29: Expression levels of the glucose transporters 1 and 4 are reduced in atrophic hearts of C26 mice. *Results are shown for the same cohort of mice as in Fig. 8. RNA was isolated from the apex of the heart using the RNeasy® Mini Kit. Transcription levels of the glucose transporters 1 (Glut1) and 4 (Glut4) were assessed for samples taken* ***A)*** *1 week,* ***B)*** *2 weeks and* ***C)*** *3 weeks after tumor implantation by using the TaqMan system. n ≥ 6, mean ± SEM. *indicates significance using Student's t-test with Welch correction, **p < 0.01, ***p < 0.001.*

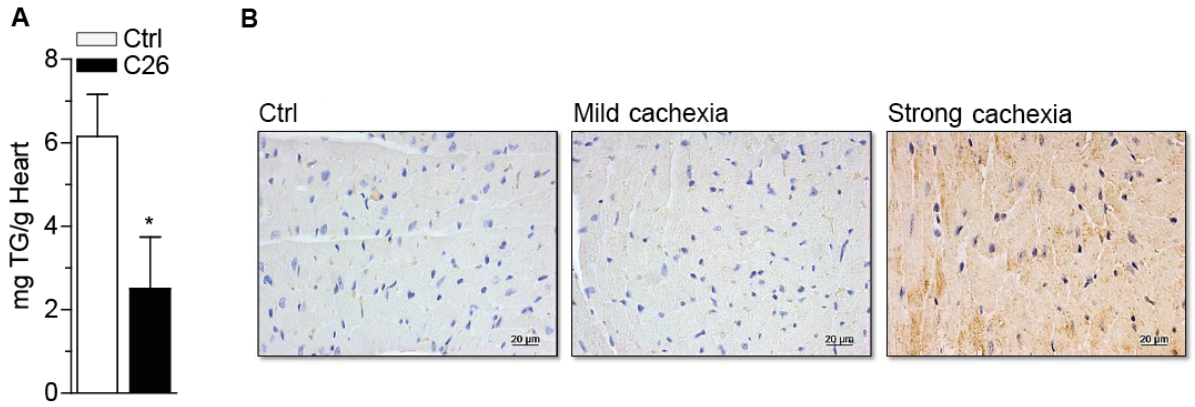

Fig. 30: Lipid storage is diminished in hearts of C26 mice. A) *TG content of whole hearts (without atria) from C26 mice and control (Ctrl) littermates was determined using the Serum Triglyceride Determination Kit. TG levels were normalized to the frozen dry heart weight. The samples used for this measurement were not from the same cohort of mice as shown in Fig. 8. Used samples were obtained from a second C26 mouse experiment with a similar setup.* ***B)*** *Representative pictures of IHC stainings from heart cross-sections of a Ctrl mouse, a C26-bearing mouse with mild cachexia and a strong cachectic C26-bearing mouse are shown. Used samples were taken from the same cohort of mice as shown in Fig. 8. Lipid droplets were visualized by staining the lipid droplet-associated protein adipophilin/perilipin-2. Magnification: 40x.* ***A)*** *n ≥ 6, mean ± SEM. *indicates significance using Student's t-test with Welch correction, *p < 0.05.*

To corroborate the previous data which indicated that FA transport and beta-oxidation in atrophic hearts from C26 mice are increased functional assays were performed. The overall mitochondrial function and palmitate-driven FA oxidation of primary neonatal rat cardiomyocytes that were exposed to conditioned medium from C26 cells for 8 h and 24 h were assessed by using the Seahorse Metabolic Flux Analyzer. First, we examined if primary neonatal rat cardiomyocytes also develop alterations in the expression of the selected FA metabolism genes and lipid storage under cachectic conditions.

As observed for the hearts expression levels of *Fatp4* were decreased at every time point and mRNA levels of *Fatp6* initially increased and finally decreased in C26-treated primary neonatal rat

cardiomyocytes (Fig. 31 A + B; FA transporter). *CD36* and *Acat2* expression levels were unchanged (Fig. 31 A + B; FA transporter + lipid synthesis and breakdown). Transcription levels of the examined beta-oxidation genes were also upregulated but not to the same extent as shown for the hearts from C26 mice (Fig. 31 A + B). Expression levels of *Lpl* were slightly increased which was also seen in the heart samples (Fig. 31 A + B; lipid synthesis and breakdown). The mRNA levels of *Dgat1* were significantly downregulated in C26-treated primary neonatal rat cardiomyocytes (Fig. 31 A + B; lipid synthesis and breakdown). This effect was not that strong in the hearts. *Acsl1* expression levels were more than two times elevated in primary neonatal rat cardiomyocytes at every time point (Fig. 31 A + B; lipid synthesis and breakdown). This drastic effect was not observed in the hearts of C26 mice.
Gene expression levels of *Acadvl*, *Hadha*, *Acat2* and *Acsl1* were also different comparing primary neonatal rat cardiomyocytes with primary adult mouse cardiomyocytes. Expression levels of the mentioned genes were decreased in the primary adult mouse cardiomyocytes (Tab. 16) and either unchanged (*Acat2, Acadvl*) or increased (*Hadha, Acsl1*) in the primary neonatal rat cardiomyocytes (Fig. 31 A + B; beta-oxidation + lipid synthesis and breakdown).

The TG content of primary neonatal rat cardiomyocytes that were exposed to C26-conditioned medium for 24 h was reduced but it did not reach significance (Fig. 32 A). Glucose uptake in the cachectic primary neonatal rat cardiomyocytes was not affected which was shown by unchanged transcription levels of *Glut1* and *Glut4* (Fig. 32 B + C).

To explore the FA oxidation capacity of primary neonatal rat cardiomyocytes under cachectic conditions metabolic flux analysis was performed. Palmitate was chosen to perform this assay because long-chain FAs are the main energy source of the heart. The metabolic flux analysis revealed that primary neonatal rat cardiomyocytes that were exposed to C26-conditioned medium for 8 h did not develop a remarkable phenotype (Fig. 33 A + B) but after 24 h treatment basal respiration (time point 1 - 4) and palmitate-driven FA oxidation (time point 5 - 7) were significantly elevated (Fig. 33 C + D). The specificity of FA oxidation was determined and confirmed by the injection of the Cpt1 inhibitor, etomoxir.

The analysis of the overall mitochondrial function of primary neonatal rat cardiomyocytes showed that basal respiration (time point 1 - 3) was reduced and maximal respiration was slightly increased after 8 h under cachectic conditions (Fig. 34 A + B). After 24 h treatment basal respiration (time point 1 - 3) was increased and maximal respiratory capacity (time point 8 - 11) was more elevated (Fig. 34 C + D). An overview of the fundamental parameters of this Seahorse assay is displayed in Figure 47.

These data indicate that the FA-dependent energy-wasting results from increased uncoupling. Furthermore, these data demonstrate that the alterations in FA metabolism are induced by tumor-secreted factors.

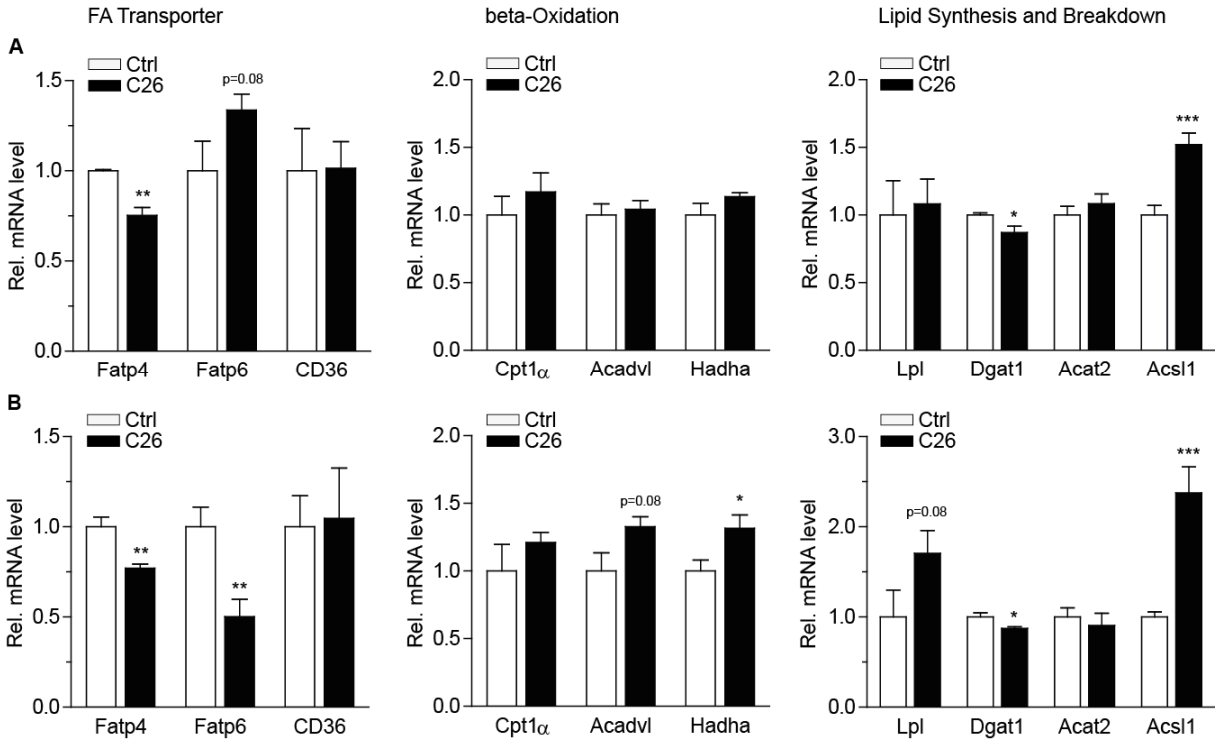

Fig. 31: Transcription levels of genes that are involved in FA transport, beta-oxidation and lipid synthesis and breakdown are altered in primary neonatal rat cardiomyocytes under cachectic conditions. *Results are shown for primary neonatal rat cardiomyocytes that were exposed to conditioned medium from C26 cells for* ***A)*** *8 h and* ***B)*** *24 h. RNA was isolated using the RNeasy® Mini Kit. Transcription levels of indicated genes were assessed by using the TaqMan system. For each time point transcription levels of genes involved in FA transport (Fatty acid transporter 4 (Fatp4), Fatty acid transporter 6 (Fatp6) and Cluster of differentiation (Cd36)), beta-oxidation (Carnitine palmitoyltransferase 1 alpha (Cpt1α), Acyl-Coenzyme A dehydrogenase very long-chain (Acadvl) and Hydroxyacyl-Coenzyme A dehydrogenase/3-Ketoacyl-Coenzyme A thiolase/Enoyl-Coenzyme A hydratase, alpha subunit (Hadha)) and lipid synthesis and breakdown (Lipoprotein lipase (Lpl), Diglyceride acyltransferase 1 (Dgat1), Acetyl-Coenzyme A acetyltransferase 2 (Acat2) and Acyl-Coenzyme A synthase long-chain family member 1 (Acsl1)) are shown. n = 4, mean ± SEM. *indicates significance using Student's t-test with Welch correction, *p < 0.05, **p < 0.01, ***p < 0.001.*

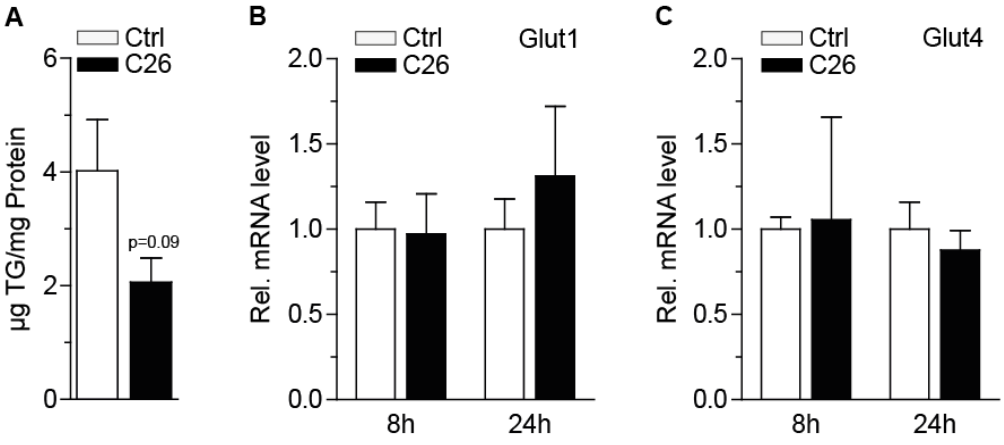

Fig. 32: Lipid storage is decreased and glucose uptake is unchanged in primary neonatal rat cardiomyocytes under cachectic conditions. *Primary neonatal rat cardiomyocytes were exposed to normal culture medium (Ctrl) or C26-conditioned medium (C26) for 8 h or 24 h.* ***A)*** *Trigylceride (TG) content was determined in cardiomyocytes treated for 24 h using the Serum Triglyceride Determination Kit. TG levels were normalized to the protein content. RNA was isolated using the RNeasy® Mini Kit. Transcription levels of the* ***B)*** *Glucose transporters 1 (Glut1) and* ***C)*** *4 (Glut4) were assessed using the TaqMan system.* ***A)*** *n ≥ 4, mean ± SEM. No significance by using Student's test with Welch correction.* ***B) + C)*** *n = 3, mean ± SEM. No significance using Student's t-test with Welch correction.*

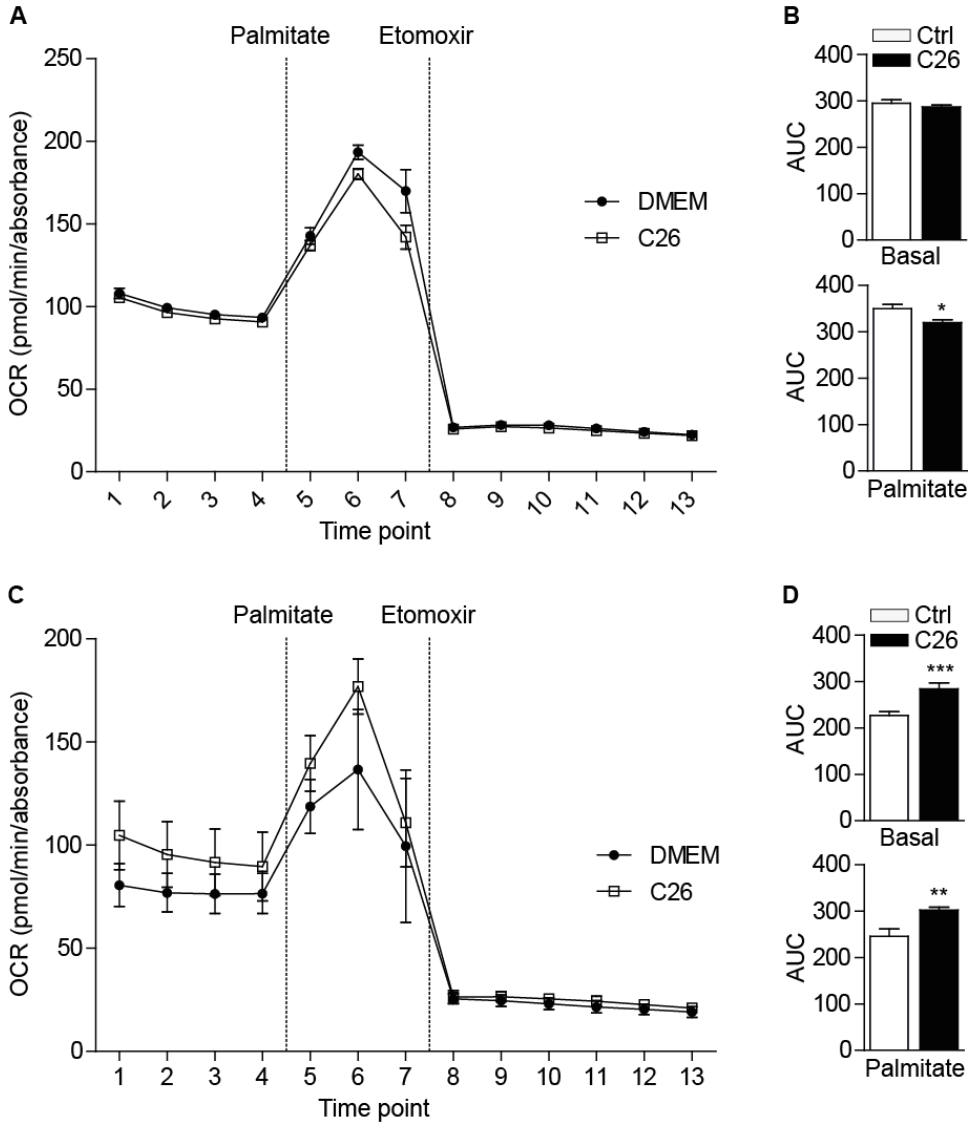

Fig. 33: Palmitate-driven FA oxidation is increased in primary neonatal rat cardiomyocytes under cachectic conditions. *Long-chain FA-driven oxidation of primary neonatal rat cardiomyocytes that were cultured in normal culture medium (DMEM) or C26-conditioned medium (C26) for* ***A) + B)*** *8 h and* ***C) + D)*** *24 h was examined using the Seahorse Metabolic Flux Analyzer.* ***A) + C)*** *Mitochondrial function is expressed by the oxygen consumption rate (OCR). 1 mM BSA-conjugated palmitate and 1 mM etomoxir were added at the indicated time points. Data were normalized to cell density (absorbance).* ***B) + D)*** *Area under the curve (AUC) was calculated for the basal and the palmitate condition. n ≥ 9, mean ± SEM. *indicates significance using Student's t-test with Welch correction, *p < 0.05, **p < 0.01, ***p < 0.001.*

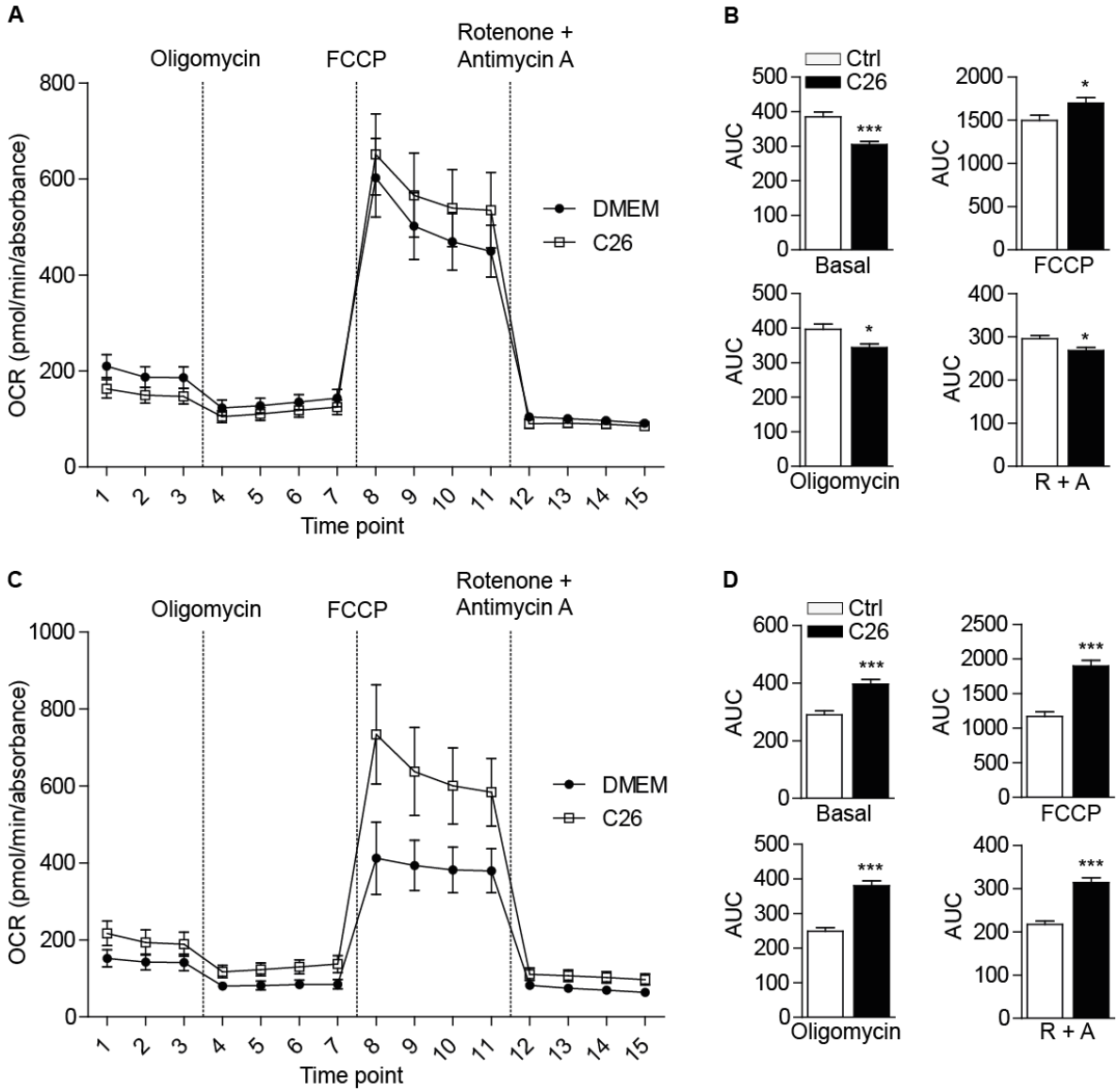

Fig. 34: Overall mitochondrial function is also altered in primary neonatal rat cardiomyocytes under cachectic conditions. *Overall mitochondrial function of primary neonatal rat cardiomyocytes that were cultured in normal culture medium (DMEM) or C26-conditioned medium (C26) for either* ***A) + B)*** *8 h or* ***C) + D)*** *24 h was assessed using the Seahorse Metabolic Flux Analyzer.* ***A) + C)*** *Mitochondrial function is expressed by the oxygen consumption rate (OCR). 2 µM oligomycin, 0.3 µM FCCP and 1 µM rotenone together with 1 µM antimycin A (R + A) were added at the indicated time points. Data were normalized to cell density (absorbance).* ***B) + D)*** *Area under the curve (AUC) was calculated for all four conditions. n ≥ 10, mean ± SEM. *indicates significance using Student's t-test with Welch correction, *p < 0.05, ***p < 0.001.*

The increase in maximal respiration in the cachectic primary neonatal primary cardiomyocytes was achieved through a higher uncoupling capacity. The so called "uncoupling proteins" and also the adenine nucleotide translocators which are all located in the inner mitochondrial membrane are involved in the regulation of the mitochondrial uncoupling process. Therefore, the gene expression levels of uncoupling protein 2 (*Ucp2*) and 3 (*Ucp3*) as well as of the adenine nucleotide translocator type 1 (*Ant1*) and type 2 (*Ant2*) were examined in C26 hearts and in primary neonatal rat cardiomyocytes. The mRNA levels of both *Ucp* genes increased in the hearts of C26-bearing mice over time (Fig. 35 A + B). The transcription levels of *Ant1* were unchanged and the gene expression levels of *Ant2* decreased significantly (Fig. 35 C + D).

Primary neonatal rat cardiomyocytes that were exposed to C26-conditioned medium for 24 h followed by 2 h treatment with Seahorse assay medium showed elevated transcription levels of *Ucp2*, *Ant1* and *Ant2* (Fig. 36 A - C). Surprisingly, the gene expression levels of *Ant1* and *Ant2* did not overlap comparing the *in vivo* and *in vitro* model. The culture conditions that were chosen for the primary neonatal rat cardiomyocytes corresponded to the conditions of the Seahorse assay that analyzed the overall mitochondrial function. The gene expression data supported the results of the metabolic flux analysis because the greatest effect on mitochondrial uncoupling was also measured after 24 h treatment with C26-conditioned medium (Fig. 34). We were not able to detect *Ucp3* either on gene expression or on protein level in primary neonatal rat cardiomyocytes.

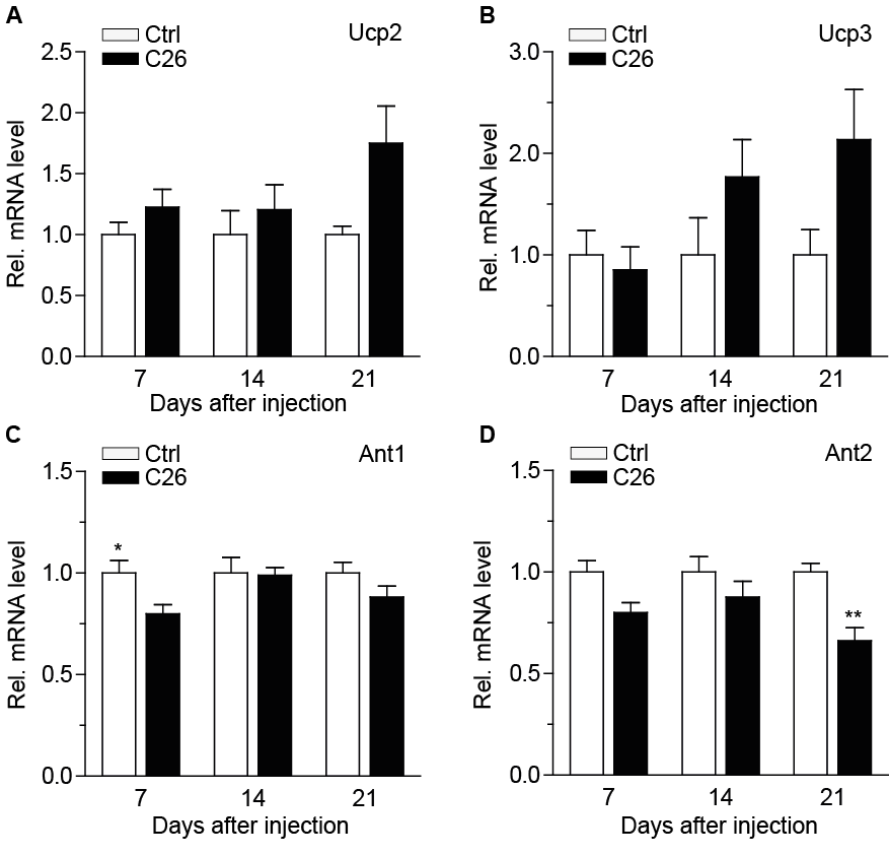

Fig. 35: Transcription levels of marker for mitochondrial uncoupling are altered in hearts of C26-bearing mice. *Results are shown for the same cohort of mice as in Fig. 8. RNA was isolated from the apex of the heart using the RNeasy® Mini Kit. mRNA levels of the uncoupling proteins* ***A)*** *2 (Ucp2) and* ***B)*** *3 (Ucp3) as well as of the adenine nucleotide translocator* ***C)*** *type 1 (Ant1) and* ***D)*** *type 2 (Ant2) were assessed by using the TaqMan system. n ≥ 6, mean ± SEM. *indicates significance using 2-way ANOVA, Bonferroni post-test, *p < 0.05, **p < 0.01.*

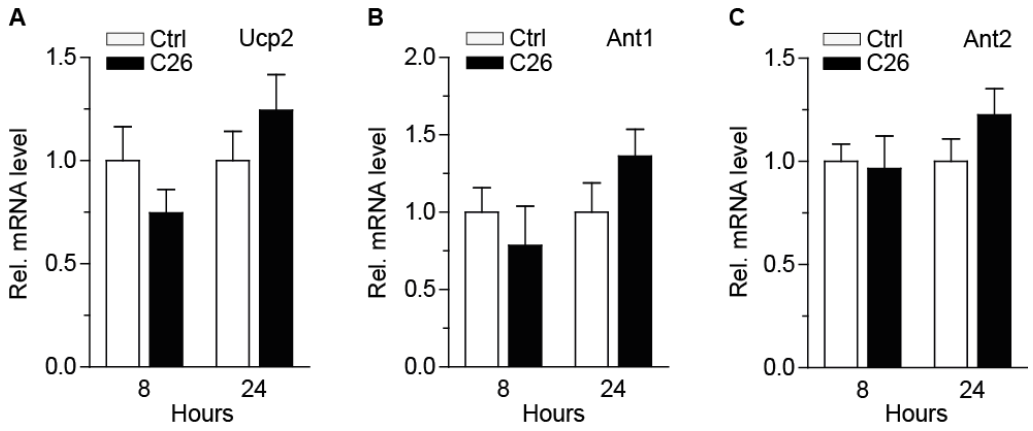

Fig. 36: Transcription levels of marker for mitochondrial uncoupling are slightly elevated in the in vitro model. *Results are shown for primary neonatal rat cardiomyocytes that were exposed to normal culture medium (DMEM) or C26-conditioned medium (C26) for 8 h and 24 h and were subsequently cultured in Seahorse assay medium for 2 h. RNA was isolated using the RNeasy® Mini Kit. mRNA levels of the* ***A)*** *uncoupling protein 2 (Ucp2) and of the adenine nucleotide translocator* ***B)*** *type 1 (Ant1) and* ***C)*** *type 2 (Ant2) were assessed by using the TaqMan system. n ≥ 3, mean ± SEM. No significance by using 2-way ANOVA, Bonferroni post-test.*

2.4.4 Validation of changes in cardiac fatty acid metabolism in APC delta 580 mice

Due do the results in chapter 2.3 which showed that the genetic mouse model for colon cancer developed a similar cardiac phenotype as the C26 mouse model, we tested the question, if the observed alterations in cardiac FA metabolism were also induced in this mouse model. In contrast to the C26 mouse experiment only samples for the end time point were available.

Changes in the examined FA metabolism gene expression profile were also detected in the hearts of APC 580/+ mice (Fig. 37 A - C). Expression patterns of the FA transporters in the hearts of APC 580/+ mice were nearly similar to the three weeks' time point of the C26 mice. The transcription levels of *Fatp4* were significantly downregulated, the mRNA levels of *Fatp6* were slightly reduced and the expression levels of *Cd36* were slightly increased (Fig. 37 A). The genes that are involved in mitochondrial beta-oxidation were regulated in the opposite direction comparing APC 580/+ and C26 hearts. Whereas, only the mRNA levels of *Acadvl* and *Hadha* were significantly reduced in APC 580/+ mice (Fig. 37 B). Additionally, the genes encoding for proteins involved in lipid synthesis and breakdown were regulated in a different way in the hearts of APC 580/+ mice compared to C26 mice. *Lpl* expression levels were unchanged, *Dgat1* mRNA levels were elevated and transcription levels of *Acat2* and *Acsl1* were significantly downregulated in APC 580/+ mice (Fig. 37 C). As observed for the C26 mice the TG levels in the hearts of APC 580/+ mice were reduced (Fig. 37 D). This was confirmed by Plin2 stainings which showed lesser and smaller lipid doplets in the hearts of APC 580/+ mice compared to control littermates (Fig. 37 E). The changes in *Glut1* and *Glut4* expression that were detected in the C26 mice could not be confirmed in the APC mouse model (Fig. 37 F).

Also the expression levels of the genes encoding for the *Ucp2* and *Ucp3* were analyzed in the APC mouse model because this was the most interesting result of the functional assays. In hearts from APC 580/+ mice transcription levels of *Ucp2* were significantly increased, whereas *Ucp3* mRNA levels were significantly decreased (Fig. 38 A + B). Transcription levels of *Ant1* were unchanged and of *Ant2* were slightly elevated in APC 580/+ mice compared to the control littermates (Fig. 38 C + D). The trend of this gene expression pattern is towards what was observed for primary neonatal rat cardiomyocytes under cachectic conditions.

The overall findings of this chapter (chapter 2.4) indicate that aberrant FA metabolism and increased energy-wasting by uncpoupling are an understudied clinical feature of colon cancer-induced cachexia. Additionally, these data support the hypothesis that tumor-secreted pro-cachectic factors induce the observed FA metabolism phenotype.

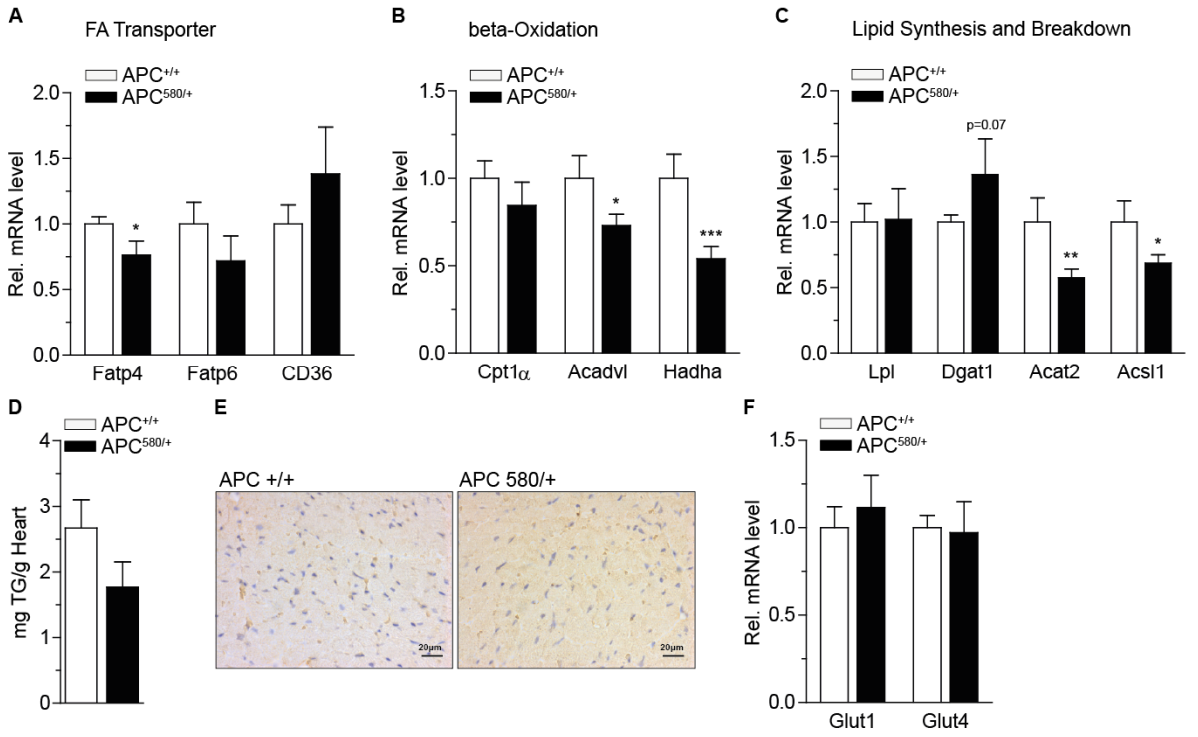

Fig. 37: Triglyceride storage and genes involved in FA metabolism are altered in APC 580/+ mice. A) - C) *Results are shown for the same cohort of mice as in Fig. 21. RNA was isolated from the apex of the heart using the RNeasy® Mini Kit. Transcription levels of indicated genes were assessed by using the TaqMan system. Transcription levels of genes involved in FA transport (Fatty acid transporter 4 (Fatp4), Fatty acid transporter 6 (Fatp6) and Cluster of differentiation (Cd36)), beta-oxidation (Carnitine palmitoyltransferase 1 alpha (Cpt1α), Acyl-Coenzyme A dehydrogenase very long-chain (Acadvl) and Hydroxyacyl-Coenzyme A dehydrogenase/3-Ketoacyl-Coenzyme A thiolase/Enoyl-Coenzyme A hydratase, alpha subunit (Hadha)) and lipid synthesis and breakdown (Lipoprotein lipase (Lpl), Diglyceride acyltransferase 1 (Dgat1), Acetyl-Coenzyme A acetyltransferase 2 (Acat2) and Acyl-Coenzyme A synthase long-chain family member 1 (Acsl1)) are shown.* ***D)*** *Triglyceride (TG) content of whole hearts (without atria) from APC 580/+ mice and age-matched littermates (APC +/+) was determined using the Serum Triglyceride Determination Kit. TG levels were normalized to the frozen dry heart weight. The samples used for this measurement were not from the same cohort of mice as shown in Fig. 21. Used samples were obtained from a second APC mouse experiment.* ***E)*** *Representative pictures of IHC stainings from heart cross-sections of an APC +/+ and an APC +/- mice are shown. Used samples were taken from the same cohort of mice as shown in Fig. 21. Lipid droplets were visualized by staining the lipid droplet-associated protein adipophilin/perilipin-2. Magnification: 40x* ***F)*** *Expression levels of the glucose transporters 1 and 4 (Glut1, Glut4) are shown for the same cohort of mice as in Fig. 21. RNA was isolated from the apex of the heart using the RNeasy® Mini Kit. Transcription levels were assessed by using the TaqMan system.* ***A) - C) + E)*** *$n \geq 6$, mean ± SEM. *indicates significance using Student's t-test with Welch correction, *$p < 0.01$.* ***D)*** *$n \geq 4$, mean ± SEM. No significance using Student's t-test with Welch correction.*

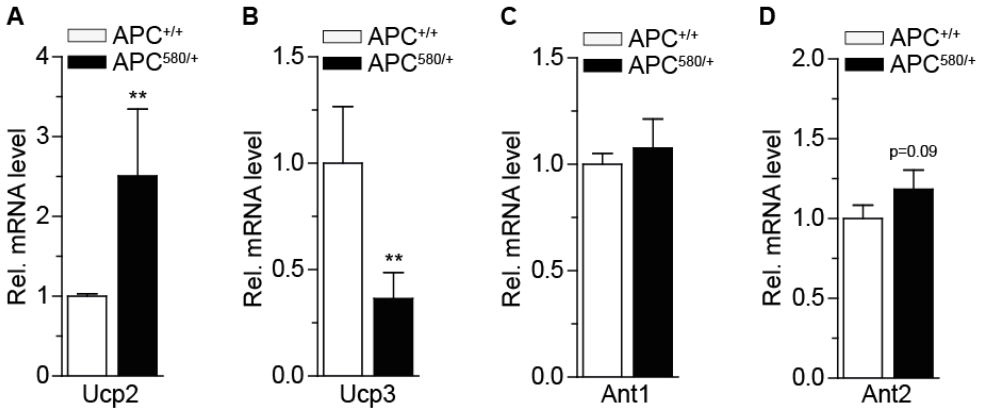

Fig. 38: Transcription levels of marker for mitochondrial uncoupling are changed in APC 580/+ mice. *Results are shown for the same cohort of mice as in Fig. 21. RNA was isolated from the apex of the heart using the RNeasy® Mini Kit. mRNA levels of the uncoupling proteins* ***A)*** *2 (Ucp2) and* ***B)*** *3 (Ucp3) as well as of the adenine nucleotide translocator* ***C)*** *type 1 (Ant1) and* ***D)*** *type 2 (Ant2) were assessed by using the TaqMan system. n ≥ 6, mean ± SEM. *indicates significance using Student's t-test with Welch correction, **p < 0.01.*

2.5 Cardiomyocyte atrophy is induced through tumor-secreted factors

The aforementioned results suggest that cardiac atrophy represents an important read-out parameter in systemic cancer cachexia. However, the question remained if the cachexia-induced effects on the heart were mediated by tumor-borne factors in a cell-autonomous manner or if they derived from secondary signals. To answer this question an *in vitro* cardiomyocyte phenotyping system was developed which was already described in chapter 2.4. To determine the area of primary cardiomyocytes under cachectic and non-cachectic conditions, they were stained against the cytoskeletal protein α-actinin as this protein is not present in fibroblasts which are to a less extend within the culture.

2.5.1 Conditioned medium of C26 cells induces atrophy in isolated primary cardiomyocytes

In line with the *in vivo* cardiac phenotype, the treatment of primary neonatal rat cardiomyocytes with C26-conditioned medium for a minimum of 8 h induced a significant reduction in cardiomyocyte size (PhD thesis Ezgi Baysal, AG Backs). The same phenotype was observed exposing neonatal rat cardiomyocytes to conditioned medium from human colon cancer cell lines such as SW480, HT-29 and HCT116 for 48 h (PhD thesis Ezgi Baysal, AG Backs). In contrast, conditioned medium from non-cachexia inducing cells such as the mouse colon cancer cell line MC38, HEK293A and COS-1 cells did not cause cardiomyocyte atrophy (PhD thesis Ezgi Baysal and personal communication, AG Backs). Shrinkage in size was also observed for primary adult mouse cardiomyocytes that were exposed to conditioned medium from C26 cells for 48 h (Personal communication, AG Backs). The induced reduction in size was reversible in both primary adult mouse cardiomyocytes and neonatal rat cardiomyocytes only by removing the conditioned medium and culturing the cells in regular cell culture medium (PhD thesis Ezgi Baysal and personal communication, AG Backs). C26-conditioned medium that was heat-inactivated at 95°C for 5 min lost its atrophy-inducing capability (PhD thesis Ezgi Baysal, AG Backs). This was not the case for C26-conditioned medium that was heated to 56°C for 30 min. Even primary neonatal rat cardiomyocytes that were cultured in 2% serum from C26-bearing mice developed atrophy after 24 h (Fig. 46) but not after treatment with serum from MC38 mice (Personal communication, AG Backs).

Consistent with the results shown for the hearts from C26-bearing mice, the expression levels of the fetal genes *Anp*, *Bnp* and *β-Mhc* as well as the transcription levels of *α-Mhc* were decreased in neonatal rat cardiomyocytes cultured in C26-conditioned medium (PhD thesis Ezgi Baysal, AG Backs). Even the mRNA levels of the E3 ubiquitin ligases *MuRF1* and *Atrogin-1* were decreased in neonatal rat cardiomyocytes after 24 h treatment with C26-conditioned medium as observed for the hearts from C26-bearing mice (PhD thesis Ezgi Baysal, AG Backs).

2.5.2 Identification of potential "cachexokines"

These data indicated that C26 cells released pro-cachectic mediators which were most probably proteins and caused cardiac atrophy in a cell-autonomous manner. To identify these "cachexokines", an unbiased differential secretome analysis of the cachexia inducing mouse colon cancer cell line C26 in comparison to the non-cachexia inducing mouse colon cancer cell line MC38 was performed.
For this purpose, click chemistry combined with pulsed stable isotope amino acid labeling was used to selectively enrich and quantify secreted proteins from both cell lines (Eichelbaum K., 2012). Two biological replicates of both cell lines were prepared for this secretome analysis. Mass spectrometry-based identification and differential secretome mapping revealed a total number of 893 secreted proteins that overlapped in both biological replicates (Fig. 39 A). The Pearson correlation between the two biological replicates was 0.93. 129 proteins out of this pool were established to be secreted at least 2-fold more by the C26 cells and 142 proteins by the MC38 cells (Fig. 39 B; all colored dots). The 129 identified proteins with relative enrichment in the cachexia-inducing C26 cells were classified as potential cachexia-inducing candidates. 53.4% of the proteins quantified in both replicates and 77.5% of the differentially secreted proteins are predicted to be secreted using SignalP (classical secretion) and SecretomeP (non-classical secretion) (Fig. 39 C + D).

2.5.3 Individual "cachexokines" are sufficient to promote cardiomyocyte atrophy

To directly test the pro-cachectic capability of the identified factors in an unbiased fashion, cDNA clones for 109 of the potential "cachexokines" were obtained and overexpressed in HEK293 A cells. For the remaining 21 proteins no cDNA clones were available. Overexpression efficiency of the *ATAXIN10* cDNA clone as representative is shown in Figure 49. Conditioned media from the transfected HEK293 A cells were collected and assayed for their atrophy-inducing potential on primary neonatal rat cardiomyocytes using an automated high-throughput 384-well plate assay. 28 of the "cachexokine"-enriched media caused atrophy in the primary neonatal rat cardiomyocytes in several screening rounds (Fig. 40; corresponding clones are marked in red). The impact on cardiomyocyte size of these candidates was additionally validated by using the *in vitro* system as was described before in chapter 2.4. This screen confirmed the results of the automated analysis (data not shown). The according protein names for the clones 1 - 109 are listed in chapter 5.11**.**

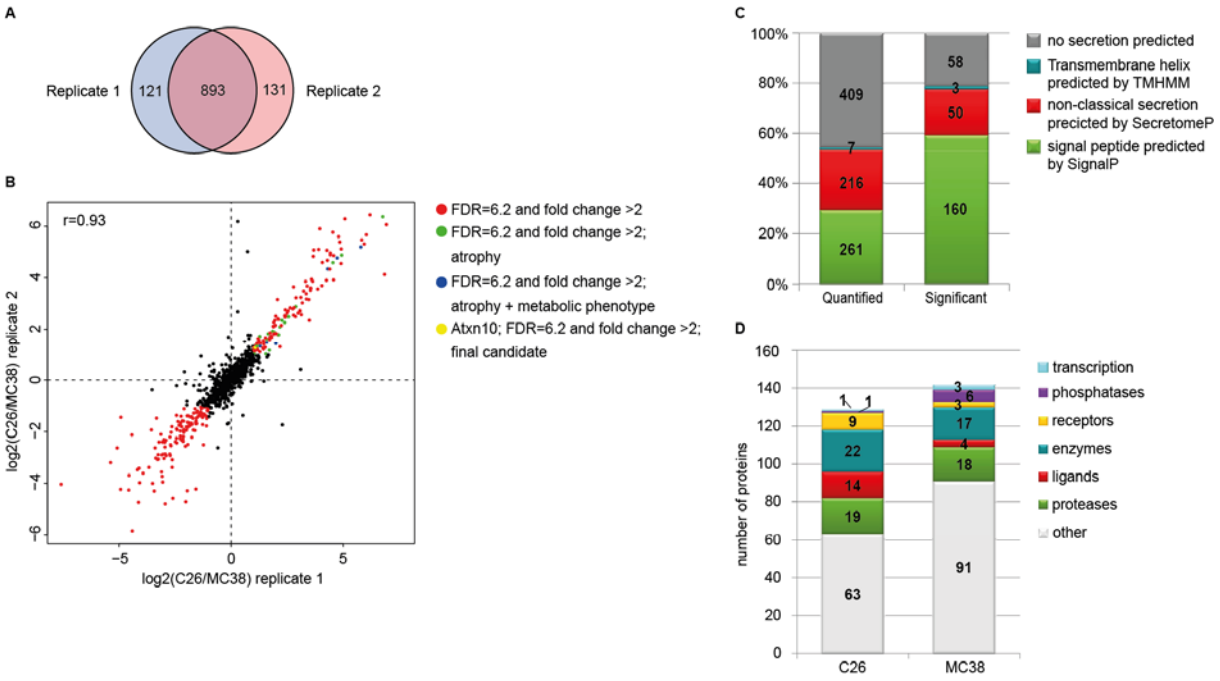

Fig. 39: Quantification of secreted proteins comparing the cachexia-inducing C26 cell line with the non-cachexia-inducing MC38 cell line. *C26 and MC38 cells were cultured in the presence of 10% serum and were labeled with AHA and SILAC for 24 h in biological duplicates. Media were collected and the newly synthesized proteins were enriched.* ***A)*** *Number and overlap of proteins quantified in the two biological replicates.* ***B)*** *Pearson correlation between the two biological replicates. Secreted proteins that showed significant differences between the two cell lines are indicated by the colored dots. Proteins that were significantly more secreted by the C26 cells and induced atrophy in primary neonatal rat cardiomyocytes are highlighted by green dots. Proteins that were significantly more synthesized by the C26 cells and induced atrophy as well as alterations in fatty acid metabolism in primary neonatal rat cardiomyocytes are indicated by blue dots. The final "cachexokine" (Ataxin10) is highlighted by a yellow dot.* ***C)*** *Classification of all quantified proteins and the significantly secreted proteins of both cell lines using SignalP (classical secretion) and SecretomeP (non-classical secretion).* ***D)*** *Enriched protein functions for proteins significantly secreted by the two cell lines (Metacore).*

2.5.4 Selective "cachexokines" provoke aberrant fatty acid oxidation

Next, the selected 28 factors were analyzed for their impact on cardiac fatty acid oxidation using metabolic flux analysis to narrow down the list of potential "cachexokines". As shown in Figure 41, 7 out of the 28 atrophy-inducing factors were able to enhance mitochondrial uncoupling and palmitate-driven FA oxidation in repeated measurements as observed for the C26-conditioned medium. The following proteins were the most highly potential "cachexokines": ADAMTS like protein 4 (Adamtsl4), ataxin 10 (Atxn10), bridging integrator 1 (Bin1), chemokine ligand 2 (Ccl2), glucosidase alpha acid (Gaa), multiple inositol-polyphosphate phosphatase (Minpp1) and syntaxin 7 (Stx7).

2.5.5 More than one "cachexokine" is necessary to induce the C26 phenotype

siRNA based knockdown strategy was performed in C26 cells to examine whether individual highly potential "cachexokines" are able to promote cardiac atrophy and changes in mitochondrial function *in vitro*. In a first setup C26 cells were transfected with a siRNA directed against one of the 7 remaining candidates. Conditioned medium from these cells was collected. As shown in Figure 51, the expression levels of the individual genes were decreased by 55 - 80%. Reduced levels of a single factor out of the selected 7 candidates were not sufficient to blunt the effects of C26-conditioned medium on cardiomyocytes size and mitochondrial function (Fig. 42).

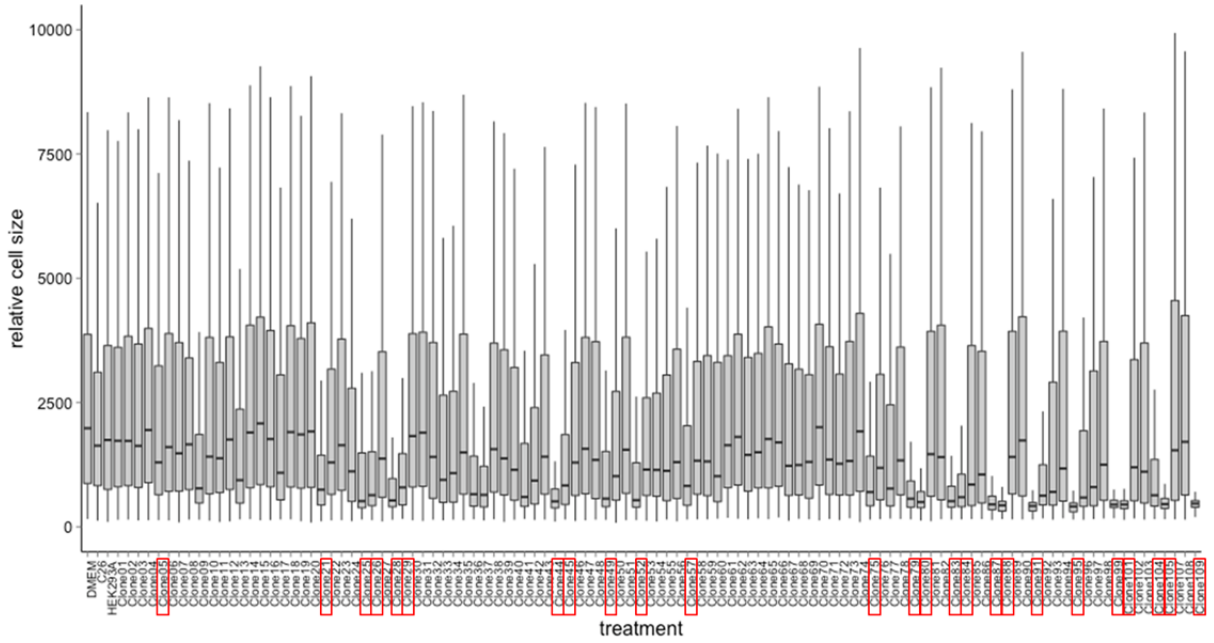

Fig. 40: Assessment of atrophy-inducing "cachexokines" using a high-throughput 384-well plate assay. *Primary neonatal rat cardiomyocytes were seeded at 6 x 10^3 cells/well on 384-well plates. Cells were treated with conditioned from untreated HEK293 A cells, HEK293 A cells that were transfected with the cDNA clones (see chapter 5.11) or C26 cells for 24 h. Cells were stained against α-actinin (secondary antibody was Alexa Fluor 488 conjugated (FITC channel)). Images were visualized automatedly and were analyzed using CellProfiler. Areas of cardiomyocytes measured in the FITC channel were displayed as boxplot (displaying the median, the upper and lower hinge representing the first and third quartiles and the whiskers extending to the highest and lowest value within 1.5x interquartile range (IQR) of the upper and lower hinge, respectively).*

As none of the 7 candidates alone could induce the expected phenotype, the idea was to see if a combined knockdown of all 7 candidates could rescue the *in vitro* phenotype. For this reason, C26 cells were treated with siRNAs directed against all 7 potential "cachexokines". A knockdown efficiency between 45 - 80% was achieved for the individual genes (Fig. 52). Conditioned medium of C26 cells with a knockdown of all 7 candidates was able to rescue the metabolic phenotype (Fig. 43) but not the shrinkage of the cardiomyocytes (data not shown).

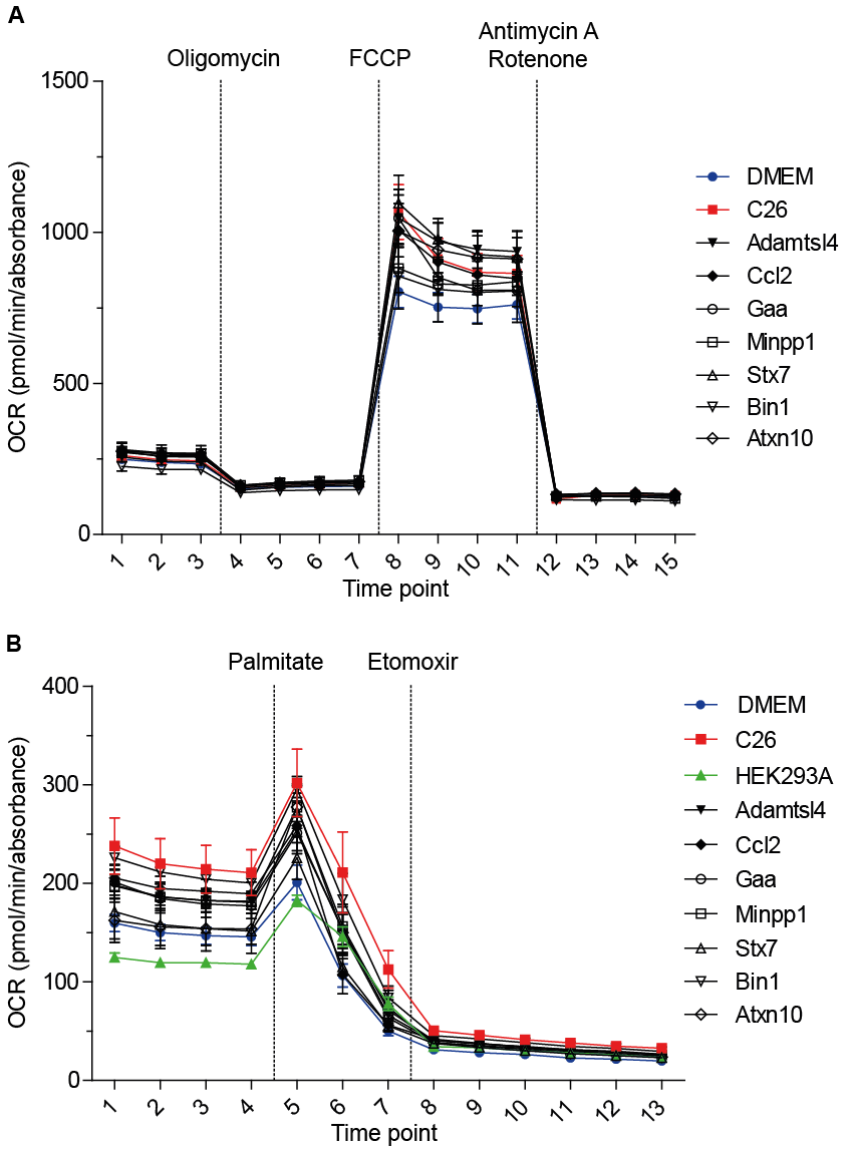

Fig. 41: Mitochondrial uncoupling and palmitate-driven FA oxidation in primary neonatal rat cardiomyocytes are increased after treatment with selective "cachexokines". *Primary neonatal rat cardiomyocytes were exposed to normal culture medium (DMEM), conditioned medium from C26 cells (C26) or HEK293 A cells that were either untreated (HEK293A) or overexpressed one of the selective candidates (Adamts like 4 (Adamtsl4), Chemokine ligand 2 (Ccl2), Glucosidase alpha acid (Gaa), Multiple inositol-polyphosphate phosphatase 1 (Minpp1), Syntaxin 7 (Stx7), Bridging integrator 1 (Bin1) and Ataxin10 (Atxn10)) 24 h before the two different Seahorse assays were performed. Mitochondrial function was expressed by the oxygen consumption rate (OCR). Data were normalized to cell density (absorbance).* ***A)*** *Assessment of the overall mitochondrial function: 2 µM oligomycin, 0.3 µM FCCP and 1 µM rotenone together with 1 µM antimycin A were added at the indicated time points.* ***B)*** *Analysis of the palmitate-driven FA oxidation capacity: 1 mM BSA-conjugated palmitate and 1 mM etomoxir were added at the indicated time points. n ≥ 5, mean ± SEM.*

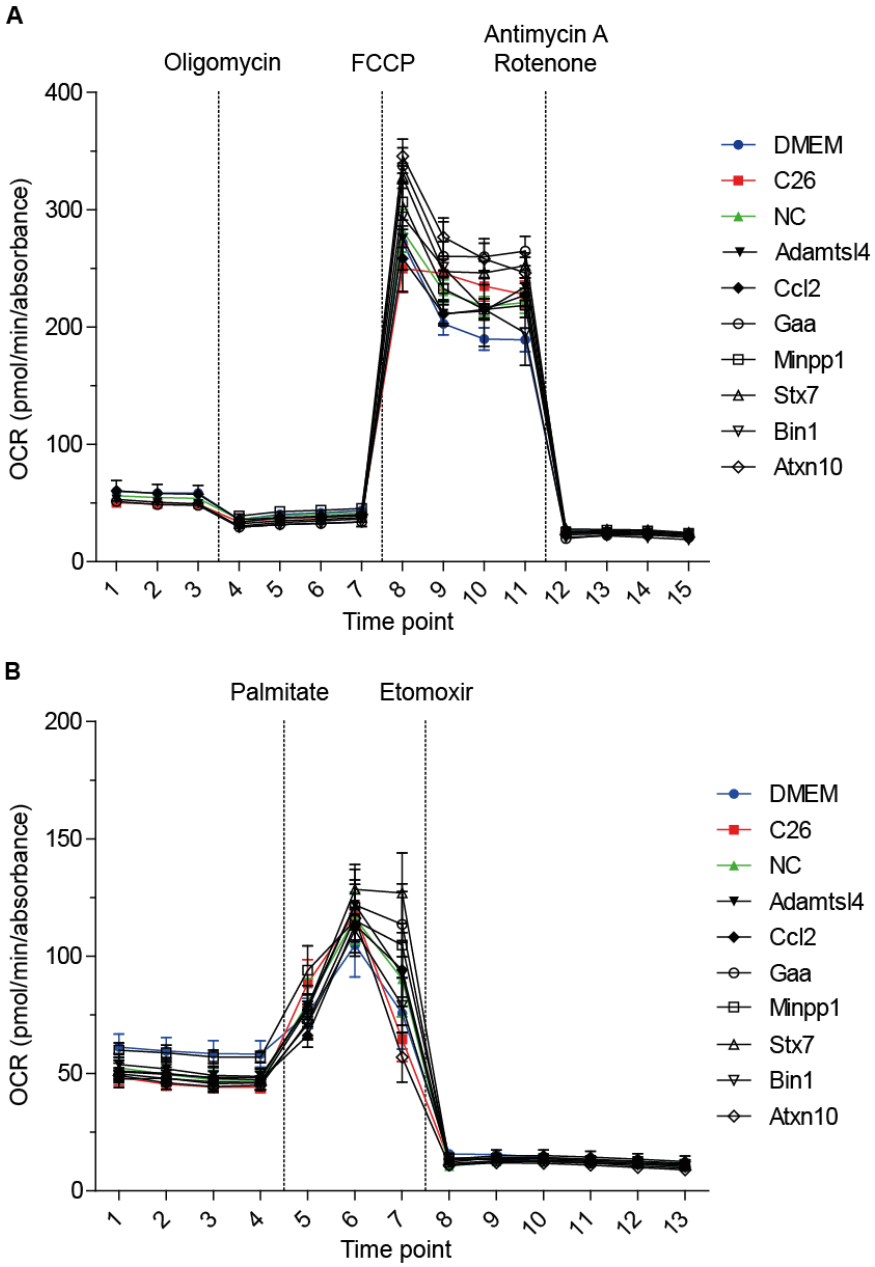

Fig. 42: Overall mitochondrial function and palmitate-driven FA oxidation did not improve through siRNA mediated knockdown of one out of 7 potential "cachexokines" in C26 cells. *Primary neonatal rat cardiomyocytes were exposed to normal culture medium (DMEM), conditioned medium from untreated C26 cells (C26) or C26 cells that were treated with either AllStars Negative Control (NC) siRNA or a siRNA directed against one of the last 7 candidates (Adamts like 4 (Adamtsl4), Chemokine ligand 2 (Ccl2), Glucosidase alpha acid (Gaa), Multiple inositol-polyphosphate phosphatase 1 (Minpp1), Syntaxin 7 (Stx7), Bridging integrator 1 (Bin1) and Ataxin10 (Atxn10)) 24 h before the two different Seahorse assays were performed. Mitochondrial function was expressed by the oxygen consumption rate (OCR). Data were normalized to cell density (absorbance).* ***A)*** *Assessment of the overall mitochondrial function: 2 µM oligomycin, 0.3 µM FCCP and 1 µM rotenone together with 1 µM antimycin A were added at the indicated time points.* ***B)*** *Analysis of the palmitate-driven FA oxidation capacity: 1 mM BSA-conjugated palmitate and 1 mM etomoxir were added at the indicated time points. n ≥ 5, mean ± SEM.*

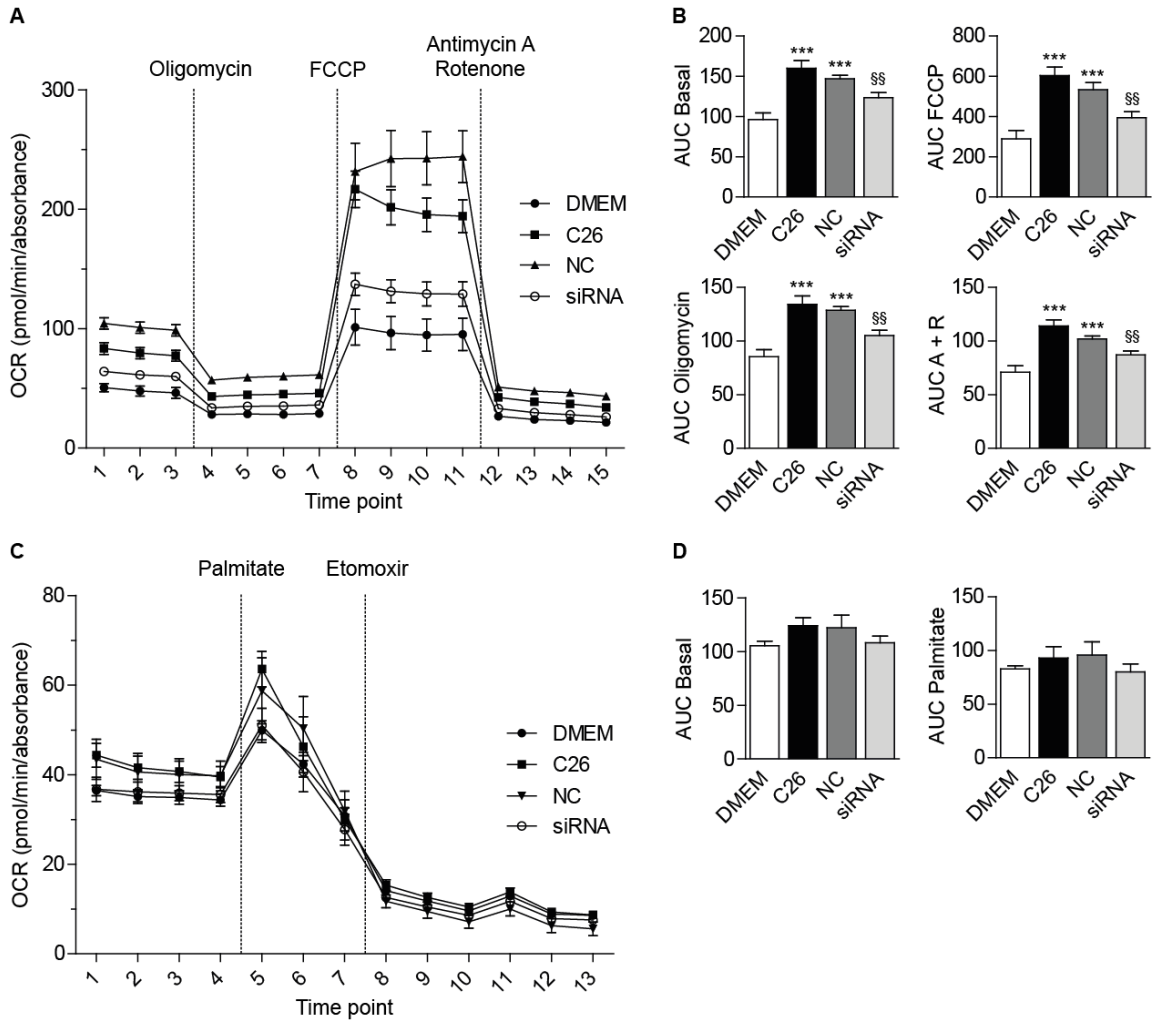

Fig. 43: Overall mitochondrial function and palmitate-driven FA oxidation are improved after siRNA mediated knockdown of all 7 potential "cachexokines" in C26 cells. *Primary neonatal rat cardiomyocytes were exposed to normal culture medium (DMEM), conditioned medium from untreated C26 cells or C26 cells that were treated with either AllStars Negative Control (NC) siRNA or siRNAs directed against all 7 remaining candidates (siRNA) 24 h before the two different Seahorse assays were performed. Mitochondrial function was expressed by the oxygen consumption rate (OCR). Data were normalized to cell density (absorbance).* ***A)*** *Assessment of the overall mitochondrial function: 2 µM oligomycin, 0.3 µM FCCP and 1 µM rotenone together with 1 µM antimycin A (R + A) were added at the indicated time points.* ***B)*** *Area under the curve (AUC) for the overall mitochondrial function was calculated for all four conditions.* ***C)*** *Analysis of the palmitate-driven FA oxidation capacity: 1 mM BSA-conjugated palmitate and 1 mM etomoxir were added at the indicated time points.* ***D)*** *Area under the curve (AUC) for the palmitate-driven FA oxidation assay was calculated for the basal and the palmitate condition. n ≥ 7, mean ± SEM.* ***B)*** **indicates significance by comparison to DMEM using 1-way ANOVA, Bonferroni post-test, *** $p < 0.001$. $^{\$}$indicates significance by comparison to C26 using 1-way ANOVA, Bonferroni post-test, $^{\$\$}$ $p < 0.01$.*

2.5.6 Ataxin10 represents a novel diagnostic marker for colon cancer-induced cachexia

Next, we aimed at transforming non-cachexia-inducing cell lines as the MC38 cells into a cachexia-inducing cell line by overexpressing one of the highly potential “cachexokines”. To filter out the final candidate, Enzyme-linked immunosorbent assays (ELISA) were performed for the 3 factors that induced the strongest phenotypes, namely Ccl2, Gaa and Atxn10. The concentrations of these factors were determined in conditioned medium from C26 and MC38 cells as well as serum and tumor tissue lysates from C26 and MC38 mice, respectively.
Surprisingly, Ccl2 levels were increased in conditioned medium of MC38 cells and in lysates from MC38 tumors as compared to C26 samples (Fig. 44 A + B). On the contrary, increased concentrations of Ccl2 were detected in serum from C26 mice compared to control littermates and even to MC38 mice (Fig. 44 C + D). Gaa levels were the same in conditioned medium from C26 and MC38 cells (Fig. 44 E). In tumor tissue lysates and serum from C26 mice levels of Gaa were elevated compared to control littermates and to samples from MC38 mice (Fig. 44 F - H). Levels of Atxn10 were strongly increased in conditioned medium from C26 cells and in C26 tumor lysates compared to MC38 samples (Fig. 44 I + J). Also in serum from C26 mice concentrations of Atxn10 were increased compared to control mice (Fig. 44 K) which was exactly the other way around for the MC38 mice (Fig. 44 L). The observation that only Atxn10 concentrations were elevated in all tested C26 samples and in serum from APC delta 580 mice (Fig. 49), while they were decreased in all measured MC38 samples indicate that this protein could serve as a diagnostic maker for at least colorectal cancer-induced cachexia.

Altogether, the results presented in this chapter clearly demonstrated the presence of circulating pro-cachectic mediators that acted independently from secondary host responses. The data also showed that more than one factor is required for the full induction of the observed cardiac phenotype.

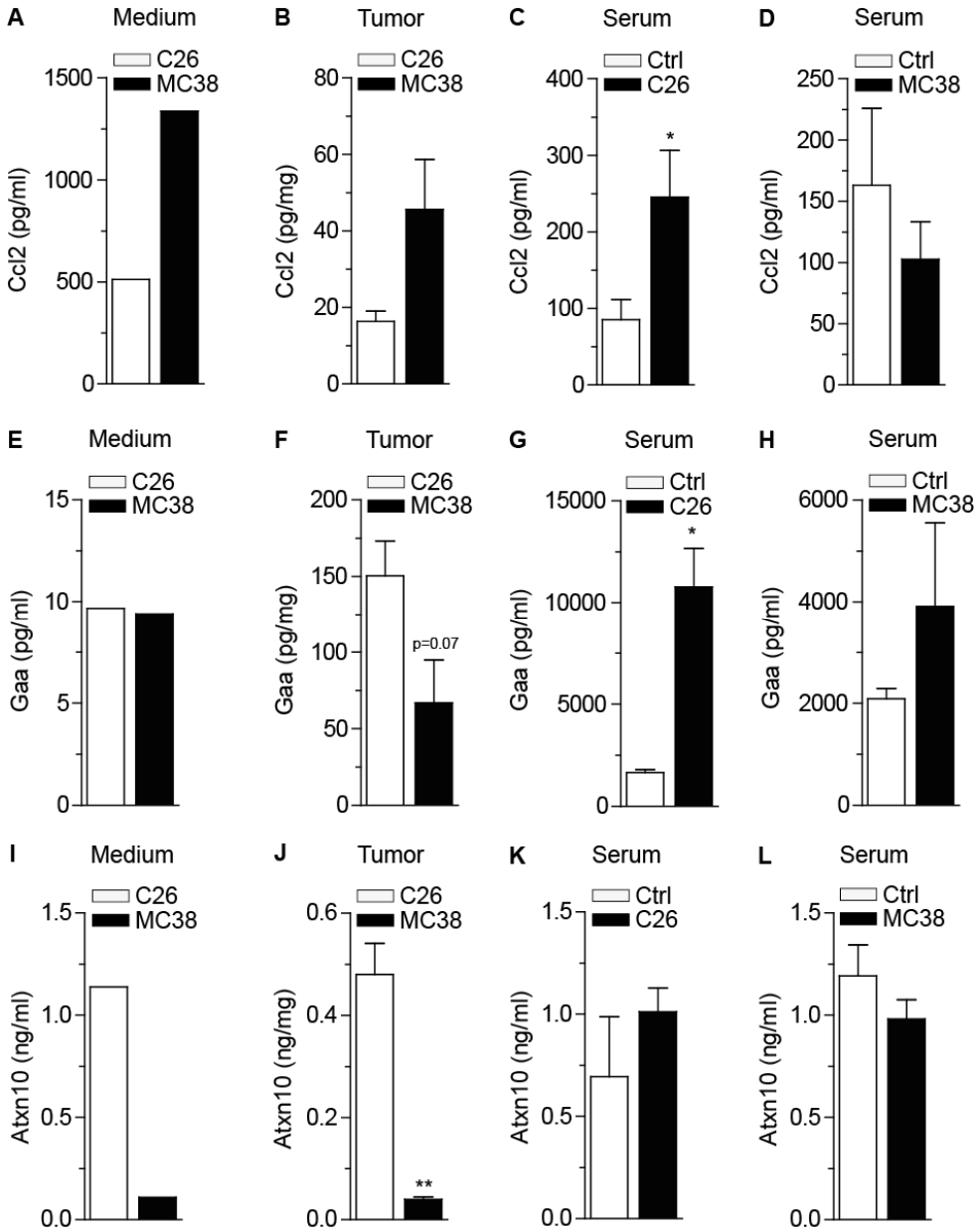

Fig. 44: Protein levels of Ccl2, Gaa and Atxn10 in different C26 and MC38 samples. *Levels of the Chemokine ligand 2 (Ccl2), Glucosidase alpha acid (Gaa) and Ataxin10 (Atxn10) were determined in* ***A), E) + I)*** *conditioned medium from C26 and MC38 cells as well as* ***B), F) + J)*** *tumor lysates and* ***C), D), G), H), K) + L)*** *sera of C26 and MC38 mice using murine-specific ELISA.* ***A), E) + I)*** *n ≤ 2, mean.* ***B) - D), F) - H) + J) - L)*** *n ≥ 4, mean ± SEM. *indicates significance using Student's t-test with Welch correction, *p < 0.05, **p < 0.01.*

3 Discussion

3.1 Cardiac dysfunction represents a clinical feature of cancer cachexia

The vast majority of previous studies have focused on skeletal muscle atrophy and adipose tissue loss as therapeutic sites of cancer cachexia; however, recent studies in our lab demonstrated that other peripheral organs (i.e. liver) (Berriel Diaz M., 2008; Jones A., 2013; Jäger J., 2014) could serve as promising target sites for clinical interventions. Studies by Burch and colleagues already suggested that heart function was impaired in cancer cachexia patients (Burch G.E., 1968). Some years later it was reported that cardiovascular insufficiency was the cause of death in 7% and a contributory factor in 3% of cancer patients (Ambrus J.L., 1975). Despite these observations, later studies focused mainly on the cancer cachexia-induced cardiac atrophy, which was also detected in our study. Until our project was initiated, it remained elusive whether cancer cachexia induced clinically relevant alterations in cardiac performance and whether other mechanisms beside the reported proteolysis of contractile proteins were altered in this disease state.

This project clearly demonstrated by using two independent cachexia mouse models and one non-cachexia mouse model for colorectal cancer that cardiac dysfunction represented an understudied clinical feature of cancer cachexia. It is possible that the observed cardiac dysfunction causes or contributes to classical cancer cachectic features such as fatigue, reduced exercise capacity and survival. These are all parameters that are also described for patients suffering from heart failure (Evangelista L.S., 2008). Therefore, it should be considered to add the assessment of cardiac function to the list of diagnostic criteria for cancer cachexia. Our data showed that the reduction in cardiac function occurred stepwise and has already begun in the pre-cachectic state which could be used for the classification of patients.

Due to the fact that more investigators realized that the heart represents an unmet medical need of cancer cachexia, we are not anymore the only laboratory showing that cardiac performance is impaired in cachectic rodent models (Tian M., 2010; Xu H., 2011; Springer J., 2014). Nevertheless, this project is the only study that developed an *in vitro* model that reliably mimics the *in vivo* situation and consequently allows the investigation of cancer cachexia-induced cardiomyocyte-specific molecular alterations.

The impairment of cardiac function could be explained by the reduced expression of the contractile proteins α- and β-MHC which we observed for the C26 *in vivo* and *in vitro* model. Comparable to the heart function, the expression declined over time. In the APC model α-MHC was also downregulated, but β-MHC was unchanged. The study from Cosper and Leinwand showed that levels of contractile proteins were decreased in atrophic hearts of C26-bearing mice but they did not observe any changes in fractional shortening and ejection fraction. They assumed that the hearts were able to adapt functionally to protein degradation up to a certain point (Cosper P.F., Leinwand L., 2011). The different findings for heart function could be explained by different stages of cachexia, different C26 cell clones, different mouse strains and/or different housing conditions. Further reasons could be that they anesthetized the animals to perform the echocardiography and that their echocardiogram was not sensitive enough. However, Springer and colleagues confirmed the downregulation of both MHCs which was associated with impaired heart function in their cachectic rat model

(Springer J., 2014). Thus, it is not completely clear whether the changes in both MHCs contribute to the impaired heart function.
In contrast to what was described for heart failure (Lompre A.M., 1984), the β-MHC expression was decreased in our C26 *in vivo* and *in vitro* models. This suggests that this change is induced by tumor-secreted factors and is not an adaptive process. However, other recent studies focusing on cancer cachexia-induced heart atrophy (Cosper P.F., Leinwand L., 2011; Tian M., 2011) reported an increase in β-MHC transcription level. Reasons that possibly account for this difference to our study are the same as already mentioned for the heart function.

Impaired heart function is often associated with fibrosis which results in stiffness (Conrad C.H., 1995). In our study, depending on the mouse model, there was no induction of fibrosis or even a decrease in appropriate markers. Additionally, trichrome stainings did not reveal an increase in collagen deposition in both animal models. However, we observed a change in the type of collagens. The expression of collagen III was downregulated and the expression of collagen I was enhanced. The ratio of the two collagen types is of significance because they have different mechanical properties. Tissues with an increase of the proportion of collagen I were characterized by reduced function due to stiffness (Lapiere C.M., 1977). Potentially, the imbalance of the two collagen types promoted the observed cardiac dysfunction. Nevertheless, the other studies reported an increase in cardiac fibrosis (Tian M., 2010; Cosper P.F., Leinwand L., 2011; Spinger J., 2014). Reasons for this difference could be the same as mentioned above.

The main proteolytic pathway involved in cancer cachexia-induced skeletal muscle atrophy is the ubiquitin-proteasome pathway which was shown to be upregulated by different pro-cachectic factors (see chapter 1.1.4.1). An upregulation of the two E3 ubiquitin ligases in the skeletal muscle was confirmed in our two mouse models. The *in vivo* and *in vitro* data of our project and also the study from Cosper and Leinwand did not observe an increase in the expression of the two E3 ubiquitin ligases Atrogin-1 and MuRF1 or in the ubiquitination of proteins. The basal activity of the UPS in the heart is significantly greater than in the skeletal muscle (Liu Z., 2000), due to the higher metabolic rate of the heart (Earl C.A., 1978). Taking this in account, Cosper and Leinwand suggested that the heart may not further upregulate the UPS (Cosper P.F., Leinwand L., 2011). This is questionable, because other recent studies dealing with this topic showed that there was an increase in expression of Atrogin-1 or both E3 ubiquitin ligases accompanied by elevated levels in total ubiquitination of proteins (Tian M., 2011; Xu H. 2011; Springer J., 2014). Additionally, the blockage of the ActRIIB pathway abolished the activation of the ubiquitin-proteasome system not only in the skeletal muscles but also in the heart (Zhou X., 2010).
A further explanation for the difference between the skeletal muscle and our observed cardiac muscle phenotype could be that the pro-cachectic factors that induce the skeletal muscle phenotype cannot bind to the heart lacking appropriate receptors or that these mediators act in a different way by regulating other pathways.
However, our project revealed that autophagy was induced. This was also shown by the other studies. Under normal conditions autophagy occurs at a low state in the heart. It is not only involved in the removal of long-lived proteins, protein aggregates and excess or damaged organelles. It is also activated by environmental changes including an increase in ROS or starvation when recycling of fatty acids and amino acids from proteins and lipids are required for survival (Gustafsson A.B., Gottlieb R.A., 2009). Until this point we can only hypothesize why autophagy is activated in the

cachectic state but most probably survival is the cause. The survival hypothesis can be supported by the fact that cardiac UCP2 expression was enhanced which is reported to be activated by elevated ROS levels (Lopaschuk G.D., 2010). Additionally, an increase in cardiac FA metabolism was shown by our study. Within this project damage of cardiac mitochondria was not investigated but the C26 mouse study from Tian and colleagues observed disrupted mitochondria in the heart (Tian M., 2010). This could also provoke an increase in autophagy.

Heart failure is normally associated with a switch to the fetal gene program including an increased expression of the natriuretic peptides ANP and BNP (Cameron V.A., Ellmers L.J., 2003). These peptides are described for example to induce lipolysis, lipid oxidation and browning of white adipose tissue and, to decrease ghrelin levels which are all features of cancer cachexia (Costello-Boerrigter L.C., 2012). Taking this in account, it was surprising that the C26 *in vivo* and *in vitro* model showed decreased expression of both natriuretic peptides. However, patient data exist demonstrating that natriuretic peptide levels can be low in patients with end-stage heart failure and poor short-term survival (Sun T.W., Wang X.L., 2007).
Due to the fact that the expression of both natriuretic peptides was reduced in the *in vitro* model, it can be concluded that this effect is induced by tumor-secreted factors and is not an adaptive response to environmental alterations. The decreased expression of the natriuretic peptides would be beneficial for the tumor. It is reported that especially ANP exerts anti-inflammatory capacity. For instance, it directly reduces the production of TNF-α by macrophages, interferes with pro-inflammatory effects of TNF-α and it can block the secretion of a wide range of adipose tissue-secreted cytokines, chemokines, and adipokines (Rubattu S., 2008). Furthermore, the usage of ANP for cancer therapy is proposed because it has significant anti-tumorigenic potential (Vesely D.L., 2013).

The severity of impaired heart function and also the expression of some molecular changes did not completely overlap comparing C26 to APC mice. This could have several reasons. The main difference between the two mouse models is that the C26 cells origin from adenocarcinoma the cancerous stage of colorectal cancer and the APC mice mainly develop adenomas which rarely transit to carcinomas (Taketo M.M., Edelmann W., 2009). Given that, it is surprising that the APC mice developed severe cachexia. Cachexia developed really fast in the C26 mice which resulted in a rapid acute response which might differ from the slowly developing alterations in the APC model. In addition, differences could originate due to the interruption of the cell-stromal connections between the tumor and its primary milieu in the C26 model. Furthermore, the results of the C26 model were more reproducible, as tumor growth and onset of cachexia were nearly synchronized. Therefore a small number of animals was sufficient to generate homogenous and significant results. The APC mice got cachectic at different time points which resulted in high variability. For that reason, the number of used animals was too low. The variability explains why for example impairment in cardiac performance was determined but did not become significant in the APC mice. In contrast to the C26 mice, the APC mice developed anemia which burdens the heart with additional stress because it has to produce more force and the delivery of oxygen is reduced. Possibly, due to the adaptation of the heart to the anemia the impairment of heart function was counteracted. The reduced oxygen delivery could also explain why β-oxidation was reduced in our APC mice.

3.2 Disruption of cardiac mitochondrial function in the cachectic state

To elucidate mechanisms which were altered in the heart by cancer cachexia, gene expression profiling was performed comparing hearts from C26-bearing mice to control littermates. However, the performance of a KEGG pathway analysis was not possible because many genes were altered but not to a significant extend. This was confirmed by performing several immunoblots to identify pathways that might be predominantly regulated. Most of the examined pathways showed minor changes but none of them were significantly regulated (data not shown). Thus, the investigation of specific pathways involved in cancer cachexia-induced cardiac atrophy was not achievable. But maybe the sum of all minor molecular changes resulted in a complex phenotype.

To identify cardiomyocyte-specific changes on molecular level a second gene expression profiling was conducted comparing C26-treated primary adult mouse cardiomyocytes to untreated cardiomyocytes. The first two pathways that appeared to be altered were associated with cardiac dysfunction. This confirmed the *in vivo* data and proved that the developed *in vitro* model resembled the *in vivo* model. The third most regulated pathway was the FA metabolism pathway. A GO-BP instead of a KEGG pathway analysis of the mouse data showed also that biological processes that are involved in FA metabolism, transport and biosynthesis were dysregulated. Further analysis revealed that FA metabolism was increased in both C26 models which was associated with reduced lipid storage, increased uncoupling and presumably futile cycle. Uncoupling and futile cycle are described to reduce cardiac efficiency by wasting ATP for non-contractile purposes which could be a further explanation for the impaired heart function observed in our cachectic mouse models.

The FA-dependent findings were unexpected because it is described that the heart switches from FAs to glucose as fuel during heart failure. Additionally, the study from Tian and colleagues suggested that the capacity of fatty acid β-oxidation is reduced in C26 mice (Tian M., 2011). Our data demonstrated that the expression of the FA metabolism genes and the glucose transporters changed in the course of cachexia. Looking at different stages of cachexia could explain the difference between their study and our study. Addiotional reasons are mentioned in chapter 3.1. Nevertheless, Sjöström and colleagues suggested that the heart is involved as energy draining organ in progressive cancer cachexia (Sjöström S., 1987). This supports our finding that the heart seems to burn FAs more than average. An increased expression of UCP2 and 3 in the skeletal muscle and in the heart of a cachectic mouse model were also shown by Busquets and colleagues. They showed that this effect was not linked to the cachexia-induced increase of FAs in the circulation but that it correlated with ROS levels (Busquet S., 2005). This matches our hypothesis that not the elevated levels of circulating FAs but rather tumor-secreted factors induced the increased FA utilization. This in turn results in enhanced ROS generation. A recent study using functional approaches confirmed uncoupling in skeletal muscles of cancer cachectic mice. The investigators suggested that mitochondria should be considered as therapeutical target for cancer cachexia treatment (Tzika A.A., 2013). Our study supports this recommendation since we also demonstrated that increased mitochondrial uncoupling represents a prominent feature of cancer cachexia that was understudied so far. Furthermore, it will be mandatory to put cancer cachexia-associated alterations in FA oxidation into perspective with additional mechanisms contributing to cardiac dysfunction such as autophagy.

The mechanisms that contributed to the activation of FA metabolic dysfunction remained unclear, but it can be speculated that tumor-secreted factors are likely responsible for the activation of this process.

The expression pattern in FA metabolism genes observed for the C26 *in vivo* and *in vitro* model is similar to what is described for obesity and diabetes, which are characterized by increased circulating FA level. However, the underlying mechanisms by which the cardiac FA metabolism phenotype is induced under diabetic conditions are not well understood. It has to be considered that circulating factors, such as cytokines, as opposed to the elevated FA levels in the bloodstream are the reason behind increased FA utilization in diabetic conditions.

3.3 Secretome analysis provides new therapeutical targets

3.3.1 Secretome profiling as source for the discovery of new biomarkers

This study provided an unbiased and functional screening setup for the discovery of tumor-secreted factors with cachexogenic properties. The established cardiomyocyte phenotyping system can also be utilized as diagnostic tool for patient samples in a high-throughput format.

Although the etiology of cancer cachexia is still unclear, reports on cancer cachexia hypothesized the cachectic phenotype is caused by combinatorial action of both tumor and host-derived mediators. Our results demonstrated that particular tumor-secreted factors were sufficient and necessary to promote the cachectic syndrome, independent from secondary host responses. Considering that the combined but not the single knockdown of the last 7 highly potential “cachexokines” was sufficient to rescue the metabolic phenotype and that the combined knockdown failed to prevent the cardiac atrophy, it can be hypothesized that the cachectic phenotype is induced by combinatorial effects of several tumor-secreted factors. Most clinical interventions focused on the pro-cachectic factors that are described for decades although these factors display weak prognostic and therapeutic potential. Looking at our data and taking in account that the interest for personalized medicine is increasing, it has to be considered that the development of new therapeutic targets has to be based on tumor-specific secretome profiling’s. The benefical outcome and high potential of the combination of secretome analysis or gene expression profiling of tumor cells with high-throughput phenotyping was recently confirmed by two studies (Lokireddy S., 2012; Kir S., 2014). Literature search revealed that secretome analysis of tumor cells as the basis for the identification of new markers is becoming more popular (some examples for colorectal cancer: Imperlini E., 2013; Zeng X., 2013; Shin J., 2014). That this was previously understudied could be explained by the fact that the procedures and machines were to expensive, suitable software and databases were missing, technical equipment for reliable high-throughput screenings were missing and the methods had some disadvantages.
One example of a method to reduce technical limitations is the secretome analysis method utilized in this study which was recently published by Eichelbaum and colleagues (Eichelbaum K., 2012). This secretome approach combines click-chemistry with SILAC which allows the growth of cells in medium supplemented with serum and the enrichment of newly synthesized proteins. Commonly used secretome approaches have the disadvantage that the cells have to be cultured in serum-free medium, because the serum creates a high background whereby proteins with low-abundance cannot be detected. Several studies showed that the behavior of cells changes during serum starvation. This was also confirmed by Eichelbaum and colleagues.
However, the best approach would allow *in vivo* secretome analysis because all secretome approaches are lacking the impact of the microenvironment.

Lokireddy and colleagues also performed a secretome analysis of C26 cells (Lokireddy S., 2012). They showed that myostatin a known pro-cachectic factor is secreted by C26 cells. We did not find this protein in our secretome, but this could be due to differences in growth conditions applied between the two studies. However, we did not confirm the lack of myostatin in the conditioned medium of our C26 cells by performing ELISA or immunoblotting. Considering that our observations for the impact of cancer cachexia on the heart differed from what was published by other investigators, we suspect that the C26 cell line utilized in our lab may be different than the C26 cells used by other labs. It is known that the growth in culture could introduce further mutations changing the behavior of cells.

3.3.2 Ataxin10: a new therapeutical target for cancer cachexia treatment?

Our data indicate that Atxn10 is a potential target for cancer cachexia treatment. Preliminary data from sera of human patients suffering from pancreatic cancer promote the assumption that Atxn10 could serve as diagnostic tool and that it has clinical relevance. However, to date we do not know by which mechanism Atxn10 induced the presented cardiac phenotype. So far, Atxn10 expression is mainly described in the background of neurodegenerative disorders. Also in this context, the function of Atxn10 remains unknown. Additionally, Atxn10 is not postulated to be secreted. Consequently, a receptor for Atxn10 is not described. One report showed that Atxn10 interacted with O-linked β-N-acetylglucosamine transferase which resulted in reduced levels of overall protein glycosylation (März P., 2006). Preliminary data showed reduced protein glycosylation in the C26 mouse model but neither in the *in vitro* model nor in the APC delta 580 mice. The glycosylation phenotype observed for the C26 mouse model overlapped with the finding that the expression of both GLUT1 and GLUT4 were reduced. It could be assumed that the reduced protein glycosylation results from overall reduced levels of intracellular glucose. A further study demonstrated that Atxn10 interacted with G-protein beta2 subunit by activating the Ras-MAP kinase-Elk-1 cascade (Waragai M., 2006). However, preliminary data did not indicate that this mechanism played a role in our context.

3.4 Conclusion and Outlook

Our data clearly demonstrated that cancer cachexia-induced decreased cardiac function which was characterized by atrophy, autophagy and disrupted FA metabolism (Fig. 45). In addition, we could show that the observed effects were mediated by tumor-secreted factors in a cell-autonomous manner. Furthermore, we provided an unbiased and functional screening setup for the discovery of new biomarkers. The most important finding was the evaluation of Atxn10 as a new therapeutical target for cancer cachexia treatment. Based on our data, we recommend assessment of cardiac function be established as routine when diagnosing cancer cachexia in patients. Furthermore, mitochondrial dysfunction has to be taken into account for the treatment of cancer cachexia-induced cardiac dysfunction and atrophy.

To provide proof-of concept and to test for a potential significance of Atxn10 to serve as marker, we are going to generate a stable cell line that overexpresses Atxn10. Therefor we will use non-cachexia-inducing cells. These Atxn10-overexpressing cells will be subcutaneously injected into SCID mice and heart function, morphology and metabolic status will be assessed.
The treatment of engineered heart tissue with conditioned medium from the Atxn10-overexpressing cells should further support the important role of Atxn10 in our settings.

To demonstrate the clinical relevance of Atxn10, expression and function of Atxn10 should be assessed in xenograft cachexia mouse models bearing human cancer cells and in patient samples.

Given that, chronic heart failure can also induce cachexia, it would be interesting to investigate the secretome of the heart as response to the cachexokines. Possibly, the heart plays a much greater role in the development of cancer cachexia as it was assumed so far.

As already mentioned, the observed FA metabolism phenotype is similar to what is described for diabetes and obesity. For that reason, it would be of interest to assess the serum levels of Atxn10 in diabetic/overweight mice and patients.

It would be also interesting to investigate the impact of the identified tumor-secreted factors on other tissue compartments. It should be taken in account that factors with pro-cachectic features can be used for the treatment of other diseases. For example, a cachexokine that induces adipose tissue atrophy can serve as promising therapeutic agent for the treatment of obesity.

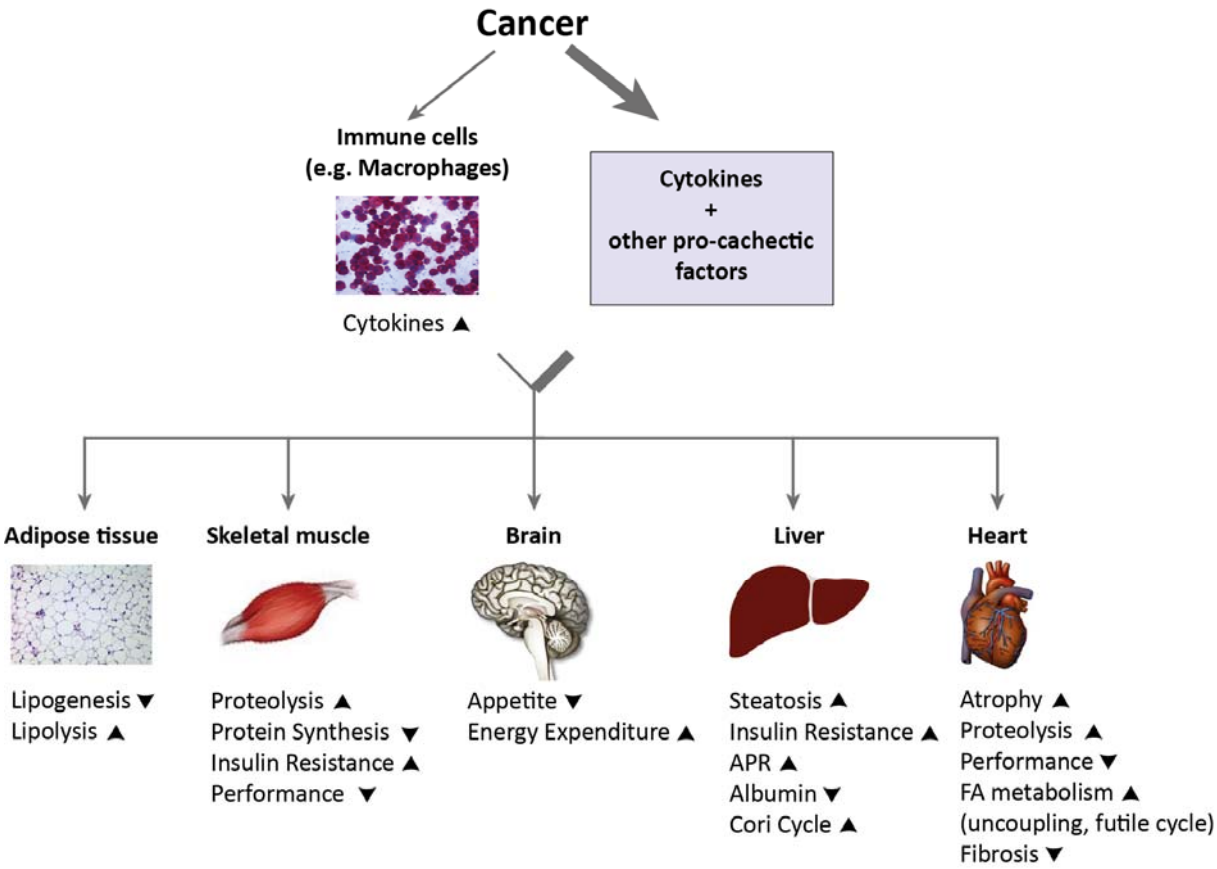

Fig. 45: Adapted overview of the main effects of cancer cachexia on different organs. *The effects of cancer cachexia on the heart that were demonstrated by our project were added to this diagram. Upward arrows indicate that these pathways are enhanced and downward arrows that they are blocked.*

4 Methods

4.1 Animal experiments

4.1.1 General procedures

4.1.1.1 Housing of experimental animals

The animals were housed according to international standard conditions with a 12 h dark and 12 h light cycle. Animal handling and experimentation was performed in accordance with National Institutes of Health (NIH) guidelines and approved by local authorities (Regierungspräsidium Karlsruhe). Mice were housed in H-TEMP™ cages from Tecniplast in a ventilated mouse housing cabinet with *ad libitum* access to regular unrestricted diet and water.

4.1.1.2 Sample collection

Blood was taken after cervical dislocation from the vena cava. Organs including liver, adipose tissues (abdominal white fat, inguinal white fat and scapular brown fat), gastrocnemius muscles and heart as well as the tumor were collected, weighed, snap-frozen in liquid nitrogen and used for further analysis.
The heart was cut into three cross sectional slices. The middle piece was taken for paraffin embedding, the upper part without the atria for protein isolation and the apex for RNA isolation. Furthermore, the left hind leg was removed and placed into hydrogen peroxide (H_2O_2) to isolate the tibia.

4.1.1.3 Sample preparation for paraffin embedding

Small tissue slices were put into 5 ml reaction tubes that were filled with freshly prepared 4% paraformaldehyde. After ~18 h tissue slides were transferred to Tissue-Tek® Mega-Cassettes® and washed under running tap water for 2 h. Afterwards, tissue cassettes were stored in 70% ethanol at 4°C for up to 6 weeks. Within this period the samples were paraffin embedded.

4.1.1.4 Preparation of tissue homogenates

Tumor pieces were weighed, transferred to dounce homogenizers containing 2 ml Dulbecco's Phosphate-Buffered Saline (DPBS, 1x) and put on ice during homogenization. Subsequently, tissue lysates were sonicated using the BioRuptor® (one cycle: 30 sec on and 30 sec off) and centrifuged for 10 min at 13,000 rpm and 4°C. Finally, supernatants were transferred to fresh 1.5 ml safe-lock tubes and stored at -80°C.

4.1.2 Mouse model

4.1.2.1 C26 murine cancer cachexia model

For tumor induction 1.5 x 10^6 C26 cells in 100 µl DPBS (1x) were injected subcutaneously into 9 - 10 week old male Balb/c mice using a 1 ml syringe with a 27G needle. Age-matched littermates were injected with 100 µl DPBS (1x). The experiment was performed over a period of 3 weeks and a cohort of mice (6 control and 10 tumor bearing mice) was sacrificed every week. In the meantime echocardiography and Pressure-Volume loop (PV loop) measurement were performed weekly to assess the cardiac function. Furthermore, body composition was determined by Echo Magnetic

Resonance Imaging (EchoMRI) analysis once a week. Body weight was determined in regular intervals.

4.1.2.2 MC38 murine cancer model

9 - 10 week old male C57BL6/J mice were injected subcutaneously with 5 x 10^5 MC38 cells in 100 µl DPBS (1x) using a 1 ml syringe with a 27G needle. Age-matched littermates were injected with 100 µl DPBS (1x). Mice were sacrificed 30 days post injection. Cardiac function was determined by weekly echocardiography. Body composition and body weight were assessed as described in capter 4.1.2.1.

4.1.2.3 Adenomatous polyposis coli (APC) delta 580 mice

Strain description

This mouse strain carries a germ-line targeted mutated allele of *Apc* in which exon 14 has been removed by cre-mediated recombination, leading to an expression of a truncated Apc protein of 605 amino acid residues, of which the first 580 amino acids correspond to the normal protein. Heterozygous mice develop multiple intestinal neoplasia in the colon and die within five month of age. Homozygous mice are embryonic lethal. Heterozygous females show nursing deficiency. Heterozygous males and wild-type C57Bl6/N Cr females were used as breeder pairs (Kuraguchi M., 2006).

Genotyping

DNA isolation

Tail biopsies were taken by the animal care takers and were stored in 1.5 ml safe-lock tubes at -20°C. Tails were thawed, 750 µl of proteinase K buffer were added to every tail along with 17.5 µl proteinase K. For digestion the tails were placed into a Thermomixer at 56°C overnight while shaking at 800 rpm. Then 300 µl of 5 M NaCl were applied to every reaction, the mixtures were shaken for 5 min and centrifuged at 13,000 rpm and 4°C for 30 min. Afterwards, 750 µl of the clear supernatants were transferred to fresh 1.5 ml safe-lock tubes. To precipitate the DNA 500 µl pre-cooled isopropanol was added to every tube. Then they were shaken for 5 min and centrifuged at 13,000 rpm and 4°C for 10 min. DNA pellets were washed with 500 µl pre-cooled ethanol and were centrifuged as before. The washing and centrifugation step was repeated once. The supernatants were discarded. DNA pellets were air-dried for 10 min at room temperature and solubilized in 50 µl of 10 mM Tris/HCl (pH 8.0). Finally, DNA was dissolved at 65°C for 10 min and stored at -20°C.

Determination of DNA concentration

DNA concentration and the degree of contamination were determined by using the NanoDrop ND-1000 spectrophotometer. Concentration was determined by measuring the absorption at 260 nm, contamination with proteins at 280 nm and with salts at 230 nm. For each measurement 2 µl DNA sample were used.

Polymerase Chain Reaction (PCR)

PCR was performed to detect the deleted region of exon 14 in the Apc gene using the primer pair A011 and A012 (see chapter 5.10). Per reaction 100 ng DNA were used. The corresponding PCR reaction mix and PCR cycling conditions are shown in Table 3 and 4.

DNA agarose gel electrophoresis

To determine the genotype of the individual mouse, the PCR products were separated by agarose gel electrophoresis using 1% agarose (DNase free) and 1 µg/ml ethidium bromide in TBE buffer (1x). 20 µl DNA sample were mixed with 4 µl of 6x Orange G loading dye and separated at 90 V for 45 min. Gel pictures were taken under UV light (254 nm) with a Gel Imager. The PCR product of the wild-type allele exhibited a size of 1.1 kb and the deleted allele of 470 bp.

Reagent	Volume	Final Conc.
PCR Master Mix (2x):	12.5 µl	
Reaction buffer (2x)		1x
$MgCl_2$ (4mM)		2 mM
dNTP-Mix (0.4 mM)		0.2 mM
Taq DNA Polymerase (0.05 U/µl)		0.025 U/µl
Forward primer A011 (12.5 µM)	1.0 µl	0.5 µM
Reverse primer A012 (12.5 µM)	1.0 µl	0.5 µM
$MgCl_2$ (25 mM)	1.0 µl	1 mM
dH_2O	add 25 µl	

***Tab. 3**: PCR reaction mix used for the genotyping of APC delta 580 mice.*

Temperature	Time	Cycle
94°C	3 min	
94°C	1 min	
55°C	2 min	35
72°C	1 min	
72°C	3 min	
4°C	Hold	

Tab. 4: PCR cycling conditions used for the genotyping of APC delta 580 mice.

Experimental set-up

Heterozygous and wild-type male mice with an age of 14 - 16 weeks were taken for an experiment. Mice were monitored until the onset of cachexia (average of age: 21 weeks). In the meantime echocardiography was performed every 2 - 3 weeks. Body weight was also determined at regular intervals. During sample collection blood was not only taken for serum preparation but also to perform blood counts.

4.1.3 Treatments

4.1.3.1 Echocardiography

A non-invasive two-dimensional transthoracic echocardiogram (2D-Echo), which is capable of imaging a cross sectional slice of the beating heart was used for all experiments.

To perform the measurement mice were depilated in the thoracic region by using hair removing cream one day beforehand. A two-dimensional parasternal short axis view and M-Mode tracings of the left ventricle of conscious mice were obtained using a Sonos 5500 echocardiogram with a linear S 15 transducer (15 Hz). M-Mode tracings were used to determine left ventricular internal diameter as the largest anteroposterior diameter in either diastole (left ventricular end diastolic diameter (LVEDD)) or systole (left ventricular end systolic diameter (LVESD)). Diameters were averaged from at least three consecutive cardiac cycles. Left ventricular fractional shortening (FS) was calculated as (LVEDD-LVESD)/LVEDD and expressed as a percentage.

4.1.3.2 Pressure-Volume loop measurement

To perform the PV loop analysis mice were anesthetized by intraperitoneal injection of a mixture of medetomidin (0.5 µg/g body weight), fentanyl (0.5 µg/g body weight) and midazolam (5 µg/g body weight). Body temperature was maintained at 37°C using a homoeothermic blanket. Measurements were performed in closed-chest. To measure the pressures and volumes, a 1.2 FR catheter was placed into the left ventricle through the carotid artery of the spontaneously breathing mice. Left ventricular volumes were extrapolated from admittance magnitude and admittance phase in real time using the ADVantage PV System. Pressure and volume data were recorded using a Scisense 404 - 16 Bit Four Channel Recorder with LabScribe2 Software.

4.1.3.3 EchoMRI measurement

EchoMRI analysis allows the determination of whole body fat mass, lean mass and free water in mice. Before the measurement body weight of the mice was assessed because this is needed for the analysis. Measurement was performed following manufacturer's instructions.

4.1.3.4 Blood serum preparation

Blood serum was obtained by incubation of blood samples at room temperature for 30 min and subsequent centrifugation for 30 min at 5,000 rpm and 4°C. The serum (upper phase) was transferred to a fresh 1.5 ml safe-lock tube and stored at -80°C.

4.1.3.5 Blood count

80 µl blood were directly transferred to MiniCollect® EDTA tubes and stored at 4°C. Blood samples were analyzed by the department of Clinical Chemistry at the University Hospital Heidelberg.

4.1.3.6 Determination of tibia length

Tibia length was assessed using a digital caliper. Each tibia was measured three times and the averaged values were taken for normalization purposes because the tibia length represents a constant parameter compared to the body weight.

4.2 Cell Biology

4.2.1 Cell culture conditions

All experiments with eukaryotic cells were performed under sterile conditions. Cells were cultivated at 37°C, 5% CO_2 and 95% humidity. All media and additives were warmed to 37°C prior to use.

4.2.2 Thawing of cells

Eukaryotic cells were stored in a liquid nitrogen tank in 1 ml aliquots. The freeze medium and the frozen cell number were different for each cell line (Tab. 5). Following thawing at 37°C cells were washed two times with culture medium. Afterwards, they were distributed equally to one or two 15 cm cell culture plates (Tab. 5) containing 20 ml culture medium.

Cell line	Freeze Medium	Cell number	Tissue culture plates
C26	Culture medium + 10% DMSO	2 x 10^6 cells/ml	2
HEK293A	DMEM + 20% FBS + 10% DMSO	2 x 10^6 cells/ml	2
MC38	93% FBS + 7% DMSO	1 x 10^6 cells/ml	1

Tab. 5: Freezing and thawing conditions of used cell lines.

4.2.3 Cultivation of C26 mouse adenocarcinoma cells and MC38 mouse colorectal carcinoma cells

Cells were cultivated on 15 cm cell culture plates in 20 ml culture medium. Cells never exceeded a confluency of 80 - 90%. They were passaged every 3 - 4 days with a split factor of 1:16 - 1:20.
For passaging, the cells were first washed with 10 ml DPBS (1x) and trypsinized. Detached cells were resuspended in 10 ml of fresh culture medium and pelleted by centrifugation at 2,000 rpm for 3 min. Finally, pellets were resuspended in fresh culture medium and splitted on new 15 cm cell culture plates.

4.2.4 Cultivation of human embryonic kidney 293 A (HEK293 A) cells

Cells were cultivated on 15 cm cell culture plates in 20 ml culture medium. Cells never exceeded a confluency of 80 - 90%. They were passaged every 3 - 4 days with a split factor of 1:20.
For passaging, the cells were washed from the cell culture plate using 10 ml fresh culture medium and were pelleted by centrifugation at 2,000 rpm for 3 min. Subsequently, the pellet was resuspended in 10 ml fresh culture medium and 500 µl of the cell suspension was plated onto a 15 cm cell culture plate containing 20 ml culture medium.

4.2.5 Preparation of conditioned medium

After reaching a confluency of ~50% the culture medium was changed. Cells were kept in this culture medium for 48 h. Then the medium was taken from the cells and the remaining cells were pelleted by centrifugation at 2,000 rpm for 3 min. Medium was aliquoted and stored at -20°C (short term) or at -80°C (long term).

4.2.6 Determination of cell number

To determine the cell count and viability for subsequent seeding of cells the Countess® Automated Cell Counter was used. According to the manufacturer's protocol, 10 µl of sample was mixed with 10 µl of Trypan Blue Staining (0.4%), pipetted into Countess® Cell Counting Chamber Slide and inserted into the machine for automated counting.

4.2.7 Detection of cell culture contamination

1 x 10^6 to 1 x 10^7 cells were harvested, transferred to a 1.5 ml safe-lock tube and pelleted by centrifugation at 2,500 rpm for 5 min. Pellet was resuspended into 100 µl DPBS (1x) and placed at

95°C for 15 min. To pellet the cellular debris the lysate was centrifuged at 10,000 rpm for 10 min. The supernatant was transferred to a new 1.5 ml safe-lock tube and stored at -20°C before submission to the company Multiplexion. Multiplexion validated the purity of the cell lines using Multiplex Cell Contamination Test (McCT) (Schmitt M., Pawlita M., 2009). Only non-contaminated cells were used for this work.

4.2.8 Transient transfection

4.2.8.1 Transfection of HEK293 A cells with cDNA expression plasmids

1 x 10^5 HEK293 A cells per well were seeded on 6-well plates 24 h prior to transfection and were transfected at 60% confluency. Cells were transfected either with ready-to-use cDNA expression plasmids (see chapter 5.11) obtained from Source BioScience or with pDest-eGFP-N1 plasmid (Addgene, Cambridge (MA, USA)) which served as transfection efficiency control. 2 µg of plasmid DNA were mixed with 80 µl of 0.25 M $CaCl_2$ and the same volume of 2x Borate Buffered Saline (BBS). The mixture was incubated for 15 - 20 min at room temperature and subsequently added to the cells dropwise. Medium was changed 24 h after transfection and conditioned medium was produced as described in chapter 4.2.5.

4.2.8.2 Transfection of C26 cells with small interfering RNA (siRNA)

C26 cells were seeded at 1 x 10^5 cells/well on 6-well plates 24 h prior to transfection and were transfected at 60% confluency. Cells were either transfected with a single siRNA or with seven siRNAs at once; used siRNAs are listed in chapter 5.12. An Alexa488 labelled siRNA from Qiagen served as control for the transfection efficiency. The siRNA was pipetted into Dulbecco's Modified Eagle's Medium (DMEM) without additives and subsequently HiPerFect Transfection Reagent was also added; the used amounts are listed in Table 6. The mixture was vortexed, incubated for 10 min at room temperature and added to the cells dropwise. Medium was changed 24 h after transfection and conditioned medium was produced as described in chapter 4.2.5.

Transfected siRNA	Final conc. of siRNA	DMEM Vol.	HiPerFect Vol.
Single	5 nM	100 µl	12 µl
Seven	5 nM (each) 35 nM (total)	100 µl	42 µl

Tab. 6: Volumes and concentrations used for the transfection of C26 cells with siRNA.

4.2.9 Primary cells

4.2.9.1 Isolation and preparation of primary neonatal rat cardiomyocytes

Hearts for cardiomyocytes isolation were taken from male and female Wistar rats at the age of 1 to 2 days. The rats were decapitated and hearts were removed by thoracotomy. First, hearts were shortly rinsed in 70% ethanol and transferred to a tube containing 50 ml DMEM. Then they were washed five times with DMEM and two times with DPBS (1x). Afterwards, hearts were cut in the tube with a sterile scissor and stored on ice. Subsequent work was done under sterile conditions. To the heart slices 25 ml 0.1% pancreatin was given. The mixture was pipetted up and down. Additional 20 ml 0.1% pancreatin were added to the hearts. The pancreatin-heart mixture was transferred to a 250 ml Erlenmeyer flask and incubated for 18 min at 37°C slowly stirring. The first supernatant was

discarded and 45 ml 0.1% pancreatin were pipetted to the hearts again. The incubation was performed as described before. In the meantime seven 50 ml centrifuge tubes containing 5 ml culture medium were prepared. The second supernatant was splitted in equal parts to the seven centrifuge tubes which then were centrifuged for 5 min at 1,000 rpm and room temperature. Supernatants were discarded and the pellets were dissolved in 2 to 4 ml culture medium. The tubes were pooled and the volume was filled up to 30 ml.
To reduce the amount of non-cardiomyocyte like epithelial cells and fibroblasts cells were pre-plated on 15 cm cell culture plates and incubated for 1 h (37°C, 5% CO_2). Afterwards, cell suspension was plated and incubated for 1 h again. Then cells were harvested, counted and finally plated on cell culture plates that were coated with 0.1% gelatin for minimum 1 h. The cardiomyocytes need two days to fully attach to the plates. In this time culture medium was exchanged once (~24 h after seeding) and no assay was started.

Plate format	Cell number	Application
6-Well	1.0 x 10^6 cells/well	RNA-/Protein isolation
12-Well	0.5 x 10^6 cells/well	RNA-/Protein isolation
24-Well	1.0 x 10^5 - 1.5 x 10^5 cells/well	α-actinin immunostaining
96-Well (Seahorse)	5.0 x 10^4 cells/well	Seahorse assays
384-Well	6.0 x 10^3 cells/well	High-throughput analysis

Tab. 7: Seeded cell numbers of primary neonatal rat cardiomyocytes on different cell culture plate formats.

4.2.9.2 Isolation and preparation of primary adult mouse cardiomyocytes

For the isolation of primary adult mouse cardiomyocytes 9 - 10 week old male Balb/c mice were anesthetized using isoflurane and hearts were excised by cutting the transverse aorta between the carotid arteries and other vessels. Hearts were mounted on a Langendorff perfusion apparatus and were retrogradly perfused with nominally Ca^{2+}-free Tyrode's solution (pH 7.42) containing 115 mM NaCl, 4.7 mM KCl, 0.6 mM KH_2PO_4, 0.6 mM Na_2HPO_4, 1.2 mM $MgSO_4$, 12 mM $NaHCO_3$, 10 mM $KHCO_3$, 10 mM HEPES, 30 mM taurine, 10 mM 2,3-butanedionemonoxime (BDM) and 5.5 mM glucose for 4 min at 37°C. Perfusion was then switched to digestion buffer I for another 3 min. A successful digestion is indicated by a swollen, slight pale and flaccid appearance of the heart. After digestion the atria were removed and discarded. Ventricles of one heart were placed into 2.5 ml digestion buffer I and cut into small pieces with preparatory scissors. Digestion was terminated by adding 2.5 ml stopping buffer I. Mixture was pipetted up and down several times with a sterile 1000 µl pipette tip (~3 min). Suspension was filtered through a 100 µm cell strainer into a 50 ml centrifuge tube and transferred to a 15 ml centrifuge tube. Cells were pelleted at 300 rpm for 2 min. All following steps were performed under sterile conditions. Subsequently, cell pellet which contains the cardiomyocytes underwent a Ca^{2+} reintroduction. Therefore, pellet was resuspended in 0.1 mM $CaCl_2$ in stopping buffer II. Cells were sedimented for 7 - 10 min until cell pellet formed. Supernatant was removed and this step was repeated with increasing concentrations of $CaCl_2$ (0.2, 0.4 and 0.8 mM). Afterwards, cell pellet was resolved in plating medium, total number of rod-shaped myocytes was calculated and cell number was adjusted to 25,000 rod-shaped myocytes/ml. Cardiomyocytes were plated at 50,000 rod-shaped myocytes/well on laminin-coated 6-well plates. After 1 h plating medium was removed and cardiomyocytes were treated with conditioned medium from C26 cells or normal cardiomyocyte culture medium for 48 h (further details see chapter 4.2.9.3).

4.2.9.3 Treatment of primary cardiomyocytes with conditioned medium

After thawing in the water bath at 37°C conditioned medium was diluted 3:1 with fresh culture medium or cardiomyocyte culture medium. Primary neonatal rat cardiomyocytes were cultured in conditioned medium that was diluted with culture medium for 24 h. Adult mouse cardiomyocytes were treated with conditioned medium that was diluted with cardiomyocytes culture medium by adjusting the concentration of BDM (10 mM) and ITS (1x) for 48 h.

4.2.9.4 Treatment of primary neonatal rat cardiomyocytes with mouse serum

Mouse serum was thawed on ice and was added in a concentration of 2% to DMEM containing 1% Penicillin-Streptomycin (Penstrep) and 8% Fetal bovine serum (FBS). Primary neonatal rat cardiomyocytes were cultured in this medium for 24 h.

4.3 Cell-based assays

4.3.1 High-throughput analysis of cardiomyocyte size

4.3.1.1 Processing of the cells

Primary neonatal rat cardiomyocytes were plated onto gelatin (0.1%) coated 384-well plates at 6 x 10^3 cells/well. Culture medium was changed after 24 - 36 h. Three days after seeding cells were treated with conditioned medium from HEK293 A cells that were transfected with the cDNA clones (see X), untreated HEK293 A cells and C26 cells for 24 h. Subsequently, cells were washed three times with DPBS (1x) and were fixated with 4% formaldehyde solution (methanol-free) for 10 min. After washing the cells again three times with DPBS (1x) they were permeabilized using 0.1% Triton solution and blocked with 5% goat serum for 30 min at room temperature. Then cells were incubated with primary antibody (anti-sarcomeric α-actinin) at 4°C overnight. The primary antibody was diluted 1:500 in 5% goat serum. Next day, cells were washed two times with DPBS (1x) and subsequently incubated with secondary antibody (Alexa Fluor® 488 anti-mouse) and in parallel with phalloidin-tetramethylrhodamine B isothiocyanate (TRITC) for 1 h in the dark. The secondary antibody was diluted 1:400 and phalloidin-TRITC 1:1000 in 5% goat serum. After three washes with DPBS (1x) cells were additionally stained with Hoechst (1:10,000) for 10 min. Finally, cells were washed two times with DPBS (1x) and stored at 4°C covered with DPBS (1x) and sealed. All steps in the protocol were performed with a volume of 100 µl per well.

4.3.1.2 Automated imaging

Imaging was done using an automated BD Pathway 855 Cellular Bioimaging System with a 20x objective (NA=0.75) in combination with a Hamamatsu ORCA-ER Digital Camera. 25 fields per well were imaged containing channels for Hoechst (DNA), which was used as the focus channel for every single image, FITC (Fluorescein isothiocyanate; α-actinin) and TRITC (actin). The FITC channel was used to detect the Alexa Fluor® 488 label.

4.3.1.3 Analysis of the images

CellProfiler cell image analysis software (version 2.0) was used to analyze the images. Object selection was based in adaptive intensity and fixed size thresholds for every single object. Object segmentation was optimized to achieve best possible resolution of single objects in dense clusters of cells. Parent objects were segmented in channel 1 (Hoechst) for data analysis. In addition, integrated

intensity of objects in channel 1, mean area of child objects in channel 2 (FITC) and mean TRITC-intensity of child objects based on segmentation in channel 2 were measured. Based on the integrated intensity of the Hoechst signal of every single nucleus, nuclei were binned into viable or apoptotic cells. Only viable cells were used for further analysis. According to a threshold that was set manually for the mean TRITC signal, cells were either identified as cardiomyocytes or non-cardiomyocytes. For the cardiomyocytes fraction, each object was measured by its area as measured in channel 2 (FITC).

4.3.1.4 Statistical analysis

Areas of cardiomyocytes which were measured in channel 2 (FITC) were displayed as boxplot (displaying the median, the upper and lower hinge representing the first and third quartiles and the whiskers extending to the highest and lowest value within 1.5x interquartile range (IQR) of the upper and lower hinge, respectively) using R.

4.3.2 Seahorse Mito Stress Assay

4.3.2.1 Preparation of the cells

Four to five days before the assay was performed 5 x 10^4 primary neonatal rat cardiomyocytes were seeded per well in 100 µl culture medium onto an XF96 PS microplate which was coated with 0.1% gelatin. No cells were plated in the four edges (A1, A12, H1, H12) of the plates as those were reference wells. Within the next 24 to 36 h the culture medium was changed. For a first evaluation cardiomyocytes were treated either with normal culture medium or with conditioned medium from C26 cells 8 as well as 24 h before the assay was started. In further experiments the cardiomyocytes were cultured in normal culture medium or conditioned medium from the following cells only 24 h before the assay was conducted: 1. Single overexpression of selective potential “cachexokines”: C26 cells, HEK293 A cells, HEK293 A cells that were transfected with cDNA clones that overexpress *ADMATSL4*, *ATXN10*, *BIN1*, *CCL2*, *GAA*, *MINPP1* or *STX7*; 2. Single knockdown of selective potential “cachexokines”: untreated C26 cells or C26 cells that were transfected either with a negative control (NC) siRNA or siRNA that was directed against *Adamtsl4*, *Atxn10*, *Bin1*, *Ccl2*, *Gaa*, *Minpp1* or *Stx7;* 3. Combined knockdown of selective potential “cachexokines”: untreated C26 cells or C26 cells that were transfected either with a negative control (NC) siRNA or siRNAs that were directed against all aforementioned genes at once.

4.3.2.2 Performing the assay - The day before the experiment

An XF96 four-port sensor cartridge was soaked in XF calibrant buffer (200 µl/well) at 37°C in the CO_2-free incubator which is part of the XF prep station from Seahorse Bioscience overnight. The unbuffered Seahorse assay medium (pH 7.4) was prepared. The XF prep station and the XF96 extracellular flux analyzer were switched on. A protocol as shown in table 9 was created for the assay.

4.3.2.3 Performing the assay - On the day of experiment

To perform the assay cells were washed with 100 µl Seahorse assay medium once and then 160 µl Seahorse assay medium was pipetted in every well. The plate was kept in the CO_2-free incubator at 37°C for 1 h. In the meantime assay compounds that were prepared following manufacturer’s

instructions were diluted in Seahorse assay medium and were loaded to the ports of the equilibrated XF96 four-port sensor cartridge according to Table 8.
The XF sensor cartridge was inserted into the XF96 extracellular flux analyzer and the protocol was started. After completion of calibration the lower part of the XF sensor cartridge was ejected by the machine and the XF96 PS microplate containing the cells was inserted. The measurement was continued according to the protocol in Table 9. At the end of the assay cells were prepared for quantification.

Compound	Port	Stock conc.	Conc. in port	Vol. in port	Conc. on cells
Oligomycine	A	2.5 mM	20 µM	18 µl	2.0 µM
FCCP	B	2.5 mM	3 µM	20 µl	0.3 µM
Antimycine A	C	2.5 mM	10 µM	11 µl	1.0 µM
Rotenone		2.5 mM	10 µM	11 µl	1.0 µM

Tab. 8: Compound setup for Seahorse Mito Stress Assay.

Command	Time	Rate
Calibrate	~25 min	
Equilibrate	2 min	
Loop Start (3x)		1 - 3
Mix	3 min	
Measure	3 min	
Loop End		
Inject Port A		
Loop Start (4x)		4 - 7
Mix	3 min	
Measure	3 min	
Loop End		
Inject Port B		
Loop Start (4x)		8 - 11
Mix	3 min	
Measure	3 min	
Loop End		
Inject Port C		
Loop Start (4x)		12 - 15
Mix	3 min	
Measure	3 min	
Loop End		

Tab. 9: Protocol for Seahorse Mito Stress Assay.

4.3.3 Seahorse Palmitate Uptake Assay

4.3.3.1 Preparation of Bovine Serum Albumin (BSA)-Palmitate-conjugate

Preparation of BSA solution

100 ml of 150 mM NaCl solution were added to a pre-warmed (37°C) 250 ml glass beaker with a stir bar and placed on a stir plate. While stirring constantly 2.267 g fatty acid free BSA was added. A pre-

warmed (37°C) 1 l glass beaker filled with 200 ml tap water was put on a heated stir plate and a thermometer was placed in the water bath. The heat was adjusted and maintained at approximate 37°C. The beaker containing the BSA solution was covered with parafilm and placed in the 1 l beaker/water bath. The dissolved BSA solution was sterile filtrated by using a bottle top filter unit under the laminar flow hood. 50 ml of the filtered BSA solution was transferred to a pre-warmed (37°C) 250 ml glass beaker, covered with parafilm and placed in the 1 l beaker/water bath, resuming stirring. To produce a 0.17 mM stock the remaining filtered BSA solution was diluted with 50 ml of 150 mM NaCl solution. The solution was aliquoted into 4 ml glass vials and stored at -20°C.

Preparation of sodium palmitate solution

44 ml of 150 mM NaCl solution was pipetted to a 50 ml Erlenmeyer flask with a stir bar and 306 mg of sodium palmitate were added to it. A second pre-warmed (37°C) 1 l glass beaker containing 200 ml tap water was put on a heated stir plate and a thermometer was placed in the water bath. The heat was adjusted and maintained at 70°C. To dissolve the sodium palmitate it was covered with parafilm and placed in the 1 l beaker/water bath while stirring.

Conjugation of sodium palmitate to BSA

40 ml of the dissolved sodium palmitate was added in 5 ml steps to the BSA while stirring at 37°C. The beaker was covered again with parafilm and stirred for 1 h at 37°C. To create a 10 mM BSA-Palmitate-conjugate working solution the volume was adjusted to 100 ml in a glass graduated cylinder with 150 mM NaCl. The pH was adjusted to 7.4. The BSA-Palmitate-conjugate working solution was aliquoted into 4 ml glass vials and stored at -20°C. It is stable for two month. During the whole preparation process and for storage glass stuff has to be used because the sodium palmitate adheres to plastic.

4.3.3.2 Performing the Seahorse Palmitate Uptake Assay

Preparation of the cells

This was done as described in chapter 4.3.2.1 for the Seahorse Mito Stress Assay.

Performing the assay - The day before the experiment

An XF96 four-port sensor cartridge was soaked overnight in XF calibrant buffer (200 µl/well) in the CO_2-free incubator of the XF prep station at 37°C. The unbuffered Krebs-Henseleit Buffer (KHB) assay medium (1x, pH 7.4) was prepared. The XF prep station and the XF96 extracellular flux analyzer were switched on. A protocol as shown in Table 11 was created for the assay.

Performing the assay - On the day of experiment

To perform the assay cells were washed with 100 µl KHB assay medium (1x) once and then 180 µl KHB assay medium (1x) was pipetted in every well. The plate was kept in the CO_2-free incubator at 37°C for 1 h. In the meantime assay compounds were diluted and loaded to the ports of the equilibrated XF96 four-port sensor cartridge according to Table 10. Before loading the BSA-Palmitate-conjugate was heated at 70°C until it dissolved.
The XF sensor cartridge was inserted into the XF96 extracellular flux analyzer and the protocol was started. After completion of calibration the lower part of the XF sensor cartridge was ejected by the machine and the XF96 PS microplate containing the cells was inserted. The measurement was

continued according to the protocol in Table 11. At the end of the assay cells were prepared for quantification.

Compound	Port	Stock conc.	Conc. in port	Vol. in port	Conc. on cells
BSA-Palmitate	A	10 mM	10 mM	20 µl	1.0 mM
Etomoxir	B	100 mM	10 mM	22 µl	1.0 mM

Tab. 10: Compound setup for Seahorse Palmitate Uptake Assay.

Command	Time	Rate
Calibrate	~25 min	
Equilibrate	2 min	
Loop Start (3x)		1 - 3
Mix	3 min	
Measure	3 min	
Loop End		
Inject Port A		
Loop Start (3x)		4 - 6
Mix	3 min	
Measure	3 min	
Loop End		
Inject Port B		
Loop Start (6x)		7 - 12
Mix	3 min	
Measure	3 min	
Loop End		

Tab. 11: Protocol for Seahorse Palmitate Uptake Assay.

4.3.4 Sulforhodamine B (SRB) staining (Indirect quantification of cell number)

After removing the assay medium from the cells 100 µl ice cold fixation buffer per well was added. Cells were fixated overnight at -20°C. Cells were washed two times with dH_2O and covered with 50 µl SRB solution per well for 30 min at room temperature while shaking and covered with aluminium foil. To remove unbound SRB solution cells were washed four times with wash solution. For the first wash the wells were entirely filled with wash solution and for the following three washing steps a volume of 200 µl per well was added. For quantification the SRB was resolved in 100 µl elution buffer per well under vigorous shaking for 10 min at room temperature and covered with aluminium foil. The absorbance was measured at 550 nm.

4.4 Histology

4.4.1 Immunostaining of cells

4.4.1.1 Anti-sarcomeric α-actinin immunostaining of primary neonatal rat cardiomyocytes

Primary neonatal rat cardiomyocytes were seeded at 1.0 x 10^5 - 1.5 x 10^5 cells per well on cover slips in 24-well plates which were coated with 0.1% gelatin. Within the next 24 - 36 h culture medium was

changed. Three days after seeding cardiomyocytes were treated with conditioned medium or with 2% mouse serum.
To perform the staining cells were washed two times with DPBS (1x) and then they were fixated with 4% formaldehyde solution (methanol-free) for 10 min at room temperature. Cells were washed with DPBS (1x) again and afterwards permeabilized with 0.3% Triton solution for 10 min at room temperature. After blocking with 5% goat serum for 30 min at room temperature cells were incubated with primary antibody (anti-sarcomeric α-actinin) at 4°C overnight. The primary antibody was diluted 1:200 in 5% goat serum. Next day, before incubating the cells with secondary antibody (Texas Red® anti-mouse) for 1 h at room temperature in the dark cells were washed two times with DPBS (1x). The secondary antibody was also diluted 1:200 in 5% goat serum. After 30 min Hoechst 33258 (1:2000) was pipetted additionally to every well. Cells were washed two times with DPBS (1x). By using one droplet of FluorSave™ Reagent the cover slips with the stained cells were fixated on object slides. All steps in the protocol were performed with a volume of 200 µl per well.

Imaging and analysis

Cardiomyocyte area was determined using colored pictures from α-actinin immunostained cardiomyocytes which were captured with a CCD camera (CC-12, Olympus Soft Imaging Solutions) under 20x magnification (BX51, Olympus) and the analySIS software. Analysis was performed in a blinded manner. Roughly 100 cells per condition were counted, and the averaged values were used for analysis.

4.4.2 Staining of paraffin embedded tissues

4.4.2.1 Adipophilin/Perilipin-2 staining

Paraffin embedded heart cross sections (1 µm) were deparaffinized using the following alcohol series: three xylol washes (10 min each), two 100% ethanol rinses (5 min each), followed by one 96%, 70% and 50% ethanol wash (5 min each) and one wash with millipore H_2O (5 min). Antigen retrieval was performed by incubating the slides three times for 6 min in 5% urea buffer. The buffer was heated up in the microwave (600 watt) until it comes to boil. Afterwards, slides were treated with a 1% hydrogen peroxide solution to block endogenous peroxide. The slides were rinsed under running tap water for 5 min followed by two washes with 1x PBS. Then they were first blocked in milk/goat serum/avidin solution for 40 min (50 µl per section), washed two times in 1x PBS, blocked in milk/goat serum/biotin solution for 30 min (50 µl per section) and again washed two times in 1x PBS. The primary antibody (anti-adipophilin) was diluted 1:100 in antibody diluent and slides were incubated together with the antibody overnight at 4°C (50 µl per section) in a humid chamber. Next day the slides were washed one time in 1x PBS, one time in 0.05% Triton solution and two times in 1x PBS (5 min each step). Afterwards, they were incubated with the secondary antibody (goat anti-guinea pig, biotinylated) that was diluted 1:750 in antibody diluent for 30 min at room temperature (50 µl per section) in a humid chamber. Meanwhile, the Avidin-Biotin Complex (ABC) reagent was prepared as followed: four drops of reagent A were added to 10 ml DPBS (1x) followed by four drops of reagent B. The solution was mixed immediately and incubated for 30 min to form complexes. The slides were washed as described before after antibody treatment. Subsequently, they were incubated with ABC reagent for 30 min (50 µl per section) followed by two 1x PBS rinses. During washing the 3,3'-Diaminobenzidine (DAB) solution was prepared as followed: one DAB tablet (silver foil) and one urea hydrogen peroxide tablet (gold foil) were dropped into 1 ml dH_2O and mixed until

dissolved. This DAB solution was pipetted directly on the sections (50 µl each) and the reaction was stopped after 2 min using tap water. Subsequently, the sections were counterstained with hematoxylin (Dako) for 1 min (50 µl per section) and washed in tap water for 3 min. Before the slides were mounted with Eukitt® they were dehydrated by using the following alcohol series: short rinses in 70% and 96% ethanol, two washes in 100% ethanol (5 min each) and three in xylol (5 min each). This staining protocol was mainly described by Straub B.K. (2008).

4.4.2.2 Hematoxylin and eosin stain (H&E)

Paraffin embedded heart cross sections (0.1 µm) were deparaffinized using the following alcohol series: two xylol washes (10 min each), two 100% ethanol rinses (5 min each), followed by one 96% and 70% ethanol wash (4 min each) and one wash in millipore H_2O (2 min). The rehydrated slides were stained in filtered hematoxylin solution (Sigma Aldrich®) for 6 min and washed under tap water for 1 min. After destaining in HCl-Alkohol (3%) for 20 sec slides were rinsed under tap water for 10 min. Subsequently, slides were stained in eosin solution for 50 sec and destained in millipore H_2O (three short dips). Dehydration was accomplished by following alcohol series: one wash in 70%, 96% and 100% ethanol (4 min each) and one xylol rinse (10 min). Finally, slides were mounted with Eukitt®.

Imaging and analysis

Cardiomyocyte area was determined using colored pictures from H&E stained cross sections which were captured with a CCD camera (CC-12, Olympus Soft Imaging Solutions) under 20x magnification (BX51, Olympus) and the analySIS software. Analysis was performed in a blinded manner. Only cardiomyocytes with a visible nucleus in the middle of the cell and an unbroken cellular membrane were measured. Around 100 cells per left ventricle were counted, and the averaged values were used for analysis.

4.4.2.3 Masson's trichrome stain

Masson's trichrome staining of histologic sections is used for the determination of collagen deposition. It is a three-colour staining protocol: 1. red: keratin, muscle and blood vessels, 2. blue: collagenous structures as connective tissue and 3. dark brown/black nuclei.
Paraffin embedded heart cross sections (0.1 µm) were heated to 58°C on a slide warmer and subsequently deparaffinized through following alcohol series: two xylol washes (10 min each), two 100% ethanol rinses (5 min each), followed by one 96% and 70% wash (4 min each) and one wash in millipore H_2O (2 min). Slides were refixed by incubation in Bouin's solution for 1 h in a water bath heated up to 58°C. Afterwards, slides were rinsed in tap water until Bouin's solution was washed out. In the meantime Weigert's iron hematoxylin stock solution A and B were mixed in equal parts to prepare a fresh working solution that was heated up to 55°C in a water bath. Slides were stained in Weigert's iron hematoxylin for 10 min in 58°C water bath and washed again with tap water for 10 min. Subsequently, slides were stained in filtered Biebrich scarlet-acid fuchsin while shaking at room temperature for 15 min. After a further washing step slides were destained in phosphomolybdic-phosphotungstic acid solution while shaking at room temperature for 20 min. The phosphomolybdic-phosphotungstic acid solution was prepared by mixing the two stock solutions and adding two volumes of millipore water. Slides were directly transferred to filtered aniline blue solution and stained for 17 min while shaking at room temperature. Slides were rinsed in tap water until excess stain was washed out. Afterwards, slides were destained in 1% acetic acid (5 qick dips)

and dehydrated through three washes in 100% ethanol and xylol (2 min each). Finally, slides were mounted with Eukitt®.

4.5 Biochemistry

4.5.1 Protein extracts from heart tissue

Frozen heart tissue slices (upper part of the heart) were transferred to 2 ml safe-lock tubes containing a pre-cooled steel bead and 500 µl Gluthation-S-Transferase (GST) buffer. Tissues were immediately homogenized using the TissueLyser for 3 min at a frequency of 30 Hz. Homogenates were transferred to 1.5 ml safe-lock tubes and 0.5% Igepal® was added to every tube. Then the samples incubated on a rotating wheel for 10 min at 4°C. Afterwards, the extracts were sonicated using the BioRuptor® (one cycle: 30 sec on and 30 sec off). Samples were centrifuged for 10 min at 13,000 rpm and 4°C. Finally, supernatants were transferred to fresh 1.5 ml safe-lock tubes and protein concentration was determined.

4.5.2 Determination of protein concentration

Protein concentration was determined using the Pierce® BCA Protein Assay Kit, following the manufacturer's instructions. Protein lysates were diluted 1:10 not to exceed the linear range of the BSA standard curve (0.1 - 2 mg/ml) and were measured in duplicates. Afterwards, parts of the protein samples were directly used for SDS-Page and immunoblotting and the remaining lysates were stored at -80°C.

4.5.3 SDS polyacrylamide gel electrophoresis (SDS-Page) and immunoblotting

For separation 20 - 40 µg protein lysate were diluted with 5x SDS loading dye and denatured for 10 min at 95°C. These protein samples and a protein molecular weight marker (PageRuler™ Prestained Protein Ladder) were loaded onto 8 - 15% SDS-polyacrylamide gels (Tab. 12) where they were separated at 120 V. Then they were transferred onto nitrocellulose membrane using a wet blot system. Blotting was performed at 80 V for 75 min or at 30 V and 4°C overnight. Transfer efficiency was verified by Ponceau S staining of the membranes and subsequently they were blocked either in 5% BSA or in 5% skim milk dissolved in Tris-Buffered Saline (TBS) for 1 h. The membranes were incubated with primary antibodies (see chapter 5.3.1) that were diluted in 5% BSA or 5% skim milk, according to the manufacturer's instruction, for 1 h at room temperature or overnight at 4°C. Afterwards, the membranes were washed three times for 10 min with TBS containing 1% Tween® 20 (TBS-T) and incubated with the secondary antibody (see chapter 5.3.2) conjugated to horse radish peroxidase (HRP) at a dilution of 1:5000 either in 5% BSA or 5% skim milk for 1 h. Then the membranes were washed with TBS-T again as described before and treated with enhanced chemiluminescence system (ECL™) Western Blotting Detection Reagent to detect specific bands. The induced chemiluminescence signal was detected using the ChemiDoc™ XRS+ System. Exposure times differed based on the quality of the specific antibody.

Components	Stacking gel	Separation gel			
	5%	8%	10%	12%	15%
H_2O	1.4 ml	2.3 ml	1.9 ml	1.6 ml	1.1 ml
30% Bisacrylamide	0.33 ml	1.3 ml	1.7 ml	2.0 ml	2.5 ml
1.0 M Tris (pH 6.8)	0.25 ml	-	-	-	-
1.5 M Tris (pH 8.8)	-	1.3 ml	1.3 ml	1.3 ml	1.3 ml
10% SDS	0.02 ml	0.05 ml	0.05 ml	0.05 ml	0.05 ml
10% APS	0.02 ml	0.05 ml	0.05 ml	0.05 ml	0.05 ml
TEMED	0.002 ml	0.003 ml	0.002 ml	0.002 ml	0.002 ml

Tab. 12: Composition of SDS-polyacrylamide gels.

4.5.4 Enzyme-linked immunosorbent assay (ELISA)

Levels of Ataxin10 (Atxn10), Glucosidase alpha acid (Gaa) and Monocyte chemotactic protein-1 (Mcp-1) were determined in conditioned media, sera and tissue homogenates using ELISA Kits. Assays were performed following the manufacturer's instructions. Some of the used samples needed to be diluted depending on the ELISA Kit (Tab. 13).

ELISA Kit	Serum	Tissue Homogenate	Conditioned medium
Atxn10	1:20	1:50	undiluted
Gaa	1:100	1:50	undiluted
Mcp-1	1:20	undiluted	undiluted

Tab. 13: Dilution conditions of serum, tissue homogenate and conditioned medium for the different ELISA Kits.

4.5.5 Quantitative secretome analysis

4.5.5.1 Pulse-labeling with AHA and SILAC

The used secretome analysis method combines click chemistry and pulsed stable isotope labeling with amino acids in cell culture (SILAC) which allows the selective enrichment and quantification of secreted proteins in the presence of serum in the media. This method was described elsewhere (Eichelbaum K. et al., 2012). A schematic overview of the processing is displayed in Figure 48.

MC38 as well as C26 cells were grown on two 10 cm cell culture dishes until they reached 60 - 70% confluency. Cells were washed with DBPS (1x) once and cultured in SILAC medium for 30 min (4 ml per dish) to deplete the amino acids methionine (met), lysine (lys) and arginine (arg). Subsequently, cells were incubated for 24 h in SILAC medium supplemented with 0.1 mM L-azidohomoalanine (AHA) and either 84 µg/ml [$^{13}C_6$, $^{15}N_4$] L-arginine and 146 µg/ml [$^{13}C_6$, $^{15}N_2$] L-lysine (heavy label) or 84 µg/ml [$^{13}C_6$] L-arginine and 146 µg/ml [4,4,5,5-D_4] L-lysine (intermediate label). Experiments were performed as independent biological duplicates with reversed SILAC labels. Media were collected, centrifuged at 2,000 rpm for 3 min, supplemented with protease inhibitor (Roche) and frozen at -80°C.

4.5.5.2 Enrichment of newly synthesized proteins and on-bead digestion

Newly synthesized proteins were first concentrated by using Amicon Ultra® Centrifugal Filters with a cut-off of 3 kDa. Concentrated media (~250 µl) were enriched using the Click-iT® Protein Enrichment Kit, following the manufacturer's instructions with slight modifications. 100 µl of alkyne agarose resin

slurry were used, and the volumes of all reagents were divided by two. The resin was washed with 900 µl dH_2O and afterwards the concentrated media, diluted in 250 µl urea buffer, as well as catalyst solution were added. The mixture incubated for 16 - 20 h at room temperature. After washing the resin with 900 µl dH_2O, 0.5 ml SDS buffer (supplied with the kit) and 0.5 µl 1 M dithiothreitol (DTT; BioRad) were added and agitated at 70°C for 15 min. The supernatant was removed, and 3.7 mg iodoacetamide in SDS washing buffer (supplied with the kit) were added and incubated for 30 min protected from light.
The resin was transferred to a spin-column (supplied with the kit) and washed with 20 ml SDS buffer, 20 ml 8 M urea in 100 mM Tris (pH 8.0), 20 ml 20% isopropanol and 20 ml 20% acetonitrile. Before adding 0.5 µg trypsin (Promega), the resin was dissolved in digestion buffer II. This was followed by an overnight incubation at 37°C. The peptide solution was collected, and the resin was washed with 500 µl dH_2O. Both solutions were combined, followed by an acidification with 20 µl 10% CF_3COOH.

4.5.5.3 Sample preparation for mass spectrometry

Acidified samples were desalted using Sep-Pak® C18 1 cc Vac Cartridges (50 mg) as described elsewhere (Villen J., Gygi S.P., 2008). The desalted peptide samples were fractionated using isoelectric focusing or strong anion exchange chromatography. An Agilent 3100 OFFGEL Fractionator in combination with Immobiline DryStrips (pH 3 - 10 nonlinear, 13 cm) was used for isoelectric focusing. Focusing was performed at a constant current of 50 mA with a maximum voltage of 4,000 V. After reaching 20 kVh, the samples were collected, acidified with CF_3COOH and desalted using StageTips (Rappsilber J., 2003). The 12 fractions were combined into six fractions. The peptide samples were dried and dissolved in 4% acetonitrile and 0.1% formic acid. Alternatively, strong anion exchange was used for the fractionation of the samples into six fractions, as described elsewhere (Wisniewski J.R., 2009) with minor adaptations.

4.5.5.4 Liquid chromatography tandem mass spectrometry (LC-MS/MS)

Peptides were separated using a nanoAcquity Ultra Performance Liquid Chromatography (UPLC) System fitted with a trapping (nanoAcquity Symmetry C18, 5 µm, 180 µm x 20 mm) and an analytical column (nanoAcquity BEH C18, 1.7 µm, 75 µm x 200 mm). The outlet of the analytical column was coupled directly to a Linear Trap Quadrupole (LTQ) Orbitrap Velos or Orbitrap Velos Pro using a Proxeon nanospray source (solvent A: 0.1% formic acid; solvent B: acetonitrile and 0.1% formic acid). Samples were loaded with a constant flow of solvent A at 15 µl/min onto the trapping column. Peptides were eluted via the analytical column at a constant flow of 0.3 µl/min. During the elution step, the percentage of solvent B increased in a linear fashion from 3% to 25% in 40 min or 110 min, followed by an increase to 40% in 4 min or 10 min and an increase to 85% in 0.1 min or 1 min for the different gradient lengths. The peptides were introduced into the mass spectrometer (MS) via a PicoTip™ Emitter (360 µm OD x 20 µm ID; 10 µm tip). Full scan MS spectra with mass range 300 -1,700 (m/z) were acquired in profile mode in the Orbitrap with a resolution of 30,000. The filling time was set at maximum of 500 msec with a limitation of 10^6 ions. The most intense ions (up to 15) from the full-scan MS were selected for fragmentation in the LTQ. Normalized collision energy of 40% was used and the fragmentation was performed after accumulation of 3 x 10^4 ions or after a filling time of 100 msec for each precursor ion (whichever occurred first). MS/MS data were acquired in centroid mode. Only multiply charged (2+ or 3+) precursor ions were selected for MS/MS. The dynamic exclusion list was restricted to 500 entries with a maximum retention period of 30 sec and a

relative mass window of 10 ppm. Lock mass correction using a background ion (m/z 445.12003) was applied.

4.5.5.5 Data analysis

The mass spectrometric raw data were processed using MaxQuant (version 1.3.0.5) (Cox J., Mann M., 2008), and MS/MS spectra were searched using the Andromeda search engine (Cox J., 2011) against mouse proteins (53,623 entries) in UniProt (Jain E., 2009), to which 265 frequently observed contaminants, as well as reversed sequences of all entries, had been added. Enzyme specificity was set to trypsin/P, and a maximum of two missed cleavages were allowed. Cysteine carbamidomethylation was used as fixed modification and methionine oxidation, protein N-terminal acetylation, as well as replacement of methionine by AHA were used as variable modifications. The minimal peptide length was set to six amino acids. The initial maximal allowed mass tolerance was set to 20 ppm for peptide masses, followed by 6 ppm in the main search and to 0.5 Dalton for fragment ion masses. False discovery rates (FDRs) for peptide and protein identification were set to 1%. At least one unique peptide was required for protein identification. The protein identification was reported as an indistinguishable “protein group” if no unique peptide sequence to a single database entry was identified. Proteins that were exclusively identified based on light SILAC labeled peptides were regarded as contaminations and removed from the final protein list.
For protein quantification a minimum of two ratio counts was set and the “requantify” and “match between runs” functions were enabled. A protein group was kept for further analysis if the number of identified peptide species carrying an intermediate or heavy label divided by the total number of peptide species detected in the complete experimental setup was higher than 0.2.
Average protein ratios were reported if they were quantified in two replicates each based on at least two ratio counts.

4.5.5.6 Statistical analysis

Statistical analysis was performed using the Limma package in R/Bioconductor (Gentleman R.C., 2004; Smyth G.K., 2004). After fitting a linear model to the data, an empirical Bayes moderated t-test was used and p-values were adjusted for multiple testing with Benjamini and Hochberg’s method. Proteins with an adjusted p-value lower than 0.062 (FDR=6.2%) and a minimum fold change of 2 in both biological replicates were considered to be differentially secreted.
Functional classification was performed using either MetaCore™ (Nikolsky Y. et al., 2005). The likelihood of a protein being truly secreted was predicted using SignalP 3.0. (Bendtsen J.D., 2004) for classically secreted proteins (containing a signal peptide) and SecretomeP 2.0. (Bendtsen J.D., 2004) for non-classically secreted proteins. Transmembrane domains were predicted using TMHMM 2.0. (Krogh A., 2001).

4.6 Molecular biology

4.6.1 RNA biology

4.6.1.1 RNA isolation from cells

Cells were harvested in 1 ml (high cell number) or 500 µl (low cell number) QIAzol® Lysis Reagent and transferred to 1.5 ml safe-lock tubes. Lysates were incubated at room temperature for 5 min to release nucleoprotein complexes before adding 200 µl and 100 µl of chloroform respectively.

Mixtures were vortexed for 15 sec, kept at room temperature for 3 min and then centrifuged for 30 min at 13,000 rpm and 4°C. The upper aqueous solution containing the RNA was transferred into a fresh 1.5 ml RNase free reaction tube. The RNA phase was then mixed with 1 volume of 70% ethanol to precipitate nucleic acids. RNA was then purified using the RNeasy® Mini Kit (high cell number) or RNeasy® Micro Kit (low cell number), following the manufacturer's instructions including DNA digestion. RNA was eluted in 30 µl and 14 µl dH_2O respectively and stored at -80°C.

4.6.1.2 RNA isolation from tissue

Frozen tissue samples were transferred into a 2 ml safe-lock tube containing 1 ml QIAzol® Lysis Reagent and a pre-cooled stainless steel bead. The samples were lysed using the TissueLyser for 3 min at a frequency of 30 Hz. Fibrous tissues as the heart or skeletal muscle have to be lysed for 6 - 9 min. Lysates were incubated at room temperature for 5 min to release nucleoprotein complexes before adding 200 µl of chloroform. Phase separation and RNA precipitation were performed as described in chapter 4.6.1.1. RNA was then purified using the RNeasy® Mini Kit, following the manufacturer's instructions including DNA digestion. RNA was eluted in 30 - 50 µl dH_2O and stored at -80°C.

4.6.1.3 Determination of RNA concentration

The RNA concentration was determined spectrophotometrically at 260 nm using the NanoDrop ND-1000 spectrophotometer. Additionally, the ratio 260 nm/280 nm was determined in order to measure protein contaminations in the samples.

4.6.1.4 Assessment of RNA quality

RNA quality was assessed using agarose gel electrophoresis. The RNA samples were denatured in RNA sample buffer. 1 µl RNA sample was mixed with 10 µl RNA sample buffer, incubated for 10 min at 65°C and 2 min on ice. Denaturated RNA samples were separated on 1% agarose gels (1% agarose (RNase free) in 1x TBE buffer) for 45 min at 90 V. RNA quality was determined visually by examination of the ratio between 28S to 18S ribosomal RNA, which is 2:1 for intact RNA.

4.6.1.5 cDNA synthesis

For synthesis of complementary DNA (cDNA), 0.5 - 1 µg of RNA was used. cDNA synthesis was performed using the First Strand cDNA Synthesis Kit, following the manufacturer's instructions. After completion, cDNA samples were diluted 10 fold in dH_2O and stored at -20°C.

4.6.1.6 Quantitative PCR

For quantitative PCR (qPCR) 5 µl of the diluted cDNA samples were pipetted in technical duplicates onto a MicroAmp® Optical 96-well reaction plate. Water served as a negative control and a sample containing no reverse transcriptase as control for genomic DNA contamination. The TaqMan probes used were obtained either from Life Technologies™ or Eurofins MWG Operon (see chapter 5.13). Depending on the used TaqMan probes two different master mixes were prepared (Tab. 14). 15 µl of the Master-Mix were transferred to every sample. Quantitative PCR was performed using the StepOnePlus™ Real-Time PCR System. RNA expression data were quantified according to the delta CT method and normalized to levels of TATA-box binding protein RNA (TBP).

Probe (Company)	Master-Mix (per reaction)	
Life Technologies™	10 µl	TaqMan® Gene Expression Master Mix
	0.5 µl	TaqMan® Primer/Probe Set
	4.5 µl	dH_2O
Eurofins MWG Operon	10 µl	TaqMan® Gene Expression Master Mix
	1.0 µl	Forward Primer (10 µM)
	1.0 µl	Reverse Primer (10 µM)
	0.5 µl	Probe (5 µM)
	2.5 µl	dH_2O

Tab. 14: TaqMan Master-Mix.

4.6.2 Microarray

4.6.2.1 Gene expression profiling

Gene expression profiling was performed using RNA extracts from the following samples: 1. primary adult mouse cardiomyocytes that were treated with normal culture medium or with conditioned medium from C26 cells for 48 h; 2. hearts from the C26 mouse experiment; 3. hearts from the MC38 mouse experiment.

RNA isolation was performed as described in chapter 4.6.1.1 and 4.6.1.2. cDNA synthesis was performed using the SuperScript® Choice System, according to manufacturer's protocol. Biotin-labeled cRNA was produced using *BioArray HighYield*® RNA Transcript Labeling Kit. Standard protocol from Affymetrix® with 3.3 µl of cDNA was used for the *in vitro* transcription (IVT). Cleanup of the IVT product was done using CHROMA SPIN™-100 columns. Spectrophotometric analysis was used for quantification of complementary RNA (cRNA). Labeled and fragmented cRNA was hybridized to GeneChip® Mouse Genome 430 2.0 arrays for 16 hours at 45°C using Affymetrix® defined protocol. Microarrays were washed using a GeneChip® Fluidics Station 450 and stained initially with streptavidin-phycoerytherin. For each sample the signal was further enhanced by incubation with biotinylated goat anti-streptavidin antibody, subsequently with biotinylated goat IgG and finally again with streptavidin-phycoerytherin. Microarrays were scanned with GeneChip® Scanner controlled by Affymetrix® Microarray Suite Software.

4.6.2.2 Microarray processing and statistical analysis

A Custom CDF Version 14 with Entrez based gene definitions was used to annotate the arrays. The Raw fluorescence intensity values were normalized applying quantile normalization. Differential gene expression was analyzed based on loglinear mixed model ANOVA (Hsieh W.P., 2003; Roy J., 2007), using a commercial software package SAS® JMP7 Genomics (version 4) from SAS® (SAS® Institute, Cary, NC, USA). A false positive rate of a=0.05 with false discovery rate (FDR) correction was taken as the level of significance. The overrepresentation analysis (ORA) is a microarray data analysis that uses predefined gene sets to identify a significant overrepresentation of genes in data sets (Subramanian A., 2005; Manoli T., 2006). Pathways belonging to various cell functions were obtained from public external databases (KEGG, http://www.genome.jp/kegg/). A Fisher's exact test was performed to detect the significantly regulated pathways. Gene Set Enrichment Analysis (GSEA), was used to determine whether defined lists (or sets) of genes exhibit a statistically significant bias in

their distribution within a ranked gene list (http://www.broadinstitute.org/gsea/; Subramanian A., 2005).

4.6.3 DNA biology

4.6.3.1 Transformation of *Eschericha coli*

One Shot® TOP10 chemically competent *Eschericha coli (E.coli)* strain was transformed by chemical transformation. 40 µl of bacterial suspension were thawed on ice. 10 µl of the suspension were transferred to a 1.5 ml safe-lock tube and mixed with 1 µg of plasmid DNA (ready-to-use cDNA expression clones obtained from Source BioScience; see chapter 5.11). After 20 min incubation on ice, a heat shock at 42°C was applied for 45 sec. Afterwards, bacteria were placed on ice for 2 min followed by an addition of 100 µl SOC medium. Bacteria were incubated at 37°C under vigorous shaking for 1 h. Subsequently, 20 µl of the bacterial culture were plated onto LB-agar plates containing ampicillin (50 µg/ml) as antibiotic. Agar plates were incubated at 37°C overnight and stored at 4°C.

4.6.3.2 Bacterial liquid cultures

Single colonies were inoculated into 50 ml LB-medium supplemented with ampicillin (50 µg/ml) as antibiotic. The cultures were incubated overnight at 37°C under vigorous shaking (~160 rpm).

4.6.3.3 Preparation of glycerol stocks from transformed *E.coli*

300 µl of the bacterial liquid cultures were mixed with the same volume of glycerol and stored at -80°C.

4.6.3.4 Preparation of plasmid DNA

Plasmid DNA was isolated from bacterial liquid cultures using the PureLink® HiPure Plasmid Midiprep Kit, following the manufacturer's instructions. Isolated DNA was stored at -20°C and the concentration was determined as described in chapter 4.1.2.3.

4.6.4 Lipids

4.6.4.1 Triglyceride extraction from tissue

Frozen tissues were weighed (minimum 70 mg heart tissue) and transferred to 2 ml safe-lock tubes. A pre-recooled (-80°C) stainless steel bead and 1.5 ml of chloroform:methanol (2:1) mixture (maintained at -80°C) were added to each tube. Tissues were lysed using a TissueLyser at a frequency of 30 Hz for 8 min. After spinning down, the lysates were mixed for 20 min on Thermomixer at 1,400 rpm and room temperature. Afterwards, samples were transferred to fresh 2 ml safe-lock tubes and centrifuged for 30 min at 13,000 rpm and 20°C. After transferring 1 ml of the supernatants to fresh 2 ml safe-lock tubes 200 µl of 150 mM NaCl were added and they were centrifuged at 2,000 rpm for 5min. In the meanwhile, 40 µl of chloroform:Triton™ X-100 (1:1) solution was pipetted into fresh 1.5 ml safe-lock tubes. 200 µl of the lower organic phase were transferred to the tubes containing the chloroform:Triton™ X-100 solution. These samples were dried with the Speedvac overnight. To the remaining Triton-lipid solutions were 200 µl of dH_2O added. Samples were mixed by placing on a rotating wheel for 1 h at room temperature and stored at -80°C until required for triglyceride (TG) determination.

4.6.4.2 Triglyceride isolation from cells

Primary neonatal rat cardiomyocytes were seeded at 1.25 x 10^5 cells per well on 6-well plates. Culture medium was changed after 24 - 36 h. Three days after seeding cells were treated with normal culture medium or conditioned medium from C26 cells for 24 h.

Then cells were washed once with DPBS (1x) and after adding 200 µl of Triton™ X-100 (TX) lysis buffer to every well plates were frozen at -80°C for at least 24 h. Afterwards, cells were thawed, transferred to 1.5 ml safe-lock tubes on ice and sonicated for two cycles (one cycle: 30 sec on and 30 sec off). Cell debris was removed by centrifugation at 13,000 rpm and 4°C for 15 min. For protein measurement 6 µl of the middle phase (fat is on top) of each supernatant was transferred to fresh 1.5 ml safe-lock tubes and 54 µl dH_2O was added (1:10 dilution). Protein concentration was determined using the Pierce® BCA Protein Assay Kit. The remaining supernatants were also transferred to fresh 1.5 ml safe-lock tubes for TG level measurement.

4.6.4.3 Determination of triglyceride levels in tissue extracts and cell lysates

For the measurement of TG level the Serum TG Determination Kit was used. This kit based on enzymatic reaction which hydrolyses the TGs and the released glycerol can be detected by a colorimetric reaction. For the preparation of a standard curve Glycerol Standard Solution was used.

Either 20 µl of extracted TGs from heart tissue or 70 µl of cell supernatants were transferred to a 96-well plate in two sample series. In order to determine a blank value (first sample series), 100 µl Free Glycerol Reagent were added to each well. To the second sample series (assay value), 100 µl TG Reagent was added. Plates were incubated at 37°C for 5 min and measured at 540 nm. TG content (TG-bound glycerol) was determined by subtracting the free glycerol (blank value) from the total glycerol (assay value).

4.7 Statistical analysis

Statistical analysis was performed either using GraphPad Prism (1- or 2-way analysis of variance (ANOVA) with Bonferroni-adjusted post-test) or Microsoft Excel (Student´s t-test with Welch correction). $p < 0.05$ was considered statistically significant. *$p < 0.05$, **$p < 0.01$, ***$p < 0.001$. Most of the data are shown as mean ± SEM (standard error of the mean).

The following protocol sections include a separate statistic section which specifically belongs to the analysis of these assays: high-throughput analysis of cardiomyocytes size (chapter 4.3.1.4), quantitative secretome analysis (chapter 4.5.5.6) and microarray (chapter 4.6.2.2).

5 Material

5.1 Animals

Strain	Origin
APC delta 580 Mice	NCI-Frederick, Frederick (MD, USA)
Balb/c Mice	Charles River, Brussels (Bel)
C57BL6/J Mice	Charles River, Brussels (Bel)
Wistar Rats	Clinic Experimental Research Unit, Heidelberg

5.2 Research Diet

Diet	Distributor
Standard Chow (Kliba Nafag; #3437)	Provimi Kliba (Kaiseraugust, CH)

5.3 Antibodies

5.3.1 Primary antibodies

Primary antibody	Dilution	Isotype	Distributor
Anti-sarcomeric α-actinin	1:200/1:500	mouse monoclonal	Sigma Aldrich®, Munich
Anti-Adipophilin/PLIN2	1:100	guinea pig polyclonal	Progen, Heidelberg
Anti-LC3B	1:1000	rabbit polyclonal	New England Biolabs®, Frankfurt
Anti-Ubiquitin	1:1000	mouse monoclonal	Santa Cruz Biotechnology, Heidelberg

5.3.2 Secondary antibodies

Secondary antibody	Dilution	Distributor
Goat anti-mouse IgG (H+L), Alexa Fluor® 488	1:400	Life Technologies™, Darmstadt
Goat anti-guinea pig IgG, Biotinylated	1:750	Thermo Scientific™, Ulm
Goat anti-mouse IgG (H+L)-HRP	1:1000	BioRad, Munich
Goat anti-rabbit IgG (H+L)-HRP	1:1000	BioRad, Munich
Goat anti-streptavidin, Biotinylated	1:50 - 1:500	Vector Labs, Burlingame (CA, USA)
Texas Red® anti-mouse IgG (H+L)	1:200	Vector Labs, Burlingame (CA, USA)

5.4 Buffers and Solutions

Buffer/Solution	Components
Borate Buffered Saline (BBS; 2x, pH 6.95)	280 mM NaCl, 50 mM Bis(2-hydroxyethyl)-2-aminoethanesulfonic acid (BES), 1.5 mM Na_2HPO_4 (filter-sterilized)
Cardiomyocyte Culture Medium	42.5 ml MEM/HBSS Medium, 0.5 ml 200 mM Glutamine, 0.5 ml PenStrep, 5 ml FBS, 1 ml 0.5 M BDM and 0.5 ml ITS (100x)

Carnitine (50 mM)	81 mg L-Carnitine, 10 ml dH_2O (filter-sterilized, aliquoted and stored at -20°C up to one month)
Culture Medium	500 ml DMEM (High Glucose, Pyruvate), 10% FBS, 1% PenStrep (stored at 4°C)
Digestion Buffer I (for 1 heart)	23 ml Tyrode's Solution, 4 mg/ml Liberase 1, 0.6% Trypsin, 0.125 mM $CaCl_2$
Digestion Buffer II	100 mM Tris (pH 8.0), 2 mM $CaCl_2$, 10% Acetonitrile
Elution Buffer	10 mM Tris Buffer (1.21 g Trizma® Base in 1 l Millipore H_2O; unbuffered, autoclaved and stored at room temperature)
Eosin Solution	0.1% Eosin G, 63% Ethanol, 1% Acetic Acid (stored at room temperature protected from light)
Etomoxir (100 mM)	25 mg Etomoxir, 737.9 µl DMSO (aliquoted and stored at -20°C)
Fixation Buffer	95% Ethanol, 5% Acetic Acid (stored at -20°C)
Formaldehyde Solution (4%)	10 ml DPBS (1x), 30 ml Formaldehyde Solution (16%; Methanol-free)
Glucose (450 g/l)	90 g Glucose, 200 ml DPBS (1x) (aliquoted and stored at -20°C)
Goat Serum (5%)	10 ml Goat Serum, 200 ml Triton Solution (0.1%) (aliquoted and stored at -20°C)
GST Buffer (Stock)	20 mM Tris/HCl (pH 7.4), 150 mM NaCl, add 1 l Millipore H_2O (autoclaved)
GST Buffer	10 ml GST Buffer (Stock), 0.1 ml Phosphatase Inhibitor Cocktail 2, 0.1 ml PMSF (100 mM), 1x miniEDTA-free-tablet (freshly prepared)
Insulin-Transferrin-Sodium Selenite (ITS; 100x)	dissolved in 50 ml dH_2O (aliquots: 1ml; stored at -20°C)
Krebs-Henseleit Buffer (KHB; pH 7.4, 5x)	32.532 g NaCl, 1.752 g KCl, 1.204 g $MgSO_4$, 0.852 g Na_2HPO_4, add 1 l Millipore H_2O (filter-sterilized and stored at 4°C)
KHB Assay Medium (pH 7.4, 1x)	10 ml KHB (5x), 40 ml dH_2O, 50 µl Glucose (450 g/l), 500 µl Carnitine (50 mM) (filter-sterilized and used at the same day)
LB-Agar	40 g LB-Agar (Luria/Miller; 10 g/l tryptone, 5 g/l yeast extract, 10 g/l NaCl, 15 g/l agar-agar), 1 l Millipore H_2O (autoclaved and handwarm liquid supplemented with antibiotic poured on petri dishes)

LB-Medium	25 g LB-Medium (Luria/Miller; 10 g/l tryptone, 5 g/l yeast extract, 10 g/l NaCl), 1 l Millipore H_2O (autoclaved)
Milk (5%)	5% Skim Milk Powder, 95% PBS (1x) (stored at 4°C)
Milk/Goat Serum/Avidin	1 ml Milk (5%), 100 µl Goat Serum, 4 drops Avidin (Blocking Kit)
Milk/Goat Serum/Biotin	1 ml Milk (5%), 100 µl Goat Serum, 4 drops Biotin (Blocking Kit)
MOPS-Buffer (10x, pH 7.0)	200 mM 3-(N-morpholino)propanesulfonic acid (MOPS), 50 mM NaAc, 10 mM EDTA
Orange G Loading Dye (6x)	70% Glycerol, 10 mM EDTA, 1 mg/ml Orange G
Paraformaldehyde (4%)	4 g Paraformaldehyde, 100 ml PBS (1x), 50 µl NaOH (1 M) (heated up to 70°C to bring in solution; stored at 4°C)
PBS (1x, pH 6.8)	137 mM NaCl, 2 mM KH_2PO_4, 10 mM Na_2HPO_4, 2.7 mM KCl
Plating Medium (for 1 heart)	42.5 ml MEM/HBSS Medium, 0.5 ml 200 mM Glutamine, 0.5 ml PenStrep, 5 ml FBS, 1 ml 0.5 M BDM and 0.5 ml 200 mM Na-ATP
PMSF (100 mM)	870.95 mg PMSF, 50 ml Isopropanol (filter-sterilized)
Proteinase K Buffer	50 mM Tris/HCl (pH 8.0), 100 mM EDTA (pH 8.0), 100 mM NaCl, 1% SDS (autoclaved)
RNA Sample Buffer (10x)	0.5 µl Ethidium Bromide, 0.5 µl Mops-Buffer (10x), 5.0 µl Formamide, 1.75 µl Formaldehyde, 1.7 µl 6x Loading Dye, 0.55 µl dH_2O
SDS Loading Dye (5x)	250 mM Tris/HCl (pH 6.8), 0.5 M DTT (AppliChem), 10% SDS, 1 mg/ml Bromophenol Blue, 50% Glycerol
SDS Running Buffer (1x)	200 mM Glycine, 25mM Trizma® Base, 0.1% SDS
SDS Transfer Buffer (1x)	25 mM Trizma® Base, 192mM Glycine, 20% Methanol, 0.01% SDS
Seahorse Assay Medium (Stock, pH 7.4)	8.3 g DMEM (Sigma Aldrich), 1 l dH_2O, 10 ml Glutamine (100x) (filter-sterilized and stored at 4°C)
Seahorse Assay Medium (pH 7.4)	50 ml Seahorse Assay Medium (Stock), 500 µl Glucose (450 g/l), 500 µl Pyruvate (100x) (filter-sterilized and stored at 4°C)
SILAC Medium	DMEM (non-GMP formulation w/o met, arg and lys), 10% FBS (dialyzed), 4 mM L-Glutamine, 100 mg/l Primocin™ (stored at 4°C)
Sodium-ATP (Na-ATP)	44 mg in 4 ml dH_2O (aliquots: 0.5 ml; stored at -20°C)

Sodium Chloride (150 mM)	9 ml 5 M NaCl, 291 ml dH_2O
Sodium Chloride (5 M)	146.1 g NaCl, 500 ml Millipore H_2O (autoclaved)
Sodium Hydroxide (1 M)	19.99 g NaOH, 500 ml Millipore H_2O (autoclaved)
Stopping Buffer I (for 1 heart)	2.25 ml Tyrode's Solution, 250 µl FBS, 3.125 ml 10 mM $CaCl_2$
Stopping Buffer II (for 1 heart)	23.75 ml Tyrode's Solution, 1.25 ml FBS
Sulforhodamine B (SRB) Solution	0.4% Sulforhodamine B Sodium Salt, 1% Acetic Acid, 98.6% Millipore H_2O (stored at room temperature protected from light)
Tris-Borat-EDTA (TBE) Buffer (1x, pH 8.0)	45 mM Trizma® Base, 45 mM Boric Acid, 1 mM EDTA
TBS Buffer (10x, pH 7.6)	24.2 g Trizma® Base, 80 g NaCl, 1 l Millipore H_2O
Tris Buffer (0.1 M, pH 10.4)	12.1 g Trizma® Base, 1 l Millipore H_2O (autoclaved)
Tris/HCl (10 mM, pH 8.0)	1.21 g Trizma® Base, 1 l Millipore H_2O (autoclaved)
Triton Solution (0.05%)	0.15 ml Triton™ X-100, 300 ml DPBS (1x)
Triton Solution (0.1%)	0.5 ml Triton™ X-100, 500 ml DPBS (1x)
Triton Solution (0.3%)	1.5 ml Triton™ X-100, 500 ml DPBS (1x)
TX Lysis Buffer	150 mM NaCl, 0.05% Triton™ X-100, 10 mM Tris/HCl (pH 8.0), 1x Protease Inhibitor Cocktail
Urea Buffer (5%)	5 g Urea, 100 ml Tris Buffer (0.1 M, pH 10.4) (prepared freshly)
Wash Solution	1% Acetic Acid, 99% Millipore H_2O

5.5 Chemicals and Reagents

Chemical/Reagent	Distributor
ABC-Reagent	Fisher Scientific, Schwerte
Acetic Acid, purum ≥ 99%	Sigma Aldrich®, Munich
L-Acidohomoalanine (AHA)	AnaSpec, Fremont (CA, USA)
Agarose	Carl Roth®, Karlsruhe
L-Arginine [$^{13}C_6$]	Cambridge Isotope Laboratories, Tewksbury (MA, USA)

L-Arginine [$^{13}C_6$, $^{15}N_4$]	Cambridge Isotope Laboratories, Tewksbury (MA, USA)
Albumin from Bovine Serum (BSA), Fatty Acid free	Sigma Aldrich®, Munich
Albumin from Bovine Serum (BSA), Fraction V	Merck Millipore, Darmstadt
Ammonium Persulfate (APS)	Carl Roth®, Karlsruhe
Ampicillin	Sigma Aldrich®, Munich
Antibody Diluent	Dako, Hamburg
Bis(2-hydroxyethyl)-2-aminoethanesulfonic acid (BES)	Sigma Aldrich®, Munich
Bisacrylamide (30%)	Carl Roth®, Karlsruhe
Boric Acid	Sigma Aldrich®, Munich
Bouin's Solution	Sigma Aldrich®, Munich
Bromophenol Blue	Sigma Aldrich®, Munich
2,3-Butanedionemonoxime (BDM)	Sigma Aldrich®, Munich
Calciumchloride ($CaCl_2$)	AppliChem, Darmstadt
L-Carnitine	Sigma Aldrich®, Munich
Chloroform	Carl Roth®, Karlsruhe
DMEM, High Glucose, Pyruvate	Life Technologies™, Darmstadt
DMEM, non-GMP formulation	Life Technologies™, Darmstadt
DMEM, Powder	Sigma Aldrich®, Munich
Difco™ Gelatin	BD, Heidelberg
Dimethylsulfoxid (DMSO)	Sigma Aldrich®, Munich
Distilled Water (dH_2O), RNase/DNase free	Life Technologies™, Darmstadt
Dithiothreitol (DTT)	AppliChem, Darmstadt
Dithiothreitol (DTT)	BioRad, Munich
Dulbecco's Phosphate-Buffered Saline (DPBS; 1x)	Life Technologies™, Darmstadt
Eosin G	Carl Roth®, Karlsruhe
Ethanol, absolute	Sigma Aldrich®, Munich
Ethidium Bromide Solution (10 mg/ml)	Carl Roth®, Karlsruhe
Ethylenediaminetetraacetic Acid (EDTA)	Sigma Aldrich®, Munich
(+)-Etomoxir Sodium Salt Hydrate	Sigma Aldrich®, Munich
Eukitt®	Sigma Aldrich®, Munich
Fetal Bovine Serum (FBS)	Life Technologies™, Darmstadt
Fetal Bovine Serum (dialyzed)	Life Technologies™, Darmstadt
FluorSave™ Reagent	Merck Millipore, Darmstadt
Formaldehyde Solution (16%), Methanol-free	Sigma Aldrich®, Munich
Formaldehyde	Th. Geyer, Renningen
Formamide	Merck Millipore, Darmstadt
GeneRuler™ 1kb DNA Ladder	Thermo Scientific™, Ulm
D-(+)-Glucose (anhydrous)	Sigma Aldrich®, Munich
L-Glutamine (100x)	Life Technologies™, Darmstadt
Glycerol	Sigma Aldrich®, Munich
Glycine	Sigma Aldrich®, Munich
Goat IgG	Sigma Aldrich®, Munich
Goat Serum	Sigma Aldrich®, Munich

Hair removing cream (without perfume)	Veet®, Mannheim
HCl-Alkohol (3%)	Carl Roth®, Karlsruhe
Hematoxylin	Dako, Hamburg
Hematoxylin Solution Meyer's	Sigma Aldrich®, Munich
HEPES	Sigma Aldrich®, Munich
HiPerFect Transfection Reagent	Qiagen, Hilden
Hoechst 33258 (10 mg/ml)	Dianova, Hamburg
Hydrogen Peroxide (30%)	Carl Roth®, Karlsruhe
Hydrochloric Acid (HCl)	Carl Roth®, Karlsruhe
Igepal® CO-520	Sigma Aldrich®, Munich
Immobiline DryStrips (pH 3 - 10 nonlinear, 13 cm)	GE Healthcare, Freiburg
Insulin-Transferrin-Sodium Selenite (ITS)	Sigma Aldrich®, Munich
Iodoacetamide	BioRad, Munich
Isoflurane	Baxter, Unterschleißheim
Isopropanol/2-Propanol	Sigma Aldrich®, Munich
LB-Agar (Luria/Miller)	Carl Roth®, Karlsruhe
LB-Medium (Luria/Miller)	Carl Roth®, Karlsruhe
Liberase 1	Roche, Mannheim
Loading Dye (6x)	Thermo Scientific™, Ulm
L-Lysine [$^{13}C_6$, $^{15}N_2$]	Cambridge Isotope Laboratories, Tewksbury (MA, USA)
L-Lysine [4,4,5,5-D_4]	Cambridge Isotope Laboratories, Tewksbury (MA, USA)
Magnesium Chloride ($MgCl_2$, 25 mM)	Thermo Scientific™, Ulm
Magnesium Sulfate ($MgSO_4$)	AppliChem, Darmstadt
Methanol	Sigma Aldrich®, Munich
MEM/HBSS	Life Technologies™, Darmstadt
miniEDTA-free Protease Inhibitor Cocktail Tablet	Roche, Mannheim
3-(N-morpholino)propanesulfonic acid (MOPS)	Carl Roth®, Karlsruhe
Orange G	Sigma Aldrich®, Munich
PageRuler™ Prestained Protein Ladder	Thermo Scientific™, Ulm
Pancreatin	Sigma Aldrich®, Munich
Paraformaldehyde	Carl Roth®, Karlsruhe
PCR-Master Mix (2x)	Thermo Scientific™, Ulm
Penicillin-Streptomycin (PenStrep)	Life Technologies™, Darmstadt
Phalloidin-Tetramethylrhodamine B isothiocyanate (TRITC)	Sigma Aldrich®, Munich
Phenylmethanesulfonyl Fluoride (PMSF)	Sigma Aldrich®, Munich
Ponceau S Solution	Sigma Aldrich®, Munich
Phosphatase Inhibitor Cocktail 2 (100x)	Sigma Aldrich®, Munich
Potassium Chloride (KCl)	Carl Roth®, Karlsruhe
Potassium Hydrogen Carbonate (KH_2CO_3)	Sigma Aldrich®, Munich
Potassium Hydrogen Phosphate (KH_2PO_4)	Carl Roth®, Karlsruhe
Primocin™	InvivoGen, San Diego (CA, USA)
Protease Inhibitor Cocktail (50x)	Sigma Aldrich®, Munich
Proteinase K (20.2 mg/ml)	Thermo Scientific™, Ulm

QIAzol® Lysis Reagent	Qiagen, Hilden
Sep-Pak® C18 1 cc Vac Cartridges (50 mg)	Waters, Eschborn
Skim Milk Powder	GERBU Biotechnik, Heidelberg
Sodium Acetate (NaAc)	AppliChem, Darmstadt
Sodium ATP (Na-ATP)	Sigma-Aldrich®, Munich
Sodium Chloride (NaCl)	Sigma Aldrich®, Munich
Sodium Dodecyl Sulfate (SDS)	Sigma Aldrich®, Munich
Sodium Deoxycholate	Sigma Aldrich®, Munich
Sodium Hydrogen Carbonate (Na_2HCO_3)	Sigma Aldrich®, Munich
Sodium Hydrogen Phosphate (Na_2HPO_4)	Sigma Aldrich®, Munich
Sodium Hydroxide (NaOH)	Sigma Aldrich®, Munich
Sodium Pyruvate (100x)	Life Technologies™, Darmstadt
Sodium Palmitate	Sigma Aldrich®, Munich
Streptavidin-Phycoerytherin (Molecular Probes®)	Life Technologies™, Darmstadt
Sulforhodamine B Sodium Salt	Sigma Aldrich®, Munich
SuperScript® Choice System	Life Technologies™, Darmstadt
Taurine	Sigma Aldrich®, Munich
TaqMan® Gene Expression Master Mix	Life Technologies™, Darmstadt
Tetramethylethylendiamin (TEMED)	Carl Roth®, Karlsruhe
Triton™ X-100	AppliChem, Darmstadt
Trizma® Base	Sigma Aldrich®, Munich
Trypan Blue Stain (0.4%)	Life Technologies™, Darmstadt
Trypsin	Promega, Mannheim
Trypsin-EDTA, 0.25% (1x)	Life Technologies™, Darmstadt
Tween® 20	Sigma Aldrich®, Munich
Urea	Sigma Aldrich®, Munich
Weigert's Hematoxylin Stock Solution A	Carl Roth®, Karlsruhe
Weigert's Hematoxylin Stock Solution B	Carl Roth®, Karlsruhe
XF Calibrant Buffer	Seahorse Bioscience, Copenhagen (DK)
Xylol	Merck Millipore, Darmstadt

5.6 Cells

Cell Type	**Origin**
Colon26 (C26)	Tumor Bank DKFZ, Heidelberg
HEK293A	ATCC, Manassas (VA, USA)
MC38	Clinical Pharmacology, Munich
One Shot® TOP10 Chemically Competent *E.coli*	Life Technologies™, Darmstadt

5.7 Consumables

Consumable	**Distributor**
8-Channel Aspirator Adaptor	Neolab, Heidelberg
6-Well Multiwell Cell Culture Plate	BD, Heidelberg
6-Well Multiwell Cell Culture Plate (Laminin coated)	BD, Heidelberg

24-Well Multiwell Cell Culture Plate	BD, Heidelberg
384-Well Microwell Cell Culture Plate	BD, Heidelberg
Amicon Ultra® Centrifugal Filters (Cut-off 3 kDa)	Merck Millipore, Darmstadt
Axygen® Wide Bore Tips (200 µl)	Corning Inc., Tewksbury (MA, USA)
BD Precisionglide® Syringe Needles (27 G)	Sigma Aldrich®, Darmstadt
Bottle-Top Vacuum Filter System (0.22 µm)	Corning Inc., Tewksbury (MA, USA)
Cell culture plate (10 and 15 cm)	BD, Heidelberg
Cell Scraper	Corning Inc., Tewksbury (MA, USA)
Centrifuge Tube (15 and 50 ml)	BD, Heidelberg
Centrifuge Tube, RNase/DNase free (15 and 50 ml)	TPP, Trasadingen (CH)
CHROMA SPIN™-100 columns	Clontech, Mountain View (CA, USA)
Combitips Advanced® (0.5, 5 and 10 ml)	Eppendorf, Hamburg
Countess® Cell Counting Chamber slide	Life Technologies™, Darmstadt
Cryogenic Vials (1.8 ml)	Starlab, Hamburg
Cover Slips (Ø 12 mm)	Menzel, Braunschweig
Cover Slips (24 x 60 mm)	Menzel, Braunschweig
Disposal Bags	Carl Roth®, Karlsruhe
Disposable Scalpels	Feather, Cuome (JP)
Dounce Homogenizer (7 ml)	Kimble-Chase, Meiningen
Folded Filters	Munktell & Filtrak, Bärenstein
Freestanding Mailing Tube with Cap (5 ml)	VWR, Darmstadt
Freezing Container, Nalgene® Mr. Frosty	Thermo Scientific™, Ulm
Gas	Camping Gaz, Hungen
Gel Staining Boxes (Mini)	Carl Roth®, Karlsruhe
Glass Vials (4 ml)	Sigma Aldrich®, Munich
Gloves (Gentle Skin)	Meditrade, Kiefersfelden
Gloves (Nitrile)	Microflex, Reno (NV, USA)
MicroAmp® Optical Adhesive Film	Life Technologies™, Darmstadt
MicroAmp® Optical 96-Well Reaction Plate	Life Technologies™, Darmstadt
Microscope Slides	Thermo Scientific™, Ulm
Millex® Syringe Filter (0.22 µm)	Merck Millipore, Darmstadt
Millex® Syringe Filter (0.45 µm)	Merck Millipore, Darmstadt
MiniCollect® EDTA Tube	Greiner Bio-One, Frickenhausen
Mini Trans-Blot® Module	BioRad, Munich
Mµlti® Safe Seal Reaction Tubes, RNase/DNase free	Carl Roth®, Karlsruhe
nanoAcquity BEH C18 (1.7 µm, 75 µm x 200 mm)	Waters, Eschborn
nanoAcquity Symmetry C18 (5 µm, 180 µm x 20 mm)	Waters, Eschborn
Nitrocellulose Membrane	GE Healthcare, Freiburg
Nunc® MicroWell™ 96-Well	Thermo Scientific™, Ulm
Parafilm® M	Bemis®, Oshkosh (WI, USA)
Pasteur Pipettes (Glass)	Brand, Wertheim
PCR Tubes (200 µl)	Kisker, Steinfurt
Petri Dishes	Greiner Bio-One, Frickenhausen
Pipette Tips, TipTower (200 and 1000 µl)	Steinbrenner, Wiesenbach
Pipette Tips for Liquidator96® (200 µl)	Mettler-Toledo, Gießen
Pocket Thermometer	Neolab, Heidelberg

PicoTip™ Emitter	New Objective, Woburn (MA, USA)
Prot/Elec™ Tips (200 µl)	BioRad, Munich
Rotilabo® Reaction Tubes Black	Carl Roth®, Karlsruhe
Safe-Lock Tubes (1.5, 2 and 5 ml)	Eppendorf, Hamburg
Screw cap (green melamine) for 4 ml glass vial	Sigma Aldrich®, Munich
Serological pipettes (5, 10, 25 and 50 ml)	BD, Heidelberg
Stainless Steel Beads (5 mm)	Qiagen, Hilden
SuperFrost® Plus Microscope Slide	VWR, Darmstadt
SOFT-JECT® Tuberculin Syringe (1 ml)	Henke Sass Wolf, Tuttlingen
3-Part Syringes, Luer-Lock (10 and 50 ml)	Terumo, Eschborn
TipOne® Filter Tips (10, 20, 100, 200 and 1000 µl)	Starlab, Hamburg
TipOne® Pipette Tips (10 µl)	Starlab, Hamburg
Tissue-Tek® Mega-Cassette®	Sakura, Staufen
Weigh Boats	Neolab, Heidelberg
Whatman Paper	GE Healthcare, Freiburg
XF96 FluxPak	Seahorse Bioscience, Copenhagen (DK)
XF96 Polystyrene (PS) Cell Culture Microplate	Seahorse Bioscience, Copenhagen (DK)

5.8 Kits

Kit	Distributor
BioArray HighYield® RNA Transcript Labeling Kit	Enzo® Life Science, Lörrach
Blocking Kit (Avidin/Biotin)	Biozol, Eching
Click-iT® Protein Enrichment Kit	Life Technologies™, Darmstadt
ECL™ Western Blotting Detection Reagents	GE Healthcare, Freiburg
First Strand cDNA Synthesis Kit	Thermo Scientific™, Ulm
GeneChip® Mouse Genome 430 2.0 array	Affymetrix®, Santa Clara (CA, USA)
Mouse Ataxin-10 ELISA Kit	Uscn Life Science, Wuhan (CN)
Mouse Gaa ELISA Kit	Uscn Life Science, Wuhan (CN)
Pierce® BCA Protein Assay Kit	Thermo Scientific™, Ulm
PureLink® HiPure Plasmid Midiprep Kit	Life Technologies™, Darmstadt
RayBio® Mouse MCP-1 ELISA Kit	RayBiotech, Norcross (GA, USA)
RNeasy® Micro Kit	Qiagen, Hilden
RNeasy® Mini Kit	Qiagen, Hilden
SIGMAFAST™ 3,3'-Diaminobenzidine (DAB) tablets	Sigma Aldrich®, Munich
Serum Triglyceride Determination Kit	Sigma Aldrich®, Munich
Trichrome Stain (Masson) Kit	Sigma Aldrich®, Munich
XF Cell Mito Stress Test Kit	Seahorse Bioscience, Copenhagen (DK)

5.9 Instruments

Instrument	Distributor
ADVantage PV System	Scisense Inc., Ontario (CN)
Agilent 3100 OFFGEL Fractionator	Agilent Technologies, Waldbronn
Analytical Balance (Summit S-203)	Denver Instrument, Bohemia (NY, USA)

Analytical Balance	Sartorius, Göttingen
Bacterial Shaker (Multitron Standard)	Infors HT, Böttmingen (CH)
BD Pathway 855 Cellular Bioimaging System	BD, Heidelberg
BioRuptor®	Diagenode, Denville (NJ, USA)
Catheter (1.2 FR; model: FT111B)	Scisense Inc., Ontario (CN)
CC-12 camera	Olympus Soft Imaging Solutions, Münster
Centrifuge (Biofugo Fresco)	Thermo Scientific™, Ulm
Centrifuge (Biofuge Pico)	Heraeus, Heilbronn
Centrifuge (Biofuge Primo)	Heraeus, Heilbronn
Centrifuge (Function Line)	Heraeus, Heilbronn
Centrifuge (Multifuge™ X3R)	Thermo Scientific™, Ulm
ChemiDoc™ XRS+ System	BioRad, Munich
CO_2-Incubator	Sanyo, Munich
Countess® Automated Cell Counter	Life Technologies™, Darmstadt
Digital Caliper	Bochem Instruments, Weilburg
Echocardiogram Sonos 5500	Philips Healthcare, Eindhoven (NL)
EchoMRI™	Echo Medical Systems, Houston (TX, USA)
Electrophoresis Chamber	Steinbrenner, Wiesenbach
Freezer (-20°C)	Liebherr, Biberach
Freezer (-80°C)	Sanyo, Munich
Fridge (4°C)	Liebherr, Biberach
Gas Stove (GASI)	Schütt, Göttingen
Gel Imager	Intas, Göttingen
GeneChip® Fluidics Station 450	Affymetrix®, Santa Clara (CA, USA)
GeneChip® Scanner	Affymetrix®, Santa Clara (CA, USA)
Hamamatsu ORCA-ER Digital Camera	Hamamatsu Photonics, Herrsching am Ammersee
Homoeothermic Blanket	Harvard Apparatus, Edenbridge (UK)
Horizontal Shaker (Duomax 1030)	Heidolph, Schwabach
Incubator (Function Line)	Hereaus, Heilbronn
Liquidator96®	Mettler-Toledo, Gießen
LTQ Orbitrap Velos (pro)	Thermo Scientific™, Ulm
Magnetic Stirrer	Carl Roth®, Karlsruhe
Magnetic Stirrer/Hotplate (MR Hei-Standard)	Heidolph, Schwabach
Magnetic Stirrer/Hotplate	VWR, Darmstadt
Microscope (Axio Vert 40 CFL)	Zeiss, Göttingen
Microscope (Axio Imager M2)	Zeiss, Göttingen
Microscope (BX51)	Olympus, Hamburg
Microtome (RM2245)	Leica, Wetzlar
Microwave	Bosch, Stuttgart
Millipore Water System (X-Cad)	TKA, Niederelbert
Mini-PROTEAN® Tetra Cell	BioRad, Munich
Mouse Cage (H-TEMP™, 335 cm^2)	Tecniplast, Hohenpeißenberg
Multichannel Pipette (Acura® manual 855; 200 µl)	Socorex, Ecublens (CH)
Multimode Microplate Reader (Mithras LB 940)	Berthold, Bad Wildbad
Multipette®	Eppendorf, Hamburg

nanoAcquity UPLC System	Waters, Eschborn
Nitrogen Tank	Thermo Electron Corp., Erlangen
pH-Meter	VWR, Darmstadt
Pipetboy acu	Integra, Fernwald
Pipettes (2, 10, 20, 100, 200 and 1000 µl)	Gilson, Middleton (WI, USA)
Pipettes (ErgoOne®; 2.5, 10, 20, 200 and 1000 µl)	Starlab, Hamburg
PowerPac™ Basis Power Supply	BioRad, Munich
PowerPac™ HC High-Current Power Supply	BioRad, Munich
Precision Balance	Kern®, Balingen
Precision Balance	Sartorius, Göttingen
Recorder (Scisense 404 - 16 Bit Four Channel)	Scisense Inc., Ontario (CN)
Rotating Wheel	Neolab, Heidelberg
Rotational-Vacuum-Concentrator (RVC 2-18 CD)	Christ, Osterode am Harz
StepOnePlus™ Real-Time PCR System	Life Technologies™, Darmstadt
Spectrophotometer (NanoDrop ND-1000)	Peqlab Biotechnology, Erlangen
Thermocycler (PTC-200)	Biozym, Oldendorf
Thermocycler (T300)	Biometra, Göttingen
Thermomixer (Comfort)	Eppendorf, Hamburg
Tissue Culture Hood	Integra, Fernwald
TissueLyser	Qiagen, Hilden
TissueLyser (MM 400)	Retsch, Haan
Titer Plate Shaker	Thermo Scientific™, Ulm
Ventilated Cabinet for Mouse Housing	Tecniplast, Hohenpeißenberg
Vortex Mixer (Vortex Genie)	Scientific Industries, Bohemia (NY, USA)
Water Bath	P-D Industrial Society, Dresden
Water Bath	Fried Electric, Haifa (IL)
XF96 Extracellular Flux Analyzer	Seahorse Bioscience, Copenhagen (DK)
XF Prep Station	Seahorse Bioscience, Copenhagen (DK)

5.10 Oligonucleotides

Oligonucleotide name	Sequence (5’ → 3’)	Origin
A011	GGC AGA TGT CTT TAT GAG	Thermo Scientific™, Ulm
A012	TAA GGG CTA ACA GTC AAT	Thermo Scientific™, Ulm

5.11 Ready-to-use cDNA expression plasmids

Item	Gene	Gene Description	Catalogue No.
1	Mmp9	Matrix metallopeptidase 9	EX-F0125-M02
2	Ccl5	Chemokine ligand 5	EX-I0332-M02
3	Ccl10	Chemokine ligand 10	EX-T7063-M02
4	Vegfc	Vascular endothelial growth factor c	EX-K2961-M02
5	Ccl2	Chemokine ligand 2	EX-Q0327-M02
6	Msn	Moesin	EX-D0144-M02
7	Ecm1	Extracellular matrix protein 1	EX-Q0384-M02

8	Ncam1	Neural cell adhesion molecule 1	EX-Z2645-M02
9	Nptx1	Neuronal pentraxin 1	EX-Y3530-M02
10	Gusb	Glucuronidase, beta	EX-C0063-M02
11	Htra1	HtrA serine peptidase 1	EX-M0558-M02
12	Edil3	EGF-like repeats and discoidin I-like domains 3	EX-M0086-M02
13	Stc2	Stanniocalcin 2	EX-S0039-M02
14	Fabp5	Fatty acid binding protein 5	EX-C0320-M02
15	Psap	Prosaposin	EX-C0110-M02
16	Vcam1	Vascular cell adhesion molecule 1	EX-Z0385-M02
17	Sema3c	Sema domain, immunoglobulin domain (Ig), short basic domain, secreted, (semaphorin) 3C	EX-M0195-M02
18	Lgals3bp	Lectin, galactoside-binding, soluble, 3 binding protein	EX-G0128-M02
19	Glb1	Galactosidase, beta 1	EX-M0629-M02
20	Ctsd	Cathepsin D	EX-F0069-M02
21	Adam15	ADAM metallopeptidase domain 15	EX-Q0369-M02
22	Gpnmb	Glycoprotein (transmembrane) nmb	EX-Z0500-M02
23	Dcn	Decorin	EX-D0091-M02
24	Hexa	Hexosaminidase A (alpha polypeptide)	EX-C0530-M02
25	Asah1	N-acylsphingosine amidohydrolase (acid ceramidase) 1	EX-T0113-M02
26	Tpp1	Tripeptidyl peptidase I	EX-Q0233-M02
27	Penk	Proenkephalin	EX-T1075-M02
28	Yars	Tyrosyl-tRNA synthetase	EX-N0050-M02
29	B2m	Beta-2-microglobulin	EX-I0035-M02
30	Ifi30	Interferon, gamma-inducible protein 30	EX-T4092-M02
31	Thop1	Thimet oligopeptidase 1	EX-C0488-M02
32	Lgmn	Legumain	EX-Z5665-M02
33	Plat	Plasminogen activator, tissue	EX-F0362-M02
34	Tpi1	Triosephosphate isomerase 1	EX-M0690-M02
35	Tkt	Transketolase	EX-Z5808-M02
36	Cpe	Carboxypeptidase E	EX-F0192-M02
37	Fscn1	Fascin homolog 1, actin-bundling protein	EX-D0369-M02
38	Zyx	Zyxin	EX-M0938-M02
39	Clstn1	Calsyntenin 1	EX-Z0535-M02
40	Sdc4	Syndecan 4	EX-D0120-M02
41	Adsl	Adenylosuccinate lyase	EX-T1756-M02
42	Mif	Macrophage migration inhibitory factor (glycosylation-inhibiting factor)	EX-H0009-M02
43	Psmb1	Proteasome (prosome, macropain) subunit, beta type, 1	EX-F0271-M02
44	Efemp2	EGF-containing fibulin-like extracellular matrix protein 2	EX-U1326-M02
45	App	Amyloid beta (A4) precursor protein	EX-Z3473-M02
46	Psme1	Proteasome (prosome, macropain) activator subunit 1 (PA28 alpha)	EX-K2703-M02
47	Gapdh	Glyceraldehyde-3-phosphate dehydrogenase	EX-C0288-M02
48	Eif6	Eukaryotic translation initiation factor 6	EX-I0088-M02
49	Ywhaq	Tyrosine 3-monooxygenase/tryptophan 5-monooxygenase activation protein, theta polypeptide	EX-A0338-M02

50	Ctsa	Cathepsin A	EX-Z3990-M02
51	Larp1	La ribonucleoprotein domain family, member 1	EX-Z1281-M02
52	Cst6	Cystatin	EX-M0688-M02
53	Pcsk9	Proprotein convertase subtilisin/kexin type 9	EX-T5627-M02
54	Tfpi	Tissue factor pathway inhibitor	EX-Q0307-M02
55	Gns	Glucosamin-6-sulfatase	EX-C0159-M02
56	Fam3c	Family with sequence similarity 3, member c	EX-V1620-M02
57	Gaa	Glucosidase, alpha; acid	EX-C0162-M02
58	Scpep1	Serine carboxypeptidase 1	EX-T2071-M02
59	Plbd2	Phospholipase B domain containing 2	EX-T4420-M02
60	Sgsh	N-sulfoglucosamine sulfohydrolase	EX-S0223-M02
61	Hexb	Hexosaminidase B (beta polypeptide)	EX-C0537-M02
62	Lipa	Lipase A, lysosomal acid, cholesterol esterase	EX-C0313-M02
63	Csf1	Colony stimulating factor 1 (macrophage)	EX-Z2504-M02
64	Ctsb	Cathepsin B	EX-F0070-M02
65	Grn	Granulin	EX-Z0297-M02
66	Rnaset2	Ribonuclease T2	EX-U1296-M02
67	Mmp14	Matrix metallopeptidase 14 (membrane-inserted)	EX-M0327-M02
68	Sqstm1	Sequestosome 1	EX-T3003-M02
69	Slc39a6	Solute carrier family 39 (zinc transporter), member 6	EX-E0757-M02
70	Dpysl2	Dihydropyrimidinase-like 2	EX-M0208-M02
71	Cd44	CD44 molecule	EX-Z0381-M02
72	Col18a1	Collagen, type XVIII, alpha 1	EX-Z1437-M02
73	Ngf	Nerve growth factor (beta polypeptide)	EX-A0708-M02
74	Hspa13	Heat shock protein 70kDa family, member 13	EX-M0019-M02
75	Timp2	TIMP metallopeptidase inhibitor 2	EX-F0292-M02
76	Cpd	Carboxypeptidase D	EX-Y2014-M02
77	Rpl30	Ribosomal protein L30	EX-F0601-M02
78	Matn2	Matrilin 2	EX-Z0402-M02
79	B4galt1	UDP-Gal:betaGlcNAc beta 1,4- galactosyltransferase, polypeptide 1	EX-Z2282-M02
80	Trim25	Tripartite motif-containing 25	EX-S0327-M02
81	B4galt5	UDP-Gal:betaGlcNAc beta 1,4- galactosyltransferase, polypeptide 5	EX-M0023-M02
82	Chst14	Carbohydrate (N-acetylgalactosamine 4-0) sulfotransferase 14	EX-T3453-M02
83	Minpp1	Multiple inositol-polyphosphate phosphatase 1	EX-U1229-M02
84	Stx7	Syntaxin 7	EX-M0706-M02
85	Sdcbp	Syndecan binding protein (syntenin)	EX-I0049-M02
86	Eif3j	Eukaryotic translation initiation factor 3, subunit J	EX-T1044-M02
87	Bin1	Bridging integrator 1	EX-Z0298-M02
88	Ddb1	Damage-specific DNA binding protein 1, 127kDa	EX-M0025-M02
89	Gnptg	N-acetylglucosamine-1-phosphate transferase, gamma subunit	EX-W1028-M02
90	Col16a1	Collagen, type XVI, alpha 1	EX-H1797-M02

91	Atxn10	Ataxin 10	EX-J0088-M02
92	Mfge8	Milk fat globule -EGF factor 8 protein	EX-M0438-M02
93	Fbn1	Fibrillin 1	EX-Y3961-M02
94	Sub1	SUB1 homolog	EX-F0878-M02
95	Mmp2	Matrix metallopeptidase 2	EX-Z5731-M02
96	Cbr3	Carbonyl reductase 3	EX-S0239-M02
97	Hspa9	Heat shock 70kDa protein 9 (mortalin)	EX-T0379-M02
98	Prdx6	Peroxiredoxin 6	EX-G0222-M02
99	Uxs1	UDP-glucuronate decarboxylase 1	EX-Z1227-M02
100	Sf3b2	Splicing factor 3b, subunit 2, 145kDa	EX-Z4525-M02
101	Zc3hav1	Zinc finger CCCH-type, antiviral 1	EX-H0226-M02
102	Qsox1	Quiescin Q6 sulfhydryl oxidase 1	EX-Z0680-M02
103	Gapvd1	GTPase activating protein and VPS9 domains 1	EX-T4435-M02
104	Adamtsl4	Adamts like 4	EX-W0661-M02
105	Arsb	Arylsulfatase B	EX-C0073-M02
106	Cachd1	Cache domain containing 1	EX-W1988-M02
107	Pxdn	Peroxidasin homolog (Drosophila)	EX-H0186-M02
108	Gxylt1	Glucoside xylosyltransferase 1	EX-E0428-M02
109	Col8a1	Collagen, type VIII, alpha 1	EX-D0218-M02

Ready-to-use cDNA expression plasmids were obtained from Source BioScience (Nottingham, UK). All ORF clones are based on the human gene sequence and do not include any tag.

5.12 siRNAs

Gene	Accession No.	siRNA
Adamtsl4	NM_144899	Mm_Tsrc1_3 FlexiTube siRNA
Atxn10	NM_016843	Mm_Sca10_4 FlexiTube siRNA
Bin1	NM_001083334, NM_009668	Mm_Bin1_5 FlexiTube siRNA
Ccl2	NM_011333	Mm_Ccl2_3 FlexiTube siRNA
Gaa	NM_001159324, NM_008064	Mm_Gaa_4 FlexiTube siRNA
Minpp1	NM_010799	Mm_Minpp1_9 FlexiTube siRNA
Stx7	NM_016797	Mm_Stx7_7 FlexiTube siRNA
Negative Control		AllStars Negative Control (NC) siRNA
Transfection Control		AllStars NC siRNA Alexa Fluor 488

FlexiTube siRNAs directed against the indicated mouse gene were obtained from Qiagen (Hilden).

5.13 Taqman probes

5.13.1 Eurofins MWG

Gene	Species	Primer/Probe	Sequence
TBP	mouse	forward	TTG ACC TAA AGA CCA TTG CAC TTC
		reverse	TTC TCA TGA TGA CTG CAG AAA
		Probe	5’ FAM-TGC AAG AAA TGC TGA ATA TAA TCC CAA GCG-3’ TAMRA

5.13.2 Life Technologies

Gene	Species	Assay ID
Acadvl	mouse	Mm00444293_m1
Acadvl	rat	Rn00563649_m1
Acat2	mouse	Mm00448823_m1
Acat2	rat	Rn00596636_m1
Acsl1	mouse	Mm00484217_m1
Acsl1	rat	Rn00689077_m1
Adamtsl4	mouse	Mm00523242_m1
Anp	mouse	Mm01255748_g1
Ant1	mouse	Mm01207393_m1
Ant1	rat	Rn00821477_g1
Ant2	mouse	Mm00846873_g1
Ant2	rat	Rn00821585_g1
Atxn10	mouse	Mm00450332_m1
ATXN10	human	Hs01001869_m1
Atrogin-1	mouse	Mm00499518_m1
Bin1	mouse	Mm00437457_m1
Bnp	mouse	Mm00435304_g1
Ccl2	mouse	Mm00441242_m1
CD36	mouse	Mm00432403_m1
CD36	rat	Rn02115479_g1
Col1a2	mouse	Mm00483888_m1
Col3a1	mouse	Mm01254476_m1
Cpt1α	mouse	Mm00550438_m1
Cpt1α	rat	Rn00580702_m1
Dgat1	mouse	Mm00515643_m1
Dgat1	rat	Rn00584870_m1
Fatp4	mouse	Mm01327409_m1
Fatp4	rat	Rn01438951_m1
Fatp6	mouse	Mm01258609_m1
Fatp6	rat	Rn01491675_m1
Gaa	mouse	Mm00484581_m1
Glut1	mouse	Mm00441480_m1
Glut1	rat	Rn01417099_m1
Glut4	mouse	Mm00436615_m1
Glut4	rat	Rn01752377_m1
Hadha	mouse	Mm00805228_m1
Hadha	rat	Rn00590828_m1
Lpl	mouse	Mm00434770_m1
Lpl	rat	Rn00561482_m1
α-MHC	mouse	Mm00440359_m1
β-MHC	mouse	Mm00600555_m1
Minpp1	mouse	Mm00487691_m1
MuRF1	mouse	Mm01185222_m1

Postn	mouse	Mm00450111_m1
Stx7	mouse	Mm00444002_m1
TBP	rat	Rn01455646_m1
Ucp2	mouse	Mm00627599_m1
Ucp2	rat	Rn01754856_m1
Ucp3	mouse	Mm00494074_m1
Ucp3	rat	Rn00565874_m1
RNA 18S	all vertebrates	Hs99999901_s1

5.14 Software

Software	Distributor
analySIS	Soft Imaging Systems, Münster
AxioVision SE64 Rel 4.8	Zeiss, Göttingen
Biomedical Powerpoint Toolkit Suite	Motifolio, Ellicott City (MD, USA)
BLAST	http://ncbi.nlm.nih.gov
CellProfiler Cell Image Analysis Software	Broad Institute, Cambridge (MA, USA)
GraphPad Prism (Version 5.04)	GraphPad Software Inc., La Jolla (CA, USA)
GSEA	http://www.broadinstitute.org/gsea/
Illustrator	Adobe Systems, San Jose (CA, USA)
ImageJ	Wayne Rasband (NIH), Bethesda (MD, USA)
ImageLab	BioRad, Munich
KEGG	http://www.genome.jp/kegg/
LabScribe2 Software	Scisense Inc., Ontario (CN)
MaxQuant (Version 1.3.0.5)	MPI, Martinsried
MetaCore™	Thomson Reuters, New York (NY, USA)
Microsoft Office	Microsoft, Unterschleißheim
Photoshop	Adobe Systems, San Jose (CS, USA)
Pubmed	http://www.pubmedcentral.nih.gov
R/Bioconductor	Fred Hutchinson Cancer Research Center, Seattle (WA, USA)
SAS® JMP 7	SAS® Institute, Cary (NC, USA)
SecretomeP 2.0.	Center for Biological Sequence Analysis, Kemitorvet (Lyngby, DK)
SignalP 3.0.	Center for Biological Sequence Analysis, Kemitorvet (Lyngby, DK)
StepOnePlus™ System Software	Life Technologies™, Darmstadt
TMHMM 2.0.	Center for Biological Sequence Analysis, Kemitorvet (Lyngby, DK)
XF96 System Software	Seahorse Biosciences, Copenhagen (DK)

6 Appendices

6.1 Supplementary figures and tables

6.1.1 Enrichment analysis of C26 hearts

Annotation Cluster 1	Enrichment Score: 8.22					
	Term	Count	PValue	List total	Pop Hits	Pop Total	FDR
GO:0043436	Oxoacid metabolic process	47	$9.1x10^{-10}$	508	479	14,219	$1.6x10^{-6}$
GO:0019752	Carboxylic acid metabolic process	47	$9.1x10^{-10}$	508	479	14,219	$1.6x10^{-6}$
GO:0006082	Organic acid metabolic process	47	$9.6x10^{-10}$	508	480	14,219	$1.7x10^{-6}$
GO:0032787	Monocarboxylic acid metabolic process	33	$2.0x10^{-9}$	508	268	14,219	$3.6x10^{-6}$
GO:0042180	Cellular ketone metabolic process	47	$2.0x10^{-9}$	508	491	14,219	$3.6x10^{-6}$
GO:0006631	Fatty acid metabolic process	25	$4.0x10^{-8}$	508	184	14,219	$6.9x10^{-5}$
GO:0006629	Lipid metabolic process	55	$5.7x10^{-8}$	508	696	14,219	$1.0x10^{-4}$
GO:0044255	Cellular lipid metabolic process	42	$2.3x10^{-7}$	508	482	14,219	$4.0x10^{-4}$

Annotation Cluster 6	Enrichment Score: 1.89						
	Term	Count	PValue	List Total	Pop Hits	Pop Total	FDR
GO:0015718	Monocarboxylic acid transport	6	0.0004	508	19	14,219	0.76
GO:0046942	Carboxylic acid transport	11	0.003	508	99	14,219	4.74
GO:0015849	Organic acid transport	11	0.003	508	100	14,219	5.01
GO:0015908	Fatty acid transport	4	0.01	508	13	14,219	16.00
GO:0015909	Long-chain fatty acid transport	3	0.02	508	7	14,219	34.27
GO:0015804	Neutral amino acid transport	3	0.08	508	13	14,219	75.15
GO:0006865	Amino acid transport	6	0.11	508	71	14,219	86.75
GO:0015837	Amine transport	7	0.11	508	92	14,219	87.12

Annotation Cluster 7	Enrichment Score: 1.85						
	Term	Count	PValue	List Total	Pop Hits	Pop Total	FDR
GO:0010876	Lipid localization	13	0.002	508	128	14,219	3.56
GO:0006869	Lipid transport	12	0.003	508	119	14,219	5.94
GO:0033036	Macromolecule localization	35	0.40	508	902	14,219	99.99

Annotation Cluster 10	Enrichment Score: 1.77						
	Term	Count	PValue	List Total	Pop Hits	Pop Total	FDR
GO:0033559	Unsaturated fatty acid metabolic process	8	0.0002	508	36	14,219	0,42
GO:0006690	Icosanoid metabolic process	7	0,001	508	34	14,219	1,99
GO:0008610	Lipid biosynthetic process	20	0,007	508	285	14,219	11,29
GO:0006633	Fatty acid biosynthetic process	9	0,008	508	81	14,219	13,35
GO:0006692	Prostanoid metabolic process	4	0,01	508	14	14,219	19,40
GO:0006693	Prostaglandin metabolic process	4	0,01	508	14	14,219	19,40
GO:0046456	Icosanoid biosynthetic process	5	0,01	508	27	14,219	22,75
GO:0006636	Unsaturated fatty acid biosynthetic process	5	0,02	508	28	14,219	25,41
GO:0046394	Carboxylic acid biosynthetic process	11	0,03	508	141	14,219	40,85
GO:0016053	Organic acid biosynthetic process	11	0,03	508	141	14,219	40,85
GO:0043450	Alkene biosynthetic process	3	0,12	508	17	14,219	89,66
GO:0019370	Leukotriene biosynthetic process	3	0,12	508	17	14,219	89,66
GO:0006691	Leukotriene metabolic process	3	0,15	508	19	14,219	93,69
GO:0043449	Cellular alkene metabolic process	3	0,17	508	21	14,219	96,28

***Tab. 15: Gene ontology enrichment analysis of biological processes (GO-BP) from hearts of C26 mice**. Analyzed samples were from C26 mice which were sacrificed two weeks after tumor cell injection and developed cachexia. Enrichment score: measure of pathway cluster enrichment over the other clusters; count: number of regulated genes within the pathway; p-value: significance of pathway enrichment; list total: number of genes within the analyzed list of target genes having at least one GO-BP annotation; pop hits: number of genes available on the entire microarray, annotated by the considered GO-BP category or annotation cluster; pop total: number of genes available on the entire microarray and having at least one GO-BP annotation; FDR: false discovery rate.*

6.1.2 KEGG Fatty acid metabolism pathways of C26-treated primary adult mouse cardiomyocytes

Gene ID	Gene Symbol	Gene Name	-log10(p-value) for Diff. of Experiment = (T) - (C)
11370	Acadvl	Acyl-CoA dehydrogenase, very long chain	2.41 (↓)
15107	Hadh	Hydroxyacyl-CoA dehydrogenase	2.49 (↓)
11522	Adh1	Alcohol dehydrogenase 1 (class I)	2.50 (↓)
97212	Hadha	Hydroxyacyl-CoA dehydrogenase/3-ketoacyl-CoA thiolase/enoyl-CoA hydratase (trifunctional protein), alpha subunit	3.64 (↓)
270076	Gcdh	Glutaryl-CoA dehydrogenase	2.25 (↓)
56752	Aldh9a1	Aldehyde dehydrogenase 9, subfamily A1	2.77 (↓)
14081	Acsl1	Acyl-CoA synthetase long-chain family member 1	4.58 (↓)
13177	Dci	Dodecenoyl-CoA delta isomerase	2.10 (↓)
110460	Acat2	Acetyl-CoA acetyltransferase 2	2.48 (↓)
11364	Acadm	Acyl-CoA dehydrogenase, medium chain	2.65 (↓)
216739	Acsl6	Acyl-CoA synthetase long-chain family member 6	2.34 (↓)
11671	Aldh3a2	Aldehyde dehydrogenase family 3, subfamily A2	2.00 (↑)

Tab. 16: Genes that were significantly regulated within the KEGG fatty acid metabolism pathway (mmu00071) in primary mouse cardiomyocytes treated with C26-conditioned medium. *Primary adult mouse cardiomyocytes were plated at 50,000 rod-shaped myocytes/well on laminin-coated 6-well plates. After 1 h plating medium was removed and cardiomyocytes were treated with conditioned medium from C26 cells (T) or normal cardiomyocyte culture medium (C; untreated) for 48 h. Genes that were further validated are highlighted in black. The p-value represents the significance of pathway enrichment. The arrows indicate whether a gene was up- or downregulated in the C26-treated cardiomyocytes.*

6.1.3 Primary cardiomyocytes treated with C26 mouse serum

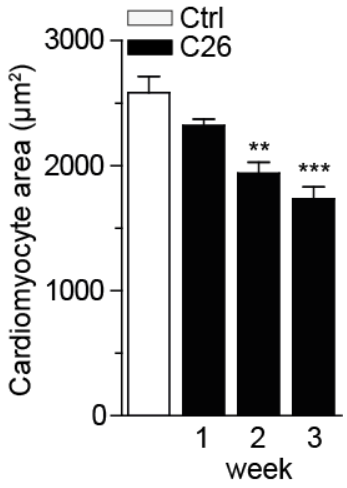

Fig. 46: Treatment of primary neonatal rat cardiomyocytes with 2% C26 mouse serum induced atrophy. *Primary neonatal rat cardiomyocytes were seeded at 1.0 x 10^5 cells per well on cover slips in 24-well plates which were coated with 0.1% gelatin. Three days after seeding the cardiomyocytes were cultured in DMEM containing 2% C26 mouse serum, 8% Fetal bovine serum (FBS) and 1% Penicillin-Streptomycin (Penstrep) for 24 h. Afterwards, cardiomyocytes were stained for α-actinin to determine the cardiomyocyte area. n ≥ 100, mean ± SEM. *indicates significance using 2-way ANOVA, Bonferroni post-test, **p < 0.01, ***p < 0.001.*

6.1.4 Seahorse Mito Stress Assay

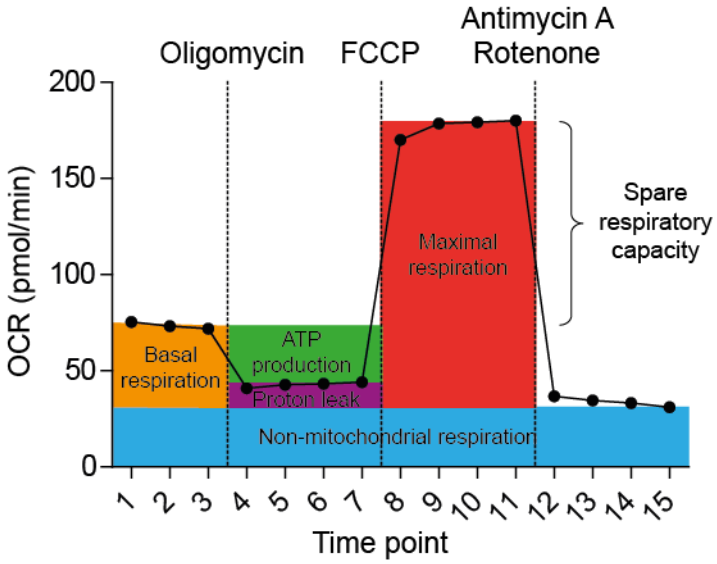

Fig. 47: Fundamental parameters of the Seahorse Mito Stress Assay. *Mitochondrial function is assessed by the oxygen consumption rate (OCR). Oligomycin inhibits adenosine triphosphat (ATP) synthase by blocking the proton channel which results in reduced oxidative phosphorylation of adenosine diphosphat (ADP) to ATP. Oligomycin will not completely block the electron flow because proton leakage/mitochondrial uncoupling will still occur. Carbonyl cyanide 4-(trifluoromethoxy) phenylhydrazone (FCCP) induces increased uncoupling by disrupting the ATP synthesis by transporting hydrogen ions through the inner mitochondrial membrane before they can be used for the oxidative phosphorylation. Antimycin A and rotenone interfere with the electron transport chain, thereby blocking the formation of the proton gradient across the inner mitochondrial membrane. Consequently, production of ATP is inhibited which results in a complete blockage of mitochondrial function.*

6.1.5 Quantitative secretome analysis

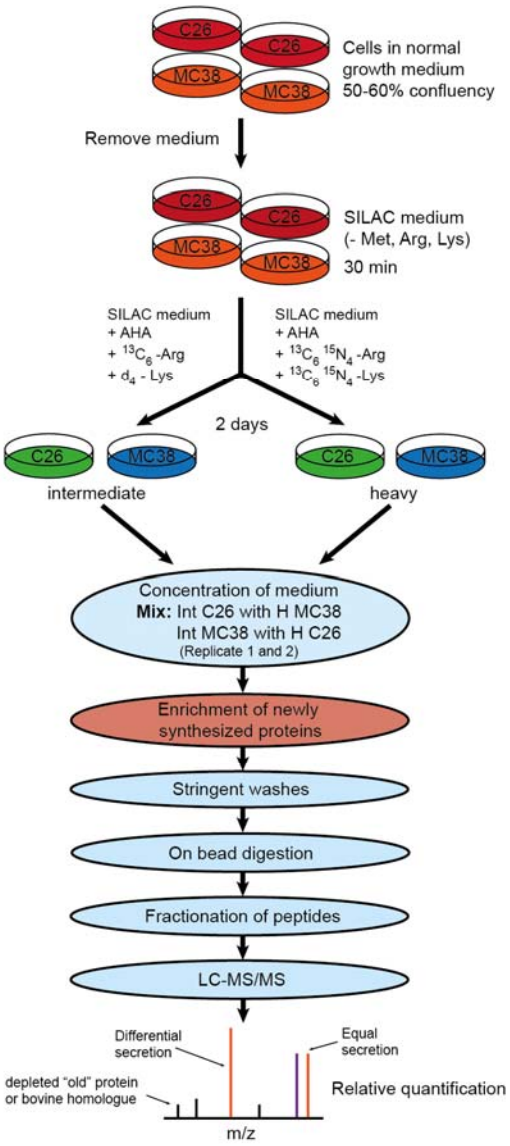

Fig. 48: Schematic overview of the sample preparation and processing for the quantitative secretome analysis. *Scheme was adapted from Eichelbaum K., 2012.*

6.1.6 Overexpression of ready-to use cDNA expression clones

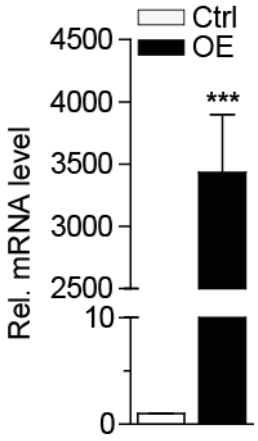

Fig. 49: Overexpression of Ataxin10 in HEK293A cells. *1 x 10^5 HEK293 A cells per well were seeded on 6-well plates 24 h prior to transfection. Cells were transfected with a ready-to-use cDNA expression plasmids carrying the human sequence for ATAXIN10 (ATXN10) (Source BioScience) using calciumphosphate transfection protocol. Medium was changed 24 h post transfection and conditioned medium was produced. RNA was isolated from untreated HEK293 A cells (Ctrl) and from HEK293A cells that were transfected with the overexpression (OE) plasmid using the RNeasy® Micro Kit. Transcription levels of ATXN10 were assessed by using the TaqMan system. n ≥ 5, mean ± SEM. *indicates significance by using Student´s t-test with Welch-correction, *** p < 0.001.*

6.1.7 Ataxin10 concentrations in APC delta 580 mice sera

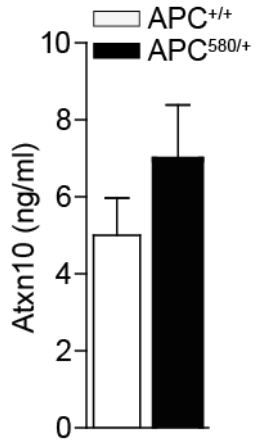

Fig. 50: Ataxin10 level in serum of APC delta 580 mice. *Levels of Ataxin10 (Atxn10) were determined using a murine-specific ELISA. n ≥ 5, mean ± SEM. No significance using Student's t-test with Welch correction.*

6.1.8 Single knockdown of cachexokines

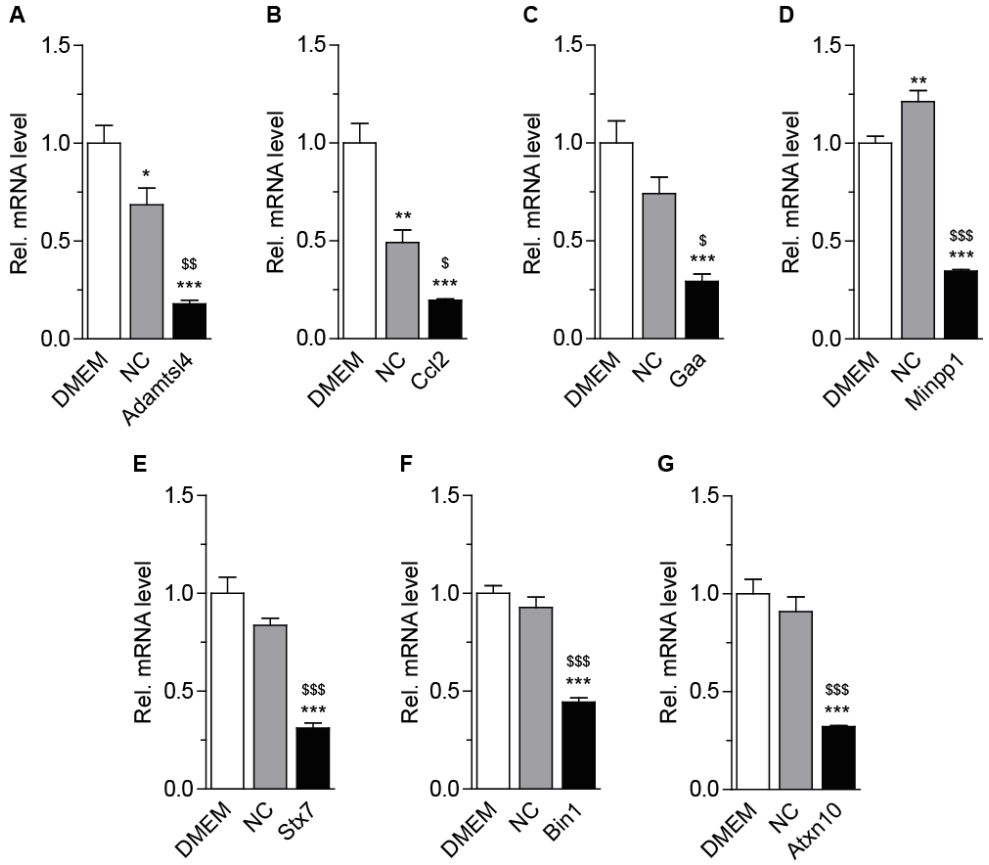

Fig. 51: Single knockdown of the highly potential "cachexokines" mediated by siRNA. *C26 cells were seeded at 1 x 10^5 cells per well on 6-well plates and were transfected 24 h later using HiPerFect Transfection Reagent and 5nM siRNA. Medium was changed 24 h post transfection and conditioned medium was produced. RNA was isolated from C26 cells that were untreated (DMEM) and C26 cells that were either transfected with negative control siRNA (NC) or with siRNA directed against the indicated genes using the RNeasy® Micro Kit. Transcription levels of indicated genes were assessed by using the TaqMan system. Relative expression levels of* ***A)*** *Adamts like 4 (Adamtsl4),* ***B)*** *Chemokine ligand 2 (Ccl2),* ***C)*** *Glucosidase alpha acid (Gaa),* ***D)*** *Multiple inositol-polyphosphate phosphatase 1 (Minpp1),* ***E)*** *Syntaxin 7 (Stx7),* ***F)*** *Bridging integrator 1 (Bin1) and* ***G)*** *Ataxin10 (Atxn10). n = 4, mean ± SEM. *indicates significance by comparison to DMEM using 1-way ANOVA, Bonferroni post-test, *p < 0.05, **p < 0.01, *** p < 0.001. $indicates significance between NC and the individual gene using 1-way ANOVA, Bonferroni post-test, $ p < 0.05, $$ p < 0.01, $$$ p < 0.001.*

6.1.9 Combined knockdown of cachexokines

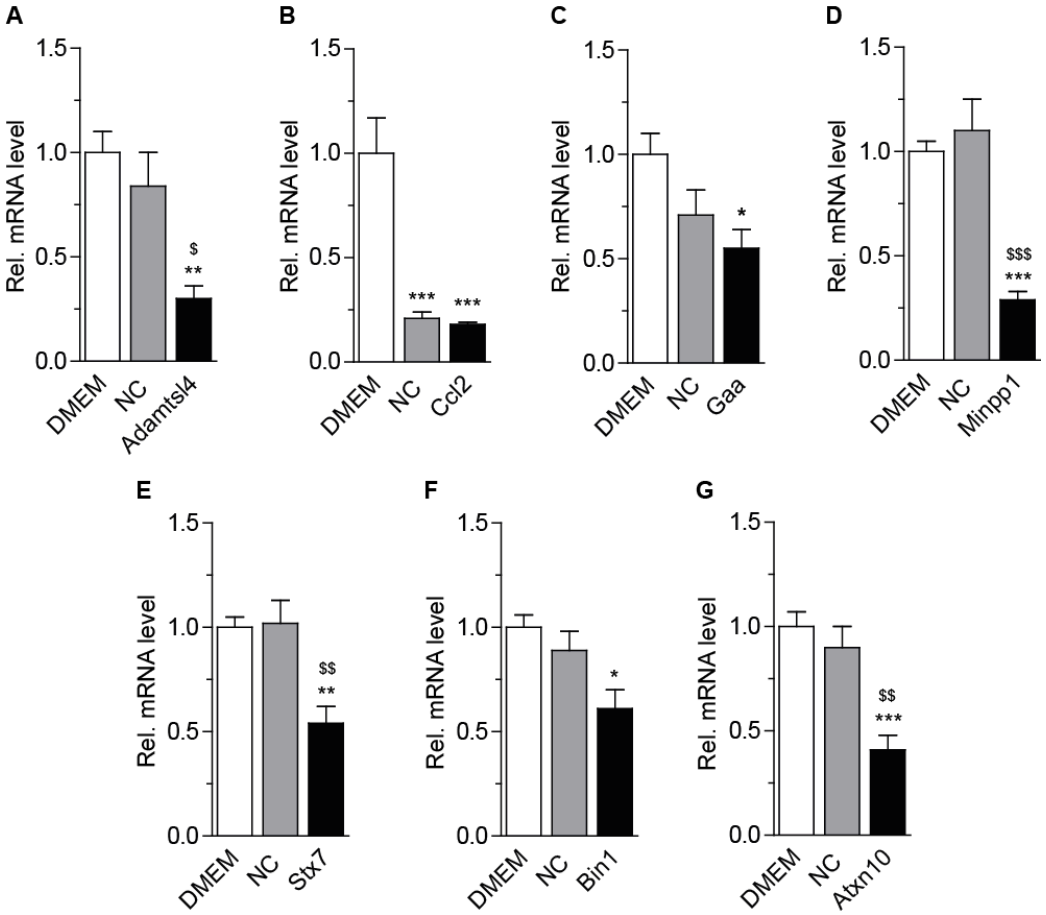

Fig. 52: Knockdown of all 7 highly potential "cachexokines" at once mediated by siRNA. *C26 cells were seeded at 1 x 10^5 cells per well on 6-well plates and were transfected 24 h later using HiPerFect Transfection Reagent and 5nM of each siRNA. Medium was changed 24 h post transfection and conditioned medium was produced. RNA was isolated from C26 cells that were untreated (DMEM) and C26 cells that were either transfected with negative control siRNA (NC) or with siRNA directed against the indicated genes using the RNeasy® Micro Kit. Transcription levels of indicated genes were assessed by using the TaqMan system. Relative expression levels of* ***A)*** *Adamts like 4 (Adamtsl4),* ***B)*** *Chemokine ligand 2 (Ccl2),* ***C)*** *Glucosidase alpha acid (Gaa),* ***D)*** *Multiple inositol-polyphosphate phosphatase 1 (Minpp1),* ***E)*** *Syntaxin 7 (Stx7),* ***F)*** *Bridging integrator 1 (Bin1) and* ***G)*** *Ataxin10 (Atxn10). n = 6, mean ± SEM. *indicates significance by comparison to DMEM using 1-way ANOVA, Bonferroni post-test, *p < 0.05, **p < 0.01, *** p < 0.001. $indicates significance between NC and the individual gene using 1-way ANOVA, Bonferroni post-test, $$ p < 0.01, $$$ p < 0.001.*

6.2 Abbreviations

ABC Reagent	Avidin-Biotin Complex Reagent
Abd.	Abdominal
ACAD	Acyl-CoA Dehydrogenase
Acadvl	Acyl-Coenzyme A Dehydrogenase Very Long-Chain
Acat2	Acetyl-Coenzyme A Acetyltransferase 2
ACC	Acetyl-CoA
Acsl1	Acyl-CoA Synthase Long-Chain Family Member 1
ActRIIB	Activin Type II Receptor
ACVR2	Activin Receptor Type 2
ADP	Adenosine Diphosphat
AHA	Azidohomoalanine
AIDS	Autoimmune Deficiency Syndrome
AMPK	Adenosine Monophosphate-Activated Protein Kinase
ANOVA	Analysis of Variance
AOM	Azoxymethane
Ant1	Adenine Nucleotide Translocase 1
Ant2	Adenine Nucleotide Translocase 1
AJCC	American Joint Committee on Cancer
Anp	Atrial Natriuretic Peptide
APC	Adenomatous Polyposis Coli
APR	Acute Phase Response
APS	Ammonium Persulfate
Arg	Arginine
Arntl	Aryl Hydrocarbon Receptor Nuclear Translocator-like
ATGL	Adipose Triglyceride Lipase
ATP	Adenosine Triphosphate
AUC	Area Under Curve
BAX	BCL2 Associated Protein X
BBS	Borate Buffered Saline
BCA	Bicinchoninic Acid
BCL2	B Cell Lymphoma 2
BDM	2,3-Butanedionemonoxime
BES	N,N-Bis(2-hydroxyethyl)-2-aminoethanesulfonic Acid
BMI	Body Mass Index
Bnp	Brain Natriuretic Peptide
bp	Base pair
BRAF	v-raf Murine Sarcoma Viral Oncogene Homolog B
BSA	Bovine Serum Albumin
C26	Colon-26, mouse colon carcinoma cell line
cAMP	Cyclic Adenosine Monophosphate
CCND1	Cyclin D1
CD36	Cluster of Differentiation 36
cDNA	Complementary DNA
CoA	Coenzyme A

Col1a2	Collagen type I alpha 2
Col3a1	Collagen type III alpha 1
Conc.	Concentration
COPD	Chronic Obstructive Pulmonary Disease
Cpt1α	Carnitine Palmitoyltransferase 1 alpha
Cr	Charles River
Cre	Cyclic recombinase
CRF	Corticotropin-releasing Factor
cRNA	Complementary RNA
CRP	C-Reactive Protein
CT	Carnitine:Acylcarnitine Translocase
Ctrl	Control
DAB	3,3'-Diaminobenzidine
DAPI	4',6-Diamidin-2-phenylindol
Dbp	D Site of Albumin Promoter Binding Protein
DCC	Deleted in Colon Cancer
Diff	Difference
Dgat1	Diglyceride Acyltransferase 1
dH_2O	Distilled H_2O
dl	Deciliter
DMEM	Dulbecco's Modified Eagle's Medium
DMSO	Dimethylsulfoxide
DNA	Deoxyribonucleic Acid
dNTP	Deoxyribonucleotide Triphosphate
DPBS	Dulbecco's Phosphate-Buffered Saline
DTT	Dithiothreitol
ECH	Enoyl-CoA Hydratase
EchoMRI	Echo Magnetic Resonance Imaging
ECL	Enhanced Chemiluminescence
E.coli	*Eschericha coli*
EDTA	Ethylenediaminetetraacetic Acid
EDV	End-Diastolic Volume
EF	Ejection Fraction
eIF2α	Eukaryotic Initiation Factor 2 alpha
ELISA	Enzyme-linked Immunosorbent Assay
ESV	End-Systolic Volume
FA	Fatty Acid
FAP	Familiar Adenomatous Polyposis
FAT	FA Translocase
Fatp	Fatty Acid Transporter
FBS	Fetal Bovine Serum
FCCP	Carbonyl cyanide 4-(trifluoromethoxy)phenylhydrazone
FDR	False Discovery Rate
FFA	Free Fatty Acid
Fig.	Figure

FITC	Fluorescein isothiocyanate
fl	Femtoliter
FoxO	Forkhead box O
FS	Fractional Shortening
Gaa	Glucosidase Alpha, Acid
GC	Gastrocnemius Muscle
GI	Gastrointestinal
GIST	Gastrointestinal Stromal Tumor
Glut	Glucose Transporter
GO-BP	Gene Ontology Biological Processes
GSEA	*Gene Set Enrichment Analysis®*
GST	Gluthation-S-Transferase
HADH	Hydroxyacyl-CoA Dehydrogenase
Hadha	Hydroxyacyl-CoA Dehydrogenase/3-Ketoacyl-CoA Thiolase/Enoyl-CoA Hydratase, Alpha Subunit
Hb	Hemoglobin
H&E	Hematoxylin & Eosin
(H+L)	Heavy and Light chain
HEK293 A	Human Embryonic Kidney 293 A cell line
HNPCC	Hereditary Non-polyposis Colorectal Cancer
HRP	Horseradish Peroxidase
hrs	Hours
HSL	Hormone Sensitive Lipase
HW	Heart Weight
Hz	Hertz
IFN-γ	Interferon-gamma
IGF-1	Insulin-like Growth Factor-1
IgG	Immunoglobulin G
IL-1	Interleukin-1
IL-6	Interleukin-6
IlL-8	Interleukin-8
IQR	Interquartile Range
ITS	Insulin-Transferrin-Sodium Selenite
IVT	*in vitro* Transcription
3-KAT	3-Ketoacyl-CoA Thiolase
kb	Kilobase
KEGG	Kyoto Encyclopedia of Genes and Genomes
KHB	Krebs-Henseleit-Buffer
KRAS	Kirsten Rat Sarcoma Viral Oncogene Homolog
LB	Ludmilla Broth
LC3	Microtubule-associated protein light chain 3
LC-MS/MS	Liquid Chromatography Tandem Mass Spectrometry
LMF	Lipid-Mobilizing Factor
Lpl	Lipoprotein Lipase
LTQ	Linear Trap Quadrupole
LV	Left Ventricular

LVEDD	Left Ventricular End-Diastolic Diameter
LVESD	Left Ventricular End-Systolic Diameter
Lys	Lysine
M-Mode	Motion-Mode
MAC16	Murine Adenocarcinoma 16
MAFbx	Muscle Atrophy F Box
MC38	Mouse Colon 38, mouse colorectal carcinoma cell line
McCT	Multiplex Cell Contamination Test
MCH	Mean Corpuscular/Cell Hemoglobin
MCP-1	Monocyte Chemotactic Protein-1
MCV	Mean Corpuscular/Cell Volume
Met	Methionine
mGPS	Modified Glasgow Prognostic Score
MHC	Myosin Heavy Chain
Min	Multiple Intestinal Neoplasia
MLH1	MutL Homolog 1
MMR	Mismatch-repair
MOPS	3-(N-morpholino)propanesulfonic Acid
mRNA	Messenger RNA
MSH2	MutS Homolog 2
MTE	Mitochondrial Thioesterase
mTOR	Mammalian Target of Rapamycin
MuRF1	Muscle RING finger 1
MYC	V-Myc Avian Myelocytomatosis Viral Oncogene Homolog
MyoD	Myogenic Differentiation
NA	Numerical Aperture
NaAc	Sodium Acetate
NC	Negative Control
NCI	National Cancer Institute
NF-κB	Nuclear Factor-kappa B
NIH	National Institutes for Health
No.	Number
OCR	Oxygen Consumption Rate
ORA	Overrepresentation Analysis
PBS	Phosphate-Buffered Saline
PCR	Polymerase Chain Reaction
PenStrep	Penicillin-Streptomycin
Per1	Period Circadian Protein Homolog 1
pg	Picogram
PI3K	Phosphatidylinositol 3 Kinase
PIF	Proteolysis-Inducing Factor
PLIN	Perilipin
PMSF	Phenylmethanesulfonylfluoride
Postn	Periostin
PPARα	Peroxisomal Proliferator Activated Receptor alpha

ppm	Parts Per Million
PS	Polystyrene
PTHrP	Parathyroid Hormone-related Protein
PV loop	Pressure-Volume loop
qPCR	Quantitative PCR
RAS	Rat Sarcoma
RDW	Red Blood Cell Distribution Width
REE	Resting Energy Expenditure
Rel.	Relative
RNA	Ribonucleic Acid
ROS	Reactive Oxygen Species
Rpm	Revolutions per minute
S6K	S6 Kinase
SCWD	Sarcopenia, Cachexia and Wasting Disorders
SDS	Sodium Dodecyl Sulfate
siRNA	Small Interfering RNA
SILAC	Stable Isotope Label with Amino Acids in Cell Culture
Smad2/3/4	Mothers against Decapentaplegic Homolog 2/3/4
SOCH	Syndrome of the Cachectic Heart
SRB	Sulforhodamine B
STAT3	Signal Transducer and Activator of Transcription 3
SV	Stroke Volume
TG	Triglyceride
Tab.	Table
Taq	Thermus aquaticus
TBE	Tris-Borat-EDTA
TBS	Tris-Buffered Saline
TBS-T	TBS-Tween
TEMED	Tetramethylethylendiamin
TGF-β	Transforming Growth Factor-beta
TGFBR2	TGF-β Receptor Type 2
TL	Tibia Length
TNF-α	Tumor Necrosis Factor-alpha
TNM	Tumor-Node-Metastases
TP53	Tumor Protein 53
TRITC	Tetramethylrhodamine B isothiocyanate
TX	Triton™ X-100
U	Units
UCP	Uncoupling Protein
UICC	Union of International Cancer Control
UPLC	Ultra Performance Liquid Chromatography
UPS	Ubiquitin-Proteasome System
UV	Ultraviolet
VCP	Valosin Containing Protein
VLDL	Very-Low Density Lipoprotein
Vol.	Volume

w/o	without
WHO	World Health Organization
ZAG	Zinc-alpha-2 Glycoprotein

6.3 Figures and Tables

6.3.1 Figures

6.3.2 Tables

6.4 References

Ambrus J.L. et al. (1975). Causes of death in cancer patients. J Med 6(1): 61-4.

Ando K. et al. (2014). Tocilizumab, a proposed therapy for the cachexia of Interleukin6-expressing lung cancer. Plos One 9(7): e102436.

Banerjee I. et al. (2007). Determination of cell types and numbers during cardiac development in the neonatal and adult rat and mouse. Am J Physiol Heart Circ Physiol 293(3): H1883-91.

Bendtsen J.D. et al. (2004). Improved prediction of signal peptides: SignalP 3.0. J Mol Biol 340(4): 783-95.

Bendtsen J.D. et al. (2004). Feature-based prediction of non-classical and leaderless protein secretion. Protein End Des Sel 17(4): 349-56.

Bennani-Baiti N., Walsh D. (2011). Animal models of the cancer anorexia-cachexia syndrome. Support Care Cancer 19(9): 1451-63.

Berriel Diaz M. et al., (2008). Nuclear receptor cofactor receptor interacting protein 140 controls hepatic triglyceride metabolism during wasting in mice. Hepatology 48(3): 782-91.

Bertram J.S., Janik P. (1980). Establishment of a cloned line of Lewis Lung Carcinoma cells adapted to cell culture. Cancer Lett 11(1): 63-73.

Beutler B., Cerami A. (1986). Cachectin and tumour necrosis factor as two sides of the same biological coin. Nature 320: 584-8.

Bibby M.C. et al. (1987). Characterization of a transplantable adenocarcinoma of the mouse colon producing cachexia in recipient animals. J Natl Cancer Inst 78(3): 539-46.

Bing C. et al. (2002). Expression of uncoupling proteins-1, -2 and -3 mRNA is induced by an adenocarcinoma-derived lipid-mobilizing factor. Br J Cancer 86(4): 612-8.

Bing R.J. et al. (1954). Metabolism of the human heart: II. Studies on fat, ketone and amino acid metabolism. Am J Med 16(4): 504-15.

Bruera E. et al. (1999). Thalidomide in patients with cachexia due to terminal cancer: Preliminary report. Ann Oncol 10(7): 857-9.

Burch G.E. et al. (1968). The cachectic heart, a clinicopathologic, electrocardiographic and roentgenographic entity. Chest 54: 5-11.

Busquet S. et al. (2005). Activation of UCPs gene expression in skeletal muscle can be independent on both circulating fatty acids and food intake. Involvement of ROS in a model of mouse cancer cachexia. FEBS Lett 579(3): 717-22.

Cameron V.A., Ellmers L.J. (2003). Minireview: Natriuretic peptides during development of the fetal heart and circulation. Endocrinology 144(6): 2191-4.

Castell J.V. et al. (1989). Interleukin-6 is the major regulator of acute phase protein synthesis in adult human hepatocytes. FEBS Lett 242(2): 237-9.

Colnot S. et al. (2004). Colorectal cancers in a new mouse model of familial adenomatous polyposis: influence of genetic and environmental modifiers. Lab Invest 84(12): 1619-30.

Conrad C.H. et al. (1995). Myocardial fibrosis and stiffness with hypertrophy and heart failure in the spontaneously hypertensive rat. Circulation 91(1): 161-70.

Corbett T.H. et al. (1975). Tumor induction relationships in development of transplantable cancers of the colon in mice for chemotherapy assays, with a note on carcinogen structure. Cancer Res 35: 2434-9.

Cosper P.F., Leinwand L. (2011). Cancer causes cardiac atrophy and autophagy in a sexually dimorphic manner. Cancer Res 71(5): 1710-20.

Costelli P. et al. (1993). Tumor necrosis factor-a mediates changes in tissue protein turnover in a rat cancer cachexia model. J Clin Invest 92: 2783-9.

Costelli P. et al. (2001). Activation of Ca2+-dependent proteolysis in skeletal muscle and heart in cancer cachexia. Br J Cancer 84(7): 946-50.

Costello-Boerrigter L.C. (2012). Cardiac natriuretic peptides: contributors to cardiac cachexia or possible anti-obesity agents or both? Diabetes 61: 2403-4.

Cox J., Mann M. (2008). MaxQuant enables high peptide identification rates, individualized p.p.b.-range mass accuracies and proteome-wide protein quantification. Nat Biotechnol 26(12): 1367-72.

Cox J. et al. (2011). Andromeda: a peptide search engine integrated into the MaxQuant environment. J Proteome Res 10(4): 1794-1805.

DeBoer M.D. (2009). Animal models of anorexia and cachexia. Expert Opin Drug Discov 4(11):1145-55.

Dewys W.D. et al. (1980). Prognostic effect of weight loss prior to chemotherapy in cancer patients. Eastern Cooperative Oncology Group. Am J Med 69(4): 491-7.

Dodson S. et al. (2011). Muscle wasting in cancer cachexia: clinical implications, diagnosis, and emerging treatment strategies. Annu Rev Med 62(1): 265-79.

Donohoe C.L. et al. (2011). Cancer cachexia: mechanisms and clinical implications. Gastroenterol Res Pract 2011: 601434.

Drott C. et al. (1989). Protein synthesis, myosin ATPase activity and myofibrillar protein composition in hearts from tumour-bearing rats and mice. Biochem J 264(1): 191-8.

Drott C., Lundholm K. (1990). Glucose uptake and amino acid metabolism in perfused hearts from tumor-bearing rats. J Surg Res 49(1): 62-8.

Earl C.A. et al. (1978). Turnover rates of muscle protein in cardiac and skeletal muscles of dog, fowl, rat and mouse: turnover rate related to muscle function. Aust J Exp Biol Med Sci 56(3):265-77.

Edelmann W. et al. (2010). Tumorigenesis in Mlh1 and Mlh1/Apc1638N mutant mice. Cancer Res 59(6): 1301-7.

Eichelbaum K. et al. (2012). Selective enrichment of newly synthesized proteins for quantitative secretome analysis. Nat Biotechnol 30(10): 984-90.

Engle S.J. et al. (1999). Transforming growth factor beta1 suppresses nonmetastatic colon cancer at an early stage of tumorigenesis. Cancer Res 59(14): 3379-86.

Evangelista L.S. et al. (2008). Correlates of fatigue in patients with heart failure. Prog Cardiovasc Nurs 23(1): 12–17.

Evans W.J. et al. (2008). Cachexia: a new definition: Clin Nutr 27(6): 793-9.

Fearon K. et al. (2011). Definition and classification of cancer cachexia: an international consensus. Lancet Oncol 12(5): 489-95.

Fearon K. et al. (2012). Cancer cachexia: Mediators, signaling, and metabolic pathways. Cell Metab 16(2): 153-66.

Fong Y. et al. (1989). Cachectin/TNF or IL-1 alpha induces cachexia with redistribution of body proteins. Am J Physiol 256(3 Pt 2): R659-65.

Fowler J.K., Godlee R.J. (1898). The diseases of the lung. Longmans, Green and Co.

Friedberg C.K. (1966). Diseases of the heart. ed. 3. Philadelphia: WB Saunders, p807.

Fu X. et al. (1991). Models of human metastatic colon cancer in nude mice orthotopically constructed by using histologically intact patient specimens. Proc Nati Acad Sci USA 88(20): 9345-9.

Gentleman R.C. et al. (2004). Bioconductor: open software development for computational biology and bioinformatics. Genome Biol 5(10), R80.

Goldberg I.J. et al. (2012). Lipid metabolism and toxicity in the heart. Cell Metab 15(6): 805-12.

Gordon J.N. et al. (2005). Thalidomide in the treatment of cancer cachexia: a randomised placebo controlled trial. Gut 54: 540-5.

Gordon J.N. et al. (2005). Cancer Cachexia. Q J Med 98(11): 779-88.

Gottlieb M.S. et al. (1983). The acquired immunodeficiency syndrome. Ann Intern Med 99(2): 208-20.

Guaitani A. et al. (1982). Walker carcinoma 256: a model for studies on tumor-induced anorexia and cachexia. Oncology 39(3): 173-8.

Gustafsson A.B., Gottlieb R.A. (2009). Autophagy in ischemic heart disease. Circ Res 104(2): 150-8.

Hirai K. et al. (1998). Biological evaluation of a lipid-mobilizing-factor factor isolated from the urine of cancer patients. Cancer Res 58(11): 2359-65.

Hsieh W.P. et al. (2003). Mixed-model reanalysis of primate data suggests tissue and species biases in oligonucleotide-based gene expression profiles. Genetics 165(2): 747-57.

Imperlini E. et al. (2013). The secretome signature of colon cancer cell lines. J Cell Biochem 114(11): 2577-87.

Inui A. (2002). Cancer anorexia-cachexia syndrome: current issues in research and management. CA Cancer J Clin 52(2): 72-91.

Jäger J. et al. (2014). Hepatic transforming growth factor-β 1 stimulated clone-22 D1 controls systemic cholesterol metabolism. Mol Metab 3(2): 155-66.

Jain E. et al. (2009). Infrastructure for the life sciences: design and implementation of the UniProt website. BMC Bioinformatics 10: 136.

Janssen K.P. et al. (2002). Targeted expression of oncogenic K-ras in intestinal epithelium causes spontaneous tumorigenesis in mice. Gastroenterology 123(2): 492-504.

Jatoi A. et al. (2010). A placebo-controlled, double-blind trial of infliximab for cancer-associated weight loss in elderly and/or poor performance non-small cell lung cancer patients (N01C9). Lung Cancer 68(2): 234-9.

Jones A. et al. (2013). TSC22D4 is a molecular output of hepatic wasting metabolism. EMBO Mol Med 5(2):294-308.

Katz A.M., Katz P.B. (1962). Disease of the heart in the works of Hippocrates. Br Heart J 24(3): 257-64.

Khal J. et al. (2005). Expression of the ubiquitin-proteasome pathway and muscle loss in experimental cancer cachexia. Br J Cancer 93(7): 774-80.

Khan Z.H. et al. (2003). Oesophageal cancer and cachexia: the effect of short-term treatment with thalidomide on weight loss and lean body mass. Aliment Pharmacol Ther 17(5): 677-82.

Kir S. et al. (2014). Tumour-derived PTH-related protein triggers adipose tissue browning and cancer cachexia. Nature, Epub ahead of print.

Krogh A. et al. (2001). Predicting transmembrane protein topology with a hidden Markov model: application to complete genomes. J Mol Biol 305(3): 567-80.

Kucherlapati M.H. et al. (2010). An Msh2 conditional knockout mouse for studying intestinal cancer and testing anticancer agents. Gastroenterology 138: 993-1002, e1.

Kuraguchi M. et al. (2006). Adenomatous Polyposis Coli (APC) is required for normal development of skin and thymus. PLoS Genet 2(9): e146.

Lapiere C.M. et al. (1977). Interaction between collagen type I and type III in conditioning bundles organization. Connect Tissue Res 5(1): 21-9.

Liu Z. et al. (2000). The ubiquitin-proteasome proteolytic pathway in heart vs skeletal muscle: effects of acute diabetes. Biochem Biophys Res Commun 276(3): 1255-60.

Lokireddy S. et al. (2012). Myostatin is a novel tumoral factor that induces cancer cachexia. Biochem J 446(1): 23-36.

Lompre A.M. et al. (1984). Expression of the cardiac ventricular alpha- and beta-myosin heavy chain genes is developmentally and hormonally regulated. J Biol Chem 259(10): 6437-46.

Lopaschuk G.D. et al. (2010). Myocardial fatty acid metabolism in health and disease. Physiol Rev 90(1): 207-258.

Lowes B.D. et al. (1997). Changes in gene expression in the intact human heart. Downregulation of α-myosin heavy chain in hypertrophied, failing ventricular myocardium. J Clin Invest 100(9): 2315-24.

Lundholm K. et al. (1978). A comparative study of the influence of malignant tumor on host metabolism in mice and man: evaluation of an experimental model. Cancer 42(2): 453-61.

März P. et al. (2006). Ataxin-10 interacts with O-linked beta-N-acetylglucosamine transferase in the brain. J Biol Chem 281(29): 20263-70.

Maltzman T. et al. (1997). AOM-induced mouse colon tumors do not express full-length APC protein. Carcinogenesis 18: 2435-9.

Manoli T. et al. (2006). Group testing for pathway analysis improves comparability of different microarray datasets. Bioinformatics 22(20): 2500-6.

Matthys P. et al. (1991). Anti-interferon-γ antibody treatment, growth of Lewis lung tumours in mice and tumour-associated cachexia. Europ J Cancer 27(2): 182-7.

Mirza K.A. et al. (2011). Attenuation of muscle atrophy by an N-terminal peptide of the receptor for proteolysis-inducing factor (PIF). Br J Cancer 105(1): 83-8.

Mjos O.D. (1971). Effect of free fatty acids on myocardial function and oxygen consumption in intact dogs. J Clin Invest 50(7): 1386-9.

Morley J.E. et al. (2006). Cachexia: pathophysiology and clinical relevance. Am J Clin Nutr 83: 735-43.

Moser A.R. et al. (1990). A dominant mutation that predisposes to multiple intestinal neoplasia in the mouse. Science 247(4940): 322-4.

Nag A.C. (1980). Study of non-muscle cells of the adult mammalian heart: a fine structural analysis and distribution. Cytobis 28(109): 41-61.

Nikolsky Y. et al. (2005). A novel method for generation of signature networks as biomarkers from complex high throughput data. Toxicol Lett 158(1): 20-9.

Norton J.A. et al. (1985). Parabiotic transfer of cancer anorexia/cachexia in male rats. Cancer Res 45: 5547-52.

Oliff A. et al. (1987). Tumors secreting human TNF/cachectin induce cachexia in mice. Cell 50(4): 555-63.

Pande S.V., Blanchaer M.C. (1971). Reversible inhibition of mitochondrial adenosine diphosphate phosphorylation by long chain acyl coenzyme A esters. J Biol Chem 246(2): 402-11.

Papanikolaou A. et al. (1997). Azoxymethane-induced colon tumors and aberrant crypt foci in mice of different genetic susceptibility. Cancer Lett 130(1-2): 29-34.

Postic C. et al. (1994). Development and regulation of glucose transporter and hexokinase expression in rat. Am J Physiol 266(4): E548-59.

Rappsilber J. et al. (2003). Stop and go extraction tips for matrix-assisted laser desorption/ionization, nanoelectrospray, and LC/MS sample pretreatment in proteomics. Anal Chem 75(3): 663-70.

Reitmair A.H. et al. (1996). Spontaneous intestinal carcinomas and skin neoplasms in Msh2-deficient mice. Cancer Res 56(16): 3842-9.

Robert-Koch-Institut und die Gesellschaft der epidemiologischen Krebsregister in Deutschland e.V. (2013). Krebs in Deutschland 2009/2010. 9. Ausgabe.

Roy J. (2007). SAS for mixed models. In J Biopharm Stat, Littell RC, Milliken GA, Stroup WW, Wolfinger RD, Schabenberger O (eds), 2nd edn, Vol. 17, pp 363-5.

Rubattu S. et al. (2008). Natriuretic peptides: an update on bioactivity, potential therapeutic use, and implication in cardiovascular diseases. Am J Hypertens 21(7): 733-41.

Schmitt M., Pawlita M. (2009). High-throughput detection and multiplex identification of cell contaminations. Nucleic Acids Res 37(18): e119.

Sheppard B.C. et al. (1990). Prolonged survival of tumor-bearing rats with repetitive low-dose recombinant tumor necrosis factor. Cancer Res 50(13): 3928-33.

Sherry B.A. et al. (1989). Anticachectin/tumor necrosis factor-alpha antibodies attenuate development of cachexia in tumor models. Faseb J 3(8): 1956-62.

Shin J. et al. (2014). Discovery of melanotransferrin as a serological marker of colorectal cancer by secretome analysis and quantitative proteomics. J Proteome Res [Epub ahead of print]

Sjöström M. et al. (1987). Ultrastructural changes and enzyme activities for energy production in hearts concomitant with tumor-associated malnutrition. J Surg Res 42(3): 304-13.

Su L.K. et al. (1992). Multiple intestinal neoplasia caused by a mutation in the murine homolog of the APC gene. Science 256(5057): 668-70.

Sun T.W., Wang L.X. (2007). Low levels of B-type natriuretic peptide predict poor clinical outcomes in patients with chronic and advanced heart failure. Med Hypotheses 68(3): 677-9.

Skulachev V.P. (1991). Fatty acid circuit as a physiological mechanism of uncoupling of oxidative phosphorylation. FEBS 294(3): 158-62.

Smyth G.K. (2004). Linear models and empirical bayes methos for assessing differential expression in microarray experiments. Stat Appl Genet Mol Biol 3, Article 3.

Springer J. et al. (2014). Prevention of liver cancer cachexia-induced cardiac wasting and heart failure. Eur Heart J 35(14): 932-41.

St John D.J. et al. (1993). Cancer risk in relatives and patients with common colorectal cancer. Ann Intern Med 118(10): 785-90.

Strassmann G. et al. (1992). Evidence for the involvement of Interleukin 6 in experimental cancer cachexia. J Clin Invest 89: 1681-4.

Straub B.K. et al. (2008). Differential pattern of lipid droplet-associated proteins and *de novo* perilipin expression in hepatocyte steatogenesis. Hepatology 47(6): 1936-46.

Subramanian A. et al. (2005). Gene set enrichment analysis: a knowledge-based approach for interpreting genome-wide expression profiles. Proc Natl Acad Sci USA 102(43): 15545-50.

Suzuki H. et al. (2013). Cancer cachexia – pathophysiology and management. J Gastroenterol 48(5): 574-94.

Takaku K. et al. (1998). Intestinal tumorigenesis in compound mutant mice of both Dpc4 (Smad4) and Apc genes. Cell 92(5): 645-56.

Taketo M.M., Edelmann W. (2009). Mouse models of colon cancer. Gastroenterology 136(3): 780-98.

Tan B.H. et al. (2008). Cachexia: prevalence and impact in medicine. Curr Opin Clin Nutr Metab Care 11(4): 400-7.

Tanaka Y. et al. (1990). Experimental cancer cachexia induced by transplantable colon 26 adenocarcinoma in mice. Cancer Res 50(8): 2290-5.

Tessitore L. et al. (1987). Regulation of protein turnover versus growth state: ascites hepatoma as a model for studies both in the animal and in vitro. Arch Biochem Biophys 255(2): 372-84.

Tian M. et al. (2010). Cardiac alterations in cancer-induced cachexia in mice. Int J Oncol 37(2): 347-53.

Tian M. et al. (2011). Evidence for cardiac atrophic remodeling in cancer-induced cachexia in mice. Int J Oncol 39(5):1321-6.

Tisdale M.J. (1997). Biology of cachexia. J Natl Cancer Inst 89(23): 1763-73.

Tisdale M.J. (2009). Mechanisms of cancer cachexia. Physiol Rev 89(2): 381-410.

Todorov P. et al. (1996). Characterization of a cancer cachectic factor. Nature 379(6567): 739-42.

Todorov P. et al. (2007). Identification and characterization of a membrane receptor for proteolysis-inducing factor on skeletal muscle. Cancer Res 67(23): 11419-27.

Tracey K.J. et al. (1988). Cachectin/tumor necrosis factor induces cachexia, anemia, and inflammation. J Exp Med 167(3): 1211-27.

Tsoli M. and Robertson G. (2013). Cancer cachexia: malignant inflammation, tumorkines, and metabolic mayhem. Trends Endocrinol Metab 24(4): 174-83.

Tzika A.A. et al. (2013). Skeletal muscle mitochondrial uncoupling in a murine cancer cachexia model. Int J Oncol 43(3): 886-94.

Vesely D.L. (2013). Natriuretic peptides' metabolic targets for treatment of cancer. J Investig Med 61(5): 816-22.

Villen J., Gygi S.P. (2008). The SCX/IMAC enrichment approach for global phosphorylation analysis by mass spectrometry. Nat Protoc 3(10): 1630-8.

von Haehling S. et al. (2010). Cachexia as a major underestimated and unmet medical need: facts and numbers. J Cachexia Sarcopenia Muscle 1: 1-5.

Waragai M. et al. (2006). Ataxin 10 induces neuritogenesis via interaction with G-protein beta2 subunit. J Neurosci Res 83(7): 1170-8.

White J.P. et al. (2011). The regulation of skeletal muscle protein turnover during the progression of cancer cachexia in the Apc(Min/+) mouse. Plos One 6(9): e24650.

Wiedenmann B. et al. (2008). A multicenter, phase II study of infliximab plus gemcitabine in pancreatic cancer cachexia. J Support Oncol 6(1): 18-25.

Wisniewski J.R. et al. (2009). Combination of FASP and StageTip-based fractionation allows in-depth analysis of the hippocampal membrane proteome. J Proteome Res 8(12): 5674-8.

Xu H. et al. (2011). Myocardial dysfunction in an animal model of cancer cachexia. Life Sci 88(9-10): 406-10.

Zag R. (1974). Development and proliferative capacity of cardiac muscle cells. Circ Res 35(2): suppl II: 17-26.

Zaki M.H. et al. (2004). CNTO 328, a monoclonal antibody to IL-6, inhibits human tumor-induced cachexia in nude mice. Int J Cancer 111: 592-5.

Zeng X. et al. (2013). Quantitative secretome analysis reveals the interactions between epithelia and tumor cells by in vitro modulating colon cancer microenvironment. J Proteomics 89: 51-70.

Zhao S. et al. (2014). Periostin expression is upregulated and associated with myocardial fibrosis in human failing hearts. J Cardiol 63(5): 373-8.

Zhou X. et al. (2010). Reversal of cancer cachexia and muscle wasting by ActRIIB antagonism leads to prolonged survival. Cell 142(4): 531-43.